FRIB HIGH RIGIDITY SPECTROMETER

CONCEPTUAL DESIGN REPORT

Zegers, Remco

FRIB High Rigidity Spectrometer

Table of Contents

1 Front Matter

1.1 Contributors

A basis for this conceptual design report was the 2014 whitepaper, titled "A high Rigidity Spectrometer for FRIB", which was written by the HRS Working Group. The HRS Working Group presently consists of scientist from the following US institutions:

US National Laboratories	US Universities & Colleges	
Argonne Nat.l Lab.	Augustana College	Ohio University
Lawrence Berkeley Nat'l Lab.	Bucknell University	Ohio Wesleyan University
Lawrence Livermore Nat'l Lab.	Central Michigan University	Rutgers University
Los Alamos Nat'l Lab.	Florida State University	Texas A&M University
Oak Ridge Nat'l Lab.	Davidson College	University of Tennessee
Foreign Institutions	Hope College	University of Notre Dame
GSI/FAIR (EU)	Indiana University	University of North Carolina/TUNL
RIBF/RIKEN (Japan)	Indiana Wesleyan University	Washington University St. Louis
TRIUMF (Canada)	Kalamazoo College	Ursinus College
University of Surrey (UK)	Michigan State University	Wabash College

Thirty-nine representative members from the Working Group have participated in bi-weekly meetings that were very beneficial for developing this report. These meetings were organized by S. Noji and R. Zegers and participants included: M. Amthor (Bucknell University), D. Bazin (MSU), T. Baumann (MSU), G. Berg (University of Notre Dame), J. Brown (Wabash College), Z. Chajecki (Western Michigan University), J. Cizewski (Rutgers University), M. Cortesi (MSU), M. Couder (University of Notre Dame), A. Couture (LANL), H. Crawford (LBLN), A. Estrade-Vaz (Central Michigan University), P. Fallon (LBNL), M. Famiano (Western Michigan University), N. Frank (Augustana College), A. Gade (MSU), H. Geissel (GSI), G. Grinyer (University of Regina), R. Grzywacz (University of Tennessee-Knoxville), P. Gueye (MSU), M. Hausmann (MSU), C. Hoffman (ANL), R. Janssens (The University of North Carolina at Chapel Hill), N. Kalantarians (Virginia Union University), T. Kubo (MSU), A. Macchiavelli (LBNL), W. Mittig (MSU), S. Mosby (LANL), S. Noji (MSU), P. Ostroumov (MSU), S. Pain (ORNL), J. Pereira (MSU), A. Plastun (MSU), M. Portillo (MSU), A. Rogers (University of Massachusetts Lowell), G. Rogachev (Texas A&M), H. Sato (RIKEN), B. Sherrill (MSU), A. Stolz, O. Tarasov (MSU), R. York (MSU), R. Zegers (MSU), A. Zeller (MSU).

In addition, nineteen members of the above group met in monthly meetings focused on the detector systems for the HRS. This meeting was organized by A. Estrade-Vaz from Central Michigan University and included: D. Bazin (MSU), T. Baumann (MSU), G. Berg (University of Notre Dame), Z. Chajecki (Western Michigan University), M. Cortesi (MSU), H. Crawford (LBLN), A. Estrade-Vaz (Central Michigan University), M. Famiano (Western Michigan University), G. Grinyer (University of Regina), R. Grzywacz (University of Tennessee-Knoxville), P. Gueye (MSU), M. Hausmann (MSU), C. Hoffman (ANL), K. Jones (University of Tennessee-Knoxville), N. Kalantarians (Virginia Union University), T. Kubo (MSU), M. Portillo (MSU), A. Rogers (University of Massachusetts Lowell), G. Rogachev (Texas A&M), O. Tarasov (MSU), R. Zegers (MSU)

Additional input from the FRIB User Community was received through Working Group meetings during the annual Low-Energy Community Meetings. Workshops focused on the HRS were held in July 2014 at MSU and August 2017 at ANL. The HRS Working Group closely coordinates with other FRIB Working Groups and the GRETA Project Team.

1.2 Acronyms and abbreviations

AC	Alternating Current
AHD	Activity Hazard Document
AI	Analog Input
ALARA	As Low As Reasonably Achievable
ALARP	As Low As Reasonably Practicable
ANL	Argonne National Laboratory
AO	Analog Output
ARIS	Advanced Rare Isotope Separator
AT-TPC	Active Target Time Projection Chamber
CAC	Credited Administrative Controls
CAESAR	CAESium iodide ARray
CCUSB	CAMAC Crate Universal Serial Bus
CD	Critical Decision
CDR	Conceptual Design Report
CEC	Credited Engineered Controls
CFF	ConFlat Flange
CREX	Calcium Radius Experiment
CTR	Cathode Ray Tube
Ctrl	Controls
DAQ	Data Acquisition
DC	Direct Current
DDAS	Digital Data Acquisition System
DI	Digital Input
DO	Digital Output
DOE	Department of Energy
DOE-SC	Department of Energy Office of Science
DOM	Dispersive Optical Model
D-PPAC	Delay line Parallel-Plate Avalanche Counter
DRR	Device Readiness Review
EHS	Environment, Health, and Safety
EPICS	Experimental Physics and Industrial Control System
ESH&Q	Environment, Health, Safety, and Quality
FRIB	Facility for Rare isotope Beams
FWHM	Full Width at Half Maximum
GDR	Giant Dipole Resonance
GET	General Electronics for TPC
GPM	Gallons per Minute
GQR	Giant Quadrupole Resonance
GRETA	Gamma-Ray Energy Tracking Array
GSI	GSI Helmholtz Centre for Heavy Ion Research
GT	Gamow-Teller

GTR	Gamow-Teller Resonance
HA	Hazard Analysis
HAGRiD	Hybrid Array of Gamma Ray Detector
HiRA	High resolution Array
HRS	High Rigidity Spectrometer
HTBL	High Transmission Beam Line
HV	High Voltage
HVAC	Heating, ventilation, and air conditioning
IAS	Isobaric Analog State
IC	Ion Chamber
IEC	International Electrotechnical Commission
IFM	Interface Module
ISGMR	Isoscalar Giant Monopole Resonance
ISM	Integrated Safety Management
ISO	International Organization for Standardization
IT	Information Technology
JLAB	Jefferson Lab
JSA	Job Safety Analysis
KPP	Key Performance Parameters
LANL	Los Alamos National Laboratory
LBNL	Lawrence Berkeley National Laboratory
LCW	Low Conductivity Water
LENDA	Low Energy Neutron Detector Array
LIGO	Laser Interferometer Gravitational-Wave Observatory
LRP	Long Range Plan
MCP	Micro Channel Plate
MONA-LISA	Modular Neutron Array - Large multi-Institutional Scintillator Array
MPS	Machine Protection System
MSU	Michigan State University
MTBF	Mean Time Between Failures
MTTR	Mean Time To Repair
NASA	National Aeronautics and Space Administration
NEC	National Electrical Code
NN	Nucleon-Nucleon
NRC	National Research Council
NSAC	Nuclear Science Advisory Committee
NSCL	National Superconducting Cyclotron Laboratory
ODH	Oxygen Deficiency Hazard
ODHCS	Oxygen Deficiency Hazard Control System
OHSAS	Occupational Health and Safety Assessment Series
ORNL	Oak Ridge National Laboratory
ORRUBA	Oak Ridge Rutgers University Barrel Array
PFGS	Prompt-Fission Gamma-ray Spectrum

PID	Particle Identification
PLC	Programmable Logic Controller
PMT	Photomultiplier Tube
PPAC	Parallel-Plate Avalanche Counter
PPEP	Preliminary Project Execution Plan
PPS	Personnel Protection System
PREX	Lead Radius Experiment
PS	Power Supply
PW	Process Water
QA	Quality Assurance
QE	Quantum Efficiency
QPH	Quench Protection Heater
QWR	Quarter-Wave Resonator
RF	Radiofrequency
RFFS	Radiofrequency Fragment Separator
RIB	Rare Isotope Beam
RIBF	Radioactive Isotope Beam Factory
RIKEN	Rikagaku Kenkyusho (Institute of Physical and Chemical Research, Japan)
RR	Risk Reduction
RSS	Radiation Safety System
RT	Room Temperature
RTM	Room Temperature Magnet
SC	Superconducting
SCM	Superconducting Magnet
SCCM	Standard Cubic Centimeters per Minute
SeGA	Segmented Germanium Array
SIL	Safety Integrity Level
SOP	Standard Operation Procedure
SπRIT-TPC	SAMURAI Pion-Reconstruction and Ion-Tracker Time Projection Chamber
TBD	To Be Determined
TEC	Total Estimated Cost
TF	Task Force
THGEM	Thick Gaseous Electron Multiplier
TKE	Total Kinetic Energy
TOF	Time of Flight
TPC	Total Project Cost
TPC	Time Projection Chamber
TTS	Transit Time Spread
UL	Underwriters Laboratories
UPS	Uninterruptible Power Supply
VAC	Voltage, Alternating Current
VANDLE	The Versatile Array of Neutron Detectors at Low Energy
VDC	Voltage, Direct Current

VMUSB	Versa Module Universal Serial Bus
WBS	Work Breakdown Structure
WFO	work for others

1.3 List of figures

17

1.4   List of tables

2 Executive summary

Note that this document represents the status of the High Rigidity Spectrometer (HRS) project in fall of 2019. The HRS design will continue to evolve in detail and be further optimized to provide best value while achieving the required performance within cost and on schedule. However, this document will not be further updated. The evolving HRS design parameters and engineering designs will be captured in parameter lists and other technical and engineering documentation.

2.1 Introduction

The Facility for rare Isotope Beams (FRIB) will be the world's premier rare-isotope beam facility producing a majority (~80%) of the isotopes predicted to exist. This unprecedented discovery potential can be realized by implementing state-of-the-art experimental equipment that can study these isotopes at the highest rates produced. The new High Rigidity Spectrometer (HRS) will substantially increase FRIB's scientific reach and productivity and address the overarching intellectual challenges from the 2015 NSAC Long Range Plan [LRP15] and the NRC Decadal Study [NRC13]. Eleven of the 17 NSAC RIB Taskforce benchmarks [NRC07], which were introduced to characterize the scientific research of a rare-isotope facility, require the use of fast beams at FRIB and benefit from the experimental program that will be performed at the HRS.

2.2 Scope

The HRS, shown in Figure 2.1, is proposed as the first major addition to the Facility for Rare Isotope Beams (FRIB) experimental facilities. The HRS consists of two segments: the High-Transmission Beam Line (HTBL) and the Spectrometer Section. The HTBL transports Rare Isotope Beams (RIBs) from the Advanced Rare Isotope Separator (ARIS) fragment separator [HAU13] focal plane (FB0) to the reaction target stationed at the entrance (FS0) of the Spectrometer Section, in which charged reaction products created at the target are analyzed. A wide variety of high-impact ancillary detector systems developed by the nuclear science community for experiments at FRIB will be used in combination with the HRS, such as the Gamma-Ray Energy Tracking Array (GRETA) [GRE17] and the Modular Neutron Array (MoNA-LISA) [BAU05].

The HRS project scope includes the design, procurement, installation, and commissioning of the technical elements including the magnets and concomitant diagnostics, controls, power supplies, and cryogenic ancillary systems. The conventional facilities are provided by Michigan State University (~$23M) with anticipated beneficial occupancy at the end of calendar 2019.

2.3 Capabilities

The key characteristic of the proposed HRS is its ability to accommodate rare-isotope beams up to magnetic rigidities of 8 Tm, matching the rigidities at which the rare-isotope production in the ARIS fragment separator is optimized for isotopes across the chart of nuclei, even with an envisioned FRIB upgrade to 400 MeV/u. Consequently, experiments with the HRS greatly increase the sensitivity of the scientific program at FRIB, in particular for experiments with the most neutron-rich isotopes that have the highest potential for discovery. In combination with the ability to use thicker reaction targets at the higher magnetic rigidities, gain factors in luminosity

of 2 to 100 will be achieved for over 90% of experiments with neutron-rich isotopes. These gains are over what will be possible with existing spectrometers at the National Superconducting Cyclotron Laboratory (S800 and Sweeper) that have a maximum magnetic rigidity of 4 Tm. The largest luminosity gains are achieved for the most neutron-rich species, including many of the nuclei that in the path of the astrophysical *r* process.
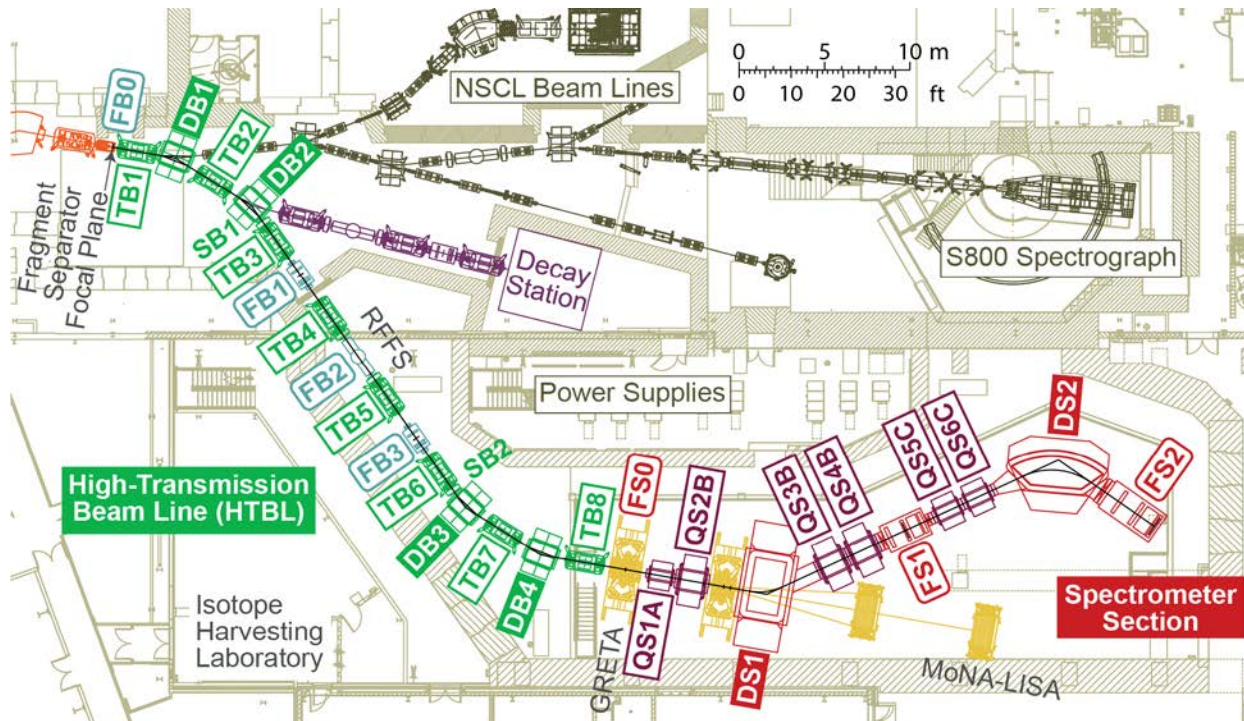
Figure 2.1 Layout of the High Rigidity Spectrometer (HRS) at FRIB, consisting of the High-Transmission Beam Line (HTBL) and the Spectrometer Section. The conventional facilities that house the HRS are under construction at FRIB and also house the Isotope Harvesting Laboratory. GRETA and MoNA-LISA are examples of ancillary detector systems that will be used in combination with the HRS.

2.4 Cost and schedule

A preliminary cost and schedule estimate have been made for the HRS project. The preliminary Total Project Cost (TPC) is about $91M in then-year dollars including a contingency of approximately 35%. Depending on funding, the project is estimated to take approximately eight years to complete.

2.5 Acquisition strategy

Michigan State University designs and establishes the HRS project with financial assistance from DOE and additional contributions provided by MSU. MSU will own the HRS, operate the HRS for DOE and MSU will be responsible for decommissioning of the HRS. The Cooperative Agreement between MSU and DOE-SC outlines the roles and responsibilities between MSU and

DOE-SC. The design, fabrication, testing, assembly, installation and commissioning of the HRS project will be mainly performed by MSU staff. Some work may be performed by national laboratories under work for others (WFO) agreements. Much of the subcontracted work to be performed for the HRS project consists of hardware fabrication. Consistent with the acquisition strategy which provides financial assistance to MSU and with DOE Contracting Officer direction, the HRS project will be regulated external to DOE through the existing regulators who regulate activities at MSU.

2.6   References

[BAU05] T. Baumann et al., Nucl. Instr. and Meth. A543, 517 (2005)

[GRE17] GRETA Conceptual Design report,
http://greta.lbl.gov/documents/ConceptualDesignReport-071717.pdf (2017)

[HAU13] M. Hausmann *et al.*, Design of the Advanced Rare Isotope Separator ARIS at FRIB, Nucl. Instrum. Meth. in Phys. Res. B, 317, 349 (2013)

[LRP15] Reaching For the Horizon, The 2015 Long Range Plan for Nuclear Science, The Nuclear Science Advisory Committee (2015)

[NRC07] Scientific Opportunities with a Rare-Isotope Facility in the United States, National Research Council; Division on Engineering and Physical Sciences; Board on Physics and Astronomy; Rare-Isotope Science Assessment Committee (2007)

[NRC13] National Research Council. *Nuclear Physics: Exploring the Heart of Matter*. Washington, DC: The National Academies Press, 2013

3 Project overview

3.1 Introduction

The Facility for rare Isotope Beams (FRIB) will be the world's premier rare-isotope beam facility producing a majority (~80%) of the isotopes predicted to exist. This unprecedented discovery potential can be realized by implementing state-of-the-art experimental equipment that can study these isotopes at the highest rates produced. Eleven of the 17 NSAC RIB Taskforce benchmarks [NRC07], which were introduced to characterize the scientific research of a rare-isotope facility, require the use of fast beams at FRIB. All of these programs require a magnetic spectrograph of the type described in this document. A new High Rigidity Spectrometer (HRS) will substantially increase FRIB's scientific reach and productivity and addresses the overarching intellectual challenges from the 2015 NSAC Long Range Plan [LRP15] and the NRC Decadal Study [NRC13]. The HRS, shown in Figure 2.1, is proposed as the first major addition to the FRIB experimental facilities.

The 8 Tm bending power of the proposed HRS matches the rigidities at which rare isotopes will be produced at FRIB, even with the envisioned FRIB upgrade to 400 MeV/u. This will enable the most sensitive experiments across the entire chart of nuclei, thereby enabling experiments with the most neutron-rich nuclei available at FRIB. In combination with the ability to use thicker reaction targets at the higher rigidity, gain factors in luminosity of 2 to 100 will be achieved for over 90% of experiments with neutron-rich isotopes. These gains are over what will be possible with existing spectrometers at NSCL (S800 and Sweeper) that have a maximum rigidity of 4 Tm. The largest luminosity gains are achieved for the most neutron-rich species.

3.2 Project organization

The High Rigidity Spectrometer (HRS) Project will deliver the scope funded by the Total Project Cost. The HRS Project has been established within the FRIB Laboratory, which is a unit within Michigan State University (MSU). The HRS Project will be managed by utilizing the expertise and processes implemented at the Laboratory for the execution of the FRIB Project. This ensures the complete integration of the HRS into FRIB to provide the full benefit of the opportunities for FRIB Users. Priorities between different activities at the FRIB Laboratory are set by the FRIB Laboratory Director, with input from the NSCL Laboratory Director, the FRIB Division Directors, and the NSCL Associate Directors.

MSU will design, build, and commission the HRS Project with financial assistance from DOE and contributions from MSU. While DOE Order 413.3B [DOE4133B] does not apply to financial assistance transactions, the project will follow best project management practices.

3.3 Work breakdown structure

The HRS Project has organized the scope of work into a Work Breakdown Structure (WBS). The WBS contains the complete definition of the HRS Project at Michigan State University and forms the basis for all phases of the project: planning, execution, control, and oversight of contracts. The HRS WBS is shown in Table 3-1. Elements are defined as specific systems, management, research and development, or pre-operations. Elements are discrete items of project work and are consistent with execution methods.

Table 3-1 Work Breakdown Structure for the High Rigidity Spectrometer

Scope for the HRS Project (HRS=L.F.CTR.M.4.18)

Description	WBS Element
Management & Support	**HRS.1**
Project Management	HRS.1.01
Project Management	HRS.1.01.01
Travel	HRS.1.01.02
Business Management	HRS.1.02
Project Controls	HRS.1.02.01
Procurement Support	HRS.1.02.02
Material Handling	HRS.1.02.03
Supplies and Services	HRS.1.02.04
Environmental, Safety, Health and Quality (ESH&Q)	HRS.1.03
Quality Assurance	HRS.1.03.01
ES&H	HRS.1.03.02
Systems Engineering & Integration	HRS.1.04
Systems Engineering	HRS.1.04.01
Documentation	HRS.1.04.02
Facility Infrastructure – MSU Contribution	**HRS.2**
Facility Infrastructure	HRS.2.01
Facility Infrastructure	HRS.2.01.01
Utilities	HRS.2.02
Utilities	HRS.2.02.01

Description	WBS Element
Experimental Systems - High Rigidity Spectrometer	**HRS.3**
High Transmission Beamline (HTBL)	HRS.3.01
High Transmission Beamline Beam Physics	HRS.3.01.01
High Transmission Beamline Diagnostics and Tracking	HRS.3.01.02
HTBL Diagnostic Devices	HRS.3.01.02.01
HTBL Tracking Detectors	HRS.3.01.02.02
High Transmission Beamline Magnets	HRS.3.01.03
HTBL Dipole Magnets	HRS.3.01.03.01
HTBL Quadrupole & Multipole Magnets	HRS.3.01.03.02
HTBL Installation, Testing, and Magnet Mapping	HRS.3.01.03.03
High Transmission Beamline Vacuum	HRS.3.01.04
High Transmission Beamline Power Supplies	HRS.3.01.05
High Transmission Beamline Cryogenics	HRS.3.01.06
High Transmission Beamline Low Level Controls	HRS.3.01.07
High Transmission Beamline Alignment	HRS.3.01.08
Spectrometer Section	HRS.3.02
Spectrometer Section Beam Physics	HRS.3.02.01
Left open intentionally	HRS.3.02.02
Spectrometer Section Magnets	HRS.3.02.03
Spectrometer Section Dipole Magnets	HRS.3.02.03.01
Spectrometer Section Quadrupole & Multipole Magnets	HRS.3.02.03.02
Spectrometer Section Installation, Testing and Magnet Mapping	HRS.3.02.03.03
Spectrometer Section Detector Support and Access to Detector Systems	HRS.3.02.04
Spectrometer Section Detector Support and Access at Reaction Target	HRS.3.02.04.01
Spectrometer Detector Support for MoNA-LISA Detector System	HRS.3.02.04.02
Spectrometer Section Detector Access Platforms	HRS.3.02.04.03
Spectrometer Section Focal Plane Detector Systems	HRS.3.02.05
Spectrometer Section High Resolution Mode Focal Plane Detector Systems	HRS.3.02.05.01
Spectrometer Section Invariant Mass Mode Focal Plane Detector Systems	HRS.3.02.05.02
Spectrometer Section Vacuum	HRS.3.02.06
Spectrometer Section Power Supplies	HRS.3.02.07
Spectrometer Section Cryogenics	HRS.3.02.08
Spectrometer Section Low Level Controls	HRS.3.02.09
Spectrometer Section Alignment	HRS.3.02.10
Central Systems	HRS.3.03
Protection Systems	HRS.3.03.01
Personnel Protection Systems	HRS.3.03.01.01
Machine Protection Systems	HRS.3.03.01.02
Network & IT	HRS.3.03.02
High Level Controls	HRS.3.03.03
Technical Utilities and Infrastructure	HRS.3.03.04

Description	WBS Element
Preoperations	**HRS.4**
Integrated Testing and Systems Commissioning	HRS.4.01
Integrated Testing	HRS.4.01.01
Commissioning	HRS.4.01.02
Performance Parameters and Completion Criteria	HRS.4.01.03

WBS elements HRS.1, HRS.3, and HRS.4 are TPC-funded and will be delivered by the HRS Project. Level 2 elements of the FRIB Project WBS are:

- HRS.1 Management and Support – Project office administrative and management activities that integrate over the entire project
- HRS.2 Facility Infrastructure – MSU Contribution –This scope will be provided by Michigan State University
- HRS.3 Experimental Systems-High Rigidity Spectrometer – All phases of design, procurement, installation, and commissioning of the experimental systems
- HRS.4 Pre-operations - integrated testing and commissioning to achieve CD-4

The performance baseline will be formulated against WBS level 3.

3.4 Performance Parameters

The Threshold Key Performance Parameters (KPPs) provided in Table 3-2 define the minimum acceptable performance required to satisfy mission need and CD-4 project completion. The stated threshold KPPs demonstrate the successful transport of a rare-isotope beam through the HTBL and the characterization of a reaction product in the Spectrometer Section.

Table 3-2 Performance Parameters for the HRS

Threshold Key Performance Parameters for the HRS
HRS operational: events recorded in the final focal plane of the Spectrometer Section from one-nucleon knockout from a rare-isotope beam transmitted through the High Transmission Beam Line to the reaction target station at the entrance of the Spectrometer Section
1. Demonstrate the operation of the High Transmission Beam Line by showing the correlation between positions and angles measured in the tracking detectors in the High Transmission Beam Line
2. Demonstrate the operation of the Spectrometer Section by showing the correlation between positions and angles measured in the tracking detectors in the final focal plane
3. Demonstrate the particle identification of particles transmitted through the Spectrometer Section by showing the correlation between time of flight and energy loss measurements in the final focal plane

3.5 Life Cycle Costs

The Life Cycle Costs include cost of implementation, operation, and decommissioning. Alternative analyses were performed [FRIB-M41800-TR-00007]. The project costs necessary to design, implement, and commission the HRS are minimized by the preferred alternative since:

- Number of design types are minimized thereby minimizing the non-recurring engineering costs,
- Iron-dominated superconducting magnet elements of the preferred alternative achieve ion-optical requirements at reduced cost and risk compared to current-dominated superconducting magnet elements with no R&D necessary.

The operating cycle costs are minimized since the magnetic elements will be energized by superconducting coils in lieu of magnetic elements energized by room temperature copper coils. Other analyses have found that HRS magnets of the alternative design are several times cheaper

to fabricate and have about 5 times smaller operational costs vs. room temperature [NOL84] and that e.g. whole-body superconducting MRIs have ~25x smaller operational costs vs. room temperature MRIs [MIN03].

The decommissioning costs will be covered by Michigan State University. The Life Cycle Costs are enumerated in the Preliminary Project Execution Plan (PPEP) [FRIB-M41800-PL-000357].

3.6 Risk assessment

The HRS Project has a risk registry to catalog, assess, track and develop management actions for discrete ("known" or forecasted) risk events and their associated potential impacts to the HRS project cost, schedule, or technical baselines. Since the HRS Project has ion optics based on simulations benchmarked by decades of MSU Rare Isotope Beam (RIB) experience and since the required hardware is similarly based upon decades of MSU utilizing superconducting driven, iron dominated magnetic elements, as well as power-supply, controls, diagnostics, and detector technology, there will be no R&D program required.

Following the FRIB Project Risk Management Plan [FRIB-T10102-PL-000213], control Account Managers have first-line responsibility for the bottom-up estimate of potential contingency as well as discrete risk identification, assessment, reporting, and development of mitigation plans and strategies as inputs to the risk register. The risk register is reviewed periodically by HRS project management to ensure risks are appropriately classified, that mitigation plans are developed and implemented where needed, and to ensure resources are allocated consistent with management priorities to reduce risk.

At the time of completion of the Conceptual Design (Fall 2019), the preliminary Total Project Cost (TPC) is about $91M in then-year dollars including a contingency of approximately 35%. Depending on funding, the project is estimated to take approximately eight years to complete. At the current state of the design, HRS project management has determined that this level of contingency in light of the risks identified is adequate to avoid undue overall risk to the proposed project.

The current risk registry entries with a high probability and critical impact on the project having a high risk ranking are given in Table 3-3. A risk is high because both probability of occurrence and impact are high. A mitigation approach is stipulated. For example, the risk from spare power supplies specifies a mitigation approach that will be implemented with inconsequential cost impact. If not appropriate, the design of large aperture spectrometer quadrupoles has a high risk, but the stipulated mitigation approach minimizes magnet failure.

Table 3-3. HRS risk registry entries with a high risk ranking.

Risk Description	Mitigation Approach	Probability of Occurrence	Risk Impact	Risk Ranking	Cost Impact	Risk Notes
Project extends 2 years due to late start	Obtain DOE-SC funding as early as possible	High	Critical	High	$5.3M	6% (2 year of $88.6M)
Large Aperture Spectrometer Quads - Adequate structural stiffness & assembly clearances to manage heat loads	Mechanical engineering design studies integrated with magnetic design	Medium	High	High	Covered by Contingency	
Spare power supplies	Reduce types, if possible use FRIB PS type to take advantage of existing spares, calculate spares required based on MTBF and MTTR	High	High	High	$75,000	5% of estimated power supply cost

3.7   ESH&Q Requirements and Plans

The various regulatory agencies both establish requirements for HRS design, establishment, and operation and provide oversight and inspection of the project's implementation of the requirements. The applicable HRS project regulatory requirements are documented in the Regulatory Requirements document [FRIB-R10103-TD-000014].   Regulating agencies include the U.S. Nuclear Regulatory Commission, the U.S. Department of Transportation, the Environmental Protection Agency, various State of Michigan agencies and Michigan State University.

The HRS Project team has committed to maintaining OHSAS 18001, ISO 14001, ISO 9001, and ISO27001 registered programs. These programs will be reviewed and compared with FRIB needs. These self-imposed and third-party registered management systems   will   assure that   FRIB maintains   the current   high   standards   for Occupational Health and Safety, Environmental Management, Quality Management, and Information Security Management required to maintain these certifications.

3.8   References

[DOE4133B] https://www.directives.doe.gov/directives-documents/400-series/0413.3-BOrder-B-chg5-minchg

[FRIB-R10103-TD-000014] FRIB Regulatory Requirements with ESH&Q inputs

[FRIB-T10102-PL-000213] FRIB Project Risk Management Plan

[FRIB-M41800-TR-000077] Alternative Analyses for High Reigidity Spectrometer (HRS) Project

[FRIB-M41800-PL-000357] Preliminary Project Execution Plan for the High Rigidity Spectrometer

[LRP15] Reaching For the Horizon, The 2015 Long Range Plan for Nuclear Science, The Nuclear Science Advisory Committee (2015)

[MIN03] Joseph Minervini, and Yukikazu Iwasa FBML. 22.68J Superconducting Magnets. Spring 2003. Massachusetts Institute of Technology: MIT OpenCourseWare, https://ocw.mit.edu . License: Creative Commons BY-NC-SA.

[NOL84] The Use of Superconducting Magnets in Spectrographs and Beam Transport Systems", J.A. Nolen Jr., Proc. Of 10th International Conf. on Cyclotrons and Their Applications, pgs. 215-221, (1984 East Lansing, MI)

[NRC07] Scientific Opportunities with a Rare-Isotope Facility in the United States, National Research Council; Division on Engineering and Physical Sciences; Board on Physics and Astronomy; Rare-Isotope Science Assessment Committee (2007)

[NRC13] National Research Council. *Nuclear Physics: Exploring the Heart of Matter*. Washington, DC: The National Academies Press, 2013

4 Science enabled with the High Rigidity Spectrometer (HRS) at FRIB

4.1 Introduction

The Facility for Rare Isotope Beams (FRIB) will be the world's premier rare-isotope beam facility, producing a majority (~80%) of the isotopes predicted to exist [ERL12, AFA13]. The scientific community envisions to make full use of this vast, new access to the nuclear landscape through experimental programs that have the furthest reach into "terra incognita" on the nuclear chart. The unprecedented access to new isotopes makes FRIB a critical component of the DOE mission to understand the fundamental forces and particles of nature as manifested in nuclear matter and will provide the necessary expertise and tools from nuclear science to meet national needs. The DOE Nuclear Physics mission, its relation to the FRIB science drivers, their reflection in the NRC decadal study "Nuclear physics: Exploring the Heart of Matter" [NRC13], the NSAC 2007 and 2015 LRP key questions [LRP07,LRP15], and the NSAC Rare Isotope Beam Taskforce 17 benchmarks [NRC07] are illustrated in Figure 4.1. The figure illustrates how the scientific goals of the field, addressing the challenges posed by the NRC Decadal Study and reiterated in the 2015 LRP, drive FRIB capabilities. The FRIB project has used the benchmarks to evaluate the facility's ability to deliver on its scientific promise. The bottom of the figure illustrates the tools required for each of the benchmarks. To achieve the goals, the need for a broad-approach technical scope was recognized that provides fast, stopped, and reaccelerated beams of rare isotopes. Of the 17 benchmarks, 11 require the use of fast beams (indicated in red in Figure 4.1) and strongly benefit from the use of a magnetic spectrograph.

Impact of a high rigidity spectrometer: The scientific impact of the FRIB fast beam science program will be substantially enhanced (by luminosity gain factors of between two and one hundred for neutron-rich isotopes, with the largest gains for the most neutron-rich species) by construction of a high-performance magnetic spectrograph. The High Rigidity Spectrometer (HRS), consisting of the High-Transmission Beam Line (HTBL) and the Spectrometer Section, will allow experiments with beams of rare isotopes at magnetic rigidities for which the maximum production rates for fragmentation or in-flight fission are achieved. This enhancement in experimental sensitivity provides access to critical isotopes not available otherwise. The scientific benefit of this additional sensitivity is discussed below. The scientific reach of the experimental program at FRIB is also enhanced by opportunities to perform experiments at beam energies in the 100-250 MeV/u range. The key spectrometer feature needed to reach the sensitivity limits of FRIB and access additional forefront science above 100 MeV/u is operation at rigidities of up to 8 Tm, appropriate even with the envisioned FRIB upgrade to 400 MeV/u. The current laboratory spectrometers are limited to 4 Tm.

The 2015 NSAC LRP recognized that the "HRS…will be essential to realize the scientific reach of FRIB" and that "Another key addition to FRIB is the proposed High-Rigidity Spectrometer, which would enable in-flight reaction experiments with the most neutron-rich nuclei available from FRIB." The strong community support was reiterated in the 2018 Low-Energy Community meeting, at which the following resolution was unanimously adopted: "The community endorses the prompt initiation and timely completion of the High Rigidity Spectrometer (HRS) construction project, an essential instrument for fast-beam experiments at FRIB."

DOE Nuclear Physics Mission is to understand the fundamental forces and particles of nature as manifested in nuclear matter, and provide the necessary expertise and tools from nuclear science to meet national needs

DOE Nuclear Physics Mission is accomplished by supporting scientists who answer overarching questions in major scientific thrusts of basic nuclear physics research

Intellectual challenges from NRC Decadal Study and the NSAC 2015 LRP

Nuclear Structure	Nuclear Astrophysics	Tests of Fundamental Symmetries	Applications of Isotopes
How does subatomic matter organize itself and what phenomena emerge?	How did visible matter come into being and how does it evolve?	Are fundamental interactions that are basic to the structure of matter fully understood?	How can the knowledge and technological progress provided by nuclear physics best be used to benefit society?

Overarching Questions from NSAC 2007 LRP

What is the nature of the nuclear force that binds protons and neutrons into stable nuclei and rare isotopes? What is the origin of simple patterns in complex nuclei?	What is the nature of neutron stars and dense nuclear matter? What is the origin of the elements in the cosmos? What are the nuclear reactions that drive stars and stellar explosions?	Why is there now more matter than antimatter in the universe?	What are new applications of isotopes to meet the needs of society?

Overarching questions are answered by rare isotope research

17 Benchmarks from NSAC RIB TF measure capability to perform rare isotope research (HRS contributes)

1. Shell structure 2. Superheavies 3. Skins 4. Pairing 5. Symmetries 13. Limits of stability 14. Weakly bound nuclei 15. Mass surface	6. Equation of State (EOS) 7. r-Process 8. $^{15}O(\alpha,\gamma)$ 9. ^{59}Fe supernovae 13. Limits of stability 15. Mass surface 16. rp-Process 17. Weak interactions	12. Atomic electric dipole moment 15. Mass surface 17. Weak interactions	10. Medical 11. Stewardship

MSU proposed technical scope is sufficient to meet all benchmarks

Figure 4.1 FRIB will allow users to answer the overarching questions from the NSAC 2007/15 Long Range Plan and the latest NRC Decadal Study, and thereby supporting the DOE Nuclear Physics Mission. The NSAC RIB TF developed 17 benchmarks to test facility capability to address these questions. Meeting these benchmarks has driven the technical scope and specifications for FRIB. The benchmarks also guide the equipment development necessary for the program.

4.2 Science with the HRS

The following sections summarize, for each of the four challenges posed by the NRC Decadal Study and reiterated in the 2015 LRP, example research programs that will be enabled when the fast rare-isotope beams produced at FRIB can be used at the optimum magnetic rigidities. The last two sections outline the opportunities afforded by a high rigidity spectrometer for nuclear reactions and discovery science at FRIB. Throughout this science section, high-impact key examples are highlighted that – once enabled – allow for broad research programs addressing the 11 benchmarks associated with fast beams, all using similar experimental approaches. In Table 4-1, an overview of the science programs afforded by the HRS is provided and linked to the relevant benchmarks. In Section 4.3, scientific specifications are determined for each of these programs, which serve as input for the conceptual design of the HRS.

4.2.1 How does visible matter organize itself

One of the key challenges identified for the field of nuclear science in the National Academies Decadal Study is: "How does subatomic matter organize itself and what phenomena emerge?" [NRC13]. Answers to this compelling question require a predictive model of atomic nuclei that is based on the fundamental interactions at play between its constituents. On the quest for this comprehensive description of nuclei and their reactions, the properties of rare isotopes have emerged as the critical constraints for improving our understanding of poorly known but essential many-body forces [FOR13]. The shortest-lived, weakly bound isotopes near the nucleon driplines also uniquely quantify the role of the particle continuum that contributes to all nuclear systems including neutron stars.

The following five subsections outline a research program focused on crucial aspects of nuclear structure research, including the study of shell structure, collectivity, and shapes; spectroscopy in the particle continuum; the exploration of the proton-neutron degree of freedom; and point out the opportunity of commensal decay spectroscopy following reactions. The key examples of this section are the spectroscopy of bound states in the most neutron-rich Ca isotopes and the spectroscopy of neutron-unbound states in the region around ^{40}Mg.

4.2.1.1 Evolution of shell structure, collectivity, and shape

The often surprising properties of nuclei beyond the valley of β stability have prompted extensive experimental and theoretical studies aimed at identifying the multiple driving forces behind the dramatic changes in nuclear shell structure that are encountered in rare isotopes. A multitude of observables are needed for a comprehensive picture of structural evolution in the quest for a predictive model. These include excitation energies, spins, parities, and transition matrix elements. Often, long semi-magic isotopic chains emerge as critical since they allow tracking shell evolution from the proton to the neutron dripline, with several doubly magic systems along the way. Complementary information is sought in regions of rapid changes in shape or collective behavior where certain drivers of structural change can be isolated. Outlined in the following are example research programs that will be enabled by a high rigidity spectrometer.

Table 4-1 Summary of HRS science programs developed by the FRIB user community. The science programs are grouped by the primary overarching NRC Decadal and 2015 LRP science questions they address. For each program, the relevant NSAC 2007 RIB Task force Benchmarks are indicated.

Group	HRS Science Program	1. Shell structure	3. Skins	5. Symmetries	6. Equation of State	7. R-process	11. Stewardship	13. Limits of Stability	14. Weakly-bound nuclei	15. Mass Surface	16. RP-process	17. Weak interactions
Nuclear Structure	At the limits of the nuclear chart: at and beyond the neutron dripline	x	x		x			x	x			
	Single-particle structure and collectivity from prompt in-beam gamma-ray spectroscopy	x				x		x				
	Fingerprints of shell evolution with isomer studies	x				x					x	
	Excited-state lifetimes as indicators of shell-evolution	x										
	Inelastic proton scattering as a probe of the pn degree of freedom	x										
	Physics along the N=Z line	x		x		x		x			x	
	Commensal decay spectroscopy following reactions	x										x
	Knock-out reactions	x										
	Quasifree scattering				x							
	Elastic scattering		x		x							
	Total reaction/interaction measurements		x		x				x			
Nuclear Astrophysics	Heavy-ion collisions				x							
	Heavy-ion EM excitations				x	x						
	Isoscalar giant resonances			x	x							
	Isovector giant resonances			x	x							x
	Time-of-flight mass measurements	x				x				x	x	
	Projectile fragmentation and in-flight fission of neutron-rich nuclei					x		x				
	Weak Reaction rates for astrophysics					x					x	x
Fundamental Symmetries	Gamow-Teller strengths, neutrinos, and the quenching of g_A	x										x
Applications	Improving nuclear structure inputs to fission models	x						x				

Exploring shell structure in isotopic chains with prompt in-beam γ-ray spectroscopy following reactions – In-beam γ-ray spectroscopy with fast beams is often used as a sensitive tool to tag an inelastic excitation or to identify and quantify the final states populated in reactions, ultimately providing cross sections for reactions to specific final states [GAD08a]. Single-particle properties tracked across long isotopic chains towards the extremes of isospin provide an opportunity to isolate specific drivers of shell evolution as function of neutron-richness and weak binding.

A high rigidity spectrometer coupled to a γ-ray detection array such as GRETA will enable the detailed prompt γ-ray spectroscopy at the very limits of FRIB reach, and the combination of the two devices will be a cornerstone of experimental equipment for discovery science at FRIB. Such programs will extend to all proton-magic isotopic chains and their vicinity, with the Z=28 Ni isotopes next in reach for ab-initio Coupled-Cluster calculations [HAG16], see for example Figure 4.2 for predictions of 2^+_1 state energies in even-even Ni isotopes out to A=80. This is only possible for the most relevant nuclei furthest away from stability when projectile beams can be used at the rigidities where their production is optimum.
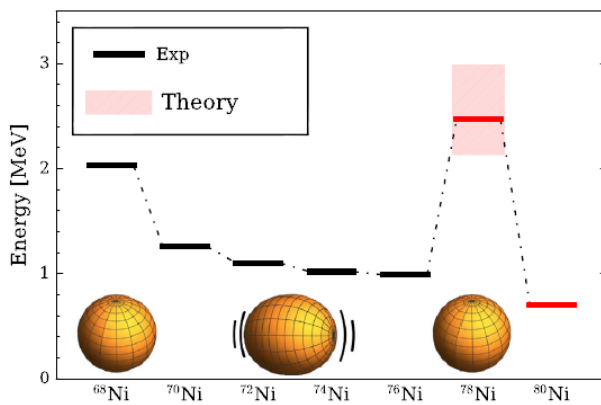
Figure 4.2: First ab-initio type Coupled Cluster calculations of 2^+ energies around the key nucleus ^{78}Ni [HAG16]. In-beam γ-ray spectroscopy at a high rigidity spectrometer at FRIB will enable spectroscopy along magic chains to benchmark ab-initio calculations and explore the effects of many-body correlations in the regime of weak binding.

Excited-state lifetimes as indicators of shell evolution – Excited-state lifetime measurements provide a model-independent approach to obtain transition matrix elements which quantify and characterize collective phenomena. Using a system comprised of a target and degrader foils (plunger device), γ rays emitted behind each foil will have different Doppler shifts and the lifetime of the state emitting the γ-ray transition can then be determined using relative γ-ray yields measured at different foil separations [IWA16]. This approach is applicable to different transition modes such as E1, M1 and E2 excitations if the level lifetimes are within measurable ranges of about one picosecond to one nanosecond. At a high rigidity spectrometer, such excited-state lifetime measurements will be performed using GRETA placed around a plunger device at the target position. The higher beam energies possible, afforded by a high rigidity spectrometer, will not only give access to new regions of the nuclear chart but also increase the reach of such recoil-distance measurements that are based on a multi-foil plunger scheme.

Rapid changes in the collectivity and shape coexistence phenomena induced by shell evolution far from stability are of great interest in the pursuit of a comprehensive understanding of nuclei [HEY11,GAD16]. A new region of interest only accessible at FRIB is the 'fifth island of inversion'

around ^{78}Ni [NOW16], where so-called normal-order and shell-breaking intruder configurations compete, which results in the appearance of two or more different intrinsic shapes and associated band structures even at low excitation energies (see Figure 4.3).
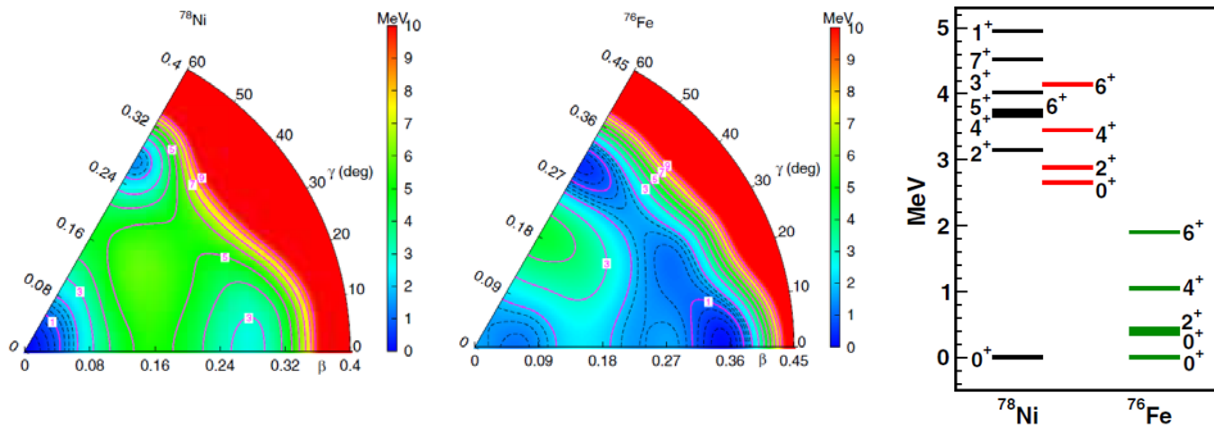
Figure 4.3 Potential energy surface for ^{78}Ni, ^{76}Fe and level schemes for the same nuclei as predicted by large-scale shell-model calculations [NOW16]. The dark blue minima indicate different deformations that the nucleus is predicted to assume at low excitation energies. Transition strength measurements at and around ^{78}Ni will reveal band structures built on the different deformations and their interconnections.

Critical excited-state lifetime measurements for the 2^+ and 4^+ states in such neutron-rich nuclei can be performed at FRIB by combining GRETA and a high rigidity spectrometer to enable measurements at optimum production yields and with the highest γ-ray energy yield. Through the measurement of transition rates for higher-lying states, the excited band character as well as associated shell configurations can be experimentally investigated for the first time in many critical regions of the nuclear chart. In this way, modification of the shell structure will be probed as a function of spin, isospin, and excitation energy, paving the way for a complete understanding of the shell evolution in rare isotopes.

Fingerprints of shell evolution with isomer studies – An experimental challenge for the powerful reaction studies proposed for medium-heavy to heavy nuclei is the occurrence of long-lived isomeric states in the reaction products as well as in the incoming projectile beam. Such isomers may be yrast traps, signal symmetries (K isomers), or connect to the particle continuum (particle-emitting isomer). In fact, these isomeric states are often direct fingerprints of shell evolution: Excited states that cross a shell gap to intrude the normal-order single-particle structure may become isomeric through their hindered decays [GAD15].

In order to identify and characterize the tell-tale important isomeric states, a new approach of tagging and identifying the population of isomeric states in the reaction products has been developed recently and applied at the S800 spectrograph at NSCL [MEI11,WIM14]. The decays of isomeric states with lifetimes between ~100 ns and several ms have been observed and event-by-event linked to the implantation event. In certain regions, such as the neutron-rich isotopes around ^{78}Ni, in-beam experiments at a high rigidity spectrometer will benefit from such detection

of delayed γ-ray or conversion electrons in the focal plane to identify and characterize the isomeric states populated.

4.2.1.2 **Key example** – Spectroscopy the most neutron-rich Ca isotopes

The proton-magic calcium isotopes with Z=20 present a unique laboratory for studying the evolution of nuclear structure with increased neutron number. Within this single isotopic chain are some of the clearest examples to date of changing single-particle energies as a result of the spin-isospin component of the nucleon-nucleon interaction, namely the appearance of new sub-shell gaps at N=32 and 34 [HUC85, STE13]. In addition, recent microscopic and ab-initio calculations [HOL12, HAG12, HER14, HOL14] have highlighted the Ca isotopes as a region critical for testing the role of many-body forces and the particle continuum.

FRIB will provide access along the $_{20}$Ca isotopic chain with unparalleled reach, allowing for detailed spectroscopy as far as N=36, and first spectroscopy out to ^{60}Ca. Benchmark tests of microscopic and ab-initio theory will be possible using direct nucleon knockout reactions. Figure 4.4 shows a simulated Doppler reconstructed spectrum of ^{60}Ca as it may be observed following a ^{9}Be(^{61}Sc,^{60}Ca+γ) one-proton knockout reaction performed at a high rigidity spectrometer with γ-ray detection using GRETA (150 hours of beam on a 500 mg/cm^2 thick target). Fast beams of neutron-rich Ca isotopes will have magnetic rigidities approaching 6 Tm and a high rigidity spectrometer will be critical to enable such nucleon knockout experiments at the optimum projectile production yields. This is demonstrated with Figure 4.4: If the same experiment was performed at the S800 [BAZ03] (with a maximum rigidity of 4 Tm), the yield would drop by a factor of 24 for the same run time, rendering the measurement essentially impossible.
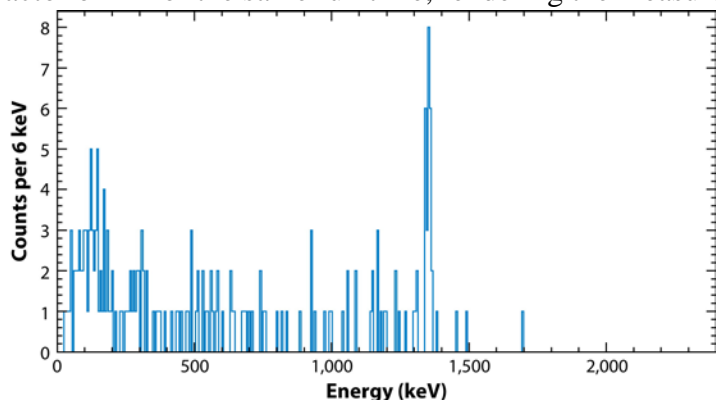
Figure 4.4 Simulation of the excitation energy spectrum of ^{60}Ca as Doppler-reconstructed with GRETA following a direct one-proton knockout reaction from ^{61}Sc at 200 MeV/u. The cross section was estimated based on [GAD14] with the 2$^+$ energy as predicted by large-scale shell model [LEN10] and full transmission of the ^{61}Sc rare-isotope beam to the reaction target was assumed. Without the factor of 24 gain in luminosity from a High Rigidity Spectrometer, this experiment will not be possible [Figure from [FAL16]].

Such in-beam γ-ray spectroscopy experiments at the limits of the nuclear chart are enabled by the increased luminosity from the use of thick reaction targets. The combined gains of projectile beam delivery at a rigidity that optimizes the rare-isotope beam production and increased luminosity through the use of thick secondary targets are often 1-2 orders in magnitude.

4.2.1.3 **Key example** – Nuclear structure in the particle continuum around ^{40}Mg

Unique opportunities for nuclear structure physics arise in various regions of the nuclear chart. Approaching the particle continuum, for example, near and beyond the neutron dripline, structural change is driven by weak binding and modified many-body correlations [DOB07]. New phenomena, such as two-neutron radioactivity or ground-state di-neutron emission, discovered at NSCL [KOH13,SPY12], emerge as unique messengers of the nuclear interior.

The structure of these neutron-unbound nuclei, populated by different reactions from fast rare-isotope beams impinging on a reaction target at the target position of a high rigidity spectrometer, will be determined from the reconstructed decay energy. This is accomplished by measuring the full 4-momenta of the neutron(s) and the projectile-like charged residue. Using invariant mass spectroscopy, the MoNA-LISA/Sweeper [BAU05,MRI09] setup at NSCL has been pioneering in the exploration of the most neutron-rich nuclei. In such experiments, typically, a one- or two-proton knockout reaction from a rare-isotope beam is used to populate an unbound state or nucleus which then immediately, within ~10^{-21} seconds, decays into the projectile-like decay daughter and one or more neutrons. The charged remnant is deflected into a suite of detectors by the Sweeper magnet while the neutrons, unaffected by the magnetic field, travel forward into the MoNA and LISA neutron arrays. Since the momentum, angle, and mass of each particle in the decay process are measured, the Lorentz vectors are known and the invariant mass or decay energy of the system can be reconstructed [BAU12].
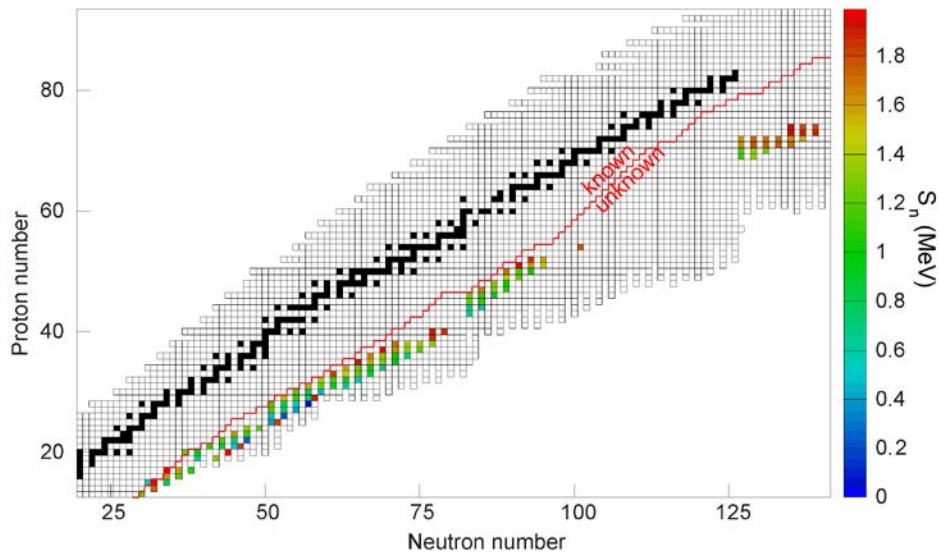
Figure 4.5 Neutron separation energies up to 2 MeV for isotopes that FRIB will produce at intensities in between 0.0001/s and 1/s, that have a neutron separation energy below 2 MeV, and that are of strong interest for invariant-mass spectroscopy. The limit of known nuclei on the neutron-rich side is indicated by the red line. Outlined isotopes provide an estimate of the limits of particle-bound isotopes from the KTUY model [KOU05]. For these very neutron-rich systems, such as around ^{84}Ni and ^{140}Sn, high luminosity is critical, which requires an experimental station that can operate at high rigidities.

As illustrated in Figure 4.5, by combining γ-ray spectroscopy with neutron invariant-mass spectroscopy, a large number of very neutron-rich systems that have low neutron-separation energies can be investigated, ranging from light to heavy nuclei. Such studies will venture deep

into terra incognita and require the highest beam luminosities, and therefore, a spectrometer that operates at high rigidities.

One region of interest are the weakly bound nuclei in the region around ^{40}Mg, where the N=28 shell closure is suspected to break down. Invariant mass spectroscopy of neutron-unbound states is critical to understand the impact of the neutron continuum on shell evolution. A recent frontier has been the study of multi-neutron correlations in the break-up of systems unbound with respect to two or more neutrons. In this region, ^{38}Na and ^{44}Mg, for example, are predicted to be unbound to the emission of four neutrons [MOE95] and their investigation is of great interest for understanding multi-neutron correlations in the continuum.

In the ^{40}Mg region, the combined gains, from accepting beams at the rigidity that optimizes their production and the luminosity afforded by a thick reaction target, over performing the experiment at 4 Tm exceed a factor of 100.

4.2.1.4 The proton-neutron degree of freedom

The proton-neutron degree of freedom and its impact on nuclear observables is among the central aspects in nuclear structure physics. Throughout physics, symmetries play a fundamental role in our basic understanding and theoretical description of nature. In nuclei, the similarity of neutrons and protons combined with the charge independence of the nuclear force is contained in the concept of isospin symmetry. Complementary approaches have been developed that probe the proton-neutron degree of freedom in the most exotic nuclei.

The following briefly outlines example programs envisioned at FRIB where inelastic proton scattering, spectroscopy along the *N=Z* line, and the investigation of spin-isospin degrees of freedom are enabled at a high rigidity spectrometer, exploring the proton-neutron degree of freedom far from stability.

Inelastic proton scattering as a probe of the proton-neutron degree of freedom – Inelastic proton scattering has been proven to be a powerful tool in the investigation of the proton–neutron degree of freedom in nuclear structure physics [ALA96]. In the proximity of a closed neutron or proton shell, the quantification of proton and neutron contributions to a transition rate provides crucial information on the relative importance of valence nucleons and the core. In inelastic proton scattering, collective modes are preferentially excited. In even–even nuclei these are most often the lowest-lying 2^+ and 3^- excited states. Hadronic scattering is complementary to Coulomb excitation, for example, since the electromagnetic (Coulomb) excitation interrogates the proton transition matrix element, M_p, only, while inelastic proton scattering probes both proton and neutron matrix elements. Deformation lengths deduced for excited states populated in proton scattering can be combined with electromagnetic reduced transition probabilities, B(E2), from Coulomb excitation or excited-state lifetime measurements, to determine the ratio of neutron to proton transition matrix elements M_n/M_p [BER83]. This ratio, for collective 2^+ states in even-even nuclei, is a sensitive indicator of a shell closure.

An inverse-kinematics proton scattering program using a liquid-hydrogen target and GRETA for γ-ray tagging would focus on key the nuclei ^{100}Sn and ^{132}Sn at $Z = 50$, the $N = 82$ nucleus ^{128}Pd, ^{50}Ni and ^{78}Ni at $Z = 28$, ^{58}Ca *at* $Z = 20$, and the $N = 28$ nucleus ^{40}Mg, for example. Such studies will only succeed if the optimum production yields can be used at the rigidities enabled by a high rigidity spectrometer.

Similarly, proton-tagged scattering measurements using an active-target time projection chamber currently under development would be used at a high rigidity spectrometer to constrain optical model parameters for exotic nuclei through proton angular distribution measurements.

Physics along the *N=Z* line – The consequences of isospin symmetry are most clearly revealed in nuclei containing equal or nearly equal numbers of protons and neutrons ($N \cong Z$) [WAR06]. With increasing mass, the proton dripline moves closer to stability and neutron-deficient nuclei beyond $N=Z$ are unbound, including one of the $T=1/2$ mirror partners. A high rigidity spectrometer will allow access to these isotopes and enable science related to isospin symmetry breaking, pairing interactions in nuclei, defining the boundaries of the proton dripline, spectroscopy and mass measurements of unbound nuclei and the physics in the vicinity of $N=Z=50$ ^{100}Sn.

In recent years, studies of mirror nuclei in the $f_{7/2}$ shell have provided information on Coulomb energy difference (CEDs) up to high spin [BEN07]. Many of these experiments have increased their reach in both spin and isospin degrees of freedom though the use of modern advanced γ-ray detector systems coupled to fast-beam spectrographs [MIL16a, MIL16b]. These types of experiments, when performed at FRIB with GRETA at a high rigidity spectrometer, will allow to push further into the *fp* shell and out to the most neutron-deficient members of an isobaric multiplet. In particular, measurements of the $T=1/2$ mirror pairs beyond ^{70}Kr and approaching ^{100}Sn will be possible to study in detail, yielding the most complete data yet at the most extreme limits along the *N=Z* line.

Little information exists on many short-lived unbound nuclei beyond the proton dripline. While some proton-unbound nuclei can and have been studied through beta-delayed proton emission [BLA07], many are only accessible using in-flight decay methods. Experiments which utilize techniques similar to those recently employed for ^{69}Br [ROG11] require a spectrometer capable of identifying and measuring the heavy decay residue. A high rigidity spectrometer would be the high-resolution tool for such proton resonance spectroscopy of dripline nuclei which lie along the *N=Z* line between rubidium and tin, with their properties nearly completely unknown. A spectrometer setup with an open geometry and ample opportunity for charged-particle detection would be needed.

For such experiments, the higher beam energy afforded by a high rigidity spectrometer will not only help to maximize the projectile rate but also increase beam purity, which is notorious on the proton-rich side of the nuclear chart at lower beam energies.

The spin-isospin degree of freedom from Gamow Teller strength – The extraction of Gamow-Teller strength distributions from intermediate-energy charge-exchange reactions provides an important tool for testing theoretical models. Gamow-Teller strength distributions are very sensitive to the evolution of nuclear shells in asymmetric systems. Since Gamow-Teller transitions are associated with spin and isospin transfer, experiments provide a rather direct window into the spin-isospin components of the nucleon-nucleon interaction [OST92, HAR01]. Rare-isotope production rates at FRIB peak at around 170-200 MeV/*u* which is near ideal for ensuring a clean one-step reaction mechanism [LOV81, OST92] and a near model-independent extraction of Gamow-Teller strengths.

A unique way of testing the goodness of a core – defining a model space in nuclear theory – uses Pauli blocking effects in charge-exchange reactions. If *N*=50 was a good neutron core on the neutron-rich side of the nuclear chart, charge-exchange reactions in the (*n,p*) direction would

proceed with little cross section and suppressed Gamow Teller strength since the transition is blocked. For example, the rare-isotope production rates at FRIB and the very efficient transmission to the HRS will allow for such experiments along N=50 from stable ^{86}Kr to neutron-rich ^{80}Zn. Gamow-Teller transitions strengths in unstable nuclei are also sensitive probes of shell-mixing [ZEG10,MEH12] and will be used across the chart of nuclei as complementary tools to other probes for mapping shell evolution.

For charge-exchange reactions in inverse kinematics, a high rigidity spectrometer will be used to detect and characterize the heavy-ion reaction products. For the (p,n) charge-exchange probe in inverse kinematics [SAS11,SAS12], existing low-energy neutron detector arrays can be used to detect recoil neutrons, in combination with the Ursinus Liquid Hydrogen target. For the (^{7}Li,^{7}Be) reaction, GRETA will be used to detect both the 430-keV γ ray from the first excited state in ^{7}Be, tagging spin-transfer, as well as γ rays emitted in-flight from the excited nucleus produced in the charge exchange. In addition, decay particles (neutrons and/or protons) emitted from reaction residues when excited above the particle-decay threshold will be detected with neutron and charged-particle detectors placed downstream from the reaction target. By employing invariant-mass spectroscopy, the excitation energy can then be determined. Below the particle decay threshold, the excitation energy can be extracted directly from the heavy ion detected in the spectrometer. An alternative to the (^{7}Li,^{7}Be) reaction is the (d,^{2}He) reaction in inverse kinematics. A time projection chamber would be used to reconstruct the momentum of the unbound ^{2}He-particle from the accurate measurement of the momentum of the two decay protons, while the projectile-like reaction residues would be detected and characterized in the HRS. From the reconstructed ^{2}He momentum, the excitation energy and scattering angle can be determined.

4.2.1.5   Opportunities with commensal decay spectroscopy following reactions

In typical fragmentation or nucleon removal experiments, a large number of very exotic nuclei can be produces and transmitted to the focal plane of a spectrometer. Downstream of particle identification detectors in the focal plane, reaction products could be implanted into an active stopper such as a Si detector array, which would act as a total-kinetic energy detector, but would also be sensitive to the signals from the subsequent α or β decays of rare reaction products. A scintillator array immediately downstream of the implantation station would be sensitive to isomeric γ rays, such as the current S800 hodoscope [MEI11,WIM14], but also to delayed γ rays in the α or β decay daughters.

Such a focal-plane detector arrangement would provide a unique opportunity to take advantage of the cocktails of rare isotopes produced in a variety of reactions delivered to the focal plane of the spectrometer in a standard experiment. These isotopes will likely be among the most exotic produced at FRIB, and innately of physics interest. Optimization of the high rigidity spectrometer focal plane will allow optimal use of FRIB beams, with decay information obtained simultaneously with the (primary) physics goals of the in-flight experiment.

4.2.2   How does visible matter come into being and how does it evolve?

Reaction and decay networks in stars, stellar explosions, and binary mergers are responsible for the ongoing nucleosynthesis in the Universe (see Figure 4.6). They power astrophysical

phenomena, such as novae, supernovae, nucleosynthesis in neutron-star collisions, and X-ray bursts. Nuclear properties determine the light curves of many objects, the elemental abundances or in the composition of meteorites and pre-solar grains. Neutron stars, the remnants of supernova explosions of massive stars, are among the most compact objects with a crust that may contain some of the most neutron-rich nuclei possible in the crust surrounding a core of unknown composition. The nuclear equation of state, electron capture rates, and the location of the neutron dripline are most important to understand these extreme objects.

One of the challenges in the field is an understanding of the *r* process thought responsible for the origin of the heavy elements in the Universe. The possible sites of the *r* process and consequently its conditions and reaction and decay sequences have remained elusive until 2017 where one *r*-process site was reported from a spectacular multi-messenger astronomy campaign following the first LIGO/Virgo observation of the gravitational wave signal, GW170817, from a neutron-star merger [ABB17]. In addition to the gravitational-wave signal originating from two neutron stars spiraling into each other, a kilonova, powered by the radioactive decay of the synthesized neutron-rich nuclear matter, was left behind, observed and characterized across the electromagnetic spectrum [KAS17]. An understanding of the radioactive decays of the rare isotopes produced during the merger is crucial to interpret the kilonova signal and connect it to elemental abundances attributed to an *r* process. The gravitational-wave signal from GW170817 also provided unprecedented information on the size, mass, and deformability of neutron stars, which directly inform the fundamental properties of dense nuclear matter – in turn, knowledge on the nuclear equation of state is crucial to deduce the energy radiated by the gravitational waves and understand the amount of neutron-rich matter released.
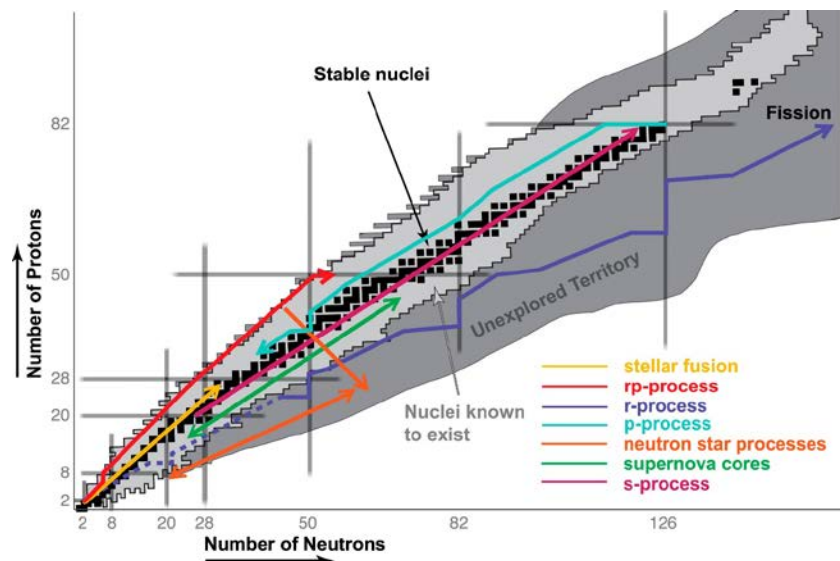
Figure 4.6 Overview of the main astrophysical processes superimposed on the chart of nuclei [AST17]. Often the most critical isotopes are farthest from stability and hence produced at low rates at FRIB. Sensitivity will be key to provide all the necessary astrophysical data [Figure from F. Timmes].

At a high rigidity spectrometer at FRIB, heavy-ion reactions can be used to constrain the nuclear equation of state, nuclear masses, needed to determine Q values in all nucleosynthesis process, including the *r* process, can be determined very far from stability through time-of-flight mass

measurements, and electron capture rates and nuclear fission can be characterized to constrain nucleosynthesis in the *r* process. This is outlined in the following sections.

4.2.2.1 **Key example** – Access nuclear masses closest to the dripline

Most nucleosynthesis processes involve rare isotopes far from stability, in particular, the *r* process and processes in the crust of neutron stars proceed along very neutron-rich nuclei. Nuclear masses are needed to understand the reaction and decay paths since they set the Q values.

Predictions from models [ERL12] agree quite well for known masses, but the divergence between different model predictions grows steadily (to several MeVs) when extrapolating into unexplored regions, in particular on the neutron-rich side. For astrophysical purposes, the present theoretical mass uncertainties need to be improved with measurement far out to anchor extrapolations. Typically, measurements of mass excesses of nuclei far from stability with a precision of 0.1-0.5 MeV are required. For the *r* process in neutron star mergers, data on a large number of very neutron-rich nuclei are needed to reveal relevant systematic trends in the mass surface (see Figure 4.7).
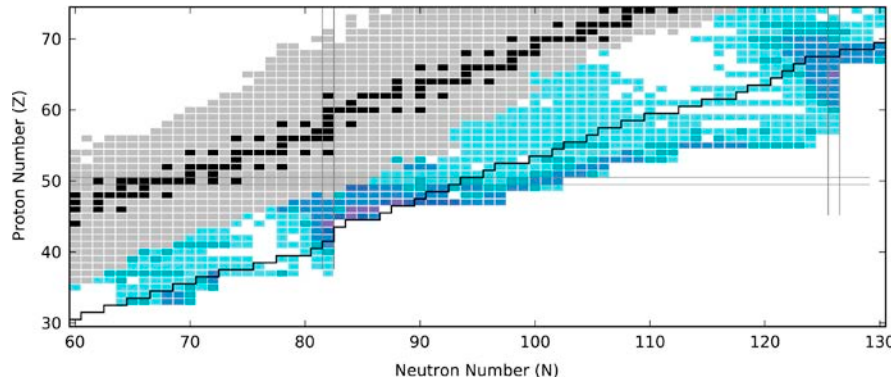
Figure 4.7 Sensitivity study for nuclear masses in an r process ensuing in a neutron star merger (Figure from [MUM16]). The darker the blue shading, the more important the nuclear mass for modeling the r process.

Far from stability, masses can be deduced efficiently from the simultaneous measurement of an ion's time-of-flight (ToF), charge, and magnetic rigidity thorough a magnetic system of a known flight path. ToF mass measurements can reach a significant fraction of the nuclei relevant for the r process and neutron star crust physics. Tens of masses can be measured in one experiment, including of shortest-lived ones closest to the neutron dripline (see [EST11, MEI13, MEI15] for the reach using NSCL's S800 analysis and spectrograph beam lines for ToF mass measurements). The flight path at a high rigidity spectrometer at FRIB would comprise the transmission and spectrometer beam lines, as well as part of the ARIS Fragment Separator.

Figure 4.8 shows that at FRIB, at the rigidities that optimize rare-isotope production, a large fraction of the nuclei on the *r*-process path (orange) up to *N*~100 can be reached with such measurements. Up to *N*~140, the less neutron-rich isotopes in the *r*-process path can be accessed and model extrapolations will be significantly improved. A large fraction of the nuclei of importance for neutron-star crustal processes (up to *N*~60) can be measured at a high rigidity spectrometer using the ToF-*Bρ* technique. Mass resolutions of better than 150 keV (FWHM) for *A*=50, 300 keV for *A*=100, and 500 keV for *A*=170 are achievable. The reach assumed for the above-mentioned opportunities assumed 1000 particles per week accumulated.
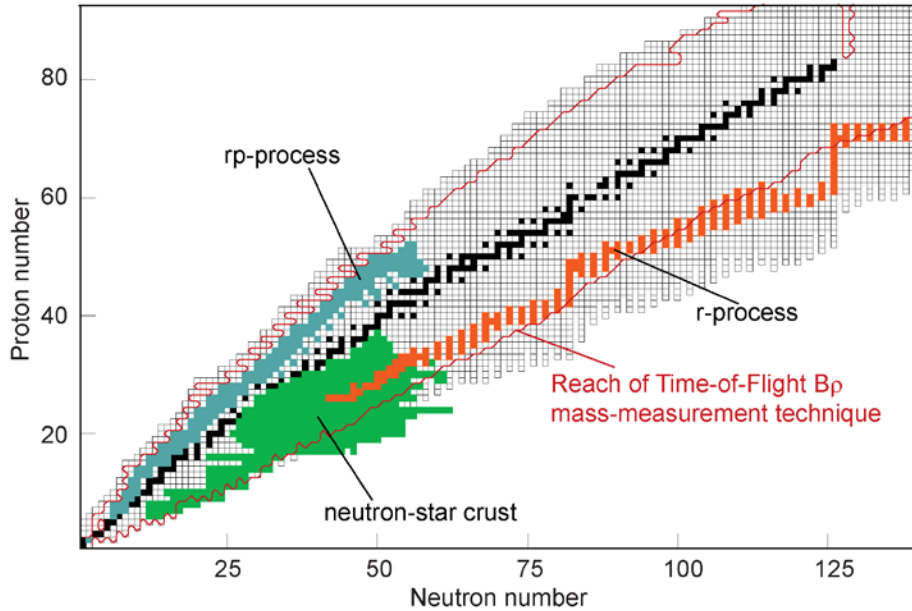
Figure 4.8 Applicability of ToF-Bρ mass measurement technique at FRIB. The reach for this technique is indicated by the red line, which indicates the RIB production rate of 1000 per week. At FRIB, a large fraction of the nuclei in the r-process path (orange) up to N~100 can be covered. Up to N~140, the less neutron-rich isotopes in the r-process path are covered and model extrapolations will be significantly improved. A large fraction of the nuclei of importance for neutron-star crustal processes (up to N~60) can be measured at the HRS using the ToF-Bρ technique. Mass resolutions of better than 150 keV (FWHM) for A=50, 300 keV for A=100, and 500 keV for A=170 can be achieved.

4.2.2.2   Weak reaction rates in nuclear astrophysics

Weak reactions involving unstable nuclei play key roles in pre-[HEG01] and late evolution of core-collapse supernovae [BET79,HIX03,LAN03,JAN07,SUL16,RIC17], thermonuclear supernovae [BRA00,IWA99,ZEG08], neutron stars and their crusts [GUP07,SCH13] and neutron-star mergers [GOR15]. For the astrophysical applications listed above, details of the Gamow-Teller strength distribution in the electron-capture/β^+ direction are most important, but transition in the β^- direction must be known with reasonable precision as well. Weak rates on rare isotopes are critical, as shown in Figure 4.9 for the example of electron captures in the late stages of core-collapse supernovae.
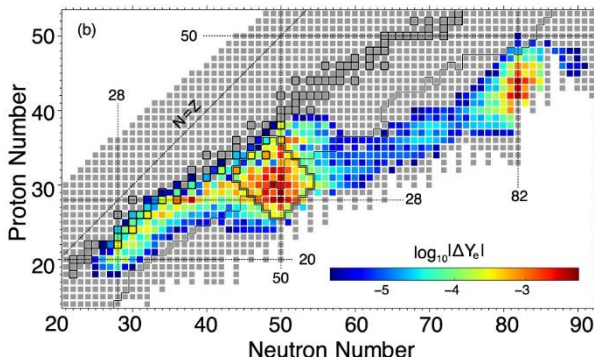
Figure 4.9 The 500 electron-capturing nuclei with the largest absolute change to the electron fraction |ΔY$_e$| up to neutrino trapping in the late stages of core-collapse supernovae [SUL16]. The most important region is in the neutron-rich region along the N=50 line, which can be studied by using charge-exchange reactions at a high rigidity spectrometer.

Many of the sensitive nuclei are far from stability, for example in the region around ^{78}Ni, and it will be critical to be able to perform the charge-exchange measurements at the rigidities where the rare-isotope production is optimized. It will be impossible to measure all the relevant Gamow-Teller strength distributions and accurate theoretical models are required to estimate the weak rates of interest for all astrophysical applications. Weak interaction rates measured for such key nuclei will serve as nuclear theory benchmarks for extrapolating into the regions out of reach experimentally.

The complete arsenal of charge-exchange probes, such as (p,n), $(d,^2\text{He})$ and $(^7\text{Li},^7\text{Be})$ in inverse kinematics, will be employed for the weak-rate measurements. The advantage of combining charge-exchange experiments with high-resolution γ-ray spectroscopy has been demonstrated [NOJ14,NOJ15,ZAM19,TIT19] and is envisioned with GRETA at a high rigidity spectrometer. As shown in Figure 4.9, the region just about ^{78}Ni is critical for constraining electron-capture rates in core-collapse supernovae and is mostly accessible for charge-exchange experiments at the HRS. Neutron-rich isotopes with proton numbers between 10 and 50 are important for heating and cooling processes in neutron-star crusts and most of the important cases [SCH13] can be reached in experiments with the HRS.

4.2.2.3   Projectile fragmentation and in-flight fission of neutron-rich nuclei

Fission properties of neutron-rich isotopes are an important input for astrophysical models of nucleosynthesis during the r-process. As the sequence of neutron captures and β decays that drives the r-process takes the matter flow towards very heavy isotopes, different fission modes (spontaneous, induced and β-delayed fission) will become the dominant reaction types [PAN05] and will impact the end-point for the r process. Therefore, fission stalls the reaction flow to the heavier masses and determines the heaviest elements that can be synthesized. Fission also affects the final abundances of the produced heavy elements. For example, when nuclei decay towards stability at the end of the neutron-capture stage, β-delayed fission will reduce the amount of cosmochronometer isotopes, such as Uranium and Thorium, that are synthesized in the r-process [THI83, SCH02]. Fission also has an important global effect on the abundance patterns of r-process isotopes in the mass region of fission fragments.

Reliable data on the isotopic distribution of fission fragments is necessary to understand this effect, in particular for an r-process scenario at sites with very high neutron density, such as mergers of binary neutron-star systems. In such neutron-rich scenarios, the reaction flow will go through several cycles of synthesis up to heavy masses, followed by fission-recycling back to intermediate mass region [KOR12, GOR13]. The distribution of fission fragments then leaves a strong imprint on the resulting r-process abundances, and can contribute to a robust abundance pattern of individual r-process events, as illustrated in Figure 4.10.

Recent progress on fission measurements [SCH01,ERL12a,CAA13,PEL13,AND10] shows the potential for having appropriate data to improve our understanding of this very complex many-body process. The ability to produce very neutron-rich heavy beams at FRIB, coupled with the high transmission to a high rigidity spectrometer and the potential for measuring fission fragments in coincidence, allows for detailed measurements of fission-fragment distributions in unexplored regions of the nuclear chart, thereby providing critical data for understanding of the physics of nuclear fission in r-process calculations.
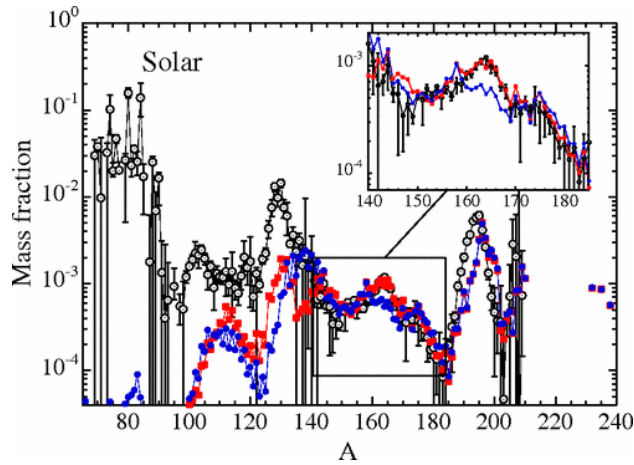
Figure 4.10 (from Ref. [GOR13]) Final abundance distributions for ejecta produced in neutron-star (of 1.35 solar masses) mergers. The blue and red dots represent results based on different models for the fission process. The open circles represent solar abundances.

4.2.2.4 **Key example** – The nuclear Equation of State from heavy ion collisions

The nuclear equation of state (EoS), particularly for neutron-rich matter, plays a significant role in supernovae and neutron-star mergers [DAN02]. The EoS describes relationships between energy, pressure, temperature, density and isospin asymmetry in a nuclear system. At low temperature, the EoS can be separated into a symmetric matter contribution that is independent of the isospin asymmetry and a poorly constrained symmetry-energy term, proportional to the square of the asymmetry [LI08]. This feature of the nuclear interaction also determines the nature and size of neutron stars and the thickness of neutron skins of nuclei [LAT01,LAT04,LAT13,LAT15]. Uncertainties in the density dependence of the symmetry energy are large [HEB10, GAN12,LAT13].

Macroscopic quantities of asymmetric nuclear matter exist in neutron stars and in type II supernovae over a wide range of densities [LAT01]. Constraints on the EoS and the symmetry energy at sub-saturation and supra-saturation densities are critical for an understanding of neutron-star properties such as stellar radii and moments of inertia, crustal vibration frequencies [LAT04,VIL04], neutron-star cooling rates [LAT04,STE05], and most recently, the interpretation of the gravitational wave signal and electromagnetic emissions from the GW170817 neutron star merger event detected by LIGO/Virgo [ABB17, RAD18].

Several consistent laboratory constraints for the density dependence of the symmetry energy exist at sub-saturation densities [TSA12, LAT13, HOR14], see Figure 4.11, while the constraints above saturation density are inconsistent [XIA08, RUS11]. The region above ρ/ρ_0 is particularly important for the interpretation of neutron star and neutron star merger properties.

At FRIB, heavy-ion collisions [LI08] will be performed to constraining the EoS, especially at supra-saturation densities, where the uncertainties are largest. The symmetry energy at high densities can be probed in heavy-ion reactions by comparing the relative emission of members of isospin multiplets, e.g. π^- vs. π^+, n vs. p, t vs. ^3He, etc., which experience symmetry potentials and symmetry forces of opposite sign [FAM06, LI05, LI05b,DIT10, XIA08].

The beam energies of 170-200 MeV/u available at FRIB allow for studies of the symmetry energy at both sub- and supra-saturation density. To reach the highest densities, heavy-ion experiments, such as for example a 175 MeV/u ^{132}Sn beam impinging on a ^{124}Sn target, require a high rigidity

spectrometer to transport the 5.25 Tm ^{132}Sn beam [LI02]. For example, at 200 MeV/u ^{132}Sn beam energy, ~1.75 ρ/ρ_0 supra saturation density is probed [LI02]. In general, experiments would simultaneously measure ratios of charged pions, neutrons/protons, light charged particles, and projectile-like fragments from heavy-ion collisions induced by neutron- and proton-rich rare-isotope beams, using among other detection systems a time projection chamber in front of the high rigidity spectrometer or inside the first dipole of the spectrometer section to track light charged particles, similar to work performed with the SπRIT-TPC at RIBF [OTS16, JHA16]. At a high rigidity spectrometer, neutrons would be detected in MoNA-LISA and heavy charged particles would be identified and analyzed in the spectrometer section. At the beam energies enabled by a high-rigidity beam transport system, 200 MeV/u vs. 105 MeV/u for the example of a ^{132}Sn beam, charged pion production increases by more than an order of magnitude, enabling the use of pion flow to probe the nuclear equation of state (see Figure 4.12). It is noted that an upgrade of FRIB to 400 MeV/u (see Section 4.3.2.6) would increase the cross sections for pion production by at least one more order of magnitude with the *NN* pion production threshold well exceeded.
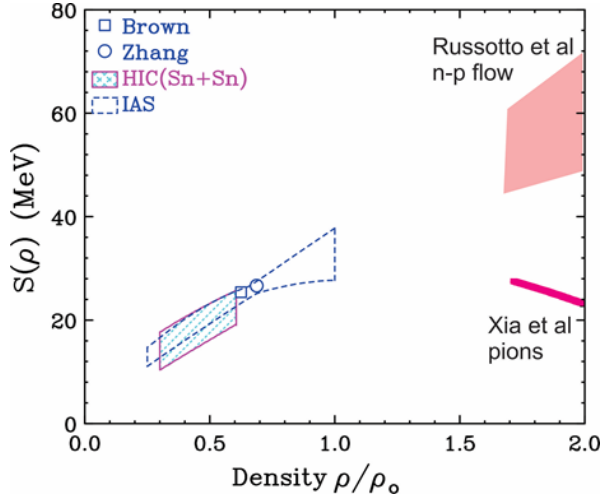
Figure 4.11 The symmetry energy S(ρ) as a function of baryon density. At sub-saturation density, the density dependence of the symmetry energy is reasonably constrained [HOR14], at supra-saturation density, the region important for neutron star and neutron star merger physics [LAT16], the measures from n-p flow and pion production differ widely and new constraints are needed that high-energy beams from FRIB can provide.
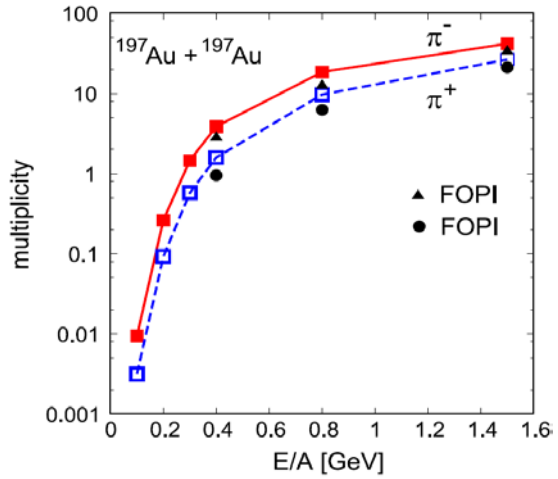
Figure 4.12 Example for the incident energy dependence of charged pion multiplicities in central collisions [IKE18]. With the HRS, ^{132}Sn projectiles would be available for experiments at 170 MeV/u and higher while a 4Tm limit would restrict the ^{132}Sn beam energy to 105 MeV/u. Experiments at high rigidity thus increase pion production by an order of magnitude and so significantly enhance the signal-to-noise in collision experiments with pion flow observables.

4.2.2.5   Properties of nuclear matter from the study of resonances

Giant resonances provide complementary constraints on the properties of nuclear matter at sub-saturation density. Below, it is briefly outlined how isoscalar and isovector giant resonances add

to the effort of constraining the nuclear equation of state by probing incompressibility or neutron-skin thicknesses.

Isoscalar Giant Resonances – The energy of the isoscalar giant monopole resonance (ISGMR) or the nuclear "breathing mode" is directly related to the nuclear incompressibility, a critical component of the nuclear equation of state. In recent years, measurements of ISGMR over series of Sn and Cd isotopes [LI07,PAT12] have provided an "experimental" value for the asymmetry term of nuclear incompressibility, K_τ ($K_\tau = -550 \pm 100$ MeV), which is derived from studying the nuclear compressibility K_A as a function of $(N-Z)/A$, as shown in Figure 4.13. This term is governed by the first and second derivatives (as a function of density) of the symmetry energy at sub-saturation densities [COL14] and, as discussed above, is important in the study of, among other objects, neutron stars. Extending these measurements to very neutron-rich isotopes is important to more precisely determine the value of this asymmetry term. Another important issue that would be addressed by ISGMR measurements in very neutron-rich nuclei is that of the "soft" monopole resonance resulting from the vibrations of the neutron skin; one would then have an incompressibility of the core and another one of the skin. This would result in ISGMR strengths at low energies—this low-lying monopole strengths is akin to low-lying dipole strength observed in many nuclei [SAV13] and has drawn strong interest [PAA07,KHA11,KHA13,HAM14].
Successful measurements of the ISGMR have been performed on ^{56}Ni [MON08] and ^{68}Ni [VAN14]. Similar to the latter experiment, at a high rigidity spectrometer at FRIB, measurements can be performed by placing an Active Target TPC (AT-TPC) filled with helium at the target station. The TPC would be used to detect the recoil particle (either the deuteron or α-particle) and the spectrometer would detect the heavy nucleus to provide a clean trigger. For example, the ISGMR could be studied in Sn isotopes with mass numbers ranging from 104 to 134 for which intensities of ~10^4 pps are available for in-beam experiments when transported through the high transmission beam line from the ARIS Fragment Separator to the high rigidity spectrometer. Such measurements have the potential to reduce the uncertainty in K_τ by more than a factor of 2 (see Figure 4.13).
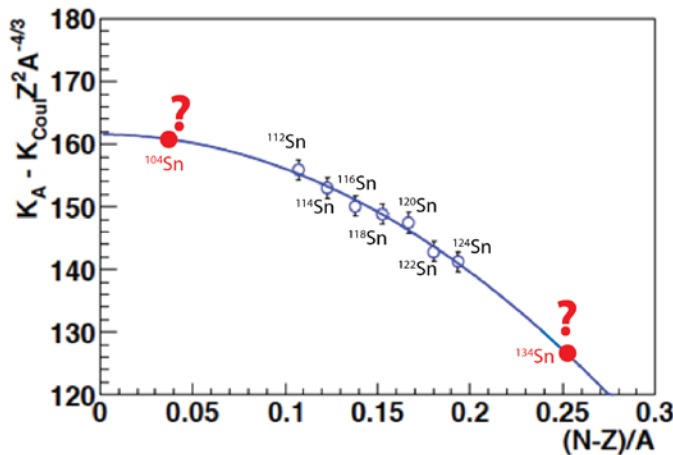
Figure 4.13 Systematics of the nuclear incompressibility, K_A (minus the Coulomb term), derived from measurement of the ISGMR in Sn isotopes, as a function of the asymmetry term $(N-Z)/A$ [LI07]. The quadratic fit to the data leads to a value for the asymmetry term of nuclear incompressibility $K_\tau = -550 \pm 100$ MeV. A measurement of the ISGMR in ^{104}Sn and ^{134}Sn to within ± 0.2 MeV would reduce the uncertainty in K_τ to less than 50 MeV.

Isovector Giant Resonances – Isovector giant resonances are associated with out-of-phase density oscillations of protons and neutrons in nuclei [HAR01,PAA07]. Their study, through charge-exchange reactions at intermediate energies, provides access to macroscopic nuclear matter properties associated with the difference between the two Fermi fluids such as the symmetry potential and the neutron-skin thickness [DAN03]. By varying the neutron-to-proton ratio along an isotopic chain, sensitivity is gained to these properties [PAA07]. Another degree of freedom arises from spin oscillations of the nucleons, leading to the isovector "spin-flip" giant resonances. The study of these resonances are thus excellent probes of isovector spin-isospin sector of the nucleon-nucleon effective interaction [FRA05], and are desirable for improving the reliability of calculations.

The two simplest isovector giant resonances are the Isobaric Analog State (IAS) and the Gamow-Teller Resonance (GTR). The energy splitting between the IAS and the centroid of the Gamow-Teller resonance provides a model-dependent measure of the neutron-skin thickness [VRE03]. The analysis of the IAS [LOC14,DAN17,LOC17] and of the Isovector Giant Dipole Resonance [KRA99,YAK06] has also been used study neutron skins. For both of these approaches, experiments with nuclei that have large neutron-to-proton asymmetries are critical to reduce the uncertainties [SAG07]. The nuclear size and density distribution are important properties of nuclei that determine the nuclear potential, single-particle orbitals and wave functions. Determination of the neutron skin thickness are critical for understanding the bulk properties of nuclei. The neutron-skin thickness is also closely related to the symmetry energy [BRO00,DAN03,SAG07, BRO13,LAT13,NAZ14], which determines, for example, the radii of neutron stars [STE05,LAT16]. The increased thickness of neutron skins in unstable neutron-rich isotopes forms a key motivation for performing such studies at FRIB.

In experiments that explore isovector giant resonances in rare isotopes, the measurement of the light recoil particle will be facilitated in a detector near the reaction target to determine the excitation energy and center-of-mass scattering angle, while the spectrometer serves to analyze the projectile-like ejectile and isolate the charge-exchange reaction (see also 4.2.1.1).

Rare isotope beams can also be employed as a probe for specific spin-isospin excitations. For example, the (^{10}Be,^{10}B+γ) [SCO17] and (^{12}N,^{12}C+γ) [NOJ18] reactions in forward kinematics have been developed to isolate the illusive isovector giant monopole resonance and isovector spin giant monopole resonance, respectively. Measuring the properties of these giant resonances is important for constraining bulk properties of nuclear matter such as the surface and volume symmetry energy coefficients. To extend these pioneering studies to heavy nuclei, FRIB beam intensities are required. The experimental will also strongly benefit from the coupling of the HRS and GRETA.

4.2.3 Probing fundamental symmetries through weak interaction studies

The properties of rare isotopes provide a window into the fundamental symmetries of nature, and offer the possibility to explore physics beyond the standard model of particle physics on energy scales that rival high-energy collider physics.

4.2.3.1 **Key example** – The quenching of g_A: Charge exchange reactions in ^{100}Sn and asymmetric systems

A fundamental weak coupling, characterized through the axial vector constant g_A, can be uniquely explored with fast-beam charge-exchange reactions. The hypothesis that the weak vector current g_V is conserved, or not renormalized by the strong interaction [FEY58], has been tested experimentally to the level of 1.2×10^{-4} [HAR14]. The axial vector constant, however, appears to be renormalized or "quenched" by the strong interaction. This quenching of g_A is apparent in the over-prediction of β-decay and two-neutrino double β decay matrix elements when using the bare value of g_A. Similarly, in charge-exchange experiments only about 50-60% of the Gamow-Teller sum-rule strength is observed at excitation energies up to the giant-resonance region (below ~20 MeV) [GAA81,GAA85]. The poorly understood mechanism of the quenching is a long-standing issue that has important implications for neutrino physics and astrophysics. An important additional question is: does whatever is responsible for this renormalization of g_A also quench neutrino-less double-β decay? An answer to this question is important for accurately estimating neutrino-less double β decay matrix elements and resulting decay rates (these may scale approximately with g_A^4) [SUH17] in the planning for ton-scale discovery experiments [NDB14]. Three mechanism are thought to contribute to the quenching of the sum-rule strength [BRO88]: 1) mixing between 1p-1h GT states and 2p-2h configurations via the strong tensor interaction moves GT strength to excitation energy beyond the GT giant resonance [HYU80,ARI99]; 2) coupling to the Δ(1232)-isobar nucleon-hole state [ERI73]; 3) meson-exchange currents. Evidence for the first mechanism, which is thought to be the strongest [BRO88], has been found [YAK05] in the analysis of (*p,n*) [WAK97] and (*n,p*) reaction data [YAK05] of ^{90}Zr. However, recent results from a (*p,n*) experiment in inverse kinematics on unstable ^{16}C [LIP18] indicate that the first quenching mechanism can be well studied in light neutron-rich isotopes, since the transition strength in the $β^+$ direction is Pauli blocked and the Gamow-Teller excitations strongly dominate the measured spectra, thereby simplifying the analysis and observation of the Gamow-Teller strength at excitation energies above the giant resonance region. Hence, (*p,n*) experiments at the HRS on very neutron-rich systems provide one way to better understand the quenching mechanism.

A second opportunity to study the renormalization of the axial-vector coupling constant g_A is by measuring charge-exchange reactions from doubly magic ^{100}Sn and investigating the Gamow-Teller strength distribution in combination with results from β-decay data [HIN12]. By studying the details of the Gamow-Teller strength distribution and its direct decay properties insight into the microscopic origin can be achieved. Such a measurement is even challenging at FRIB and the ^{100}Sn beam would be needed at optimum production rigidity and be transported with minimal losses to a thick Hydrogen target for performing a ^{100}Sn(*p,n*) experiment in inverse kinematics. Experimental sensitivity will be critical to enable measurement of this and similar charge-exchange reactions. In addition, an open geometry at forward scattering angles for the detection of decay protons is necessary to elucidate the microscopic structure of the Gamow-Teller strength distribution.

4.2.4 Applications – **Key example**: Improving models of nuclear fission

Nuclear fission represents a challenging and complex many-body process with significant impact on derivative nuclear technologies in the fields of nuclear energy, defense, and homeland security. Driven by the importance of fission, the evolution of this sub-field is ongoing, with significant advances taking place on both experimental and theoretical/computational fronts.

Recent theoretical work has investigated the sensitivity of fission model parameters to the prompt fission γ-ray spectrum (PFGS) [TAL12, STE13a], and is complemented by next generation PFGS measurements on the major actinides [JAN13,ULL14,OBS13]. The model uses a Monte-Carlo Hauser-Feshbach approach to calculate the spectrum and correlations between neutrons and γ rays emitted from fission fragments, and the predictive capability is ultimately limited by incomplete knowledge of the nuclear structure of the neutron-rich fission fragments involved.

The broad range of intense neutron-rich beams available at FRIB can be exploited to improve the nuclear structure underpinning these calculations. In particular, γ-ray spectroscopy following fragmentation reactions could inform these calculations directly through the measurement of discrete, low-lying states. A sensitive, high rigidity spectrometer with a large momentum and angle acceptance, combined with the efficiency and resolution of GRETA would allow surveys across large sections of the nuclear landscape for neutron-rich nuclei between mass numbers of 80 and 140. The fission process of heavy nuclei, excited by surrogate reactions to simulate neutron-capture, can be studied provided sufficient sensitivity and rigidity is available. To study the correlations between fission fragments, the ability to detect and analyze both fission fragments simultaneously would be a game changer. For this purpose, it is advantageous that experiments are performed at high rigidities, as the kinematic focusing of the fission fragments towards forward scattering angles in the laboratory frame increases, which reduces the requirement for the acceptance of a spectrometer and makes such unique measurements feasible.

4.2.5 **Key example** – A game changer for nuclear reactions

FRIB's beam energy range for rare isotopes – from keV/u to 200 MeV/u – will enable a broad arsenal of direct, compound, and heavy-ion nuclear reaction mechanisms to be applied for the extraction of key nuclear properties, while also providing benchmarks in the quest for a needed unified description of nuclear structure and nuclear reactions [NAV16]. Nuclear reactions are among the prime experimental tools used to address the science thrusts of the field, including nuclear structure physics, nuclear astrophysics, the study of fundamental symmetries, and the application of isotopes. At the highest energy range, for which measurements can only be realized at a high rigidity spectrometer, certain classes of direct reactions can be optimally used to probe the structure of the nucleus and nuclear matter.

Figure 4.14 sketches the energy regimes that will be used at FRIB for certain reactions together with the broad science topics or observables that are addressed. Already at 100 MeV/u, the rigidities of ^{40}Mg and ^{84}Ni exceed 4 Tm. For ^{40}Mg and ^{60}Ca, rigidities exceeding 6.1 and 5.5 Tm, respectively, are needed to accommodate reactions beyond 150 MeV/u. The rigidities that would optimally be used to probe skin nuclei in a regime where the conditions for required theoretical approximations to the reaction mechanisms are met exceed 6 Tm for ^{84}Ni and ^{140}Sn.
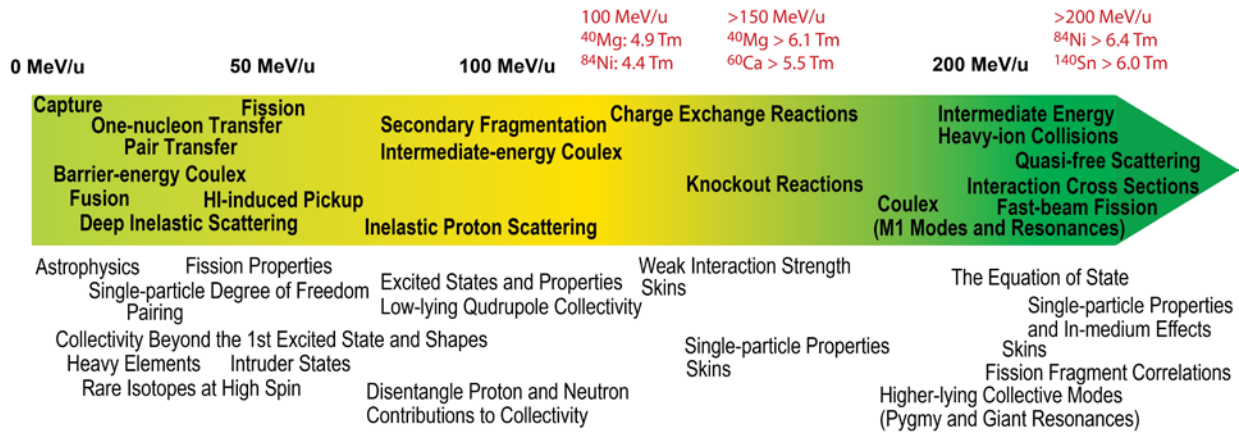
Figure 4.14 Sketch of the energy regimes where certain reactions, accessing specific science topics or observables, would optimally be used at FRIB. For some of the key nuclei discussed throughout the science section, rigidities above 4 Tm are required already to achieve beam energies of 100 MeV/u.

Below, the advantages of achieving the high beam energies afforded by a high rigidity spectrometer at FRIB are discussed for some of the reactions mentioned throughout the science section.

Knockout reactions – Direct one-nucleon knockout reactions from fast exotic beams have been developed into a powerful technique, extending the detailed study of the nuclear wave function to short-lived rare isotopes [HAN03, GAD08b]. Heavy-ion, e.g. ^{9}Be or ^{12}C, induced one-nucleon knockout reactions at intermediate beam energies have been successfully applied at rates of less than 1 particle/s. The shape of the longitudinal momentum distribution of the projectile-like residue carries the information on the orbital angular momentum (*l*-value) of the knocked-out nucleon. Gamma-ray spectroscopy in coincidence with the heavy knockout residue provides the identification of the final state [GAD08a]. In comparison to reaction theory, spectroscopic factors, which relate to the occupation number of single-particle orbitals, can be derived from measured partial cross sections to individual final states of the residue. One-nucleon knockout reactions thus provide an identification of single-particle components in the ground-state wave function of the rare-isotope projectile and a measure of the relative separation and occupation of singe-particle levels.

Figure 4.15 illustrates the momentum resolution requirements for one-neutron knockout from ^{204}Pt. This reaction would provide single-neutron structure at the key *N*=126 neutron shell closure which is not only interesting from a nuclear structure point of view but also is relevant for the *r* process. The theoretical cross sections that enter all knockout work use a reaction theory description [TOS99, TOS01] in the framework of straight-line trajectories (eikonal approach) and sudden approximation. Both approximations, sudden and eikonal, become increasingly more accurate at the higher projectile energies that are afforded by FRIB together with a high rigidity spectrometer. These energies together with the identification of the removed proton or neutron with charged-particle or neutron detectors will enable the use of the reaction framework in the optimum energy regime, without kinematic limits for the removal of the most deeply-bound nucleons [FLA12], and with a direct probe of knockout mechanism via light-particle detection [BAZ09]. For the extraction of l-values in the studies of nuclear shell structure, symmetric

longitudinal momentum distributions of the knockout residues are observed at RIBF beam energies of around 200 MeV/u, see for example [KOB12], while at the lower NSCL energies of about 70-90 MeV/u, pronounced tails are encountered [GAD05]. With the high beam energies possible at a high rigidity spectrometer, orbital angular momenta can be assigned unambiguously from symmetric longitudinal momentum distributions of the residue, allowing to track the evolution of nuclear structure with unprecedented clarity.
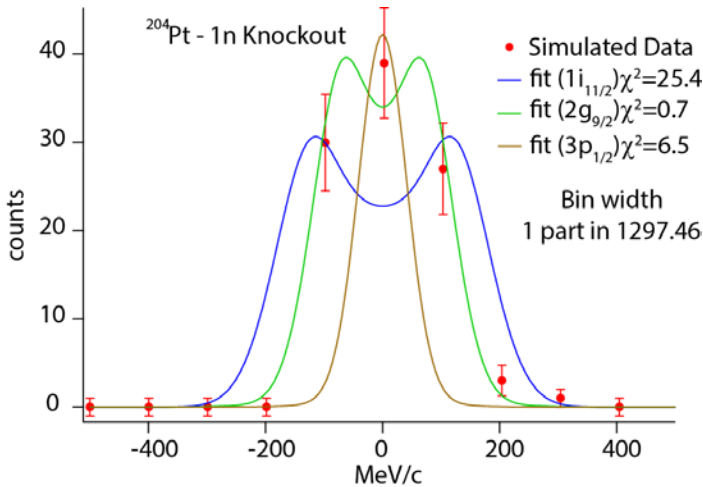
Figure 4.15 Simulated momentum distribution of ^{203}Pt following the knockout of a neutron from the $2g_{9/2}$ orbital of ^{204}Pt, fitted by theoretical distributions assuming either p, g, or i orbital angular momenta. The χ^2 values clearly indicate $g_{9/2}$ as the best fit, in spite of the limited statistics. A momentum resolution for the ^{203}Pt residue of better than 1 in 1300 is required to discriminate between the involved orbital angular momenta in this mass region.

Quasifree scattering – As discussed above, knockout reactions are powerful tools for extracting information on the nuclear wave function. The relatively strong absorption makes the reaction probability peak near the surface of the nucleus. Similar arguments hold for transfer and Coulomb break-up reactions. To probe deeper into the nucleus, nucleon knockout reactions using protons as the probe, i.e. (*p,2p*) and (*p,pn*), have been used. Spectral functions of protons and neutrons in the wide range from valence nucleons to the deeply bound core states can be investigated. In addition, by studying cluster knockout reactions, such as (*p,pd*) or (*p,pα*), nucleon-nucleon correlations and cluster structures in nuclei can be probed. As a consequence of being deeply bound, nucleons become sensitive to in-medium modifications [KRE95], which will affect the observables measured in these quasifree reactions.

At FRIB, the energy of rare-isotope beams will be below the optimum regime for spectroscopic use of quasifree knockout studies since distortions and in-medium effects in general will play an important role at 100 MeV/u in the (*p,2p*) equal-sharing scenario. However, this in turn provides the interesting opportunity, if spectroscopic information is known, to probe the elusive in-medium modifications, providing a unique window into the role of in-medium effects in very asymmetric nuclear matter [LI93, LI94, CHE03, LI05, SAM06, JIA07]. The optimum condition for using quasifree scattering as a spectroscopic tool to access spectral functions is an incoming beam energy of about 400 MeV/u. In that case, the energies of the outgoing nucleons still fall mostly in the energy window with minimum distortions [FRA95] (200 MeV/u in the exit channel for the equal sharing scenario). This optimum projectile beam energy regime may become available at FRIB following an energy upgrade to 400 MeV/u (See also Section 4.3.2.6).

Heavy-ion electromagnetic excitations – Electromagnetic excitations induced by heavy ions (Coulomb excitation) at intermediate and relativistic beam energies have long been used to provide detailed information about collective degrees of freedom in nuclei [BER88, GLA98]. Excitations of rare isotopes can be studied by scattering these particles of a stable high-Z target. The exchange of virtual photons, when the rare-isotope beam passes through the Coulomb field of the high-Z target, results in high cross sections for collective excitations. Contributions from interactions mediated by the strong nuclear force are reduced at very forward scattering angles. For a given secondary beam and target, the sensitivity for exciting a particular collective state strongly depends on the choice of the beam energy [GLA98]. Below 100 MeV/u, the first excited 2^+ state is most strongly excited. Above 200 MeV/u, the excitation probability for the higher-lying Giant Dipole Resonance (GDR) and Giant Quadrupole Resonance (GQR) increases steeply.

To efficiently study the GDR and GQR at FRIB, experiments should be performed close to the beam energies at which the rare-isotope production rates are maximum (170-200 MeV/u). Especially the excitation of the GDR is of great interest, since its properties provide a probe of the charge distributions in nuclei. A fragmentation and a shift of the GDR strength towards lower excitation energies was predicted for heavier nuclei as the neutron dripline is approached [SUZ90]. This redistribution of strength is due to changes in the nuclear mean field as a function of N/Z combined with the proximity of the continuum for all particle-hole excitations [ZEL06]. Such a redistribution of strength towards lower energies was, for example, observed in studies of the GDR in ^{130,132}Sn [ADR05]. Exploration of the existence and low-lying dipole strength in neutron-rich nuclei is not only of importance for understanding collective motions in asymmetric nuclei, they are also important for understanding the relative abundances produced in the astrophysical r process [SAV13]. Although during much of the r process, photodisintegration and radiative capture are in equilibrium, near the end of the process, nucleosynthesis depends on the absolute rates of the (n,γ) and (γ,n) processes and the latter will be affected by the low-lying dipole strength. For example, in the region near the above-mentioned cases of ^{130,132}Sn, several waiting points in the r-process path are nearby and could be affected.

Measurements require projectile beam energies that exceed the 4 Tm limit for neutron-rich nuclei and the detection of the heavy fragment, as well as photons and neutron emitted in the decay of the excited nucleus. At a high rigidity spectrometer, MoNA-LISA and GRETA would be well suited for coincident neutron and γ-ray spectroscopy.

4.2.6 **Key example** – Discovery science: The skin nuclei ^{84}Ni and ^{140}Sn

New opportunities and surprises are expected from access to unusual nuclear systems at the extremes of isospin. FRIB will produce nuclei with the most extreme N/Z ratios, including very neutron-rich systems in which the excess neutrons will arrange to form a skin. ^{84}Ni and ^{140}Sn are examples of such nuclei that are expected to have significant neutron skin thicknesses, 0.51 fm and 0.36 fm, respectively [ERL12], as compared to stable isotopes that have skins closer to 0.1 fm thickness. Aside from the importance of the neutron skin thickness for the nuclear equation of state, outlined in Sections 4.2.2.4 and 4.2.2.5, reactions induced by nuclei with extreme neutron skins may be the only way to study neutron matter in the laboratory. For the two examples given above, the total luminosity gains of performing reactions at a high rigidity spectrometer over existing spectrographs limited to 4 Tm are 79-fold and 5.5-fold for ^{84}Ni and ^{140}Sn, respectively.

For both the Ni and Sn proton magic chain, the skin thicknesses can be characterized along isotopic chains with a variety of methods of which interaction cross section and proton scattering measurements potentially have the furthest reach. These two techniques as performed at a high rigidity spectrometer at FRIB are briefly outlined below.

Elastic scattering – Whereas charge radii can be determined by through electron scattering, muonic atoms, and laser spectroscopy via isotopic shift measurements, matter radii, which are needed to deduce the neutron radii, can be probed in hadronic scattering. Elastic proton scattering has already been applied to, for example, the cases of ^{4}He, ^{6}He and ^{8}He [ALK97], ^{40}Ca, ^{48}Ca [CLA03] and ^{208}Pb [KAR02, CLA03]. Such studies are complementary to the reaction/interaction cross section measurements outlined below since they carry different systematic uncertainties. They also complement the more model-independent extraction of neutron skin thicknesses from parity-violating electron scattering experiments at JLAB [ABR12,PAS11,MAM13], which is confined to stable nuclei at present. Systematic studies over isotopic chains extending to very neutron-rich nuclei will provide additional constraints on the equation of state as the increase in skin is mapped as function of the isospin.

The key to ensuring that proton elastic scattering data provide accurate information on density distributions and matter radii is the confirmation that the extracted parameters are beam-energy independent [CLA03,KAR02]. This can be done by analyzing the elastic differential cross section within a consistent theoretical framework over a wide range of momentum transfers (i.e. up to large scattering angles) for a variety of beam energies. With a high rigidity spectrometer at FRIB, it will be possible to pursue such experiments for very neutron-rich systems up to high beam energies. Sufficient statistics could be acquired using thick Hydrogen targets or active-target time-projection chambers. Elastic scattering experiments in inverse kinematics off the proton are also motivated by recent advances made in the framework of the dispersive optical model (DOM) to quantify the spectral strength in the continuum orbits that are filled in the independent particle model [MUE11,MAH14]. The key breakthrough in the DOM analysis is that it links structure information directly with continuum physics and produces a paradigm shift in which nuclear reactions and structure can be analysed as different aspects of the same underlying science.

Total reaction/interaction measurements – Absorption measurements are complementary to elastic proton scattering. They can also provide information about the matter radii of isotopes [OZA01]. Traditionally, two types of measurements have been used. In reaction cross section (σ_R) measurements the total probability of interactions between a nucleus and a target is determined from a measurement of the particles transmitted through a target without any interaction. In interaction cross section (σ_I) measurements, the total probability of a reaction between a nucleus and a target is measured for which the nucleus changed proton and/or neutron number. The difference between σ_R and σ_I are inelastic-scattering events, i.e. events in which energy and momentum are transferred between projectile and target but the neutron and/or proton number does not change: $\sigma_R = \sigma_I + \sigma_{inelastic}$. More recently, charge-changing cross sections (σ_{CC}) have been developed for probing the point-proton distribution rms radii (usually referred to as the proton rms radii) of nuclei [BLA92]. Combining σ_R or σ_I and σ_{CC} (or the proton rms radii obtained from other probes) provide a way to determine the neutron rms radii. Such a technique has been applied on

neutron-rich nuclei at incident beam energies of ~200 MeV/*u* and higher [TER14, EST14, YAM11].

These analyses are model-dependent and rely on the application of Glauber models in the optical limit, which are optimally applied at several 100s of MeV/*u*. Amos et al. [AMO06] also studied the prospect of using the reaction cross sections on protons as a tool to measure the spatial distribution of neutrons in exotic nuclei. They showed that by folding nuclear structure densities with effective in-medium nucleon-nucleon interactions, good descriptions of the reaction cross section data can be achieved at energies from 65-200 MeV/*u*. These results have paved the way for studies of reaction cross sections at FRIB. At lower beam energies, the separation between inelastic and elastic channels is feasible without γ-ray spectroscopy even for relatively massive nuclei. With a high rigidity spectrometer, studies can be performed over a wide beam-energy range, reaching the ones where Glauber model approaches are increasingly reliable, which will help to constrain systematic uncertainties. In addition, being able to achieve the highest rare-isotope beam intensities for the most neutron-rich nuclei is critical and can only be accomplished if the beams can be used at the rigidities that optimize their production.

4.3 Science Specifications

In Table 4-2 the scientific requirements for the HRS based on the envisioned science program described in section 4.2 and Table 4-1 are summarized and sorted by the key scientific questions of the NRC Decadal study [NRC13] and the 2015 NSAC Long-Range Plan [LRP15]. These scientific specifications have been established by the members of the HRS working group based on the 2014 HRS whitepaper [HRS14] and additional and more detailed studies of the scientific program. For this purpose, 35 representative members of the working group met in biweekly meetings. In addition, the full working group met during the low-energy community meetings and organized workshops to collect broad input from the FRIB user community.

Because of the wide variety of experiments that will be run with the HRS, it is important to establish clear specifications imposed by the broad scientific program. In practice, many of the experiments have overlapping specifications. Therefore, in establishing a summarized list of scientific specifications, a set of "prototypical" experiments was chosen that encompass the specifications of other experiments.

The scientific specifications for the HRS can be divided into two groups. The first set of specifications pertain to the Spectrometer Section and is motivated by the detailed conditions for optimizing each of the scientific programs. These specifications include the need to place and interface with ancillary detector systems that are necessary to perform the experiments foreseen by the user community. The specifications that pertain to the Spectrometer Section are detailed in Section 4.3.1.

The second set of specifications is mandated by the goal to perform experiments with nuclei that have the most extreme neutron-to-proton ratios and are produced at the lowest rates at FRIB. Consequently, optimization of the luminosity of experiments performed at the HRS is key to meeting the needs of the FRIB user's community. This is important for all scientific programs listed in Table 4-1 and primarily sets specifications for the High-Transmission Beam Line (HTBL) that transports beams from the ARIS Fragment Separator to the reaction target of the HRS. The specifications that impact the luminosity are described in Section 4.3.2.

Table 4-2 Specifications for the HRS for each of the scientific programs listed in Table 4-1. In the bottom three rows, the specifications are summarized by operational mode of the HRS, as described in Section 4.3.1.6.

	HRS Science Program	Maximum mass number	Minimum mass resolving power	Minimum charge resolving power	Time of flight resolution (ps)	Minimum flightpath charged particles (m)	Minimum momentum resolving power	Minimum spectrometer solid angle (msr)	Angular resolution (mrad)	Minimum space around target (cm)	Minimum momentum acceptance (dp/p in %)	Maximum neutron flight path (m)	Minimum neutron solid angle (msr)	Unreacted beam rejection	Maximum Rigidity (Tm)	Mode: (H)igh Resolution, (I)nvariant Mass, (M)ass measurement
Nuclear Structure	At the limits of the nuclear chart: at and beyond the neutron dripline	132	220	85	150	11	290	10	5	90	±5	15	32	y	8	I
	Single-particle structure and collectivity from prompt in-beam gamma-ray spectroscopy	238	400	156	150	25	1500	10	10	123	±2.5		-	y	8	H
	Fingerprints of shell evolution with isomer studies	238	400	156	150	25	1500	10	10	123	±2.5		-	y	7	H
	Excited-state lifetimes as indicators of shell-evolution	238	400	156	150	25	1500	10	10	123	±2.5		-	y	8	H
	Inelastic proton scattering as a probe of the pn degree of freedom	238	400	156	150	25	>400	5	10	123	±2.5		-	y	8	H
	Physics along the N=Z line	100	170	156	150	11	1500	10	10	-	±2.5		-	y	5	H
	Commensal decay spectroscopy following reactions	238	400	156	150	25	>400	10	10	-	±2.5		-	-	8	H
	Knock-out reactions	238	400	156	150	25	1500	10	10	123	±2.5		-	y	8	H
	Quasifree scattering	238	400	156	150	25	1500	5	10	123	±2.5		-	y	8	H
	Elastic scattering	238	400	156	150	25	1000	10	10	123	±2.5		-	y	7	H
	Total reaction/interaction measurements	238	400	156	150	25	1000	10	10	123	±2.5		-	y	8	H
Nuclear Astrophysics	Heavy-ion collisions	-	-	-	-	-	-	-	-	-	-	(15)	(32)	-	8	I
	Heavy-ion EM excitations	238	400	156	150	25	1000	10	5	123	±2.5		-	-	8	H
	Isoscalar giant resonances	238	400	156	150	25	>400	10	10	100	±2.5		-	-	6	H
	Isovector giant resonances	238	400	156	150	25	1500	10	5	123	±2.5		-	y	6	H
	Time-of-flight mass measurements	238	10000	156	30	90	>10000	<10	-	-	±0.5		-	-	7	M
	Projectile fragmentation and in-flight fission of neutron-rich nuclei	238	400	156	150	25	1500	15	10	123	±2.5		-	y	6	H
	Weak Reaction rates for astrophysics	238	400	156	150	25	1000	10	5	123	±2.5		-	y	6	H
Fundamental Symmetries	Gamow-Teller strengths, neutrinos, and the quenching of g_A	238	400	156	150	25	1500	5	10	123	±2.5		-	y	7	H
Applications	Improving nuclear structure inputs to fission models	238	400	156	150	25	1500	15	10	123	±2.5		-	y	6	H
Specifications Summary by Mode																
	High Resolution	238	400	156	150	25	1500	15	5	123	±2.5		-	y	8	H
	Invariant Mass	132	220	85	150	11	290	10	5	90	±5	15	32	y	8	I
	Mass Measurement	238	10000	156	30	90	>10000	<10	-	-	±0.5		-	-	7	M

60

4.3.1 Scientific Specifications for the Spectrometer Section: accommodating the diverse scientific program of the HRS user community

To meet the objectives of the FRIB Scientific User Committee of FRIB, the Spectrometer Section must accommodate a broad spectrum of experiment types. Each of these experiment types have their own specifications. In Table 4-2, the specifications for each experimental program that affect the scope and properties of the Spectrometer Section are specified as:

- Maximum mass number
- Minimum mass resolving power
- Minimum charge resolving power
- Time of flight resolution
- Minimum flightpath for charged particles
- Minimum momentum resolving power
- Minimum spectrometer solid angle
- Angular resolution
- Minimum space around target for the placement of ancillary detector systems
- Minimum momentum acceptance
- Maximum neutron flight path for programs that involve the detection of in-flight neutrons
- Minimum neutron solid angle for programs that involve the detection of in-flight neutrons
- Whether the program requires unreacted beam rejection in the focal plane of the spectrometer
- Maximum Rigidity

Some of the specifications, such as for the momentum and mass resolving powers, depend on the exact beam energy. For the purpose of the values in Table 4-2, a beam energy of 160 MeV/u has been used in the determination of the specifications. In the following, prototypical experiments that were used to set these specifications are described.

4.3.1.1 Prototypical experiment I: Single-particle structure and collectivity from prompt in-beam γ-ray spectroscopy

As described in Section 4.2.1.1, experiments aimed at elucidating the evolution of shell structure and properties of nuclei far away from the valley of stability by using in-beam γ-ray spectroscopy are an important motivation for the construction of the HRS. By combining the Gamma-Ray Energy Tracking Array (GRETA) [GRE17] with the HRS, the world's most sensitive in-beam γ-ray spectroscopy facility will be created, which is necessary to perform experiments such as those aimed at investigating spectroscopy of the most neutron-rich calcium isotopes (see Section 4.2.1.2). It is important that experiments can be carried out at magnetic rigidities for which the rare-isotope production rates are maximized. For the very neutron-rich isotopes, this requires that the spectrometer can operate up to a rigidity of 8 Tm (See Section 4.3.2.1). The optimization of the luminosity for experiments with rare isotopes at the HRS will be discussed in detail in Section 4.3.2.

Experiments that combine the HRS and GRETA will be carried out with rare-isotope beams across the chart of nuclei, requiring that particles can identified and resolved up to high mass numbers

(A~238). A mass resolving power ($R_m = m/\Delta m$, where Δm is the width in Full Width at Half Maximum (FWHM)) of 400 is required to achieve a separation of four standard deviations between neighboring mass units Hence, by making a $\pm 2\sigma$ mass cut, only 5% of the events are lost, which is equal to the maximum loss in transmission through the HTBL to the Spectrometer Section Target (see Section 4.3.2). It is not uncommon that the mass of the particles of interest different by one unit from a contaminant peak that is much stronger. At a separation of four standard deviations, a signal-to-background ration of about four can be achieved if the production of the neighboring contaminant is 100 times stronger than the production of the particle of interest and an asymmetric cut of $-\sigma$ to $+2\sigma$ is made around the peak of interest. This scenario can be considered an extreme case and the signal-to-noise ratio of 4 is sufficient to carry out the program summarized in Section 4. The mass resolving power is estimated as follows:

$$ R_m = \frac{m}{\Delta m} = \frac{D_x}{\delta x_f \oplus M_x \delta x_i} \oplus \gamma^2 \frac{\text{ToF}}{\delta \text{ToF}}, $$

in which M_x and D_x are the horizontal magnification and dispersion of the spectrometer, respectively; x_i and x_f are the positions of the trajectories relative to the central trajectory in the initial (achromatic) object and final (dispersive focus) locations; γ is the Lorentz factor, and ToF is the time of flight. The $\oplus$ operator denotes the addition in quadrature of independent quantities[1], and δ indicates the uncertainty (in FWHM) for a parameter. Hence, the specification for the mass resolving power imposes constraints on the detector system used for tracking and identifying particles: the resolution of the focal-plane detector (δx_f) of the Spectrometer Section must at least be 1 mm, and a time-of-flight (δToF) resolution of 150 ps (FWHM) must be achieved. By using these parameters, and using a typical beam image spot size (δx_i) at the target of 5 mm, the specification to achieve a mass resolving power of 400 requires a flight-path length from the reaction target to the focal-plane detectors of the Spectrometer Section of at least 25 m.

To select the isotopes of interest, it is also necessary to identify the charge number. Similar to the requirement for the mass resolving power, a 4σ separation between isotopes with a difference in charge number by one is needed to limit the loss in events by a $\pm 2\sigma$ cut to 5%. This requirement corresponds to a charge resolving power ($R_Z = Z/\Delta Z$) of 156 for $Z=92$, where ΔZ is the resolution (FWHM).

An advantage of performing in-beam γ-ray spectroscopy experiments with fast beams is that the reaction products that are detected in the Spectrometer Section in coincidence with γ-rays in GRETA, are strongly forward boosted. A spectrometer acceptance of 10 msr (± 50 mrad in the dispersive and non-dispersive directions) is sufficient to collect the reaction products. Based on the experience experiments with the S800 [BAZ03] spectrograph, a momentum acceptance ($\delta p/p$) of $\pm 2.5\%$ is required to carry out experiments efficiently. With such a momentum acceptance, the momentum distribution of the recoiling particle after interacting with the target can be measured in a single rigidity setting of the spectrometer for experiments with nuclei with mass greater than approximately 30. This is important for reducing the beam-time required to measure the full momentum distribution.

---

[1] $\delta a \oplus \delta b = \sqrt{(\delta a)^2 + (\delta b)^2}$

As the largest detector array that will be placed at the target station of the Spectrometer Section, GRETA imposes a constraint on the area around the target that must be available in general for the placement of a wide variety of detector systems. Therefore, the HRS working group closely coordinates with the GRETA project team and established that at least 123 cm must be kept free upstream and downstream of the reaction target, as illustrated in Figure 4.16.

Besides GRETA, there are a wide variety of other devices that will be placed around the target for specific experiments. A sample of these detector systems is shown in Figure 4.17 and include detectors systems for γ-rays, charged particles, and neutrons.
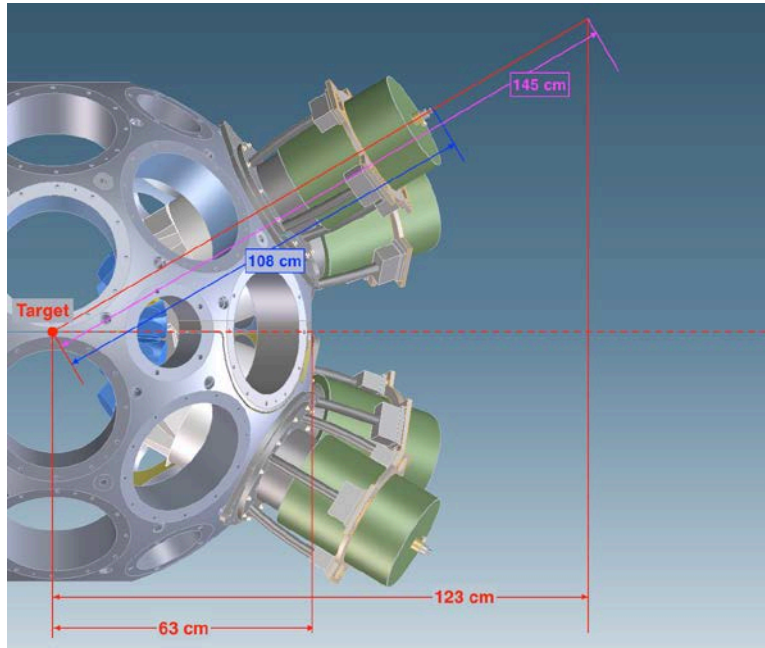
Figure 4.16 Illustration of the amount of space that must be kept available to place and operate GRETA at the reaction target. The radius of the frame holding the GRETA detectors if 63 cm, and the distance from the target to the end of a detector module is 108 cm. Additional space is required to insert a liquid-nitrogen bayonet, adding 37 cm to that distance. When projected onto the beam axis, this leads to a specification to leave at least 123 cm of space for GRETA.

4.3.1.2   Prototypical experiment II: Knock-out reactions

As described in Section 4.2.5, direct and heavy-ion nuclear reaction studies at the HRS will be crucial for understanding key nuclear properties and the mechanisms in which nuclei interact. Integral to such studies is the ability to accurate reconstruct the momenta of the charged particles in the Spectrometer Section. Knockout experiments from heavy nuclei (see the case of neutron knockout in Figure 4.15) provide a strong constraint on the momentum resolving power (R_p) that needs to be achieved. The momentum resolving power is determined by:

$$R_p = \frac{p}{\delta p} = \frac{D_x}{\delta x_f \oplus M_x \delta x_i}.$$

In order to detect identify the angular momentum carried by the knocked-out neutron from ^{204}Pt, the momentum resolving power must be at least 1300 with a beam-spot image size of 5 mm

(FWHM) and a focal-plane detector resolution of 1 mm (FWHM). To perform similar experiments up the highest mass number (238), a momentum resolving power of 1500 is specified.

a) GRETA b) LANL-Apollo c) CAESAR d) HiRA
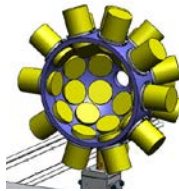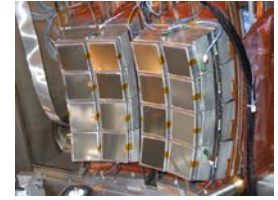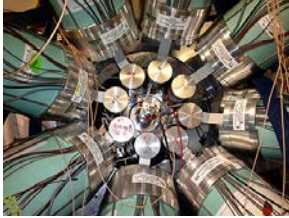
e) SeGA f) NSCL-Köln Plunger g) HAGRiD h) ORRUBA
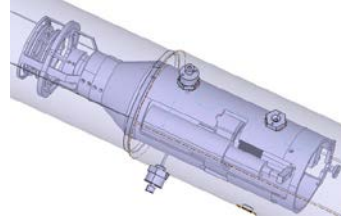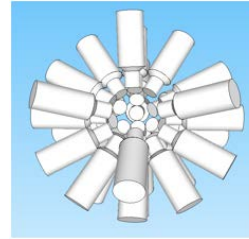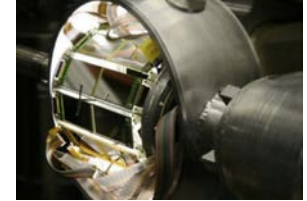
i) LENDA & VANDLE j) AT-TPC k) SπRIT-TPC
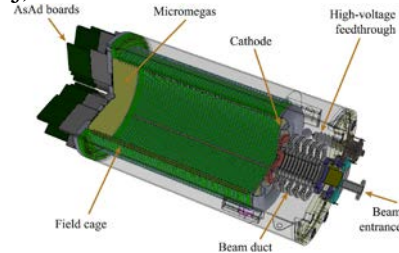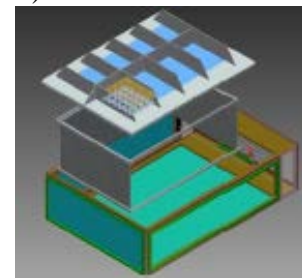
Figure 4.17 Existing detector systems that will be placed around the target for experiments with the HRS: a) Gamma Ray Energy Tracking Array (GRETA) [GRE17]; b) LaBr(Ce)+CsI(Tl) array Apollo [COU15]; c) CAESium-iodide scintillator Array (CAESAR) [WEI10]; d) High-Resolution Detector Array (HiRA) [WAL07]; e) Segmented Germanium Array (SeGA) [SEG01]; f) NSCL- Köln Plunger [IWA16]; g) Hybrid Array of Gamma Ray Detector (HAGRiD) [SMI18]; h) Oak Ridge Rutgers University Barrel Array (ORRUBA) [PAI07]; i) Low-Energy Neutron Detector Array (LENDA) [PER12] and Versatile Array of Neutron Detectors at Low Energy (VANDLE) [PET16]; j) The Active Target Time Projection Chamber (AT-TPC) [AYY17]; k) The SπRIT-TPC [OTS16, JHA16].

In addition to being able to accurately measure the momenta of the charged particles in the HRS, it is important for some experiments that unreacted beam particles can be blocked prior to entering the spectrometer focal plane detectors and possibly limiting the intensity with which the experiment can be performed. This is particularly important for experiments at the Spectrometer Section, since the likelihood that unreacted beam particles are within the momentum acceptance of the spectrometer becomes higher for heavier beams because the magnetic rigidities of the unreacted beam particles and desired reaction products are often close. The necessary unreacted-beam rejection factor varies strongly from one experiment to another. In experiments with unreacted beam rates that are far below the rate capabilities of the focal plane detectors or where the unreacted beam has a rigidity very different from the particles of interest and does not enter the focal plane, no rejection is required. In the worst case, a high-intensity (10^6 pps) beam must be

rejected with at least 99% efficiency to prevent the rate in the focal plane detectors to exceed the capabilities of the detectors. In cases where unreacted beam rejection is needed, it is important to have a focus at a location prior to the tracking detectors, so that unreacted beam particles can be intercepted by using beam blockers, while minimizing the interference with the measurement of the particles of interest. To achieve good momentum resolving power and to create the possibility to block unreacted beams, it will be necessary to use the dispersion-matching technique, as discussed in section 4.3.2.7.1.

4.3.1.3 Prototypical experiment III: Invariant-mass spectroscopy at and beyond the neutron dripline

As discussed in Section 4.2.1.3, unique opportunities arise at FRIB by being able to study weakly and neutron-unbound systems, in which new and exotic phenomena associated with very large neutron-to-proton asymmetry are expected. Such experiments require invariant-mass spectroscopy in which the momentum vectors of one or more neutrons that are emitted in flight from the neutron-unbound system and the charged residual nucleus are used to reconstruct the unbound system. For that purpose, the MoNA-LISA plastic-scintillator neutron detector array [BAU05,MRI09] is used. To achieve sufficient resolution in the reconstructed neutron momentum vectors, the detector must be placed sufficiently far away from the target. Invariant-mass spectroscopy experiments with neutrons benefit from being able to use the fast beams made available by the HRS as the neutrons are strongly forward boosted and can be detected with good efficiency even when placed far away. By placing the detectors further, the neutron velocity measurement gains accuracy as the relative uncertainty in the time-of-flight is reduced. Experiments with MoNA-LISA placed up to 15 m from the target are envisioned, which imposes a constraint on the layout of the HRS within the experimental hall.

The ability to measure neutrons at forward angles sets a stringent requirement on the ion-optical elements of the Spectrometer Section placed immediately after the target: they cannot block the path of the neutrons towards MoNA-LISA. A sweeper magnet with a large gap is thus required to sweep the charge particles away from the beam axis. The location of the target and the depth and the gap sizes of the sweeper magnet set the vertical acceptance for the neutrons emitted in flight.

At least 90% geometrical coverage for neutrons emitted in flight from an $A=40$ system with an excitation energy of less than 2 MeV at 180 MeV/u (see Section 4.2.1.3) must be achievable for a distance of 8 m between the target and the MoNA-LISA array, which corresponds to a solid-angle coverage of 32 msr, as shown in Figure 4.18. In practice, it is the angular acceptance for neutrons in the vertical direction ($\pm$90 mrad) which is the primary constraint as it sets the gap height of the sweeper magnet. Up to vertical angular acceptances of $\pm$90 mrad, the gain in geometrical efficiency for the neutron detection increases linearly with increased angular acceptance. At larger vertical angular acceptances, the gain in geometrical acceptance saturates because it is constrained by the size of the MoNA-LISA neutron array, rather than the acceptance of the neutrons passing through the sweeper magnet. For larger distances between the target and the MoNA-LISA array, the gain in geometrical acceptance achieved by increasing the vertical angular acceptance of the neutrons saturate more quickly. Hence, a vertical angular acceptance of $\pm$90 mrad is an appropriate choice. To optimize the vertical acceptance for the neutrons, it is preferable to place the target close to the sweeper magnet (50 cm), but if additional detectors must be placed around the target, a larger

distance might be necessary. A distance between the target and the edge of the sweeper magnet of 90 cm would allow for the placement of GRETA with its forward ring of detector removed, which is beneficial for experiments in which γ-ray and neutron invariant-mass spectroscopy are performed simultaneously (see Figure 4.5). The use of GRETA requires that the magnetic field at the location of its detectors is less than 600 Gauss, which is an important consideration when it is placed near the Sweeper magnet.

Invariant-mass spectroscopy will be mostly carried out in experiments with neutron-rich rare isotopes of mass number below 132 and charge number below 50, requiring a magnetic rigidity of 8 Tm (See Section 4.3.2.1). The specifications for the mass and charge resolving power of the charged residual nucleus in the Spectrometer Section for such experiments are not as stringent as for other types of experiments and R_m=220 and R_Z=85 are sufficient to achieve sufficient mass and charge separation (four standard deviations) as for the types of experiments performed with heavier systems. To achieve this mass resolving power a flight path for the time-of-flight measurement of 11 m is necessary. For invariant-mass spectroscopy beyond mass 132, a higher resolving power and thus a longer flightpath is required. The specifications for the momentum resolving power of the Spectrometer Section are less stringent (R_p=290) than for most other experiments, as the accuracy of the invariant-mass reconstruction is dominated by the measurement of the neutron momentum vector. At the momentum resolving power of 290, the loss in invariant mass resolution for the A=40 system compared to a perfect momentum determination is only 10% if MoNA-LISA is placed at 15 m from the target (for which the best neutron time-of-flight resolutions are achieved). For similar reasons, the angle of the charge particle must be determined with a resolution (FWHM) of 5 mrad. At this resolution, the loss in invariant-mass resolution is only 10% compared to a measurement in which a perfect angular measurement is achieved is only about 10% compared to a resolution of 5 mrad. If MoNA-LISA is placed closer to the target, the benefits of a better momentum and angular resolution for the charged particle become smaller. It is further noted that the gain in invariant-mass resolution by placing MoNA-LISA 2 meters further downstream (17 m instead of 15 m) is about 10% as well, so that the contributions from the tracking of the charged particles and neutrons are balanced under these circumstances.

It is important that the momentum acceptance of the Spectrometer Section is larger than necessary for most other experiment types. A momentum acceptance ($\delta p/p$) of ±5% is required to perform invariant-mass spectroscopy of the light neutron-rich systems as the momentum kicks induced by the decaying neutrons become significant. The solid-angle covered by the spectrometer must be similar (10 msr) to that of other experiment with fast rare-isotope beams in inverse kinematics, in order to capture the charged particles that decayed in flight For the case of relatively night nuclei such as the A=40 system described above, the scattering angle of the charged particle after the emission of a single neutron is less than 15 mrad, even at high excitation energies. Consequently, even if several neutrons are emitted in flight, the charged particle will still be detected if angular ranges of ±50 mrad are covered in the dispersive and non-dispersive directions.

Although the focus in this section is on the kinematics reconstruction of unbound states that emit neutrons, it is important to point out that several other types of experiments also rely on the detailed reconstruction of momentum vectors to reconstruct excitation energies and scattering angles that are necessary for the interpretation of the data. Examples include the (^{7}Li,^{7}Be) reaction in inverse

kinematics (see Section 4.2.1.4), the (^{10}Be,^{10}B) and (^{12}N,^{12}C) reactions in forward kinematics (see Section 4.2.2.5), and quasifree scattering experiments (see Section 4.2.5). These experiments therefore also require the good angular resolution of 5 mrad for the charged particle track. In addition, having such a good angular resolution is also important for heavy-ion Coulomb excitation experiments (See Section 4.2.5), where angular cuts are necessary to constrain the impact parameter of the reaction, and for elastic scattering experiments, for which the angular distribution has to be measured for constraining matter radii and density distributions (see Section 4.2.6).
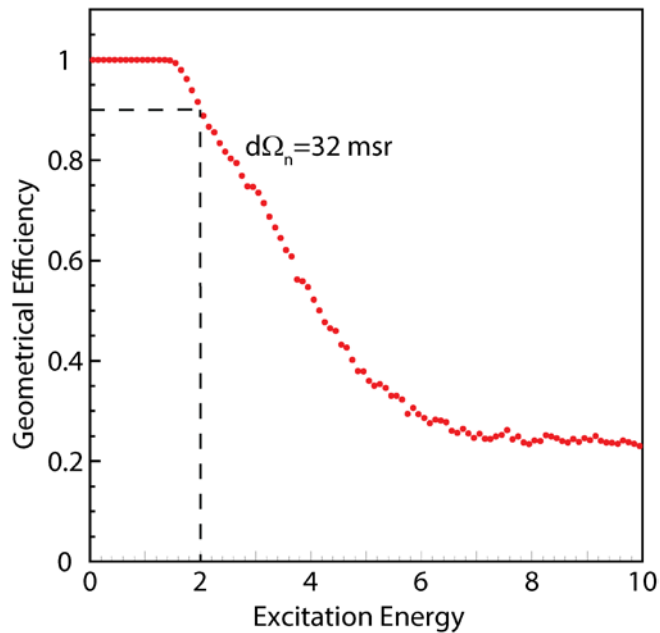
Figure 4.18 The geometrical efficiency as a function of excitation energy for neutrons emitted from an unbound system with mass number 40 at 180 MeV/u. A coverage of 90% is achieved up to an excitation energy of 2 MeV for a neutron solid angle coverage of 32 msr.

4.3.1.4   Prototypical experiment IV: In-flight fission

As discussed in Section 4.2.4, in-flight fission experiments with fast beams enable the measurement of both fission fragments simultaneously, which provides a unique opportunity to study the correlations between the fission fragments and to gain a better understanding of the fission mechanism. In-flight fission experiments in which both fission fragments must be detected in the Spectrometer Section pose a constraint on the angular acceptance, as a large fraction of the fission cone must be within the acceptance. This is demonstrated in Figure 4.19, in which the efficiency of detection of fission pairs for different angular acceptances of the Spectrometer Section are shown for in-flight fission of at 200 MeV/u. The excitation energy was set at 20 MeV. The simulation was performed in LISE^{++}, taking into account the angular acceptances of the Spectrometer Section. Three different angular acceptances are shown in combination with a momentum acceptance of 3%. For angular acceptances of ±60 mrad (dispersive direction) by ±60 mrad (non-dispersive direction) and ±50 mrad (dispersive) by ±75 mrad (non-dispersive), the averaged efficiencies for the detection of both fission fragments are comparable and around 10%,

sufficient for performing in-flight fission studies. For smaller angular acceptances, such as ±50 mrad (dispersive) by ±50 mrad (non-dispersive) as shown in Figure 4.19 as well, the efficiency is much less than 10% on average, and close to 0 for certain mass numbers. The latter would be very detrimental for detailed studies of fission. Therefore, a minimum solid angle of 15 msr is determined as the minimum requirement for in-flight fission studies.

It is noted that for the asymmetric acceptance of ±50 mrad (dispersive) by ±75 mrad (non-dispersive), the efficiency is relatively flat as a function of mass number. For the symmetric acceptance of ±60 mrad (dispersive) by ±60 mrad (non-dispersive), the efficiency is higher around the central mass number, and lower for asymmetric fission pairs.
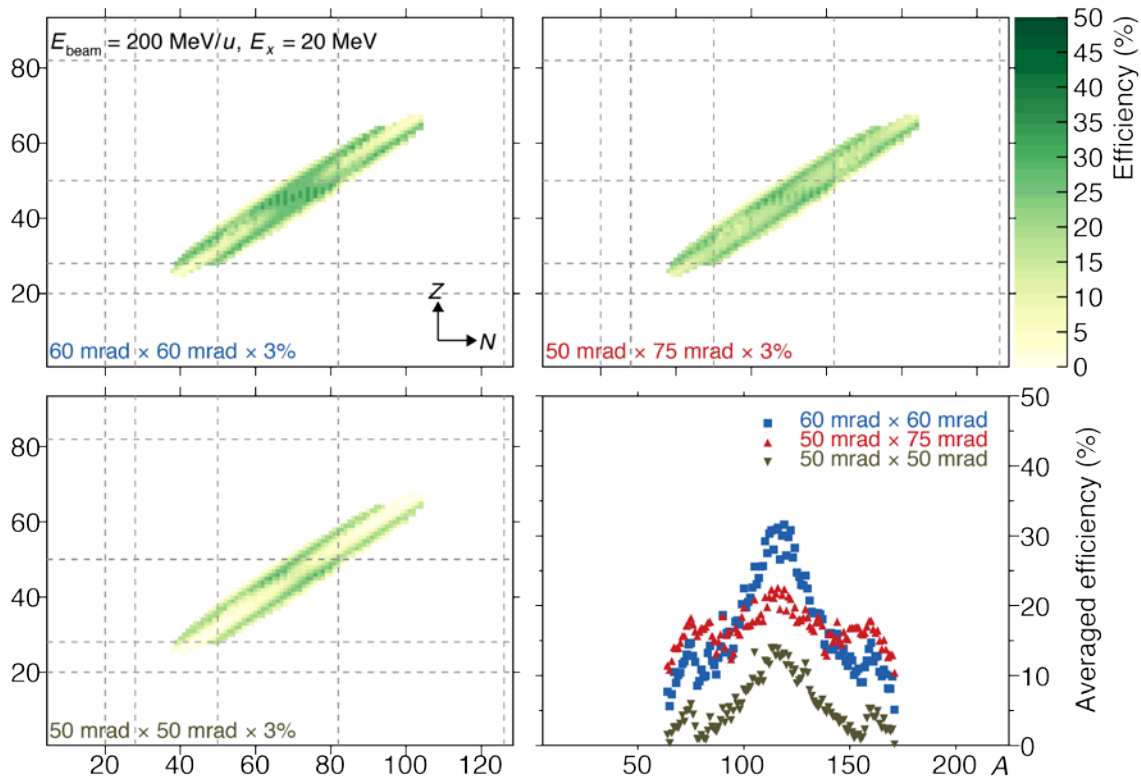
Figure 4.19 Simulations of in-flight fission at 200 MeV/u in which both fission products are detected in the Spectrometer Section. In the top and bottom-left panels, the efficiency for detecting fission pairs is plotted as function of neutron (N) and proton number (Z). In the top-left panel the angular acceptances was set to ±60 mrad (dispersive direction) by ±60 mrad (non-dispersive direction); in the top-right panel the angular acceptances was set to ±50 mrad (dispersive direction) by ±75 mrad (non-dispersive direction); in the bottom-left panel the angular acceptances was set to ±50 mrad (dispersive direction) by ±50 mrad (non-dispersive direction). The bottom-right plot shows the averaged efficiency for the detection of both fission pairs as a function of mass number for each of the three angular acceptances.

4.3.1.5   Prototypical experiment V: Time-of-flight magnetic-rigidity mass measurements

As discussed in Section 4.2.2.1, time-of-flight magnetic rigidity (ToF-$B\rho$) mass measurements provide a unique opportunity to simultaneously measure a large number of nuclear masses that define the mass surface far from the valley of stability and constrain theoretical models. Such data

are important for astrophysical modeling, in particular the *r* process. ToF-*Bρ* measurements are different than all other experiments foreseen with the HRS and, therefore, pose different constraints. A schematic overview of ToF-*Bρ* measurements as foreseen is shown in Figure 4.20. This scheme is based on successful experiments performed at NSCL with the S800 [EST11,MEI13,MEI15]. A cocktail beam of rare-isotopes passed through a time-of-flight start detector and tracking detector which are placed in the fragment separator. By operating the HTBL in dispersion-matched mode (see Section 4.3.2.7.1), the rigidity of the beam can be measured at the target station of the HRS by measuring the position in the dispersive direction. Unlike other experiments at the HRS, the spectrometer is used to analyze the beam particles rather than the reaction products: all nuclei will be detected at the same position in the focal plane of the Spectrometer Section, where a time-of-flight stop detector and energy loss detectors for particle identification must be placed. To achieve the desired mass resolution of 10^{-4}, a time-of-flight resolution of better than 30 ps must be achieved. In addition, dedicated detectors for tracking at the Fragment Separator and the target position at the entrance of the Spectrometer Section are required that achieve ~0.35-mm (FWHM) position resolution. In order to achieve a mass resolving power of 10000, the momentum resolving power (R_p) must be better than 10000 for the ToF-*Bρ* measurements. The acceptance requirements for the Spectrometer Section (less than 10 msr solid angle and ±0.5% in momentum) are less stringent as for other experiments, as no reaction takes places at the target in front of the Spectrometer Section.
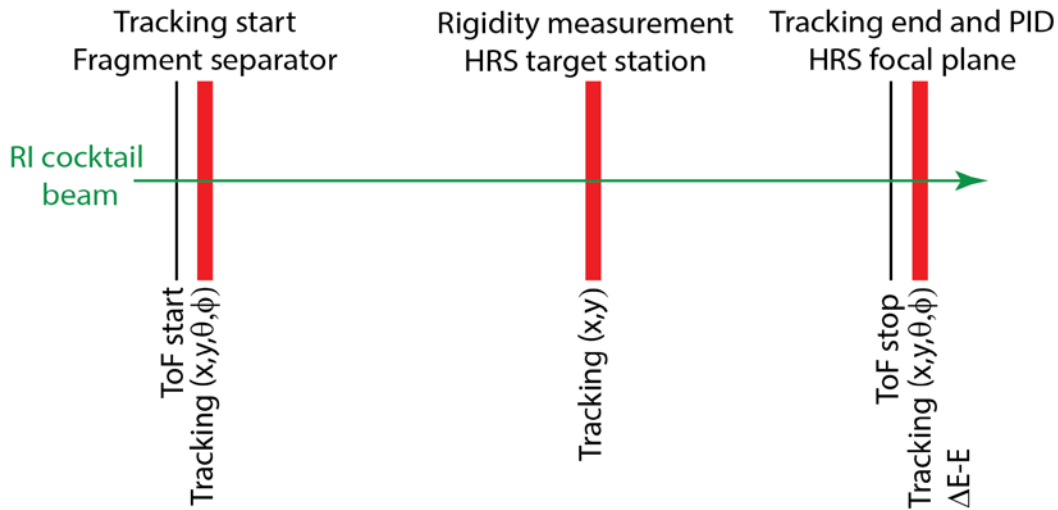
Figure 4.20 Schematic overview of ToF-Bρ measurements. A cocktail of rare-isotope beams passes through ToF and tracking detectors in the fragment separator. The magnetic rigidity is measured at the target location of the Spectrometer Section. The time-of-flight stop signal comes from a detector placed in the focal plane of the Spectrometer Section, where tracking and ΔE-E measurements are performed to do particle identification (PID).

4.3.1.6   Overview of specifications for the Spectrometer Section of the HRS: three basic modes of operation

Based on the specifications for the experimental programs in Table 4-2, three basic modes of operation were identified, that have very different sets of specifications: a high-resolution mode,
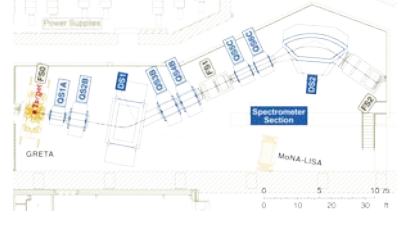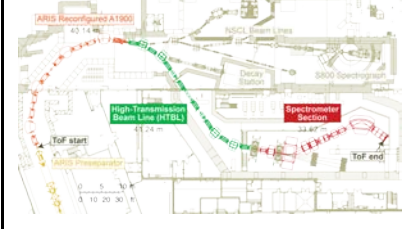
an invariant-mass mode, and a time-of-flight mass-measurement mode, which are briefly described below. An overview of the basic functionalities of these three modes in provided in Table 4-3.

High-resolution mode: This mode is necessary for a large fraction of the experimental types listed in Table 4-1 and the science program described in Section 4.2. It allows for the particle identification of the heaviest nuclei (A=238), which requires a flight path of 25 m in the Spectrometer Section to achieve a mass resolving power of at least 400, with a time-of-flight resolution of 150 ps. In this mode, a relatively high momentum resolving power of 1500 with a beam spot size of 5 mm (FWHM) must be achieved with achromatic beam transport (See Section 4.3.2.7.1) even without tracking the incoming beam. The specifications for the momentum acceptance (±2.5%) and solid angle coverage (15 msr) are sufficient for a large fraction of the experimental programs, including in-flight fission experiments that require a solid-angle coverage of 14.4 msr. The space around the target station is sufficient for the placement of all ancillary detector systems, including GRETA. In this mode, there is no strict specification on the solid angle coverage of neutrons at forward scattering angles. The rigidity requirement is 8 Tm. Optionally, tracking detectors in the HTBL (See Section 4.3.2.7.2) can be utilized to achieve a higher momentum resolution through the determination of the momentum of the incoming beam. Similarly, tracking detectors in the HTBL can be used to determine the angle of the beam particles on target and to improve the angular resolution of the reconstructed scattering angle. As discussed in Section 4.3.2.3, the use of tracking detectors in the beam line introduces the production of charge-states of the beam particles, in particular for beams with a high atomic number. This reduces the beam intensity (as beam particles in a charge-state other than preferred have different magnetic rigidity and will not be transported to the target) and potentially introduces contaminations. Therefore, as an alternative, one can operate the HTBL in dispersion-matched beam transport mode (See Section 4.3.2.7.1), in which the momentum spreads and the angular spreads associated with the different momenta are cancelled out. In that case, tracking detectors are not needed to achieve a resolution better than the momentum and angular spreads in the beam, but at the cost of beam intensity. Similar to the experiments presently carried out with the existing S800 Spectrometer, the choices related to the use of tracking detectors and beam transport modes depends strongly on the goals and constraints for particular experiments.

Neutron invariant-mass mode: This mode is necessary for experiments in which fast neutrons must be detected with a large solid angle coverage (32 msr) at forward angles, which is necessary for the neutron invariant-mass spectroscopy experiments (see Section 4.2.1.3), as well as heavy-ion collision experiment aimed at elucidating the Equation of State (see Section 4.2.2.4). In this mode, the specifications for mass and momentum resolving power of the Spectrometer Section of the HRS are less stringent than for the high-resolution mode (R_p=290 and R_m=220, respectively), but the momentum acceptance specification is larger (±5%). A key specification for this mode is the 32-msr solid-angle coverage for the neutrons at forward angles. A neutron flight-path length of up to 15 m must be accommodated. Less space for the placement of ancillary detectors is needed, but the use of GRETA with its most forward detector ring removed should be possible (at least 90 cm space up- and downstream of the target). Because the constraints on the momentum and mass resolving power are less stringent than for the high-resolution mode, experiment in the

neutron invariant mass mode will predominantly be performed with achromatic beam transport through the HTBL (See Section 4.3.2.7.1). The large size of the beam spot associated with operating in dispersion-matched beam transport mode through the HTBL is detrimental to resolution of the neutron angular measurement, which must be avoided to achieve good resolutions in the reconstructed invariant-mass spectra.

Table 4-3 Overview of the three operational modes for the Spectrometer Section

High Resolution Mode	Neutron Invariant-Mass Mode	ToF-Bρ Mass Measurement Mode
Provides the full capabilities of the HRS and meets the specifications for majority of the science program	Meets the specifications for invariant-mass spectroscopy experiments in which neutrons are detected in the MoNA-LISA array	Achieves a long flight path from the beginning of the ARIS Reconfigured A1900 to the Focal Plane of the HRS required for ToF-Bρ mass measurements

ToF-Bρ mass measurement mode: This mode is specific for the ToF-*Bρ* mass measurements (see Section 4.2.2.1). The Reconfigured A1900 of the ARIS Fragment Separator [HAU13], the HTBL, and the Spectrometer Section of the HRS must serve to create a very long flight path of at least 90 m. From the ion-optical point of view, the Spectrometer Section is operated in the same way as in the high-resolution mode, whereas the HTBL is operated such that these two are dispersion-matched and the entire system is doubly-achromatic. By using dedicated detector systems for the ToF measurements, resolutions of better than 30 ps must be achieved to perform mass measurements with a mass resolving power of 10^4. A momentum resolving power of better than 10^4 is required, but since there are no reactions that are being studied there are no stringent specifications on the momentum and angular acceptance of the Spectrometer Section.

Each of the experimental programs is categorized in one of the operational modes in the most right-hand side column of Table 4-2. Then, the specifications for each of the modes was determined by considering all the relevant experimental programs and taking the most constraining value for each of the specified values. These summarized specifications are shown at the bottom of Table 4-2. For convenience, these summarized specifications are shown in a separate table in Table 4-4. This table served as input for the ion-optical and detector designs.

Table 4-4 Overview of the specifications of the Spectrometer Section, listed for the three main modes of operation: high-resolution, neutron invariant-mass, and ToF-Bρ mass-measurement modes.

Mode Specification for	High-resolution	Neutron invariant-mass	ToF-Bρ mass-measurement
Maximum mass number	238	132	238
Mass resolving power	400	220	10000
Charge resolving power	156	85	156
Time-of-flight resolution (ps)	150	150	30
Flight path for charged particles (m)	25	11	90
Momentum resolving power	1500	290	>10000
Spectrometer solid angle (msr)	15	10	3
Angular resolution (mrad)	5	5	-
Space around target (cm)	123	90	-
Momentum acceptance ($\delta p/p$ in %)	±2.5	±5	±0.5
Neutron solid angle (msr)	-	32	-
Neutron flight-path length (m)	-	15	-
Unreacted beam rejection	yes	yes	-
Maximum magnetic rigidity (Tm)	8	8	7

4.3.2 Scientific specifications for the HTBL: optimizing the luminosity for experiments at the HRS

The vast majority experiments that will be performed with the HRS will be with rare-isotope beams that are far from stability and beam intensities will typically be (much) less than 10^6. The most demanding experiments with the highest scientific impact will be with beams of rare isotopes furthest from the valley of stability. For the majority of these experiments, the achievable luminosity is most important. The experimental luminosity is a product of three basic parameters: 1) the intensity of the rare-isotope beam produced in the ARIS Fragment Separator; 2) the transmission efficiency of rare-isotope beams from the fragment separator to the target station of the HRS; and 3) the thickness of the reaction target placed at the target station of the Spectrometer Section. These parameters and the specifications they impose on the HTBL are briefly discussed in the following subsections, followed by additional scientific specifications for the HTBL, which are related to the beam transport modes and beam diagnostics, tracking and other devices.

4.3.2.1 The intensity of the rare isotope beam produced in the ARIS Fragment Separator

Figure 4.21 presents an overview of the estimated magnetic rigidities for which the rare-isotope beam production rate is maximized at the exit of the ARIS Fragment Separator for FRIB at 200 MeV/*u*. Except for the most proton-rich isotopes, the optimal rigidity exceeds 4 Tm and ranges up to 8 Tm for light, very neutron-rich isotopes. However, the magnetic spectrometers presently available at NSCL, the S800 spectrograph and the Sweeper magnet, as well as the beam lines leading to these devices are limited to a rigidity of about 4 Tm, resulting in significantly reduced rare-isotope beam intensities for FRIB. This limitation will prevent substantial segments of the science outlined in Section 4.2 from being accomplished. Therefore, it is important that the HTBL

can transmit high-rigidity beams to the reaction target and that the Spectrometer Section can analyze the products produced from reactions with such beams.
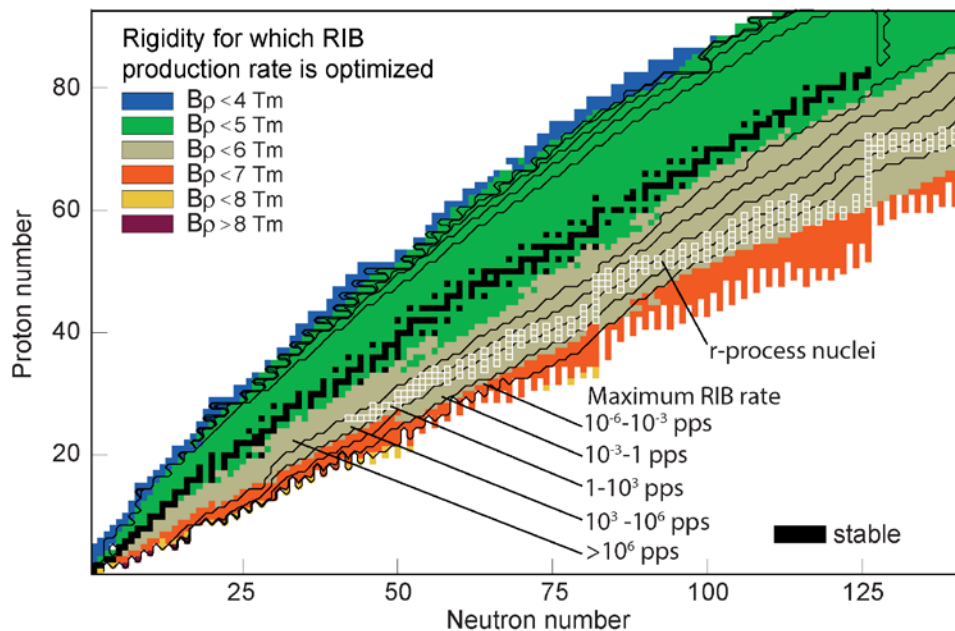
Figure 4.21 Magnetic rigidities for which the rare-isotope production rate across the chart of nuclei is optimized[2]. This varies across the nuclear chart with the highest rigidities needed for the most neutron-rich species.

4.3.2.2 The transmission efficiency of the beam line.

The beam line used to transport the rare-isotope beams from the ARIS Fragment Separator to the reaction target should accommodate the emittance and rigidity of these beams. Their emittance will exceed what can be accommodated in the beam lines to existing spectrometers at NSCL. Therefore, the beam line to the target station of the HRS must be optimized to minimize transmission losses to less than 5% for the rare-isotope beams delivered by the ARIS Fragment Separator in achromatic beam-transport mode. Consequently, a significant gain in luminosity can be achieved with the HRS in comparison to experiments with the existing S800 Spectrograph and Sweeper Magnet. To perform these optimizations, six representative rare isotope beams which are important for the scientific program as discussed in Section 4.2, were selected for which full end-to-end simulations (from the production target in the fragment separator to the target station of the HRS) were performed, as detailed in Section 5.4. These beams are listed in Table 4-5. These six beams are representative of the envisioned program and are distributed across the chart of isotopes. Therefore, they provide a good sample to ensure that the specification for the transmission efficiency is met. Five of these beams are on the neutron-rich side of the chart of isotopes, where the required rigidities to optimize the beam intensity are highest, and one is on the proton-rich side of the chart of isotopes. The table lists the rigidity of each beams before the wedge (which serves as the upper limit of the rigidity for which each beam can be produced) and after the wedge, which

---

[2] From FRIB Estimated Rates Version 1.08 https://groups.nscl.msu.edu/frib/rates/fribrates.html

for each case was selected to optimize the purity of the rare isotope beams. The latter values were used in the end-to-end simulations.

Table 4-5 Overview of six representative rare-isotope beams that were used to optimize the transmission efficiency of the beam line from the ARIS Fragment Separator to the Targets Station of the HRS. Transmission studies were performed in end-to-end Monte-Carlo simulations (from the production target at the ARIS Fragment Separator to the Target Station of the Spectrometer Section), including the placement of a wedge to optimize the purity of the beams.

Transmission of Representative RIBs	Production Mechanism	Rigidity at maximum RIB intensity (Tm)	Rigidity after wedge (Tm)
^{40}Mg	fragmentation	7.25	6.68
^{60}Ca	fragmentation	6.43	5.94
^{84}Ni	in-flight fission	6.16	5.80
^{100}Sn	fragmentation	4.15	3.73
^{140}Sn	fragmentation	5.44	4.88
^{204}Pt	fragmentation	5.05	3.98
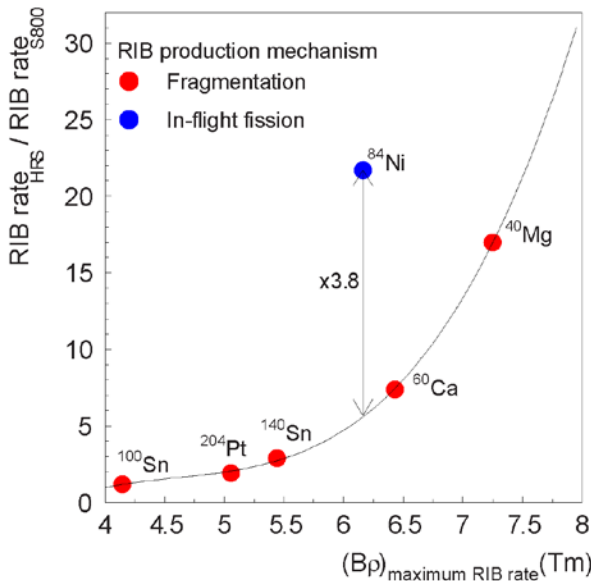
Figure 4.22 Gain in rare-isotope beam rate in the HRS compared to performing experiments with the existing S800 Spectrograph. These gains are estimated in end-to-end Monte-Carlo simulations as detailed in Section 5.4. The solid line indicates the trend of the gain in rate as a function of magnetic rigidity for rare isotopes produced by in-beam fragmentation. For rare isotopes produced via in-flight fission (here exemplified by ^{84}Ni) the gain is much higher than indicated by this trend line, due to the severe limitations imposed by the transmission to the S800 compared to the HRS.

The rare-isotope beam intensity at the target station of the HRS for each of these beams was compared with the beam intensity that can be achieved by using the S800 spectrograph instead of the HRS, taking into account the rigidity limitation of 4 Tm for the latter and transporting the beams through the existing beam line to the S800 spectrograph. The results of that study are shown in Figure 4.22, where the ratio of the rare-isotope beam rate for HRS and the S800 Spectrograph are plotted as a function of the rigidity for which the rare-isotope beam rate is optimized. For isotopes produced by in-flight fragmentation, the gain factor increases to about 17 for the case of ^{40}Mg. The case of ^{84}Ni doesn't follow the smooth trend line established for the other cases because it is produced by in-flight fission rather than fragmentations. Since isotopes produced by in-flight fission have very large beam emittance associated with the fission cone, the development of an

optimized beam line is especially important for achieving a high transmission to the experimental station.

4.3.2.3 Charge-state production

The production of charge states when rare-isotope beams interact with tracking detectors, targets, and other materials that are placed in the path of the beam are an important consideration for the design of experiments with the HRS. An optimized beam line allows tracking detectors to be inserted for the purpose of measuring event-by-event the momentum and time-of-flight of isotopes in the beam. These event-by-event measurements allow individual beam ions to be identified. Although tracking detectors are thin and the energy losses are relatively small, a significant complication arises from the production of different charge states of a single isotope upon passage through these detectors, which results in a loss of beam intensity and contamination of the secondary beams. A similar issue occurs at the target of the experimental station. The production of multiple charge states increases significantly for high-Z beams and at lower beam energies. To study such effects, calculations were performed with the code GLOBAL [SCH98], which is integrated in LISE++ [TAR16]. GLOBAL was developed for beam energies in the range of 80 to 1000 MeV/u. The production of charge-states for the following scenarios was considered:

- Equilibrium charge-state production (e.g. through thick reaction targets). ^{9}Be was chosen as a typical target material.
- Charge-state production through a 130-μm thick plastic scintillator, which is a typical thickness for a beam-line timing detector.
- Charge-state production through a set of PPAC tracking detectors systems. These PPACs, which have an effective thickness of about 1.8 mg/cm^2 are discussed in more detail in section 7.3.1.2.
- Charge-state production for the case in which the beam line has no tracking detectors or other materials, except for the rest gas present at the required vacuum levels (10^{-5} Torr)

Except for case 3), for which only the nucleus ^{204}Pt was studied, calculations were performed for initial beams of ^{60}Ca (Z=20), ^{140}Sn (Z=50), and ^{204}Pt (Z=78, Z-Q=2) for magnetic rigidities ranging from 4 Tm to 8 Tm. These beams are representative for the scientific program with the HRS and span a wide Z range. The results are shown in Figure 4.23. The left column shows the results for charge-state production in ^{9}Be at equilibrium thickness, which ranges from ~20 mg/cm^2 for ^{60}Ca at 4 Tm to ~420 mg/cm^2 for ^{204}Pt at 8 Tm. Clearly, for Z=20 (^{60}Ca), charge-state production is very small. For Z=50 (^{140}Sn), an increase in beam intensity results in an increase in Z-Q=0 charge-state production, and a higher rigidity is clearly advantageous. For Z=78, with Z-Q=2 (^{204}Pt^{76+}), the situation is more complex: at lower rigidities, the production of the Z-Q=2 charge state is dominant, but at higher rigidities, the production of the Z-Q=1 charge state is strongest. For experiments with high-Z beam, experiments must be carefully designed to strike an optimal balance between charge-state production, target thickness, and other considerations that affect the choice of beam energy.

For beams passing through materials that are thinner than the equilibrium thickness (scintillator and PPACs) for which the results are shown in the middle and right columns of Figure 4.23, the results for Z=20 and Z=50 are comparable to the results for passing through ^{9}Be at equilibrium

thickness, although the gain made in predominantly populating the Z-Q=0 charge state for Z=50 is significantly stronger with increasing beam rigidity. For Z=78, the production of the Z-Q=2 charge state is rather independent of the rigidity, but doesn't exceed 60% after passing through the PPACs. Consequently, the use of timing and tracking detectors in the beam transport must be carefully considered in the planning of experiments as well.

Finally, the charge-state production in the rest gas of the beam line vacuum was evaluated. It was found that, even for the highest Z, the production of charge states different from that of the initial rare-isotope beam is less than 0.1% at a pressure of 10^{-5} Torr, when considering the whole distance from the beginning of the HTBL to the final focal plane of the HRS. This is much smaller than the charge-state production in tracking detectors and targets.
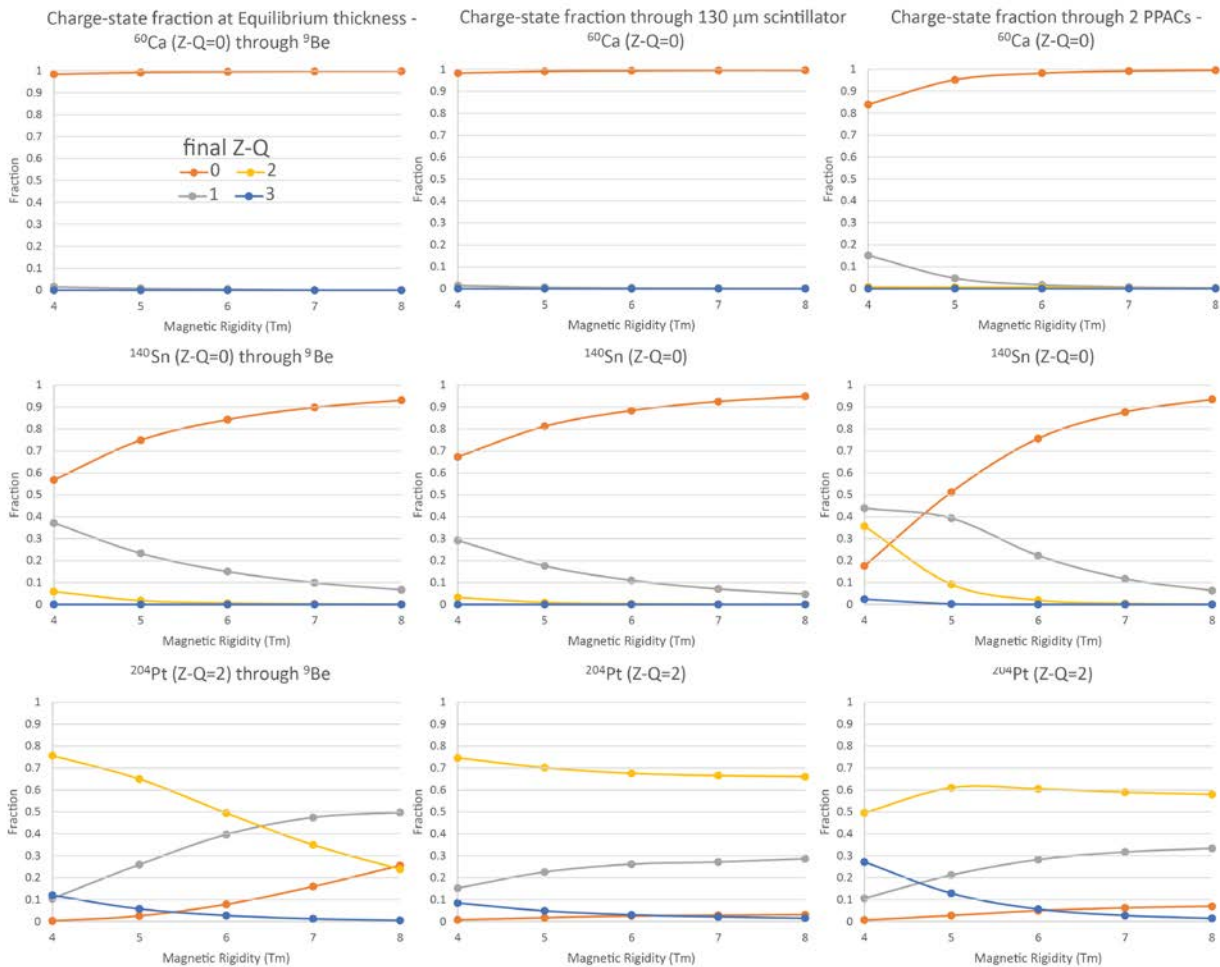
Figure 4.23 Charge-state distributions after ^{60}Ca (top row), ^{140}Sn (middle row), and ^{204}Pt (bottom row) beams pass through a ^{9}Be target at equilibrium thickness (left column), a 130-μm thick plastic scintillator (middle column), and a set of tracking PPACs (right column). Orange, grey, yellow, and blue lines refer to final charge states of Z-Q=0, 1, 2, and 3, respectively.

4.3.2.4 The thickness of the reaction target at the spectrometer.

By performing experiments at higher beam energies, the luminosity can be increased significantly due to the fact that thicker reaction targets can be used. The impact of this effect is exemplified in Figure 4.24(a) for the case of in-beam γ-ray spectroscopy after proton knockout from ^{61}Sc in a ^{9}Be target. To achieve a Doppler-reconstructed γ-ray energy resolution of 2%, the change in rigidity due to the loss in velocity $[\Delta(v/c)]$ in the target must be limited to 5%. At a rigidity of 4 Tm, a target thickness of less than 175 mg/cm^2 would be required. At a rigidity of 5.95 Tm, at which the production rate of ^{61}Sc is maximized, a target thickness of less than 700 mg/cm^2 would be required. From this consideration, an increase by a factor of 4 in luminosity is achieved by operating at the higher rigidity and allowing for a thicker target. Figure 4.24(b) shows the gain factor in luminosity of performing experiments at the HRS with a maximum rigidity of 8 Tm compared to performing experiments at the S800 spectrograph with a maximum rigidity of 4 Tm, as a function of proton number Z and the magnetic rigidity of the HRS
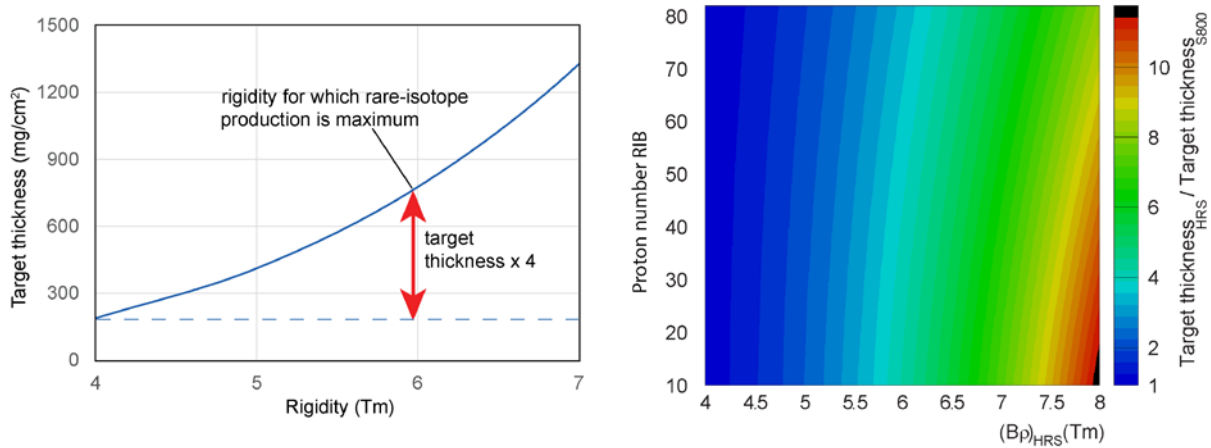
Figure 4.24 (a) Illustration of the luminosity gain that can be achieved by performing experiments at rigidities for which the rare-isotope production rate is maximum. In the case of proton knockout from ^{61}Sc, populating ^{60}Ca, a 4 times thicker target can be used assuming that the change in velocity in the target does not exceed 5% in order to maintain a Doppler-reconstructed γ-ray energy resolution of better than 2%. (b) Luminosity gain factor due to the use of thicker reaction targets achieved by performing experiments up to 8 Tm by using the HRS compared to performing at 4 Tm by using the S800 magnetic spectrograph, as a function of proton number of the rare-isotope beam (y-axis) and rigidity used in the HRS (x-axis).

4.3.2.5 Overall luminosity gains with the HRS

The luminosity for experiments is a combination of the rare-isotope beam production rate, the transmission efficiency, and the target thickness that can be utilized in the experiments, with the exception of ToF-$B\rho$ measurement for which the target thickness does not contribute. Based on the combined production and transmission efficiency studies of Sections 4.3.2.1 and 4.3.2.2, and the gains achieved by using thicker targets discussed in Section 4.3.2.4, the total luminosity gain by using the HRS compared to using the existing S800 Spectrograph was calculated with:

$$\text{luminosity gain} = \frac{\text{RIB Rate at HRS Reaction Target}}{\text{RIB rate at S800 Reaction Target}} \times \frac{\text{HRS Reaction Target Thickness}}{\text{S800 Reaction Target Thickness}}$$

The results for the six representative beams of Table 4-5 are shown in Table 4-6. The gains are small for proton-rich ^{100}Sn for which the rigidity at which the production rate is optimized is close to 4 Tm, but become very high for very neutron-rich rare-isotope beams that require the high magnetic rigidity of the HRS. The gain factor for the most rigid representative beam (^{40}Mg) exceeds 100. Based on the systematics established in the previous section, the luminosity gains were estimated for all isotopes across the chart of nuclei, as shown in Figure 4.25.

Table 4-6 Luminosity gains for experiments at the HRS compared to performing experiments at the existing S800 Spectrometer for the six representative rare-isotope beams of Table 4-5.

Representative RIB	Rigidity (Tm) after FRIB separator for maximum RIB rate	(RIB Rate at HRS reaction target)/ (RIB Rate at S800 reaction target)	(HRS reaction target thickness)/ (S800 reaction target thickness)	Luminosity gain = product of ratios
^{40}Mg	6.68	17	6	**102**
^{60}Ca	5.94	7.4	3.2	**24**
^{84}Ni	5.80	22	3.6	**79**
^{100}Sn	3.73	1.2	1	**1.2**
^{140}Sn	4.88	2.9	1.9	**5.5**
^{204}Pt	3.98	1.9	1	**1.9**

For over 90% of the neutron-rich rare isotopes, gain factors in luminosity of 2 to 100 are achieved. For the most asymmetric neutron-rich isotopes, such as ^{40}Mg, luminosity gains of more than a factor of 50 can be achieved. For neutron-rich isotopes up to N=50 that are produced with rates of 0.001-1 pps, luminosity gain factors exceed a factor of 20. For heavier neutron-rich isotopes, gain factors of 2-10 are achieved. For nearly all nuclei in the path of the r-process, the gain factors lie between 5 and 20. The average luminosity gain factor for neutron-rich isotopes is about 10. On the proton-rich side of the chart of the nuclides, gain factors of up to 2 are achieved, with an average of 1.5.

For ToF-$B\rho$ experiments, in which case no gain in luminosity is achieved by using a thick reaction target, the gain is solely due to the increased rare-isotope beam rate by being able to run at high rigidities, as listed in the 3rd column of Table 4-6. Gains range from ~2-20 for neutron-rich isotopes, including those in the path of the r process.
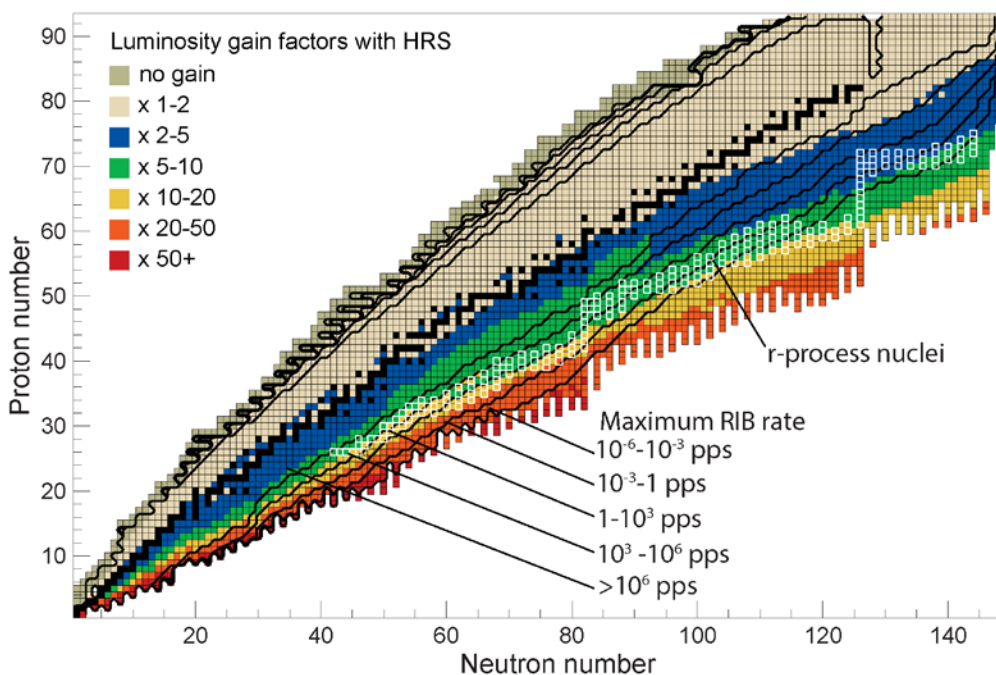
Figure 4.25 Estimated luminosity gain factors that can be achieved by using the HRS compared to using the existing S800 Spectrometer across the chart of nuclei. The rare-isotope production rates are indicated by solid lines and the nuclei shown with white boundaries correspond to the path of the astrophysical r process.

4.3.2.6   Additional luminosity gains with the HRS after an upgrade of FRIB to 400 MeV/u

The optimum magnetic rigidities shown in Figure 4.21 are for the present (200 MeV/u) capabilities of FRIB. As discussed below, a magnetic rigidity of 8 Tm is appropriate even with upgraded FRIB (400 MeV/u) energy.

An energy upgrade of the FRIB accelerator is envisioned in the future, which would increase the optimum rigidity for the production of RIBs as well. Therefore, even though the specification for achieving a rigidity of 8 Tm in the HTBL and the Spectrometer Section of the HRS is only necessary for relatively light neutron-rich isotopes, a much larger region of nuclei will benefit from the 8-Tm rigidity capability once an upgrade from 200 MeV/u to 400 MeV/u for FRIB has been completed. The estimated gains in beam intensity delivered to the HRS target station in light of a possible 400-MeV/u energy upgrade of FRIB are shown in Figure 4.26, assuming that the HTBL and Spectrometer Section of the HRS can bend rare isotopes that have rigidities of up to 8 Tm. Strong gains (more than a factor of 4) are predicted across a very large fraction of the chart of nuclides. Elements produced by in-flight fission ($20<Z<40$ and $40<N<80$) benefit strongly (up to a factor of 15) as the fission-cone becomes more forward peaked.

In addition to the gains in beam intensity, the luminosity for experiments at the HRS when FRIB is upgraded to 400 MeV/u increases further due to the fact that even thicker reaction targets can be used at the target station FS0. For the most neutron-rich nuclei the additional gain in luminosity due the ability to use thicker reaction targets, is on average a factor of 3, based on a similar analysis as the ones discussed in Section 4.3.2.4.

In Figure 4.27, the magnetic rigidities for which the production of rare-isotope beams is optimized are plotted across the chart of nuclei. Because of the higher beam energies, it becomes highly advantageous to use thick production targets because multi-step reactions can strongly increase the yield for the most exotic systems. As a consequence, the optimum magnetic rigidities are lower than what might have been expected on the basis of extrapolations from the calculations at 200 MeV/u, where targets of sufficient thickness to optimize the contribution from multistep production mechanisms are for most cases not feasible. In addition, due to the strong contribution from multi-step processes to the production of rare isotopes, the yield as a function of target thickness (and magnetic rigidity) for FRIB at 400 MeV/u changes much more slowly compared to the production rate for FRIB at 200 MeV/u. Consequently, except for a region of light neutron-rich isotopes below $Z=25$ and around $Z=45$, magnetic rigidities of 8 Tm are sufficient to achieve the optimum production rates of rare isotopes. For the lighter neutron-rich isotopes, relatively high production rates are already achieved at FRIB 200 MeV/u and the gains at 400 MeV/u are minor. For the neutron-rich systems around $Z=45$, the gain in production rate when operating at optimal rigidity (~8.5-9 Tm) is small compared to operating at 8 Tm (less than a factor of 2). It is concluded that a magnetic rigidity of 8 Tm is sufficient to achieve the optimum production rate for the vast majority of rare isotopes produced at FRIB at 400 MeV/u, and that the gains by achieving an even higher rigidity are small.
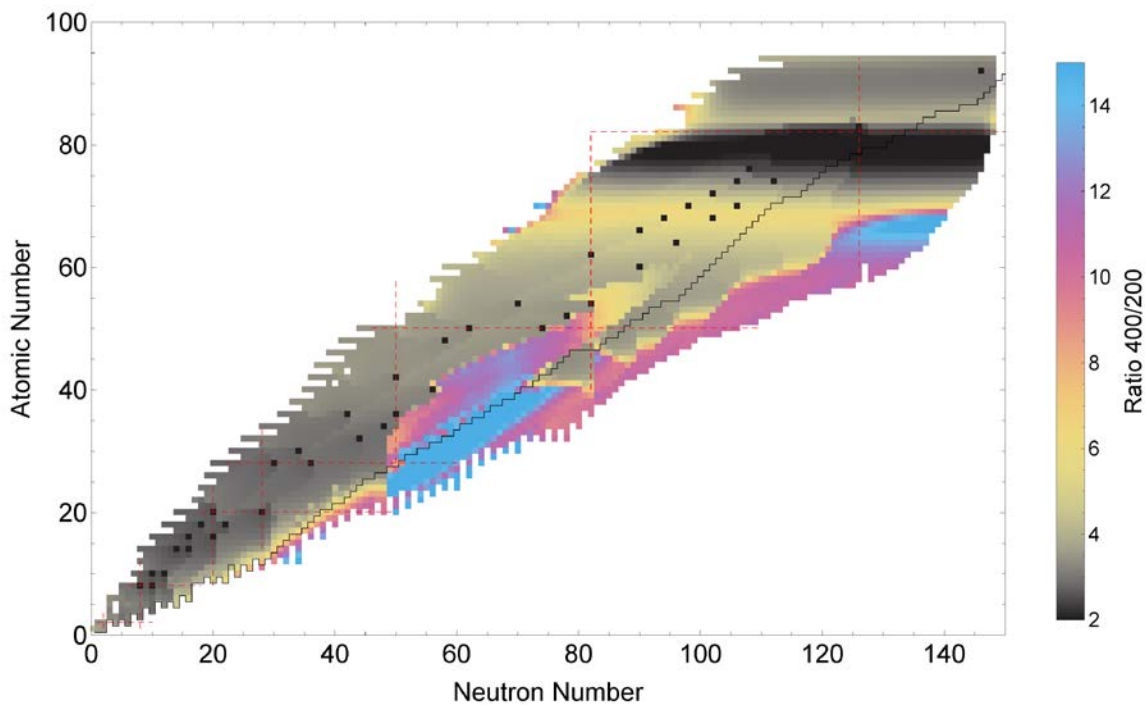
Figure 4.26 Ratio of RIB yields for FRIB with 200 MeV/u capability and 400 MeV/u capability after an energy upgrade. The gain in beam intensity is a factor of 5-10 for the most neutron-rich isotopes, assuming that beams with a rigidity of up to 8-Tm can be transmitted to the target station of the HRS. The black squares designate primary beams used.
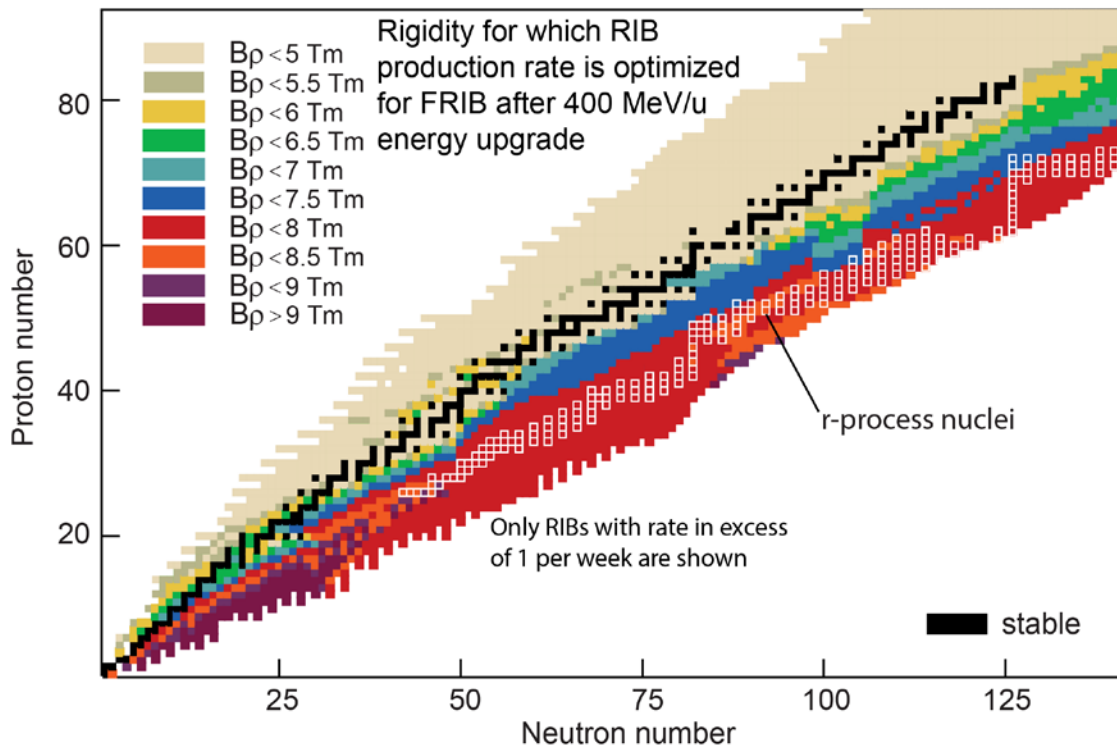
Figure 4.27 Estimated rigidities for which the production rates of rare isotope beams is optimized after a 400 MeV/u energy upgrade of FRIB.

4.3.2.7 Additional specifications for the beam transport from the ARIS Fragment Separator to the target station of the HRS.

In addition to the specifications on the transmission of the rare-isotope beams, there are additional scientific specifications for the beam transport from the ARIS Fragment Separator [ARI13] to the target station at the entrance of the Spectrometer Section. These pertain to the different beam transport modes that the HTBL must accommodate (see Section 4.3.2.7.1), as well as the need to insert beam-diagnostic and tracking-detector stations in the beam line (Section 4.3.2.7.2), an RF fragment separator for beam purification of proton-rich rare-isotope beams (Section 4.3.2.7.3), and the length of the HTBL for the purpose of TOF-$B\rho$ mass measurements (Section 4.3.2.7.4).

4.3.2.7.1 Beam transport modes

The HTBL must be able to be operated in an achromatic mode, as well as in a dispersion-matched mode. The choice of which beam transport to use depends on the type and scientific goals of the experiment and both beam-transport modes have been used in the operation of the S800 Spectrograph at NSCL, as well as other spectrometers operated at other (rare-isotope beam) facilities.

In the achromatic beam-transport mode, for which the beam is doubly focused (x and y) and doubly achromatic (lateral and angular) at the reaction target, the transmission of rare-isotope beams to the reaction target is optimized. In this mode, the momentum spread of the beam particles in contributes to the momentum spread of ejectiles from the reaction target, as shown in Figure

4.28(a). Therefore, the momentum resolution in the focal plane is limited by the momentum spread of the beam. In addition, beam particles that do not react in the target produce a wide image in a focal plane of the spectrometer as they are laterally dispersed and cannot be easily blocked. To improve the momentum and angular resolutions in the achromatic beam transport mode, it is necessary to measure the momentum and angle of individual beam particles with tracking detectors in the beam lines, so that they can be corrected for on an event-by-event basis. However, such event-by-event tracking imposes restrictions on the beam intensity and induces the production of charge-states.

In experiments at the HRS in which the momentum resolution must be better than the momentum spread of the beam particles without employing event-by-event tracking, or in which the unreacted beam particles must be focused in a focal plane such that they can be blocked prior to entering the detector systems, the dispersion matching technique must be applied, as shown in Figure 4.28(b). In this beam-transport mode, the beam is dispersed on the target such that it matches the dispersion matching condition, i.e. the dispersion of the beam line is the same as that of the reverse spectrometer. In addition to lateral dispersion matching, angular dispersion matching is also applied to cancel the angular spread of the beam particles associated with their differences in momenta. The disadvantage of the dispersion-matched beam transport is that the momenta of the beam particles must be restricted in order to not create too large of a beam spot on the target.
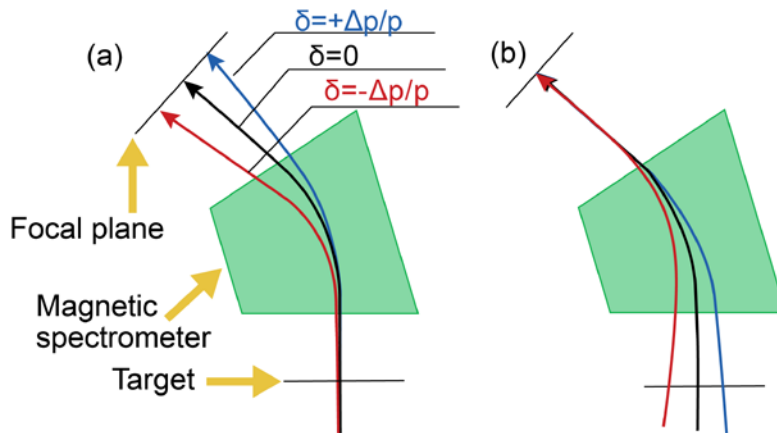
Figure 4.28 Illustration of different beam transport modes: (a) achromatic beam transport, in which the momentum spread ($\pm\Delta p/p$) in the beam contributes to the size of the image in the focal plane of the spectrometer; (b) lateral and angular dispersion-matched beam transport, in which the dispersion on target is additionally correlated with the angles of the incoming particles, such that the angular spreads of the beam particles associated with their differences in momenta are cancelled out in the spectrometer. The rays indicate particles with different momenta. Figure is adapted from [FUJ02].

4.3.2.7.2 Beam tracking and diagnostics specifications

Secondary rare-isotope beams produced by in-flight projectile fragmentation have relatively large beam emittances and are often a mixture of several isotopes. The presence of cocktails of isotopes in the beam is advantageous for efficiently measuring reactions on more than one rare isotope simultaneously, as long as reactions involving different components in the cocktail beam can be identified by using detector in the beam line. Therefore, depending on the specific experiment

performed at the HRS, a variety of diagnostics and tracking detectors are required, for which appropriate space must be made available in the HTBL. For beam tuning purposes, viewers are necessary to quickly inspect the beam spots at various locations along the beam line. Timing detectors are needed to perform event-by-event beam particle identification and are also necessary to determine beam intensities. Tracking detectors are required for measuring the momenta and angles of beam particles in the achromatic beam transport mode. The momentum resolving power for the incoming beam must be compatible with that specified for the experimental programs in Table 4-4 (R_p>1500). For the determination of the angle at the reaction target in front of the Spectrometer Section of the incoming beam particles a resolution of 5 mrad must be achieved. This is particularly important for experiments where stringent angular cuts are necessary (e.g. for heavy-ion Coulomb excitation) or where the accurate knowledge of the reaction angle is critical for reducing the uncertainties in the kinematical reconstruction (e.g. in invariant-mass spectroscopy). These detector systems must have appropriately sized sensitive areas to diagnose the full emittances of the rare-isotope beams based on the ion-optical properties of the HTBL discussed in Section 5, achieve the position (better than 1 mm), timing (better than 150 ps for most experiments, and better than 30 ps for the ToF-$B\rho$ measurements) for analyzing the properties of the beam, and be able to operate at high rates (a few hundred kHz for tracking detectors and at least 1 MHz for timing detectors) to perform event-by-event tracking when necessary for the experiments.

4.3.2.7.3 Accommodation of a RF Fragment Separator for the purification of proton-rich rare-isotope beams.

The HTBL must provide a slot of sufficient length for the future insertion of an RF fragment separator (RFFS), although the RFFS is not part of the scope of the HRS project. An RFFS can be very useful for improving the purity of very proton-rich beams, for which less proton-rich contaminants can otherwise attain levels that hinder the experiment or render it unfeasible. As an example, for measurements with doubly magic ^{100}Sn (see Section 4.2.3.1), the availability of an RFFS will be extremely beneficial.

At beam energies available at FRIB, momentum distributions of fragments produced via projectile fragmentation exhibit exponential-like tails on the low momentum side. Since proton-rich isotopes are found at lower magnetic rigidities than their more stable counterparts, low momentum tails of more abundant contaminants will overlap the region of interest for the desired nucleus, leading to significant levels of unwanted fragments. In the case of ^{100}Sn, the purity of the beam is estimated at about 1.2×10^{-5}. With a production rate of about 8 ^{100}Sn isotopes per second, about 7×10^{5} contaminant isotopes would be in the beam, making it very difficult to track and isolate the events of interest.

The RFFS uses the time microstructure of the beams accelerated by the FRIB accelerator (with an RF frequency of 80.5 MHz) to deflect particles according to their time-of-flight, in effect producing a phase filtering [BAZ09]. The deflected, unwanted contaminants are then blocked by slits placed downstream of the RFFS. Based on simulations in LISE^{++} [BAZ02,TAR08,TAR16] (see also Figure 4.30), a deflection angle of ±8.5 mrad is required to efficiently improve the purity of a ^{100}Sn beam by a factor of ~300 (from a fraction of ^{100}Sn in the beam of 1.2×10^{-5} to 4×10^{-3}), assuming a realistic beam spot image size of 5 mm (FWHM). At this improved level of purity,

only 2000 contaminant isotopes are in the beam, making it feasible to track and identify events associated with [100]Sn particles. To obtain this level of purification, operation at 20.125 MHz is required as at higher RF frequencies, the RF bunches overlap, as shown in Figure 4.30. To operate at 20.125 MHz, it is required that the FRIB accelerator delivers the beams at a frequency of 20.125 MHz, which can be achieved by using a beam chopper.

Besides the RFFS itself, a station for diagnosing the filtering is required, which can coincide with diagnostics and tracking detectors needed for general beam diagnostics and tracking as discussed in Section 4.3.2.7.2. To perform particle identification of the components in the beam after the RFFS, which is necessary for diagnosing the operation of the RFFS, detectors to measure energy loss are additionally required for particle identification.

A conceptual design of an RFFS that would provide the necessary level of contaminant reduction was developed by the FRIB Accelerator Physics Department to estimate the space specifications in the HTBL from the ARIS Fragment Separator to the Spectrometer Section. This conceptual design, shown in Figure 4.29, is based on a Double Quarter-Wave Resonator (QWR) cavity [BLA85] and has a large gap of 18 cm between the 2.26-m long electrodes, which is necessary to transmit large emittance rare-isotope beams. It operates at 20.125 MHz and has a gradient of 17 kV/cm to achieve the angular deflection of ±8.6 mrad. The total length of this RFFS is 2.6 m long. Additional magnetic steering magnets placed immediately prior and after the RFFS are required to keep the particles of interest along the central beam axis for further transmission along the beam line.
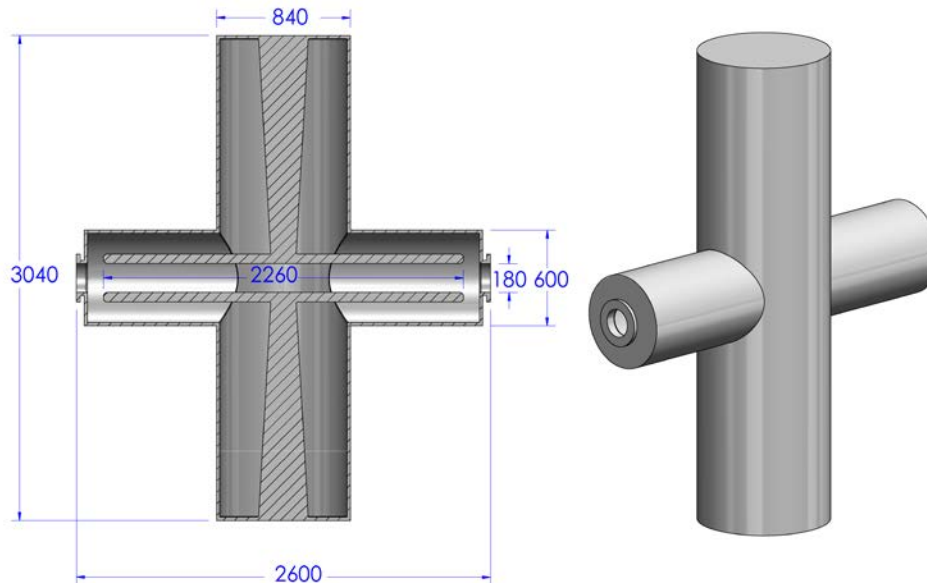
Figure 4.29 Conceptual design of a Double Quarter-Wave Resonator (QWR) cavity that serves as an RF Fragments Separator for the HRS. It operates at 20.125 MHz and provides an angular deflection of ±8.6 mrad to achieve a contaminant suppression of a factor of about 300 for the case of [100]Sn. The dimensions in the figure are in mm.
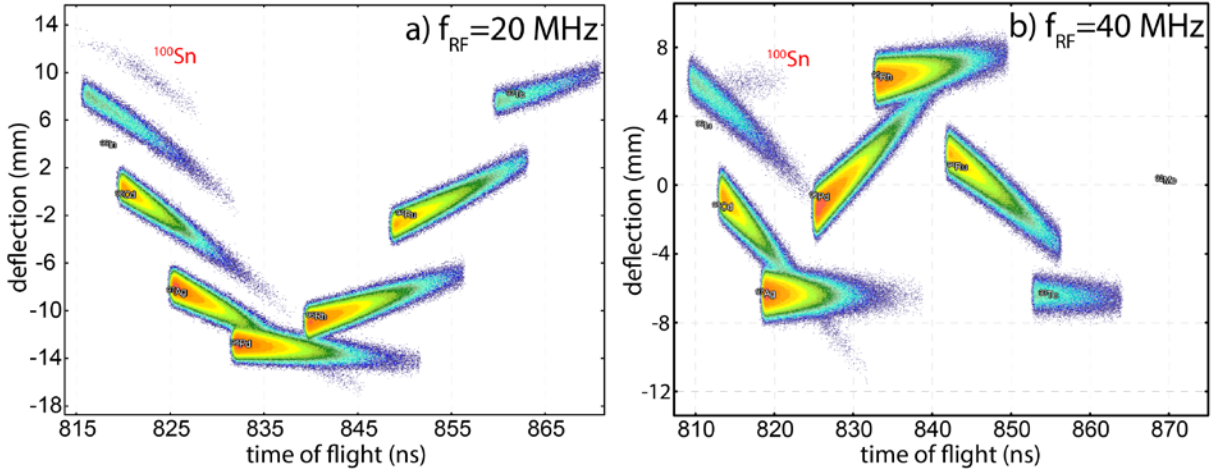
Figure 4.30 LISE^{++} Simulation of the operation of an RFFS placed in the HTBL for the purification of a ^{100}Sn beam. In a) the operation at a frequency of 20.125 MHz is simulated. With a cut on the deflection position (y-axis) by using slit, it is possible to reduce the contamination from particle other than ^{100}Sn particles by a large fraction. At a frequency of 40.25 MHz, shown in panel b), the RF bunches overlap and the ability to purify the ^{100}Sn beam by using slits is strongly reduced compared to operation at 20.125 MHz.

4.3.2.7.4 Constraints on the length of the HTBL for the purpose of ToF-$B\rho$ mass measurements.

The HTBL plays a special role in ToF-$B\rho$ mass measurements (see Section 4.2.2.1 and 4.3.1.5). Besides the delivery of the beams to the Spectrometer Section in dispersion-matched beam-optics mode, the HTBL contributes majorly to the flight-path length from the start (in the Reconfigured A1900 of the ARIS Fragment Separator) to the end (in the final focal plane of the Spectrometer Section) of the ToF measurement. With a position resolution for the tracking detectors of 0.35 mm (FWHM), and a ToF resolution of 30 ps, the total flight-path length has to exceed 90 m to achieve a mass resolving power of 10000. For the position measurements and the ToF measurements, dedicated detectors can be used, as relatively small areas need to be covered in the direction transverse to the beam line. These dedicated detectors are outside of the scope of the HRS.

4.3.2.8 Summary of the Specifications for the High Transmission Beam Line

In Table 4-7 the main specifications for the HTBL discussed in in this section are summarized. These include the specifications for the optimized transmission of rare-isotopes beams, the magnetic rigidity, beam-transport modes, the length of the beam line, and the ability to perform tracking and diagnosis of beam particles and to insert an RF fragment separator in the future.

Table 4-7 Scientific Specifications for the Beam Transport through the High Transmission Beam Line to the Spectrometer Section of the HRS.

Specification for	Specification
Maximum rigidity	8 Tm
Minimum beam transport efficiency	95% in achromatic beam transport mode
Available beam transport modes	Achromatic and dispersion-matched modes that deliver beams to the Spectrometer Section with properties appropriate for achieving the scientific program of the HRS
Minimum time-of-flight path length for ToF-$B\rho$ mass measurements	90 m when combined with the ARIS Reconfigured A1900 and the Spectrometer Section of the HRS
Beam tracking capabilities	Ability to determine the momentum (with a resolving power of at least 1500) and angle (with a resolution of better than 5 mrad) at the Spectrometer Section reaction target by using tracking stations in the HTBL
Rare isotope separation	Ability to insert a Radio-Frequency Fragment Separator with a length of 2.6 m as well as associated steering magnets

4.4   References

[ABB17] B. P. Abbott et al. (LIGO Scientific Collaboration and Virgo Collaboration), Phys. Rev. Lett. 119, 161101 (2017).

[ABR12] S. Abrahamyan et al., Phys. Rev. Lett. 108, 112502 (2012)

[ADR05] P. Adrich et al., Phys. Rev. Lett. 95, 132501 (2005)

[AFA13] A. V. Afanasjev, S. E. Agbemava, D. Ray, P.Ring, Phys. Lett. B 726, 680 (2013).

[ALA96] N. Alamanos and P. Chomaz-Roussel, Ann. Phys. Fr. 21, 601 (1996)

[ALK97] G. D. Alkhazov et al., Phys. Rev. Lett. 78, 2313 (1997)

[AMO06] K. Amos et al., Phys. Rev. Lett. 96, 032503 (2006).

[AND10] A. Andreyev et al., Phys. Rev. Lett. 105, 252502 (2010)

[ARI99] A. Arima, Nucl. Phys. A 646, 260 (1999).

[AYY17] Y. Ayyad et al., Nucl. Instr. And Meth, in Phys. Res. A 880, 166 (2017)

[AST17] A. Arcones et al., Prog. Part. Nucl. Phys. 94, 1, (2017)

[BAU05] T. Baumann et al., Nucl. Instr. and Meth. A543, 517 (2005)

[BAU12] T. Baumann, A. Spyrou and M. Thoennessen, Rep. Prog. Phys. 75, 036301 (2012)

[BAZ02] D. Bazin et al., Nucl. Instrum. Meth. Phys. Res. A 482, 307 (2002)

[BAZ03] D. Bazin et al., Nucl. Instrum. Meth. Phys. Res. B 204, 629 (2003)

[BAZ09] D. Bazin et al., Nucl. Instrum. Meth. Phys. Res. A 606, 314 (2009)

[BAZ09] D. Bazin et al., Phys. Rev. Lett. 102, 232501 (2009)

[BEN07] M.A. Bentley and S.M. Lenzi, Prog. in Particle and Nucl. Phys. 59, 497 (2007)

[BER83] A.M. Bernstein et al., Comments Nucl. Part. Phys. 11, 203 (1983)

[BER88] Carlos A. Bertulani and Gerhard Baur, Phys. Rep. 163, 299 (1988)

[BET79] H. A. Bethe et al., Nucl. Phys. A 324, 487 (1979)

[BLA85] E. W. Blackmore et al., Nucl. Instr. And Meth, in Phys. Res. A 234, 235 (1985)
[BLA92] B. Blank et al., Z. Phys. A 343, 375 (1992)
[BLA07] B. Blank and M. Borge, Prog. in Part. and Nucl. Phys. 60(2) 403 (2007)
[BRA00] F. Brachwitz et al., Astrophys. J. 536, 934 (2000)
[BRO88] B. A. Brown and B. H. Wildenthal, Annu. Rev. Nucl. Part. Sci., 38, 29 (1988)
[BRO00] B.A. Brown, Phys. Rev. Lett. 85, 5296 (2000)
[BRO13] B.A. Brown, Phys. Rev. Lett. 111, 232502 (2013)
[CAA13] M. Caamano et al, Pys. Rev. C 88, 024605 (2013)
[CLA03] B.C. Clark, L.J. Kerr and S. Hama, Phys. Rev. C 67, 054605 (2003)
[COL14] G. Colò, U. Garg, and H. Sagawa, Eur. Phys. J A 50, 26 (2014)
[COU15] A. J. Couture, LANL report LA-UR-15-28115 (2015)
[DAN02] P. Danielewicz, R. Lacey, W.G. Lynch, Science 298, 1592 (2002)
[DAN03] P. Danielewicz, Nucl. Phys. A 727, 233 (2003)
[DAN17] Paweł Danielewicz, Pardeep Singh, Jenny Lee, Nucl. Phys. A958, 147 (2017)
[DOB07] J. Dobaczewski et al., Prog. In Part. and Nucl. Phys. 59, 432 (2007)
[ERI73] M. Ericson and A. Figureau and C. Thévenet, Phys. Lett. B 45, 19 (1973).
[ERL12] J. Erler et al., Nature 486, 509 (2012) and references therein.
[ERL12a] J. Erler et al, Phys. Rev. C 85, 025802 (2012)
[EST11] A.Estrade et al., Phys. Rev. Lett. 107, 172503 (2011)
[EST14] A. Estrade et al., Phys. Rev. Lett. 113, 132501 (2014)
[FAM06] M.A. Famiano et al., Phys. Rev. Lett. 97, 052701 (2006)
[FAL16] P. Fallon, A. Gade, and IY Lee, Annu. Rev. of Nucl. and Part. Sci. 66, 321 (2016)
[FEY58] R. P. Feynman and M. Gell-Mann, Phys. Rev. 109, 139 (1958)
[FLA12] F. Flavigny et al., Phys. Rev. Lett. 108, 252501 (2012)
[FOR13] C Forssén et al., Phys. Scr. T152, 014022 (2013).
[FRA05] S. Fracasso and G. Colò, Phys. Rev. C 72, 064310 (2005)
[FRA85] M.A. Franey and W.G. Love, Phys. Rev. C 31, 488 (1985)
[FUJ02] H. Fujita et al., Nucl. Instrum. Meth. Phys. Res. A 484, 17 (2002)
[GAA81] C. Gaarde et al., Nucl. Phys. A369, 258 (1981)
[GAA85] C. Gaarde, Proc. Niels Bohr Centennial Conference on Nuclear Structure, Copenhagen, 449c (1985)
[GAD05] A. Gade et al., Phys.Rev. C 71, 051301(R) (2005)
[GAD08a] A. Gade and T. Glasmacher, Prog. in Part. and Nucl. Phys. 60, 161 (2008)
[GAD08b] A. Gade et al., Phys. Rev. C 77, 044306 (2008)
[GAD14] A. Gade et al., Phys. Rev. Lett. 112, 112503 (2014)
[GAD15] A. Gade, Eur. Phys. J. A 51, 118 (2015)
[GAD16] A. Gade and S. N. Liddick, J. Phys. G: Nucl. Part. Phys. 43, 024001 (2016)
[GAN12] S. Gandolfi, J. Carlson, S. Reddy, Phys. Rev. C 85,032801(R) (2012)
[GLA98] T. Glasmacher, Annu. Rev. Nucl. Part. Sci. 48, 1 (1998)
[GOR13] S. Goriely et al, Phys. Rev. Lett. 111, 242502 (2013)
[GOR15] S. Goriely et al., Mon. Not. R. Astron. Soc. 452, 3894 (2015)
[GRE17] GRETA Conceptual Design report,
http://greta.lbl.gov/documents/ConceptualDesignReport-071717.pdf, (2017)

[GUP06] Sanjib Gupta et al., Astrophys. J. 662, 1188 (2006)

[HAG12] G. Hagen et al., Phys. Rev. Lett. 109, 032502 (2012)

[HAG16] G. Hagen, G. R. Jansen, T. Papenbrock, Phys. Rev. Lett. 117, 172501 (2016)

[HAM14] Ikuko Hamamoto and Hiroyuki Sagawa, Phys. Rev. C 90, 031302(R) (2014).

[HAN03] P.G. Hansen, J.A. Tostevin, Annu. Rev. Nucl. Part. Sci. 53, 221 (2003)

[HAR01] M.N. Harakeh and A. van der Woude, Giant Resonances, Fundamental High-Frequency Modes of Nuclear Excitations, Oxford Studies in Nuclear Physics 24, Clarendon Press, Oxford, 2001

[HAR14] J.C.Hardy and I.S.Towner, Phys. Rev. C 91, 025501 (2015)

[HAU13] M. Hausmann, Nucl. Instrum. Meth. in Phys. Res. B, 317, 349 (2013)

[HEB10] K. Hebeler, A. Schwenk, Phys. Rev. C 82, 014314 (2010)

[HER14] H. Hergert et al., Phys. Rev. C 90, 041302(R) (2014)

[HEG01] A. Heger, S.E. Woosley, G. Martinez-Pinedo, K. Langanke, Ap. J. 560, 307 (2001)

[HEY11] Kris Heyde and John L. Wood, Rev. Mod. Phys. 83, 1467 (2011)

[HIX03] W.R. Hix et al., Phys. Rev. Lett. 91, 201102 (2003)

[HOL12] J. D. Holt et al., J. Phys. G: Nucl. Part. Phys. 39, 085111 (2012)

[HOL14] J. D. Holt et al., arXiv.1405.7602 (2014)

[HOR14] C.J. Horowitz et al., J. Phys. G 41, 093001 (2014)

[HRS14] HRS Working group, A high Rigidity Spectrometer for FRIB (2014)

[HUC85] A. Huck et al., Phys. Rev. C 31, 2226 (1985)

[HYU80] H. Hyuga and A. Arima and K. Shimizu, Nucl. Phys. A 336, 363 (1980)

[IWA99] K. Iwamoto et al., Astrophys. J. Suppl. 125, 439 (1999)

[IWA16] H. Iwasaki et al., Nucl. Instrum. Method. in Phys. Res. A 806, 123 (2016)

[JAN07] H.-T. Janka et al., Phys. Rep. 442, 38 (2007)

[JAN13] M. Jandel, et al., Los Alamos Report LA-UR-12-24975, 2013

[JHA16] G. Jhang et al., Journal of Korean Physics Society, 69, 144 (2016)

[JIA07] Wei-Zhou Jiang, Bao-An Li, and Lie-Wen Chen, Phys. Rev. C 76, 044604 (2007)

[KAS17] D. Kasen et al., Nature 551, 80 (2017)

[KAR02] S. Karataglides et al., Phys. Rev. C65, 044306 (2002)

[KHA11] E. Khan, N. Paar, D. Vretenar, Phys. Rev. C 84, 051301(R) (2011)

[KHA13] E. Khan et al., Phys. Rev. C 87, 064311 (2013)

[KOB12] N. Kobayashi et al., Phys. Rec. C. 86, 054604 (2012)

[KOH13] Z. Kohley et al., Phys. Rev. Lett. 110, 152501 (2013)

[KOU05] H. Koura, T. Tachibana, M. Uno, and M. Yamada, Prog. Theor. Phys., vol. 113, 305 (2005)

[KOR12] O. Korobkin et al, Mon. Not. R. Astron. Soc. 426, 1940 (2012)

[KRA99] A. Krasznahorkay et al., Phys. Rev. Lett. 82, 3216 (1999)

[KRE95] G. Krein et al., Phys. Rev. C 51, 2646 (1995)

[LAN03] K. Langanke, G. Martinez-Pinedo, Rev. Mod. Phys. 75, 819 (2003)

[LAT01] J. M. Lattimer, M. Prakash, ApJ, 550, 426 (2001)

[LAT04] J.M. Lattimer, M. Prakash, Science 304, 536 (2004)

[LAT13] J. M. Lattimer and Y. Lim, ApJ 771, 51 (2013)

[LAT16] J. M. Lattimer and M. Prakash, Phys. Rep. 621, 127 (2016)

[LEN10] S. M. Lenzi, F. Nowacki, A. Poves, and K. Sieja, Phys. Rev. C 82, 054301 (2010)

[LI02] B. A. Li, Nucl. Phys. A 708, 365 (2002)

[LI05] B.A. Li, L.W. Chen, Phys. Rev. C 72, 064611 (2005)

[LI05b] B.A. Li, G.C. Yong, W. Zuo, Phys. Rev. C71, 014608 (2005)

[LI07] T. Li et al., Phys. Rev. Lett. 99, 162503 (2007)

[Li08] Bao-An Li et al., Phys. Rep. 464, 113 (2008)

[Li93] G. Q. Li and R. Machleidt, Phys. Rev. C 48, 1702 (1993)

[Li94] G. Q. Li and R. Machleidt, Phys. Rev. C 49, 566 (1994)

[LIP18] S. I. Lipschutz, Ph.D. Thesis, Michigan State University (2018); S. I. Lipschutz et al., submitted for publication

[LOC14] Bui Minh Loc, Dao T. Khoa, and R. G. T. Zegers, Phys. Rev. C 89, 024317 (2014)

[LOC17] Bui Minh Loc, Naftali Auerbach, and Dao T. Khoa, Phys. Rev. C 96, 014311 (2017)

[LOV81] W. G. Love and M. A. Franey, Phys. Rev. C 24, 1073 (1981)

[LRP07] The Frontiers of Nuclear Science, A Long Range Plan, Nuclear Science Advisory Committee (2007)

[LRP15] Reaching For the Horizon, The 2015 Long Range Plan for Nuclear Science, The Nuclear Science Advisory Committee (2015)

[MAH14] M.H. Mahzoon *et al.,* Phys. Rev. Lett. 112, 162503 (2014)

[MAM13] J. Mammei et al., CREX: PARITY-VIOLATING MEASUREMENT of the WEAK CHARGE DISTRIBUTION of ^{48}Ca to 0.02 fm ACCURACY

[MEI11] K. Meierbachtol et al., Nucl. Instrum. Method. in Phys. Res. A 652, 668 (2011)

[MEH12] R. Meharchand et al., Phys. Rev. Lett. 108, 122501 (2012)

[MEI13] Z. Meisel and S. George, IJMS 349, 145 (2013)

[MEI15] Z. Meisel et al., Phys. Rev. Lett. 114, 022501 (2015)

[MIL16a] S. A. Milne, M. A. Bentley et al., Phys. Rev. Lett. 117, 082502 (2016)

[MIL16b] S. A. Milne, M. A. Bentley et al., Phys. Rev. C 93, 024318 (2016)

[MOE95] P. Moeller, J.R. Nix, and W.J. Swiatecki, At. Data Nucl. Data Tables 59, 185 (1995)

[MON08] C. Monrozeau et al., Phys. Rev. Lett. 100, 042501 (2008)

[MRI09] MRI-Consortium: Development of a Neutron Detector Array by Undergraduate Research Students for Studies of Exotic Nuclei, NSF grants 0922335, 0922409, 0922446, 0922462, 0922473, 0922537, 0922559, 0922622, and 0922794

[MUE11] J.M. Mueller *et al.*, Phys. Rev. C83, 064605 (2011)

[MUM16] M.R. Mumpower et al., Prog. Part. Nucl. Phys. 86, 86 (2016)

[Nav16] P. Navrátil, S. Quaglioni, G. Hupin, C. Romero-Redondo and A. Calci, Phys. Scr. 91, 053002 (2016).

[NAZ14] W. Nazarewicz, P.-G. Reinhard, W. Satuła, and D. Vretenar, Eur. Phys. J. A 50, 20 (2014).

[NDB14] Neutrinoless Double Beta Decay Report, NSAC, 2014 http://science.energy.gov/~/media/np/nsac/pdf/docs/2014/NLDBD_Report_2014_Final.pdf

[NOJ14] S. Noji et al., Phys. Rev. Lett 112, 252501 (2014)

[NOJ15] S. Noji et al., Phys. Rev. C 92, 024312 (2015)

[NOJ18] S. Noji et al., Phys. Rev. Lett. 120, 172501 (2018)

[NOW16] F. Nowacki, A. Poves, E. Caurier, and B. Bounthong, Phys. Rev. Lett. 117, 272501 (2016)

[NRC07] Scientific Opportunities with a Rare-Isotope Facility in the United States, National Research Council; Division on Engineering and Physical Sciences; Board on Physics and Astronomy; Rare-Isotope Science Assessment Committee (2007)

[NRC13] National Research Council. *Nuclear Physics: Exploring the Heart of Matter*. Washington, DC: The National Academies Press, 2013

[OBS13] A. Obserstedt, et al., Phys. Rev. C 87, 051602(R) (2013)

[OST92] F. Osterfeld, Rev. Mod. Phys. 64, 491 (1992)

[OTS16] H. Otsu et al., Nucl. Instrum. Meth. in Phys. Res. B 376, 175 (2016)

[PAA07] N. Paar, D. Vretenar, E. Khan, and G. Colò, Rep. Prog. Phys. 70, 691 (2007).

[PAI07] S. Pain et al., Nucl. Instr. And Meth, in Phys. Res. B 261, 1122 (2007)

[PAN05] I. V. Panov et al, Nucl. Phys. A 747, 633 (2005)

[PAS11] K. Paschke, K. Kumar R. Michaels, P.A.Souder, G.M. Urciuoli et al., JLAB Exp E12-11-101, PREX-II: PRECISION PARITY-VIOLATING MEASUREMENT OF THE NEUTRON SKIN OF LEAD

[PAT12] D. Patel et al., Phys. Lett. B 758, (2012)

[PER12] G. Perdikakis et al., Nucl. Instr. And Meth, in Phys. Res. A 686, 117 (2012)

[PET16] W. A. Peters, Nucl. Instr. And Meth, in Phys. Res. A 836, 122 (2016)

[PEL13] E. Pellereau et al, EPJ Web of Conf. 62, 06005 (2013)

[RAD18] D. Radice et al., Ap. J. Lett. 852, 1 (2018)

[RIB07] Report to NSAC of the Rare-Isotope Beam Task Force

[RIC17] S. Richers et al., Phys. Rev. D 95, 063019 (2017)

[ROG11] A.M. Rogers et al., Phys. Rev. Lett. 106, 252503 (2011)

[RUS11] P. Russotto et al., Phys. Lett. B 697, 471 (2011)

[SAG07] H. Sagawa et al., Phys. Rev. C 76, 024301 (2007)

[SAM06] F. Sammarruca and P. Krastev, Phys. Rev. C 73, 014001 (2006)

[SAS11] M. Sasano et al., Phys. Rev. Lett. 107, 202501 (2011)

[SAS12] M. Sasano et al., Phys. Rev. C 86, 034324 (2012)

[SAV13] D. Savran, T. Aumann, and A. Zilges, Prog. Part. Nucl. Phys. 70, 210 (2013)

[SCH98] C. Scheidenberger, Th. Stöhlker, W.E. Meyerhof, H. Geissel. P.H. Mokler, B. Blank, Nucl. Instr. Meth. Phys. Res. B 142, 441 (1998).

[SCH01] K.-H. Schmidt, Nucl. Phys. A 693, 169 (2001)

[SCH02] H. Schatz et al, Astrophys. Jour. 579, 626 (2002)

[SCH13] H. Schatz et al., Nature (London) 505, 62 (2013)

[SCO17] M. Scott et al., Phys. Rev. Lett. 118 172501 (2012)

[SEG01] W. F. Mueller et al., Nucl. Instr. and Meth. A466, 492 (2001)

[SMI18] K. Smith et al., Nucl. Instr. And Meth, in Phys. Res. B 414, 190 (2018)

[SPY12] A. Spyrou et al., Phys. Rev. Lett. 108, 102501 (2012)

[STE05] A.W. Steiner, M. Prakash, J.M. Lattimer, P.J. Ellis, Phys. Rep. 411, 325 (2005)

[STE13] D. Steppenbeck et al., Nature 502, 207 (2013)

[STE13a] I. Stetcu, et al., Phys. Rev. C 88 (2013) 044603

[SUL16] C. Sullivan et al., Ap. J. 816, 44 (2016)

[SUH17] J. T. Suhonen, Front. Phys. 5, 55 (2017) and references therein.

[SUZ90] Yasuyuki Suzuki, Kiyomi Ikeda and Hiroshi Sato, Prog. Theor. Phys. 83, 180 (1990).

[TAL12] P. Talou, et al., Proceedings of the 5th International Conference on Fission, Sanibel Island, Nov. 2012 (pp. 581-588)

[TAR16] O. B. Tarasov and D. Bazin, Nucl. Instr. And Meth, in Phys. Res. B 376, 185 (2016)

[TAR08] O. B. Tarasov and D. Bazin, Nucl. Instr. And Meth, in Phys. Res. B 266, 4657 (2008)

[TER14] S. Terashima et al., Prog. Theor. Exp. Phys. 101D02,(2014)

[TIT19] R. Titus et al, Phys. Rev. C 100 045805 (2019)

[THI83] F.-K. Thieleman et al, Z. Phys. A 309, 301 (1983)

[TOS01] J.A. Tostevin, Nuclear Phys. A 682, 320c (2001)

[TOS99] J.A. Tostevin, J. Phys. G 25, 735 (1999)

[TSA12] M.B. Tsang et al., Phys. Rev. C 86, 015803 (2012)

[ULL14] J. L. Ullmann, et al., Phys. Rev. C 89, 034603 (2014)

[VAN14] M. Vandebrouck et al., PRL 113, 032504 (2014)

[VIL04] A.R. Villarreal, T.E. Strohmayer, ApJ, 614, L121 (2004)

[VRE03] D. Vretenar, N. Paar, T. Niksic, P. Ring, Phys. Rev. Lett. 91, 262502 (2003)

[WAK97] T. Wakasa et al., Phys. Rev. C 55, 2909 (1997)

[WAL07] M.S. Wallace et al., Nucl. Instr. And Meth, in Phys. Res. A 583, 302 (2007)

[WAR06] D.D. Warner, M.A. Bentley, and P. Van Isacker, Nature Physics 2, 311 (2006)

[WEI10] D. Weisshaar et al., Nucl. Instr. And Meth, in Phys. Res. A 624, 615 (2010)

[WIM14] K. Wimmer et al., Nucl. Instr. And Meth, in Phys. Res. A 769, 65 (2014)

[XIA08] Zhigang Xiao et al., Phys. Rev. Let. 102, 062502 (2009)

[YAK05] K. Yako et al., Phys. Lett. B 615, 193 (2005).

[YAK06] K. Yako, H. Sagawa, and H. Sakai, Phys. Rev. C 74, 051303(R) (2006)

[YAM11] T. Yamaguchi et al., Phys. Rev. Lett. 107, 032502 (2011)

[ZAM19] J. C. Zamora et al., Phys. Rev. C 100, 032801(R) (2019)

[ZEG08] R.G.T. Zegers et al., Phys. Rev. C 77, 024307 (2008)

[ZEG10] R.G.T. Zegers et al., Phys. Rev. Lett. 104, 212504 (2010)

[ZEL06] Vladimir Zelevinsky and Alexander Volya, AIP Conf. Proc. 819, 493 (2006)

5 High Transmission Beam Line (HTBL) of the HRS

In this section, the properties of the High Transmission Beam Line (HTBL) of the HRS are described, based on the scientific requirements motivated and provided in Section 4.3.2. The Work Breakdown Structure (WBS) for this section is given in Table 5-1. After an introduction and a brief overview of the HTBL given in Section 5.1, the scientific requirements are summarized in Section 5.2, and the design approach and the preferred alternative is described in Section 5.3. In Section 5.4, the performance of the HTBL is demonstrated by end-to-end simulations. The capabilities afforded by the preferred alternative of the HTBL is summarized in Section 5.5. The specifications of the magnetic elements, the diagnostics and detectors, and the vacuum components are given in Section 5.6, which will be the input for the corresponding systems. Commissioning plans for the HTBL are given in Section 8.

The ion-optical calculations for the HTBL (and the Spectrometer Section described in Section 6) were performed with the transfer-matrix-type ion-optics code COSY INFINITY [COS11], which is capable of computing Taylor maps for arbitrarily complicated fields (including fringe fields) to arbitrary order by utilizing differential-algebraic techniques. COSY INFINITY performs all its calculations in the following coordinate system. The indices of the matrix elements denote the positions in the horizontal dispersive (x) and vertical non-dispersive planes (y), the parameter $a = p_x/p_0$ ($b = p_y/p_0$) is the ratio of the dispersive (p_x) and non-dispersive (p_y) the total momentum (p_0), and the parameter δ_K denotes $\delta K/K$, where δK is the deviation from the central kinetic energy K, where x-a and y-b are canonically conjugate to each other. The normalized momenta a and b are approximately equal to the dispersive and non-dispersive geometrical angles (x' and y') when they are small. For simplicity, the energy deviation $\delta_K = \delta K/K$ will be all converted to the normal momentum deviation $\delta_p = \delta p/p$ in this document. As presented in Section 9.4.1, the quadrupole magnets used in the HTBL are of the same design of the existing quadrupoles used in the A1900 fragment separator, the field profiles acquired from the actual field mapping have been incorporated in calculations in COSY INFINITY that are presented in this section. This includes the excitation dependence of the effective length of magnetic fields of the triplets, which is parameterized based on measurements.

Table 5-1 WBS for the HTBL ion-optical design

Experimental Systems - High Rigidity Spectrometer	HRS.3
High Transmission Beamline (HTBL)	HRS.3.01
High Transmission Beamline Beam Physics	HRS.3.01.01

5.1 Introduction and overview

The layout of the HTBL is shown in Figure 5.1. The nomenclature for the various elements is described in Figure 5.2. The HTBL connects the Reconfigured A1900 of the ARIS Fragment Separator with the Spectrometer Section, starting at the final focal plane of the Reconfigured A1900 Fragment Separator (FB0) and ending at the location of the reaction target of the Spectrometer Section (FS0). The HTBL has eight quadrupole triplets (TB1 through TB8), four dipole magnets (DB1 through DB4), and two vertical steering magnets (SB1 and SB2). At the

intermediate focal planes FB1 and FB3, vacuum chambers are installed that house beam diagnostics equipment (viewers) and detectors for the tracking of momenta and angles of the beam on an event-by-event basis and for particle identification.
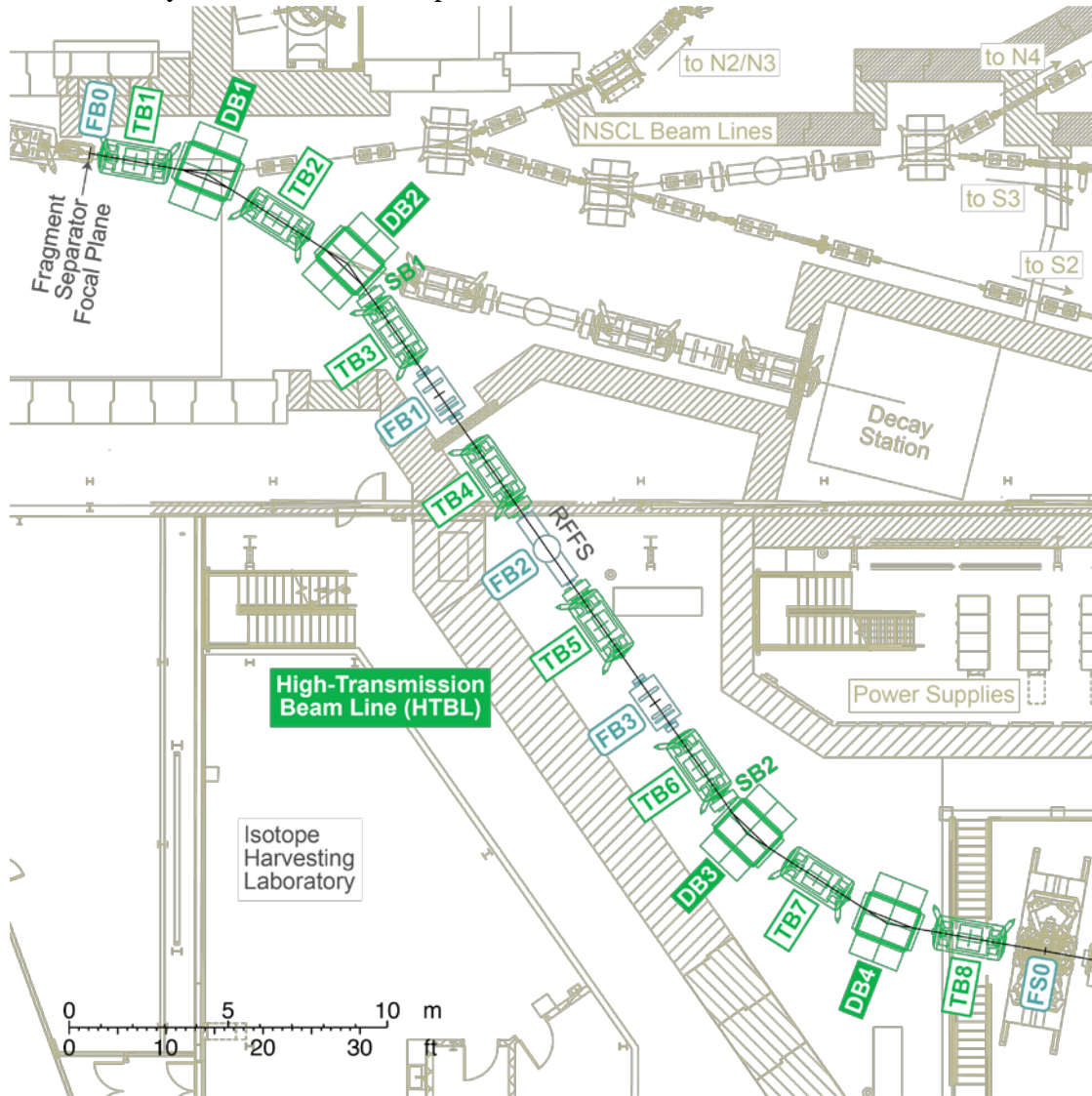
Figure 5.1 Layout of the High-Transmission Beam Line (HTBL), beginning at FB0.
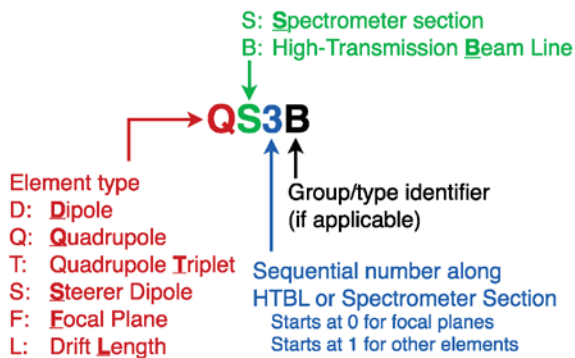
Figure 5.2 Nomenclature of elements of the HTBL and Spectrometer Section of the HRS.

It is noted that the initial sections of the HTBL also provide beam transport to other experimental areas. A triplet TB1 and switching dipole DB1 are used to deliver beam to existing beam lines to the beam-stopping areas (vaults N2, N3, and N4) and to the fast-beam areas (vaults S2 and S3). The beam-stopping areas provide thermalized beams to the experimental areas focused on in-beam laser-spectroscopy, high-precision mass spectroscopy and other high-precision studies, and decay spectroscopy with thermalized beams. The beam-stopping areas also provide thermalized beams to the Reaccelerator (ReA), which provides beams with an energy of several MeVs to additional experimental areas at FRIB. Fast beams in S2 are used for a variety of experiments and, prior to the completion of the HRS, neutron invariant-mass experiments with the existing sweeper magnet and the MoNA-LISA neutron array will be carried out in this vault. The S3 vault houses the S800 spectrometer. Both the Sweeper magnet and S800 spectrometers have maximum magnetic rigidities of 4 Tm.

In addition to TB1 and DB1, a triplet TB2 and a switching dipole DB2 are necessary for delivering rare-isotope beams from the ARIS Fragment Separator to a new Decay Station, as shown in Figure 5.1. This Decay Station consist of a versatile setup for the detection of photons, charged particles, and neutrons emitted from rare isotopes that are stopped in the center of the station.

5.2   Requirements for the HTBL

Section 4.3.2 detailed the scientific specifications for the HTBL, which were summarized in Section 4.3.2.8. Specification Table 4-7 provides the requirements for the ion-optical design of the HTBL and for convenience provided in Table 5-2. To optimize the luminosity for experiments at the HRS, the HTBL must be able to transport beams with a magnetic rigidity of up to 8 Tm as discussed in Section 4.3.2.1. The HTBL must optimize the transmission of rare-isotope beams from the ARIS Fragment Separator at the magnetic rigidities at which the production rates of those beams are maximized. The rare-isotope-beam transport efficiency must exceed 95%. In addition to an achromatic beam transport mode, the HTBL must be able to dispersion-match the Spectrometer Section by creating the matching resolving power of that of the Spectrometer Section as described in Section 4.3.2.7.1. For ToF-$B\rho$ mass measurements, the HTBL, in conjunction with the Spectrometer Section and the Reconfigured A1900 of the ARIS Fragment Separator must at least have a length of 90 m, as described in Section 4.3.2.7.4. The HTBL must accommodate beam tracking and diagnostic stations, as described in Sections 4.3.2.7.2 and 4.3.2.7.3. Finally, the HTBL must be able to perform rare-isotope-beam separation for proton-rich species with an RF fragment separator, as described in Section 4.3.2.7.3. For which the HTBL must provide 2.6 m of space for inserting a Radio-Frequency Fragment Separator, based on its conceptual design, as well as associated steering magnets.

Table 5-2 Requirements for the design of the HTBL. This table reproduces the specifications of Table 4-7.

Requirement for	Requirement
Maximum rigidity	8 Tm
Minimum beam transport efficiency	95% in achromatic beam transport mode
Available beam transport modes	Achromatic and dispersion-matched modes that deliver beams to the Spectrometer Section with properties appropriate for achieving the scientific program of the HRS
Minimum time-of-flight path length for ToF-$B\rho$ mass measurements	90 m when combined with the ARIS Reconfigured A1900 and the Spectrometer Section of the HRS
Beam tracking capabilities	Ability to determine the momentum (with a resolving power of at least 1500) and angle (with a resolution of better than 5 mrad) at the Spectrometer Section reaction target by using tracking stations in the HTBL
Rare isotope separation	Ability to insert a Radio-Frequency Fragment Separator with a length of 2.6 m as well as associated steering magnets

5.3 Design approach and preferred alternative for the HTBL

To connect the ARIS Fragment Separator with the Spectrometer Section, the HTBL must transport the beam over a significant distance (~40 m) while providing the ion-optical properties for the scattering of the beam particles at the reaction target in front of the Spectrometer Section.

A combination of bending (dipole) and focusing (quadrupole and higher orders) magnets is required to achieve such a transport. In addition, as discussed in Section 5.2, the layout must accommodate the beam delivery to the other experimental areas of FRIB. As described in Section 4.3.2.7.1, to be able to operate in dispersion-matched beam transport mode, sufficient resolving power must be created in the HTBL to meet the dispersion-matching conditions. The resolving power can only be created by the dipole field and the total bending angle in the HTBL must be sufficiently large, which constrains the layout. Finally, the symmetry of the layout of the entire beam line is very beneficial for reducing the higher-order ion-optical aberrations due to cancellation effects.

Based on these general considerations, a separated dipole scheme was adopted for the HTBL. In addition to delivering the beam to the Spectrometer Section, the first dipole (DB1) can bend the beam left towards the existing stopped- and fast-beam experimental vaults, and the second dipole (DB2) can bend the beam left towards the new FRIB Decay Station. This has the additional advantage that the FRIB Decay Station also benefits from the high bending capability and excellent beam transmission through the initial stage of the HTBL. After these two right-bending dipoles, the left-bending third and fourth dipoles (DB3 and DB4) direct the beam towards the reaction target FS0. Each of the four dipoles of the HTBL bend the beam by 22.5 degrees and the entrance and exit sections of the HTBL are parallel to each other (i.e. no net bending angle). These dipoles must be capable of bending beams with rigidities of up to 8 Tm. The HTBL must be furnished with quadrupole magnets to shape the beam for necessary ion-optical properties and good transmission efficiency. The dipoles and the quadrupoles are placed so that the section from FB0

to FB1 is symmetric with respect to TB2, the section from FB1 to FB3 is symmetric with respect to FB2, and the section from FB3 to FS0 is symmetric with respect to TB7, while the entire HTBL is symmetric with respect to FB2, with the exception of minor modifications due to the space constraints around FB0 and FS0. At FS0, a large space is required to facilitate the implementation of large ancillary detectors such as GRETA.

5.3.1 Realization of achromatic and dispersive transport modes

Figure 5.3 schematically illustrates how the HTBL realizes both achromatic and dispersive transport modes. To achieve achromaticity at the end of the HTBL, the dispersion created by the first two dipoles (DB1 and DB2) and by the last two dipoles (DB3 and DB4) must cancel each other. This is done by implementing an even number of intermediate foci between dipoles DB2 and DB3. Since it is not feasible to transport the beam without any focus between DB2 and DB3, two foci were created as shown in Figure 5.3(a). Two dispersive sections (TB1-DB1-TB2-DB2-TB3 and TB6-DB3-TB7-DB3-TB8) are connected by a non-dispersive telescope consisting of two triplets TB4 and TB5. The first dispersive section gives rise to a dispersive focus at FB1. The telescope makes the next dispersive focus at FB3, reversing the sign of the dispersion. The momentum tracking can be performed at these dispersive foci FB1 and FB3, as described in the next section. The dispersion accumulated up to this point is cancelled in the second dispersive section, and the target location FS0 becomes a double achromatic $[(x|\delta) = (x'|\delta) = 0]$ focus. At FS0, in addition to point-to-point focusing $[(x|x') = (y|y') = 0]$, parallel-to-parallel imaging $[(x'|x) = (y'|y) = 0]$ is achieved simultaneously, which makes the transport matrix of the entire HTBL almost equal to the identity matrix. Also note that the telescope provides a parallel beam in the non-dispersive direction at FB2, which is necessary for operating an RF Fragment Separator in that location.

To make the HTBL dispersive, on the other hand, it is tuned so that the dispersions created by the four dipole magnets add and accumulate. This is accomplished by providing an odd number of foci between the right-bending DB2 dipole magnet and the left-bending DB3 dipole magnet, as opposed to the even number of foci in the achromatic mode. The simplest solution has only one focus in the middle of the HTBL, in which the upstream dispersive section (TB1-DB1-TB2-DB2-TB3-TB4) and the downstream dispersive section (TB5-TB6-DB3-TB7-DB4-TB8) directly connected to each other as shown in Figure 5.3(b).

5.3.2 Achromatic beam-transport mode

As described in Section 4.3.2.7.1, this achromatic beam-transport mode is designed to optimize the transmission of rare-isotope beams through the HTBL. Figure 5.4 shows first-order beam transport in achromatic mode, and Table 5-3 lists the associated first-order matrix elements. Note that, as mentioned above, the HTBL is not perfectly symmetric in that the space around FS0 is greater than that around FB0. Consequently, the overall magnifications in the horizontal and vertical direction became larger than unity, which in turn made the angular magnifications smaller than unity. The narrow angular profiles near the reaction target are advantageous for experiments such as in-beam γ-ray spectroscopy with GRETA, since its closely-packed detector modules will restrict the aperture diameter of the beam pipe that can be used.
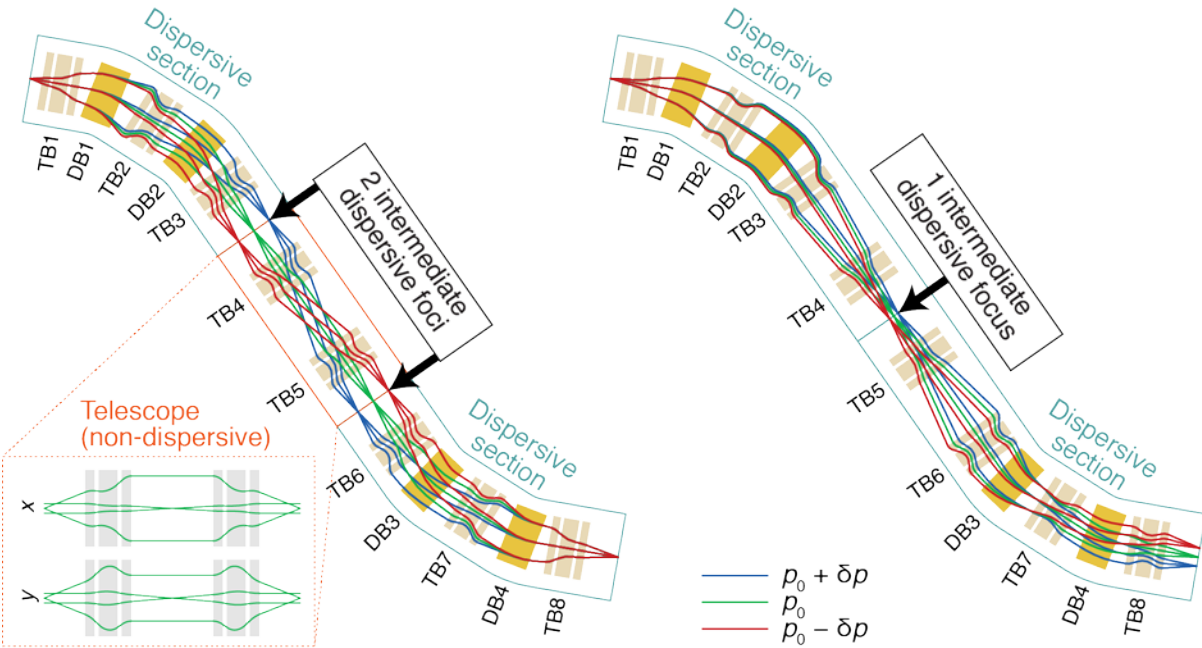
Figure 5.3 This figure schematically illustrates how the HTBL realizes both (a) achromatic and (b) dispersive beam-transport modes. See text for details.

At the location of the dispersive foci FB1 and FB3, it is possible to track the momenta of beam particles by measuring the position deviation with position-sensitive tracking detectors. Momentum tracking is necessary to achieve a momentum resolution that is better than the momentum spread of the beam. The 1st-order ion-optical resolving power in momentum is about 3000 for a beam spot of 1 mm. It is also possible to measure angles at FB1 and FB3 (by using a pair of tracking detectors) to infer the incoming beam angle at FS0, which is necessary in cases where the angular spread of the beam at FS0 determined by the emittance of the rare-isotope beam is larger than the desired angular resolution of the beam.

To understand the detailed properties of the HTBL and to realistically estimate the transmission of the rare-isotope beams through the HTBL, simulations that included the aperture sizes of the magnetic elements and the beam pipe were carried out. These are described in Section 5.4 and employ the same methods as used for the ARIS Fragment Separator.

5.3.3 Dispersion-matching beam transport mode

Figure 5.5 shows the first-order beam transport in dispersive mode, where the lateral and angle dispersions are matched to those of the full Spectrometer Section from FS0 to FS2. Table 5-3 lists the corresponding first-order matrix elements. In order to achieve dispersion matching between the HTBL and the Spectrometer Section, the position and angular dispersions $[(x|\delta)$ and $(x'|\delta)$, respectively] need to match the requirements set by the ion-optical properties of the Spectrometer Section. These conditions for the momentum dispersion are $(x|\delta)_B = -(x|\delta)_S/(x|x)_S$ and for the angular dispersion are $(x'|\delta)_B = (x'|x)_S(x|\delta)_S - (x|x)_S(x'|\delta)_S$, where the matrix elements with

subscripts B and S are for those of the HTBL (from FB0 to FS0) and the Spectrometer Section (from FS0 to FS2), respectively. Due to the large resolving power of the Spectrometer Section $[(x|\delta)_S/(x|x)_S \sim 10]$, the HTBL requires a correspondingly large dispersion $[(x|\delta)_B]$.
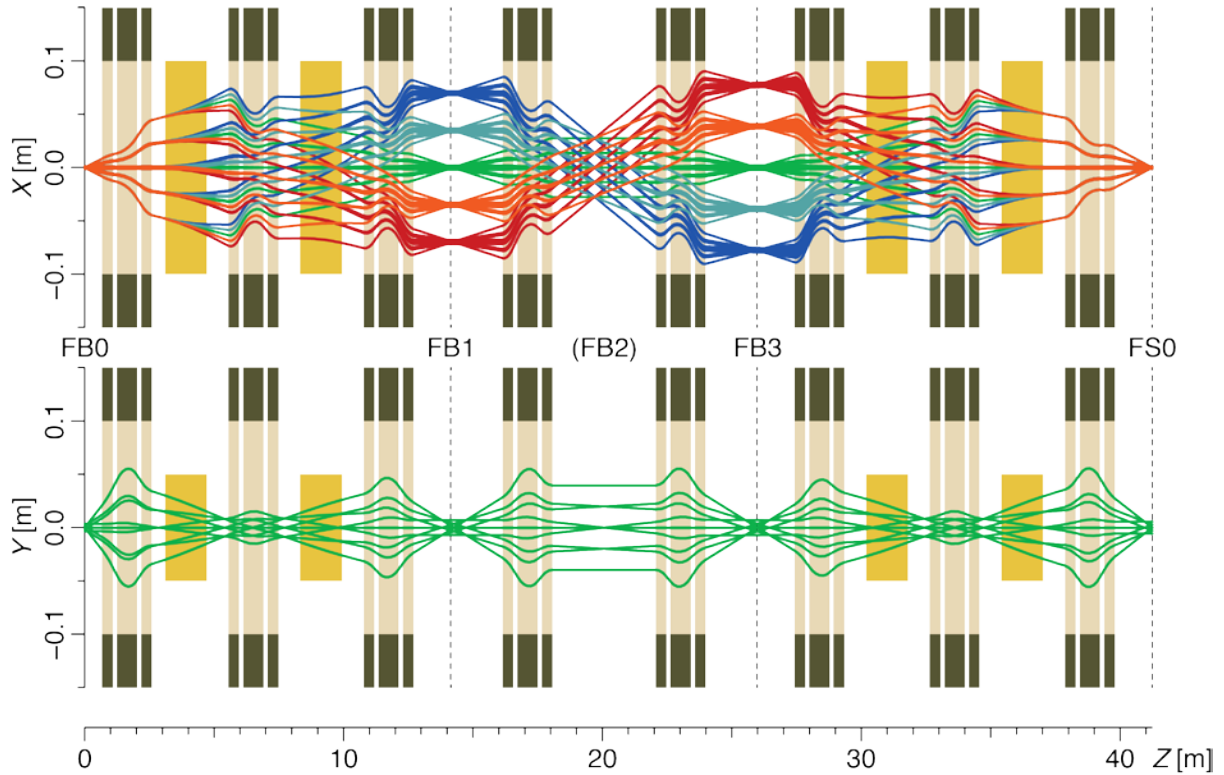
Figure 5.4 Trajectory plots for the achromatic beam transport through the HTBL in the dispersive (top) and the non-dispersive (bottom) planes in first order. The dipole magnets are shown as orange boxes, with their heights representing the good-field regions (±10 cm) and vertical gaps (±5 cm). The quadrupoles (within a triplet) are shown as light-brown boxes, with their heights representing the warm-bore aperture sizes. The dark boxes on both ends extending to the pole-tip radii (15 cm), denote the cryostat vessels in which the sextupole and octupole coils are housed. The ensemble of rays correspond to the phase space of ^{40}Mg coming out from the Reconfigured A1900 of the ARIS Fragment Separator with its optimal settings: $\delta x_{max} = 1.2$ mm, $\delta x'_{max} = 12.5$ mrad, $\delta y_{max} = 3.4$ mm, $\delta y'_{max} = 31.2$ mm, and $\delta p_{max}/p = 1.54\%$ (at 6.68 Tm). The different colors for the dispersive-plane trajectories correspond to the different momenta, which all coincide in the non-dispersive plane in this first-order plot.

Because of this requirement, the beam spot size in the dispersive direction at FS0 (reaction target of the Spectrometer Section) becomes large. For example, for a momentum spread $\delta p/p$ of ±0.5% a beam spot of about ±5 cm is required. It is understood that the transmission efficiency of the dispersive beam transport is compromised due to this expanded beam envelope in this mode. The transmission efficiency depends on the emittance of the rare-isotope beam, and needs to be evaluated on a case-by-case basis. Also note that the large beam-spot size at FS0 may affect the placement and use of ancillary detectors.

In this mode, high momentum resolution can be achieved without momentum tracking of the beam particle. Therefore, the use of tracking detectors at the dispersive foci FB2 and FS0 is, in general, not foreseen during experiments, although for specific applications in which precise information about the absolute angle at the target is needed, it is an option. However, if it is required to know the angle and position of the beam accurately on an event-by-event basis at FS0, tracking just prior to FS0 can be performed.

The dispersion-matched beam transport of the HTBL is also used for ToF-$B\rho$ mass measurements (see Section 4.3.1.5). The entire HRS (the HTBL and the Spectrometer Section) becomes doubly achromatic, and the magnetic rigidity ($B\rho$) is determined by measuring the position with tracking detectors installed at the dispersive focus FS0. By combining the Reconfigured A1900 of the ARIS Fragment Separator (40.14 m), the HTBL (41.24 m), and the Spectrometer Section (33.62 m), a total flight-path length of 115 m is created, which meets the requirement that the flight-path length be greater than 90 m.

Similar to the achromatic mode, end-to-end simulations that include the aperture sizes of the magnetic elements and the beam pipe components were carried out for the dispersion-matched beam-transport mode, which are described in Section 5.4.

The use of dispersion-matched beam transport is useful for unreacted-beam rejection, because the beam will be well localized at the focal plane where the dispersion-matching is done.When the full Spectrometer Section is dispersion-matched as described above, the unreacted beam comes into a sharp focus at FS2, where the beam can be blocked with variable slits. The HTBL can also be tuned such that it dispersion-matches the Spectrometer Section from FS0 to FS1 only (i.e. partial dispersion matching). In this case the matching conditions are different from those for the full dispersion-matching case, and accordingly the beam transport is different from what is shown in Figure 5.5. Depending on the difference between the rigidity of the reaction product of interest and that of the beam, the partial dispersion matching may be beneficial because by blocking the beam at the intermediate focus FS1, one can keep the intense beam from reaching to the final focus without having to intercept the desired reaction products, and prevent possible background counts on the focal-plane detectors by stopping the beam far upstream. The present layout of the HRS allows for the flexibility to choose the best point to intercept the beam depending on the specific experimental conditions.
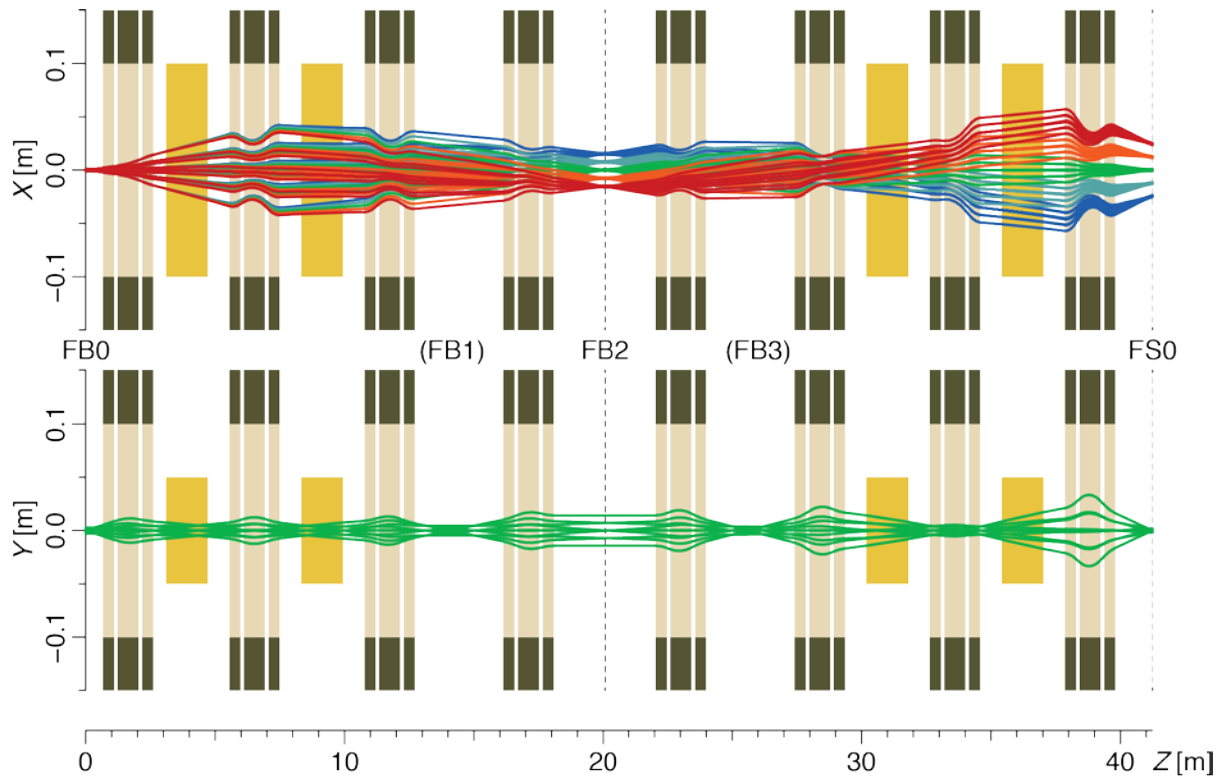
Figure 5.5 Same as Figure 5.4 but for the dispersion-matched beam transport through the HTBL. The ensemble of trajectories correspond to the phase space of ^{204}Pt from the ARIS Fragment Separator: δx_{max} = 1.0 mm, $\delta x'_{max}$ = 3.2 mrad, δy_{max} = 2.9 mm, $\delta y'_{max}$ = 8.0 mrad, and $\delta p_{max}/p$ = 0.25% (at 3.98 Tm).

Table 5-3 First-order matrix elements of the HTBL in the achromatic beam-transport mode and in the dispersion-matched beam-transport mode. Only the ten non-trivial matrix elements are listed

		Achromatic			Dispersion-matched	
		FB1	FB3	FS0	FB2	FS0
$(x\|x)$	$= R_{11}$	-1.57	1.75	-0.96	−0.89	0.99
$(x\|x')$ [m/rad]	$= R_{12}$	0.05	0.00	0.00	0.01	0.00
$(x'\|x)$ [rad/m]	$= R_{21}$	-0.03	0.04	0.04	−0.53	−0.01
$(x'\|x')$	$= R_{22}$	-0.64	0.57	-1.04	−1.12	1.01
$(x\|\delta)$ [m]	$= R_{16}$	4.53	-5.03	0.00	6.49	−10.31
$(x'\|\delta)$ [rad]	$= R_{26}$	0.00	0.04	0.00	0.23	3.80
$(y\|y)$	$= R_{33}$	2.06	-2.07	-1.65	−0.08	−0.70
$(y\|y')$ [m/rad]	$= R_{34}$	-0.06	0.01	0.00	1.78	0.00
$(y'\|y)$ [rad/m]	$= R_{43}$	0.00	0.04	-0.01	−0.56	−0.47
$(y'\|y')$	$= R_{44}$	0.49	-0.48	-0.61	0.00	−1.42

5.3.4   Angular and momentum acceptance

The angular and momentum acceptances of these two beam transport modes were evaluated by means of Monte-Carlo simulations. In these simulations, first-order transfer matrices obtained in

100

COSY INFINITY were loaded in LISE^{++}, with the warm-bore aperture sizes for the quadrupoles, the good-field regions in the dispersive plane, and the vertical gap sizes in the non-dispersive plane for the dipoles taken into account. Transmitted from a point source at FB0, beam particles that had a sufficiently large phase space (momentum and angles) distribution were transported through the HTBL, and only those that reached FS0 are included in Figure 5.6. Here, uniform distributions were used for simplicity. The beam envelopes depicted are shown in the top panels for both the dispersive and non-dispersive planes, while the bottom panels show the correlations between the momentum and the angles at FB0, which represent the angular and momentum acceptances of the HTBL. In the achromatic beam-transport mode, the angular acceptances are $\Delta x' = \pm 20$ mrad and $\Delta y' = \pm 52$ mrad, and the momentum acceptance is $\Delta p/p = \pm 2\%$, and in the dispersion-matched beam-transport mode, they are $\Delta x' = \pm 9$ mrad and $\Delta y' = \pm 24$ mrad, and $\Delta p/p = \pm 0.7\%$
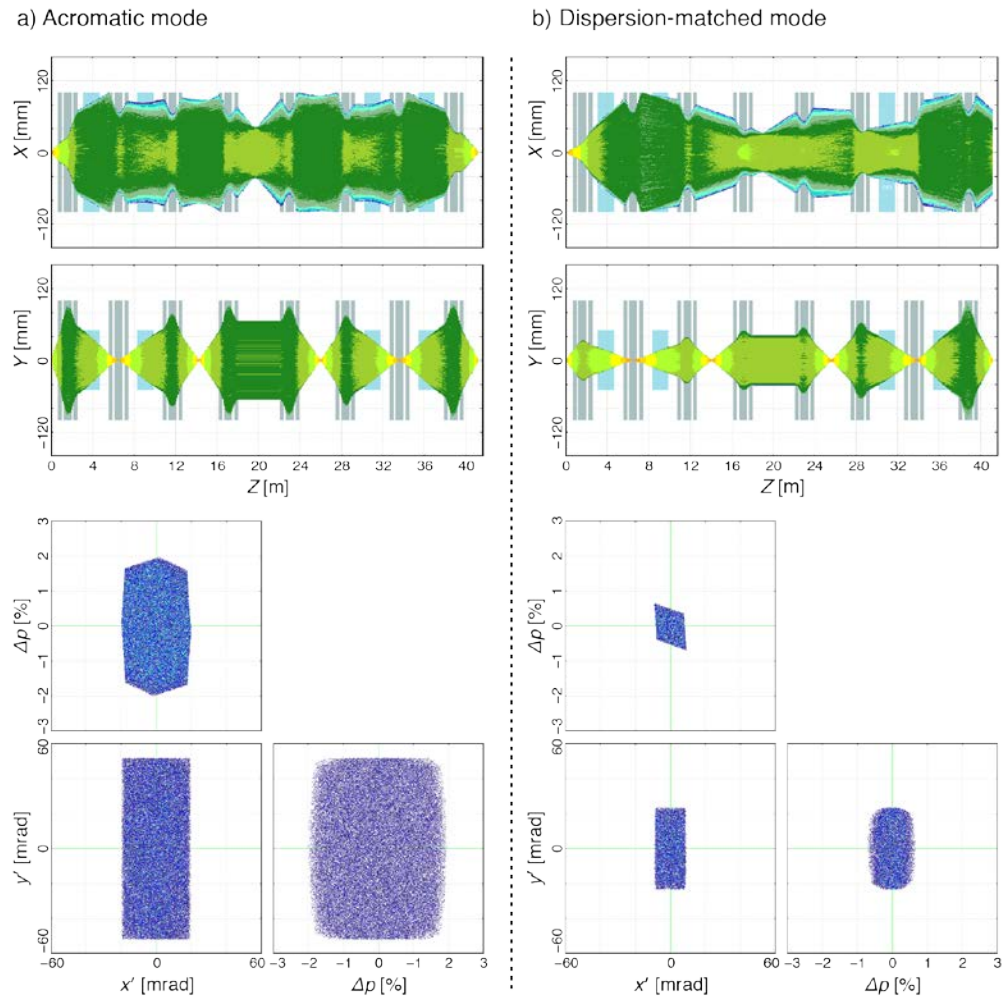
Figure 5.6 Envelopes (top), and angular and momentum acceptances (bottom) for (a) the achromatic and (b) the dispersion-matched beam-transport modes of the HTBL as simulated in LISE++, by using the first-order transfer matrices obtained from COSY INFINITY.

5.3.5 Ion-optical calculations at higher orders

For the HTBL, it is important to keep the higher-order aberrations in the beam transport under control by using hardware correctors such as sextupole and octupole coils. As opposed to the spectrometer proper downstream of the reaction target where higher-order corrections can be done by software (as are done for the S800 Spectrograph), the efficacy of software corrections before the reaction target is limited. As shown in Figure 5.7, where calculations up to 5th order in COSY INFINITY with and without the correctors are compared for the achromatic beam-transport mode, the higher-order aberrations do not significantly impact the transmission efficiency through the HTBL and the beam spot size at the target location is small even without the hardware corrections.
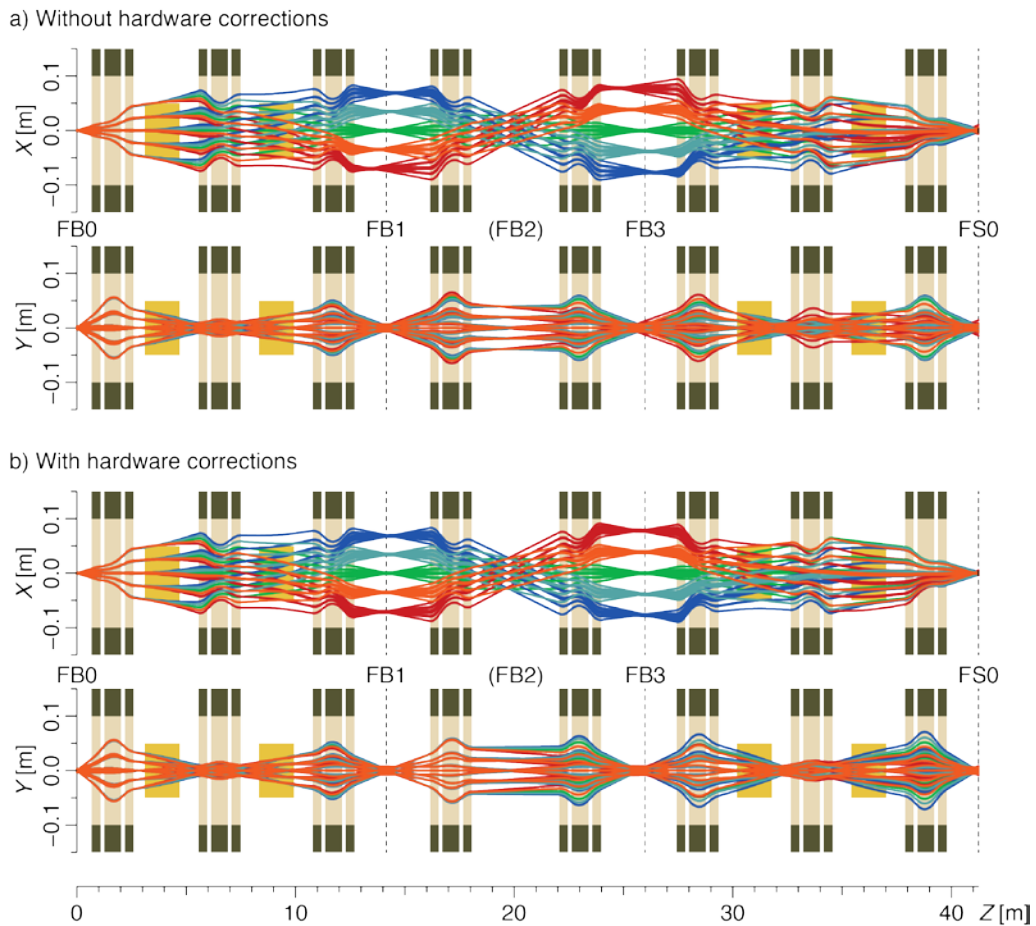
Figure 5.7 Trajectory plots for the achromatic beam-transport mode of the HTBL up to and including 5th order. The ensemble of trajectories correspond to the same phase space as shown in Figure 5.4. Panel a) provides the trajectories without hardware corrections (sextupole and octupole coils embedded on the quadrupoles). For panel b) these coils were adjusted to minimize higher-order aberrations.

This is due to the symmetric configuration of the HTBL, which cancels some of the higher-order terms. However, it should be noted that without hardware corrections, the intermediate foci are tilted, which deteriorates the resolution of the momentum tracking at these locations. These must be corrected as in Figure 5.7(b) so that precision of the momentum tracking is not compromised. This also applies to the dispersion-matched beam transport mode.

Here, the field profiles from quadrupole triplet field measurements were used. Even without the hardware correctors (Figure 5.7a), the higher-order aberrations are not large, due to the symmetric design of the HTBL, and do not cause significant transmission losses. However they cause inclinations of the dispersive foci at FB1 and FB3 and an increased beam spot size at FS0, which would result in deteriorated resolutions in momentum tracking of the beam or in reaction analysis in the Spectrometer Section. These aberrations can almost completely be corrected by the corrector coils, as shown in Figure 5.7b. The effects above the 6th order are insignificant, and those for the dispersion-matched mode are not large and can be corrected in the same way.

5.4 End-to-end simulations

To ensure that the requirements listed in Table 5-2 are met, comprehensive end-to-end simulations were performed by using the RIB-specific output of the ARIS Fragment Separator at FB0 as input to the HTBL and tracked through to the Spectrometer Section production target at FS0. The beams used for these studies were chosen based on the scientific program of the HRS as discussed in Section 4.3.2.2 and listed in Table 4-5. These beams are listed in Table 5-4, which provides the phase spaces of the beams at the end of the ARIS Fragment Separator (FB0). Of the beams produced by in-beam fragmentation (^{40}Mg, ^{60}Ca, ^{100}Sn, ^{140}Sn, and ^{204}Pt), ^{40}Mg has the largest phase space. However, its phase space is still significantly smaller than that of ^{84}Ni, which is produced by in-flight fission. For detailed Monte-Carlo studies, the third-order transport matrices calculated in COSY INFINITY of the ARIS Fragment Separator and HTBL were loaded into the LISE^{++} [BAZ02,TAR08,TAR16] program. As has been already mentioned, the excitation dependence of the effective lengths of magnetic fields of the quadrupoles is included in these calculations. The detailed physical aperture sizes of the beam lines, magnet bores and dipole gaps were taken into account when estimating the transmissions.

Table 5-4 Rare-isotope beam phase spaces at the end of the ARIS Fragment Separator (FB0) obtained from Monte-Carlo Simulations in LISE^{++}. The dimensions shown in the table are $\pm 2\sigma$ values.

RIB (production mechanism)	x [mm]	x' [mrad]	y [mm]	y' [mrad]	$\delta p/p$ [%]
^{40}Mg (fragmentation)	±1.2	±12.5	±3.4	±31.2	±1.54
^{60}Ca (fragmentation)	±1.0	±12.8	±1.7	±32.6	±1.44
^{84}Ni (in-flight fission)	±1.0	±20.5	±1.7	±63.3	±1.6
^{100}Sn (fragmentation)	±0.7	±9.5	±3.4	±10.3	±0.6
^{140}Sn (fragmentation)	±1.0	±6.8	±2.0	±16.9	±1.0
^{204}Pt (fragmentation)	±1.0	±3.2	±2.9	±8.0	±0.25
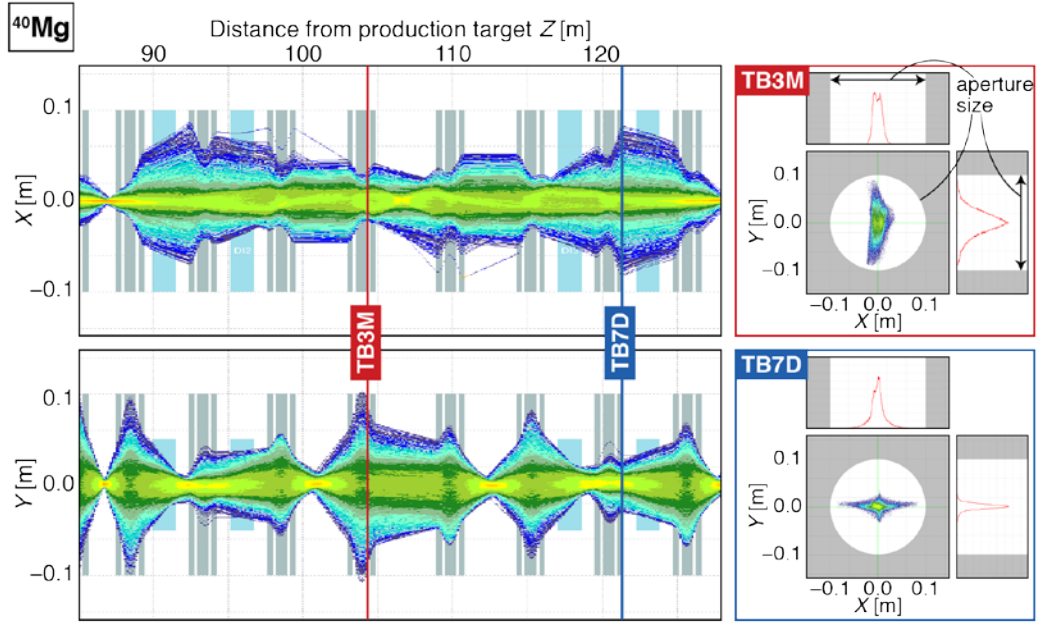
Figure 5.8 Results of end-to-end Monte-Carlo simulation for the transport of a ^{40}Mg rare-isotope beam performed in LISE^{++} by including up transport matrix elements up to 3rd order. Only the HTBL is shown in the figure. The left-top (bottom) panel displays the Monte-Carlo simulated profiles in the horizontal (vertical) planes. Dipole magnets are indicated in blue and quadrupole elements (with their sextupole and octupole coils) are indicated in grey. The right-top (bottom) panel displays the x-y image and its projection onto both axes with the aperture sizes at the exit of the TB3M (TB7D) quadrupole.
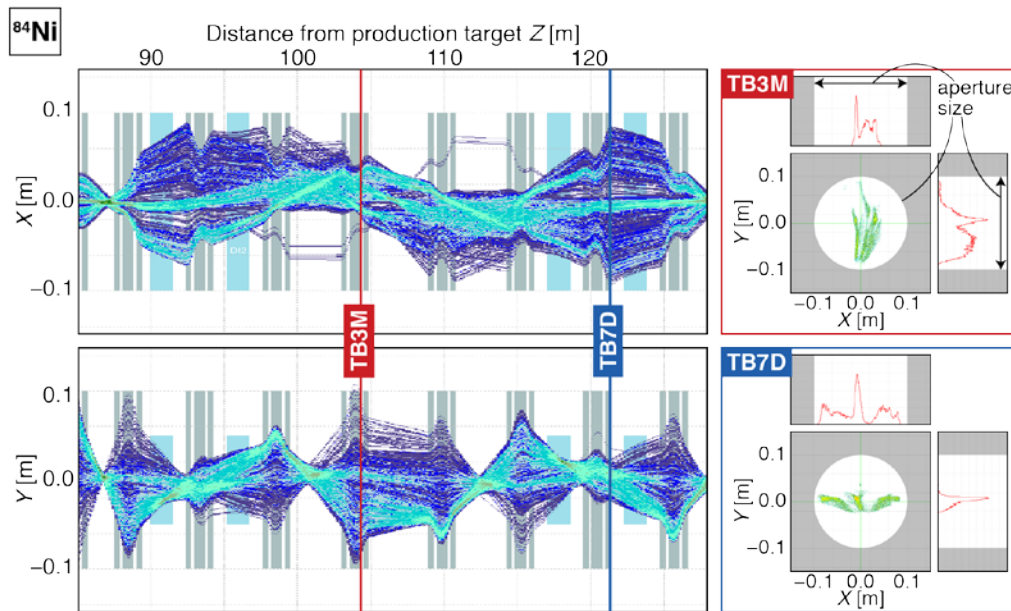
Figure 5.9 Same as Figure 5.8, but for a ^{84}Ni beam. Note that, since ^{84}Ni is produced by in-flight fission, the shape of the x/y distribution is not a simple bell-shaped curve, as can be seen on the right panels.

104

For each of the beams, elements of and transport through the ARIS fragment separator were optimized to achieve the highest production rate with a reasonable purity in a similar fashion as would be done in preparation of a real experiment, resulting in the phase spaces provided in Table 5-4. As examples of the Monte-Carlo simulations, the results for the case of ^{40}Mg and ^{84}Ni are shown in Figure 5.8 and Figure 5.9, respectively. Although not shown in these figures, these simulations included the transport to the Preseparator and Reconfigured A1900 stages (which together make up the ARIS Fragment Separator), so that the details of the transport through these stages are included in the transmission through the HTBL, rather than parametrizing the phase space at the entrance of the HTBL.

The main results of the Monte-Carlo simulations for each of the representative beams of Table 4-5 in achromatic beam-transport mode through the HTBL are provided in Table 5-5. Besides the transmission (in the final column), this table also provides the basis parameters for the production of each of the rare-isotope beams. The transmission is from the end of the ARIS fragment separator (FB0) until the end of the HTBL (FS0), which is the location of the reaction target of the Spectrometer Section. For all the six representative beams, the transmission efficiencies through the HTBL are 100%.

Table 5-5 Overview of the results from the end-to-end Monte-Carlo Simulations performed in LISE^{++} for the transmission in achromatic beam-transport mode and dispersion-match transport mode of the six representative rare-isotope beams of Table 4-5. Except for the case of ^{84}Ni, which is produced through in-flight fission, all beams are produced by in-flight fragmentation. The primary beam, production target, momentum acceptance in the Preseparator (prior to momentum compression), degrader, and rigidity used in the simulations are shown in columns 2, 3, 4, 5, and 6, respectively. The last two columns give the transmission of the rare-isotope beam from FB0 (the end of the ARIS fragment separator) to FS0 (the location of the reaction target at the end of the HTBL) for each of the transport modes

RIB	Primary Beam	Target thickness (Carbon)	Momentum acceptance achromatic/ dispersion matched	Al Degrader thickness	Magnetic Rigidity of HTBL	Transmission Achromatic transport	Transmission Dispersion-matched transport
^{40}Mg	^{48}Ca, 239.5 MeV/u	11 mm	±5%/±0.5%	4.1 mm	6.68 Tm	100%	82%
^{60}Ca	^{82}Se, 236.6 MeV/u	5.87 mm	±5%/±0.5%	2.5 mm	5.94 Tm	100%	81%
^{84}Ni (fission)	^{238}U, 202 MeV/u	1.35 mm	±5%/±0.5%	2 mm	5.80 Tm	100%	TBD
^{100}Sn	^{112}Sn, 242.4 MeV/u	3.6 mm	±3.3%/±0.5%	1 mm	3.72 Tm	100%	96%
^{140}Sn	^{160}Gd, 218.5 MeV/u	2.9 mm	±5%/±0.5%	1.5 mm	4.89 Tm	100%	98%
^{204}Pt	^{208}Pb, 209.9 MeV/u	1.8 mm	±1.55%/±0.5%	2 mm	3.98 Tm	100%	100%

End-to-end simulations in LISE^{++} were also performed for the dispersion-matched transport for the case of ^{204}Pt. For the limited momentum acceptance of ±0.5% corresponding to a beam-spot size of target of about ±5 cm, the transmission to FS0 (location of the reaction target at the end of the HTBL) is 100%. For the lighter beams, the transmission in the dispersion-matched transport is lower, owing to the larger beam emittances. The transmission in dispersion-matched transport

mode for the case of ^{84}Ni, produced by fission, will require further study and optimization and, therefore, listed as "To be determined".

The Monte-Carlo simulations are also helpful for estimating the properties of the beam and the requirements for tracking detectors placed along the HTBL. To illustrate this for the achromatic mode, the left panel of Figure 5.10 shows the correlation between momentum and position at FB1 (location of the first tracking stations in the HTBL) for a ^{40}Mg rare-isotope beam. The strong correlation between momentum and position at FB1 makes it possible to determine the momentum of the incoming beam particles from the measurement of the position at FB1. The right panel of Figure 5.10 shows the correlation between the dispersive position at FS0 and the dispersive angle at FB0. The upright locus indicates that point-to-point focus is achieved $[(x|x') = 0]$ at this location in the dispersive plane. This illustrates an example of a measurement of transfer-matrix elements with which the beam transport is established. Figure 5.11 shows the correlation between momentum and position/angle at the reaction target FS0 at the end of the HTBL for a ^{204}Pt beam transported through the HTBL operated in dispersion-matched beam-transport mode. The lateral and angular dispersion at the target, which corresponds to the slant of the locus of the correlation, matches that of the Spectrometer Section, thereby enabling the dispersion-matching technique necessary for performing a subset of the experiments with the HRS.
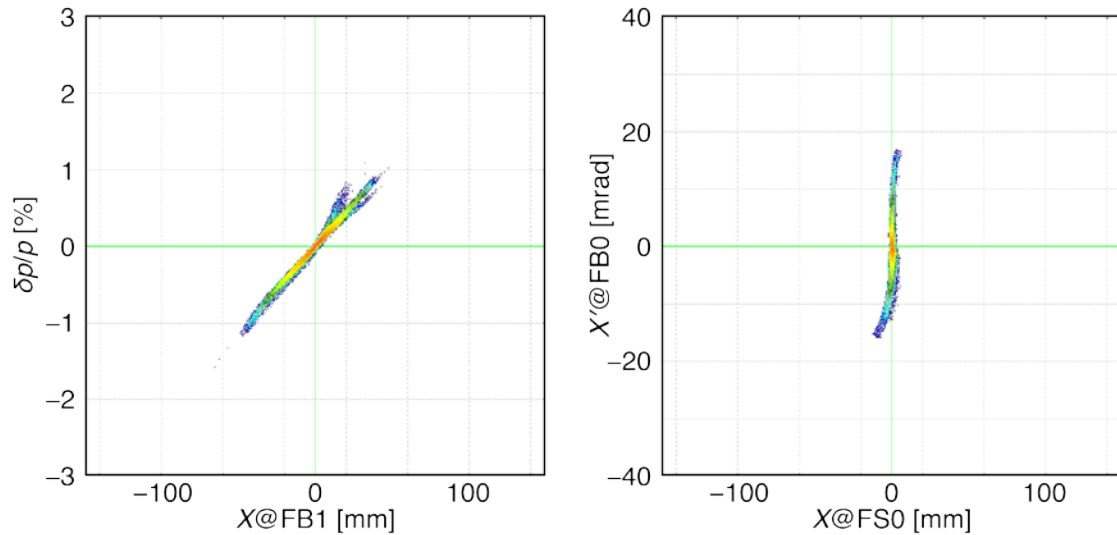
Figure 5.10 (left) Correlation between momentum deviation (relative to the momentum of the central ray) and position (x) in the dispersive plane at FB1 for a 40Mg rare-isotope beam as simulated in LISE^{++} in 3rd order. The strong correlation makes it possible to determine the momentum of beam particles by measuring the location in a tracking detector placed at FB1. (right) Correlation between angle at FB0 (x') and position (x) at FS0 for the ^{40}Mg rare-isotope beam. The (inverse of the) slant corresponds to the transfer-matrix element $R_{12} = (x|x')$, and the upright locus indicates that point-to-point focus is achieved $[(x|x') = 0]$ at this location in the dispersive plane.
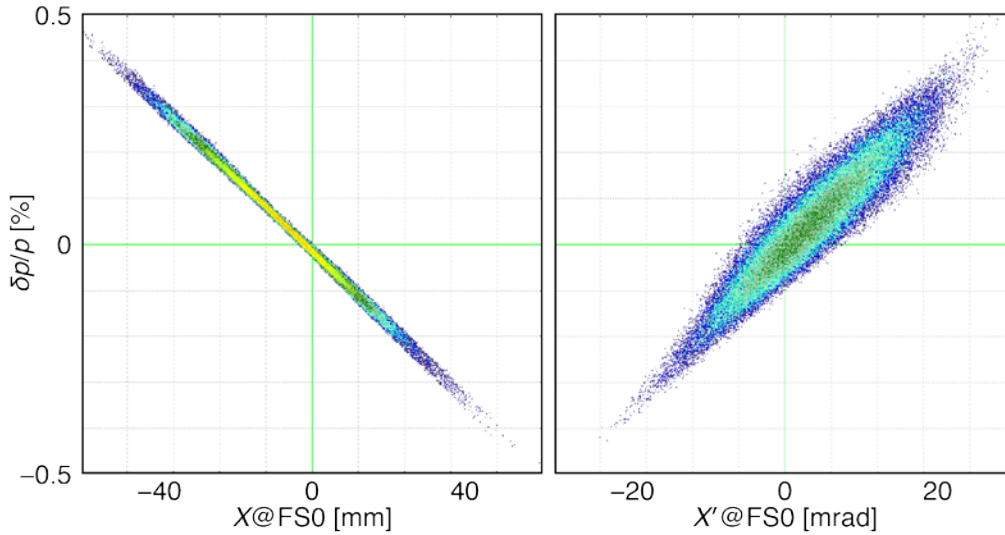
Figure 5.11 (left) Correlation between momentum deviation (relative to the momentum of the central ray) and position (x) in the dispersive plane at the reaction target at FS0 (end of HTBL) for a ^{204}Pt beam transported in dispersion-matched beam transport mode. (right) Same as left, but with angle (x') instead of position. The slants of these correlations correspond to the transfer-matrix elements R_{16} = -103 mm/% and R_{26} = 38.0 mrad/%. The broader locus of the right panel is due to the initial angular spread of the beam, unlike the position that has a narrower locus because of the small beam spot at production target, and hence at FB0.

5.5 Preferred HTBL alternative meets requirements

The capabilities of the HTBL afforded by the preferred ion-optical alternative with regard to the scientific requirements described in Section 5.2 are summarized as follows.

1. The preferred ion-optical alternative is feasible at the required maximum magnetic rigidity of 8 Tm.

2. As demonstrated in the end-to-end simulations, the transmission efficiencies through the HTBL exceeds the required 95% for all the six representative rare-isotope beams.

3. Both achromatic and dispersive beam-transport modes are available, and the latter realizes the full dispersion matching to the Spectrometer Section.

4. The flight-path length of the HTBL is 41.24 m, and when combined with the Reconfigured A1900 of the ARIS Fragment Separator (40.14 m) and the Spectrometer Section (33.63 m), it provides a 115-m long flight path for ToF-$B\rho$ mass measurements, meeting the 90-m requirement.

5. From the start of the HTBL to an intermediate focus FB1, with the horizontal magnification of $M_x = (x|x) = -1.57$ and the dispersion $D_x = (x|\delta) = 4.98$ m, the momentum resolving power is 2000 for a beam spot of $\delta x_{image} = 1.41$ mm (FWHM) and the resolution of position determination of $\delta x_{fp} = 1$ mm (FWHM) at FB1, which exceeds the required momentum resolving power of 1500. Also, the angular magnifications of $(x'|x') = 0.61$ and $(y'|y') = -0.80$, the incoming angle at the reaction target can be inferred with a resolution of 4 mrad (FWHM), which exceeds the required 5 mrad (FWHM) for the resolution of angular

determination of 2 mrad (FWHM) at FB1. These numbers are similar at the other intermediate focus FB3. Measurements at FB1 and FB3 could be combined to get an even more precise determination of the momentum and angle.

6. The HTBL can accommodate an RFFS with a length of 2.6 m as well as associated steering magnets at FB2 as shown in Figure 5.12. The beam is parallel in the non-dispersive plane at FB2 both in achromatic and dispersive beam-transport mode, which is suited for the operation of an RFFS.

5.6 Technical specifications for the HTBL

This section describes the specifications of technical components to realize the beam transport modes in the HTBL. The specifications of the magnetic elements are given in Section 5.6.1, those of the diagnostics and detectors are given in Section 5.6.2, and those of the vacuum systems are given in Section 5.6.3.

5.6.1 Magnetic elements

5.6.1.1 Quadrupole triplets

All the eight quadrupole triplets are of the same design. The triplet used in the HTBL consists of three quadrupoles that have short (upstream), long (middle), and short (downstream) field lengths, where the up- and downstream quadrupoles are identical. All the three quadrupoles must have embedded sextupole and octupole coils to correct for higher-order aberrations as discussed in Section 5.3.4. Detailed specifications are summarized in Table 5-6.

Table 5-6 Specifications of the two types of the quadrupole magnets used in the HTBL. Each quadrupole has embedded sextupole and octupole coils. These triplets are labeled TB1-TB8 in Figure 5.1.

Label	FSQB	FSQC
Quantity (in 8 quadrupole triplets)	16	8
Effective field length (nominal) (m)	0.40	0.79
Pole-tip radius (m)	0.15	0.15
Warm-bore radius (m)	0.10	0.10
Quadrupole maximum field strength (T@poletip)	2.50	2.50
Quadrupole good-field region radius (m)	0.10	0.10
Field quality (% not quadrupole)	1%[#]	1%[#]
Sextupole maximum field strength (T/m^2)	10	10
Octupole maximum field strength (T/m^3)	50	50

[#]: *Sum of all non-quadrupole components, relative to the quadrupole amplitude, evaluated at 80% of the warm-bore radius at maximum excitation.*

One of the three types of the quadrupole triplets that are presently used in the A1900 Fragment Separator and will be used for the Reconfigured A1900 of the ARIS Fragment Separator satisfies the specifications given in Table 5-6. Therefore, these quadrupole triplets will be identical to the A1900 triplet, as described in Section 9.4.1. It is regarded as a natural choice because it matches the phase space of rare-isotope beams delivered from the ARIS Fragment Separator in which the same magnet design is used. The measured field data of these triplets were included in detailed

ion-optical models, the calculations presented in Sections 5.3 and 5.4 utilized them to emulate all effects, such as the dependence of the effective length on the field gradient magnitude.

Initial estimates of the necessary field quality were that an integrated field non-uniformity (sum of all non-quadrupole components) of better than 1% be achieved. To assess the effects of the field quality on the ion optics, 3D field profiles extracted from actual field mapping of an existing triplet have been included in the calculations in COSY INFINITY up to 5th order. It was verified by these calculations that the designed ion-optical properties could be realized by employing the existing triplet design.

5.6.1.2 Dipole magnets

All the four dipole magnets are of the same design. They are rectangular magnets whose entrance and exit pole faces are rotated by half the bending angles. The use of rectangular magnets optimizes the beam delivery to the other experimental areas of FRIB as discussed in Section 5.2, which does not negatively impact the beam transport in the HTBL. The specifications are listed in Table 5-7.

Table 5-7 Specification of the dipole magnets used in the HTBL. These dipoles are labeled as DB1-DB4 in Figure 5.1.

Label	DBx (x = 1, 2, 3, 4)
Quantity	4
Bending radius (m)	4.10
Maximum rigidity (Tm)	8.0
Maximum field (T)	~2.0
Bending angle (deg)	22.5
Arc length for central ray (m)	1.61
Vertical gap size (m)	±0.05
Good field region (m)	±0.10
Field quality (% not dipole)	0.5#
Pole-face rotation entrance (deg)	11.25
Pole-face rotation exit (deg)	11.25

\# Preliminary estimate

As will be described in Section 9.4.2, the actual implementation of these dipoles is based on this Transfer-Hall dipole, but scaled to a higher rigidity.

5.6.1.3 Steerer dipole magnets

The design of the HTBL includes two vertically-steering dipole magnets, SB1 and SB2, as indicated in Figure 5.1. The upstream steerer (SB1) adjusts the beam centroid at the middle of the HTBL (FB2), and the downstream steerer (SB2) adjust the trajectory to the reaction target location (FS1). The magnitude of the first-order matrix element $(y|y')$ is about 1 for both from SB1 to FB2 and from SB2 to FS0. To be able to adjust the beam centroid by 10 mm at FB2 and FS0, a 10-mrad vertical angle deflection at the steerer location is required. The current design of these steerers has a length of 40 cm, which corresponds to a bending radius of 40 m. For a rigidity of 8 Tm, the required field strength is 0.2 T. These are normal-conducting magnets, as opposed to the

superconducting dipoles DB1—DB4. The specifications for the steerer magnets are provided in Table 5-8.

Table 5-8 Specification of the steerer dipole magnets used in the HTBL. These steerer dipoles are labeled as SB1 and SB2 in Figure 5.1.

Label	SBx (x=1or 2)
Quantity	2
Length (m)	0.40
Gap size (m)	±0.10
Maximum Rigidity (Tm)	8
Maximum deflection angle (mrad)	10
Maximum field (T)	0.20

The specifications for the long-term current stability of the power supplies for these magnetic elements of the HTBL, including the room-temperature steerer dipole magnets, follow those of the FRIB Experimental Systems Division [FRIB-T31209-SP-000152].

5.6.2 Diagnostics and detectors

The goals of HTBL diagnostics & detector system are defined as follows:

- To facilitate initial commissioning of the HRS,
- To facilitate tuning prior & during experiments by enabling characterization of beam properties and transmission efficiency,
- To provide event-by-event tracking & timing information for physics analysis, and
- To enable long-term stable operation & provide appropriate machine protection.

To achieve these goals, the specifications for the diagnostics and detectors have been formulated as described in this section.

As shown in Figure 5.1, the preferred alternative of the HTBL contains two primary diagnostic stations, located at FB1 and FB3. These stations contain a variety of systems to diagnose the properties of the rare-isotope beam and to provide event-by-event tracking capability for the experimental program. The following provides a brief summary of the required diagnostics systems for the HTBL. These systems are selected based on nearly two decades of experience with tuning beam of rare isotopes from the A1900 fragment separator to the existing spectrometers at NSCL and are further detailed in Section 7.

- FB1, FB2, and FB3 must contain simple beam viewer systems with corresponding cameras that provide immediate visual feedback for beam tuning
- FB1 and FB3 must contain a set of fast position detectors that provide event-by-event position and angle information
- FB1 and FB3 must contain plastic scintillator timing detectors that provide event-by-event timing measurement for beam-particle identification
- In addition, FB3 must be equipped with an energy loss detector appropriate for beam-particle identification. This is not only useful for regular beam-tuning purposes, but also crucial for tuning and diagnosing the operation the RF Fragment Separator (see Section 4.3.2.7.3) in the future.

It should be noted that, depending on the requirements for a particular experiment, timing, position and angular tracking might be required just prior to the reaction target at FS0. Therefore, a beam viewer, tracking detectors and a fast timing detector should be available for FS0 as well. Figure 5.13(a) shows a schematic layout of the detector configuration of the diagnostic systems used at FB1/FS0, and Figure 5.13 (b) shows the layout at FB3, including variable slits and an energy-loss detector.
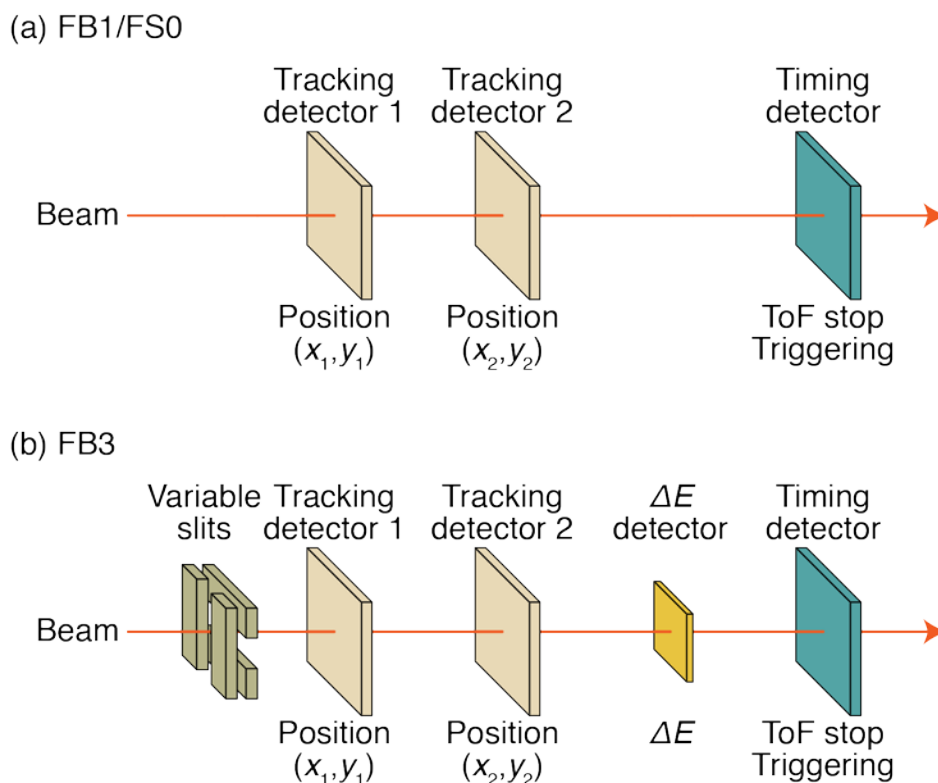
Figure 5.13 Schematic layout of the detector configuration of the diagnostic systems used at (a) FB1/FS0 and (b) FB3.

The properties of the position tracking detectors are determined by the need to achieve a sufficiently accurate determination of the momentum and angle of the incoming rare-isotope beam. The main requirement is a momentum resolving power of 1500 (See Table 4-4). This means that in achromatic beam-transport mode, the momentum of the incoming beam must be determined with a significantly better resolution so as not to limit the resolving power of the measurements in the Spectrometer Section. Based on the ion-optical properties of the HTBL shown in Table 5-3, and realistic beam dimensions (see Table 5-4) at the entrance of the HTBL, a momentum resolving power of ~2000 can be achieved with a position resolution of 1 mm (FWHM) in a tracking detector placed at FB1 or FB3. This is sufficient not to limit the momentum resolution of the measurement in the Spectrometer Section. Momentum tracking in both the FB1 and FB3 boxes can be combined to further improve the resolving power of the beam-momentum tracking. In addition, position and

angle tracking detectors, as well as a timing detector, can be installed just prior to the reaction target at FS0, depending on the needs of a particular experiment. Momentum tracking in both the FB1 and FB3 chambers is also important during the tuning of the beam transport, especially since correlations between the beam properties at each location can be studied.

When event-by-event tracking needs to be performed, the maximum intensity of the rare-isotope beams is limited by the rate capabilities of the tracking detectors. Therefore, fast tracking detectors must be employed that can operate at rates of at least several hundred kHz. Timing measurements should be performed at rates that exceed 1 MHz with a resolution of better than 150 ps.

Based on extensive experience with energy-loss detectors for particle identification, the energy loss detector in FB3 should achieve an energy resolution of better than 3% for α particles of 5.5 MeV. Note that these energy-loss detectors are only used during beam characterization and not during regular data taking for experiments. Therefore, they do not need to be operated at high beam rates.

All detectors used in the HTBL should be sufficiently large to cover the transverse beam profiles at their locations. Although the beam envelopes at FB1 and FB3 are relatively small in the vertical direction, the tracking detectors should accommodate larger envelopes that might be encountered in the beam tuning. Therefore, the dimensions in the horizontal and vertical directions of the tracking detectors are chosen to be 20×20 cm^2. The energy-loss detector in FB3 must cover an area of 20×5 cm^2.

The diagnostics and detector systems installed in FB1 and FB3 must be retractable. All detectors will be read out through data acquisition systems that run Laboratory-supported data-acquisition software. For machine protection purposes, near the location of FB1 a beam blocker and a wall-plug must be installed, which are similar to such devices used at NSCL, to safely intercept the rare-isotope beams prior to entering the HRS experimental areas.

The technical requirements for the diagnostics and detector systems of the HTBL are summarized in Table 5-9 for the general detector system requirements. Table 5-10 shows the requirements for the viewers used in the HTBL, Table 5-11 the requirements for the tracking and timing detectors, and Table 5-12 the requirements for the energy-loss detectors in the HTBL.

Table 5-9 General detector system requirements for the HTBL

Parameter	General Detector System Requirement
Remotely retractable	Yes
Positioning accuracy	≤ 0.5 mm (transverse to the beam) ≤ 1 mm (along the beam axis)
Accessibility	Replacement possible within < 4 hours
Vacuum requirement	10^{-5} Torr vacuum compatible

Table 5-10 Viewer system requirements for the HTBL

Parameter	Viewer System Requirement
Single particle detection	No
Transmission	No
Coating	Thin luminescent layer: emits light when exposed to heavy ion beam
Effective area	20×20 cm^2 (with fiducials for calibration)

Table 5-11 Tracking and timing detector requirements for the HTBL

Parameter	Tracking/Timing Detector Requirement
Transmission	100%
Single particle detection	Yes
Thickness	Tracking ➔ ≤ 10 mg/cm^2 Timing ➔ ≤ 100 mg/cm^2
Effective area	Tracking ➔ 20x20 cm^2 Timing ➔ 20x20 cm^2
Resolution (FWHM)	Position ➔ ≤ 1 mm Timing ➔ ≤ 150 ps
Rate capability	Tracking ➔ ≥ a few hundred kHz Timing ➔ ≥ 1 MHz

Table 5-12 Energy-loss detector requirements for the HTBL

Parameter	ΔE Detector Requirement
Transmission	100%
Effective area	5×5 cm^2 each (with fiducials for calibration) 4 aligned detector for 20x5 cm^2 coverage
Thickness	≤ 500 µm
Energy resolution	≤ 3% (@ 5.5 MeV α-particles)
Rate capability	≥ 1000 Hz

5.6.3 Vacuum systems

With the lattice design of the HTBL established, the locations of the magnet are fixed on the floor layout with the conceptual designs of the magnets complete, the dimensions of the vacuum chambers (beam pipes) have been identified. Also, with the standard sets of diagnostic instruments defined, the dimensions of the diagnostic chambers have been identified.

The general requirement for the standard vacuum systems for the HTBL is that the systems be able to evacuate to the pressure of 10^{-5} Torr (see also Section 6.5.3). At this level, the lateral, angular, and energy spreads due to interactions with residual gas in the beam line do not contribute significantly to the uncertainties in the tracking of the particles. The production of charge states other than that of the rare-isotope beam in the rest gas at this pressure level is negligible (<0.1%), especially when compared to charge-state production in beam line tracking detectors and the

reaction target, as discussed in Section 4.3.2.3. Hence, it poses not an additional constraint on the vacuum level that must be achieved.

The operation of the HTBL requires gate valves to isolate diagnostic chamber during access to diagnostic equipment in chambers needed during experiments, and the gate valves separates each section with dedicated pumping station with vacuum gauges. Finally, the locations of necessary bellows to accommodate alignment have been identified.

5.7 References

[BAZ02] D. Bazin et al., Nucl. Instrum. Meth. Phys. Res. A 482, 307 (2002)

[BAZ03] D. Bazin et al., Nucl. Instrum. Meth. Phys. Res. B 204, 629 (2003)

[COS11] M. Berz and K. Makino, MSU Report MSUHEP 101214 (2011), 060804-rev (2013)

[FRIB-T31209-SP-000152] FRIB-T31209-SP-000152-R005, Superconducting Magnet Power Supplies Specifications (2015)

[TAR16] O. B. Tarasov and D. Bazin, Nucl. Instr. and Meth, in Phys. Res. B 376, 185 (2016)

[TAR08] O. B. Tarasov and D. Bazin, Nucl. Instr. and Meth, in Phys. Res. B 266, 4657 (2008)

6 Spectrometer Section of the HRS

In this section, the properties of the Spectrometer Section of the HRS are described, based on the scientific requirements motivated and provided in Section 4.3.1. The Work Breakdown Structure (WBS) is given in Table 6-1. A brief overview of the Spectrometer Section is given in Section 6.1, the scientific requirements are summarized in Section 6.2, and the design approach, the preferred alternative, and the results of detailed ion-optical simulations are presented in Section 6.3. The capabilities afforded by the preferred alternative of the Spectrometer Section is summarized in Section 6.4. The specifications of the magnetic elements, the diagnostics and detectors, and the vacuum components are given in Section 6.5, which serve as the requirements for the corresponding subsystems. Commissioning plans for the Spectrometer Section are given in Section 8. As for the HTBL in Section 5, the ion-optical calculation for the Spectrometer Section were performed with COSY INFINITY [COS11]. The magnetic field profiles extracted from the magnetostatic models in ANSYS-Maxwell [ANS18] based on conceptual designs of the magnets, which will be presented in Section 9.2.2, have been incorporated in calculations in COSY INFINITY that are presented in this section. This includes the excitation dependence of the effective length of magnetic fields of both the dipoles and quadrupoles, which is parametrized based on the magnetostatic calculations.

Table 6-1 WBS for the Spectrometer ion-optical design

Experimental Systems - High Rigidity Spectrometer	**HRS.3**
Spectrometer Section	**HRS.3.02**
Spectrometer Section Beam Physics	**HRS.3.02.01**

6.1 Introduction and overview

The layout of the Spectrometer Section is provided in Figure 6.1. The nomenclature scheme follows that provided in Figure 5.2. The Spectrometer Section starts at FS0, the location of the reaction target. A variety of ancillary devices can be placed around the reaction target (see Figure 4.17). In Figure 6.1, GRETA is shown around the reaction target, being the largest of these ancillary devices. FS0 is followed by two quadrupole magnets (QS1A and QS1B), which guide the trajectories of the desired reaction fragments into the rest of the Spectrometer Section. QS1B is followed by the large-gap Sweeper Dipole magnet DS1, which bends the charged fragments to the left by 35°. The Sweeper Dipole magnet DS1 is followed two quadrupoles, QS3B and QS4B, which guide the particles to the first focal plane FS1. FS1 is followed two additional large-bore quadrupoles, QS5B and QS6B, which guide the particles into the Spectrometer Dipole DS2. DS2 bends the particles by 60° into the final focal plane FS2.

Most types of experiments envisioned with the HRS must use the full Spectrometer Section to achieve the scientific goals. However, for invariant-mass spectroscopy experiments that involve fast neutron detection with the MoNA-LISA neutron-detector array installed at forward angles, the reaction target is placed just in front of DS1 so that neutrons can be detected with optimal acceptance through the gap of DS1, not limited by the apertures of the quadrupoles QS1A and QS2B, as shown in Figure 6.1. In that case, the measurement with ancillary detectors requires that they are placed just prior to DS1 as well, as indicated by the placement GRETA in the figure. The

intermediate focus FS1 serves as the final focus, and the downstream magnets (QS5C, QS6C, and DS2) are not used.
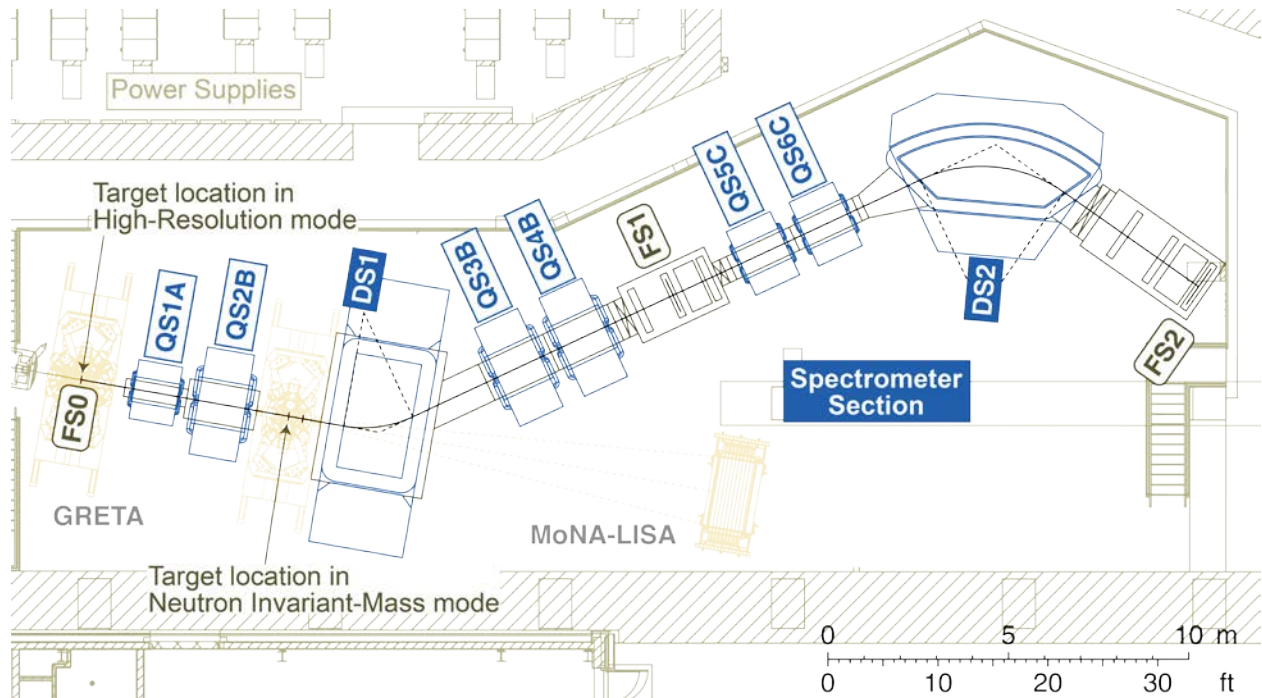
Figure 6.1 Layout of the Spectrometer Section of the HRS starting at FS0, showing dipoles DS1 and DS2, quadrupoles QS1A, QS2B, QS3B, QS4B, QS5C, and QS6C, focal planes FS1 and FS2, and possible locations for GRETA and MoNA-LISA.

6.2 Requirements for the Spectrometer Section

The Spectrometer Section must enable the diverse scientific program described in Section 4.2 with requirements for a wide range of experiment types described in Table 4-4. Based on the requirements for the Spectrometer Section discussed in Section 4.3.1, three operational mode were identified in Section 4.3.1.6, with requirements for each detailed in Table 4-1. For convenience, Table 4-1 is reproduced in Table 6-2. The three modes are:

- The high-resolution mode, which is used for a large fraction of the experiment types
- The neutron invariant-mass mode, which is used for invariant-mass spectroscopy in which the MoNA-LISA neutron detector array is employed
- The ToF-$B\rho$ mass-measurement mode, which is used for mass measurements only

While the ion-optical layout of the high-resolution mode is the same as that of the ToF-$B\rho$ mass-measurement mode, the neutron invariant-mass mode has a distinct layout, but with the same hardware configuration as the other two modes. The maximum magnetic rigidity for each of these modes is 8 Tm, but the requirements are mostly different otherwise. Therefore, to accommodate the requirements of all the three modes while utilizing the same hardware and infrastructure, a separated-dipole configuration as shown has been adopted.

117

Table 6-2 Requirement for the three operational modes of the Spectrometer Section of the HRS (see also Table 4-1).

Specification for	Mode High-resolution	Neutron invariant-mass	ToF-Bρ mass-measurement
Maximum mass number	238	132	238
Mass resolving power	400	220	10000
Charge resolving power	156	85	156
Time-of-flight resolution (ps)	150	150	30
Flight path for charged particles (m)	25	11	90
Momentum resolving power	1500	290	>10000
Spectrometer solid angle (msr)	15	10	3
Angular resolution (mrad)	5	5	5
Space around target (cm)	123	90	-
Momentum acceptance ($\delta p/p$ in %)	±2.5	±5	±0.5
Neutron solid angle (msr)	-	32	-
Neutron flight-path length (m)	-	15	-
Unreacted beam rejection	yes	yes	-
Maximum magnetic rigidity (Tm)	8	8	7

6.3 Design approach and preferred alternative for the Spectrometer Section

In the following, the design approach for each of the three operational modes is described within the framework of the preferred layout of the Spectrometer Section.

6.3.1 High-resolution mode

The high-resolution mode is required for a large fraction of the experiment types envisioned for the HRS. Experiments performed in this mode will involve rare isotopes across the chart of nuclei, including very heavy isotopes. Therefore, this mode must achieve good mass resolving power by means of a time-of-flight measurement, requiring a flight path of at least 25 m. This is achieved by utilizing the full Spectrometer Section, from FS0 to FS2, as shown in Figure 6.2. The large space around the reaction target FS0 accommodates ancillary detectors, represented by GRETA, the largest of the ancillary detector systems, in Figure 6.2. Quadrupole magnets after the target guide the particles into the sweeper magnet DS1, which is critical for achieving full transmission of the required emittance through the full Spectrometer Section and for gaining the momentum and mass resolving powers required for the experimental program. Since DS1 and DS2 bend the beam in the opposite directions, an intermediate focus at FS1 is needed to accumulate dispersions. This intermediate focus can also be utilized to intercept the unreacted beam and prevent it from entering the final focal plane FS2.
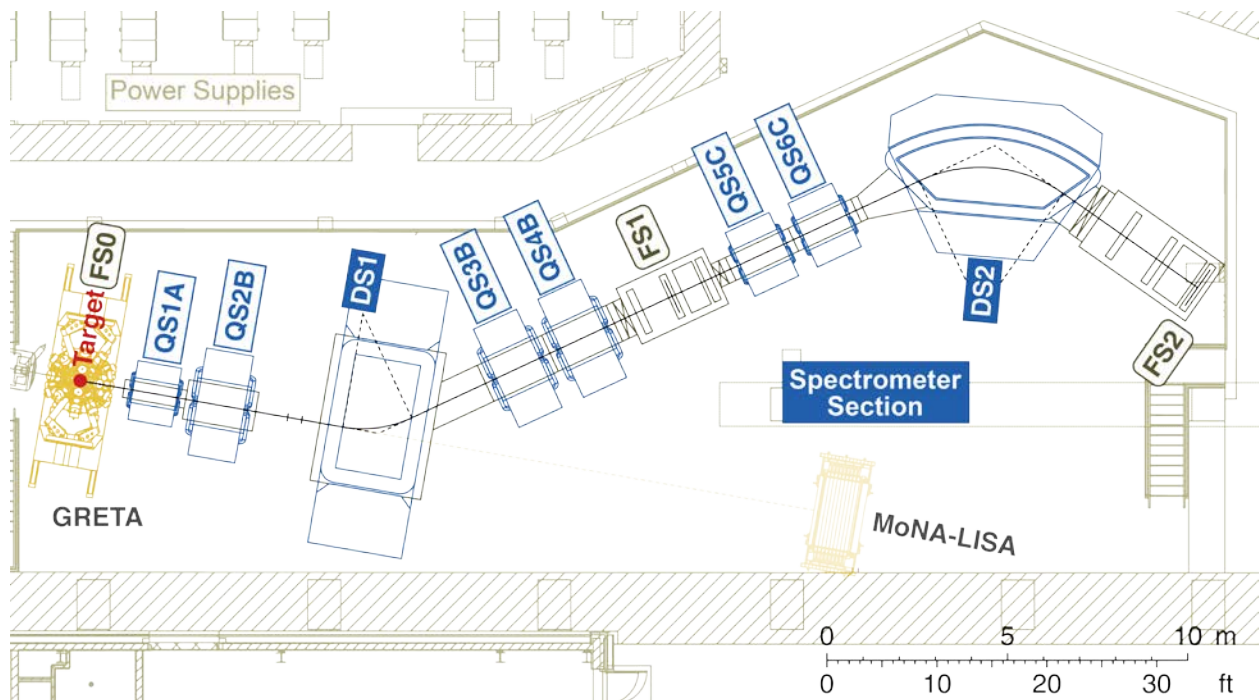
Figure 6.2 The layout for the high-resolution mode of the Spectrometer Section. The reaction target is located at FS0 and reaction products are bent by DS1 (to the left) and DS2 (to the right) into the FS2 focal plane, and guided by six quadrupoles.

The first-order ion-optical beam transport of the Spectrometer Section in the high-resolution mode is shown in Figure 6.3. The panel (a) shows the beam transport in the dispersive (x) plane and the panel (b) shows the beam transport in the non-dispersive (y) plane. In this ion-optical design, the following considerations were taken into account:

- Quadrupole QS1A expands the beam in the dispersive direction to maximize the magnetic flux enclosed by the rays passing through DS1 to achieve the required resolving power, while it focuses the beam in the non-dispersive direction. QS2B, with a large bore size, having the opposite polarity to QS1A, optimize the transmission through the dipole DS1.

- DS1 is rectangular in shape, and is installed so that particles enter DS1 perpendicular to its pole face, which facilitates the implementation of ancillary detectors. This also provide the benefit that the downstream pole face focuses the beam in the non-dispersive direction as it makes an angle of 35° with the central trajectory.

- Quadrupoles QS3B and QS4B must capture the particles exiting from DS1 and direct them through the rest of the Spectrometer Section. These quadrupoles have to be placed sufficiently far downstream of DS1 to ensure they do not interfere with the path of neutrons for the neutron invariant-mass mode.

- At the intermediate focus FS1, after a flight path of almost 17 m from the FS0, point-to-point focusing is nearly achieved [$(x/x')=0.05$] in the dispersive plane. The ion optics is tuned to optimize the transmission: the angular dispersion vanishes [$(x'|\delta)=0$] in the dispersive plane and parallel-to-point [$(y/y)=0$] and point-to-parallel [$(y'|y')=0$] imaging conditions are achieved in the non-dispersive plane. Although, there is not a perfect focus at FS1, it is sufficiently close to allow for efficient beam rejection at this location. Relaxing

this focus requirement slightly made it easier to optimize other important ion-optical properties of the full Spectrometer Section, such as dispersion and transmission.
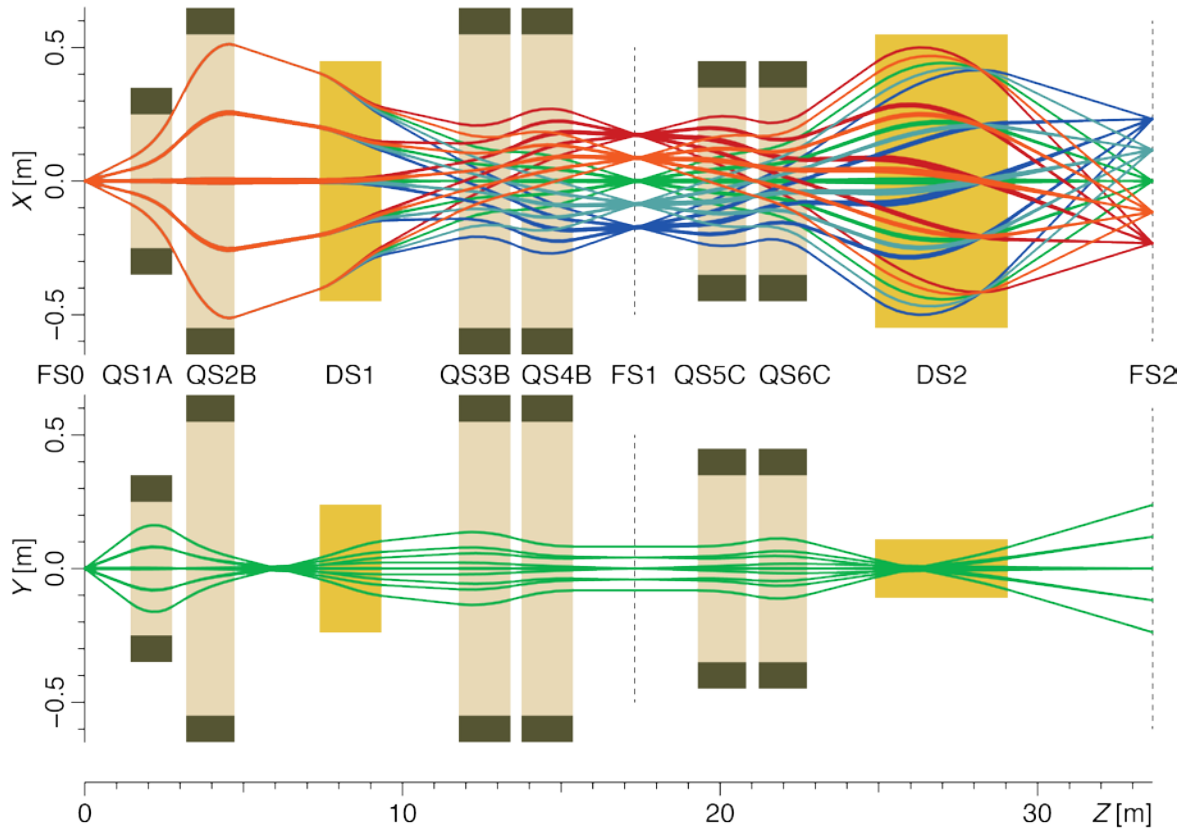
Figure 6.3 Trajectory plots for the High-Resolution mode through the Spectrometer Section in the dispersive (top) and the non-dispersive (bottom) planes in first order. The ensemble of trajectories correspond to those within the acceptance limits defined by the scientific requirements, i.e., $\delta x'_{max} = 60$ mrad, $\delta y'_{max} = 90$ mrad, and $\delta p_{max}/p = 3\%$. Position divergences at FS0 of $\delta x_{max} = \delta y_{max} = 3$ mm are used to depict the trajectories. As in the previous figures, the heights of the orange and light-brown boxes represent aperture sizes of the dipole and quadrupole magnets, respectively. The dark boxes on both ends of the quadrupole magnets denote the space where the sextupole and octupole coils are housed.

- Quadrupoles QS5C and QS6C, which transport the beam particles to DS2, can have smaller bore sizes than QS3B and QS4B. The beam is expanded in the horizontal plane in DS2 to gain resolving power. In the vertical direction a focus is created inside of DS2 to optimize the transmission.
- DS2 is a sector magnet with pole-face rotations of 20° at the entrance and the exit (symmetric with respect to the center). The pole-face rotations are such that they provide horizontal focusing and vertical defocusing, which help shape the envelope of particles toward the final focus FS2.
- At FS2, after a flight path of 32.4 m from FS0, point-to-point focusing [$(x/x')=0$] is achieved in the dispersive plane. Operating the HTBL in dispersion-matched mode (See Section 5.3.3) can be highly advantageous for reducing the spot size and intercepting the

unreacted beam particles. In the non-dispersive plane, parallel-to-point [$(y/y)=0$] imaging is achieved to provide the highest accuracy in the reconstruction of the vertical component of the scattering angle after the target.

- The quadrupole pole-tip field strengths were kept below 2.5 Tm.

The first-order transfer-matrix elements of the high-resolution mode are listed in Table 6-3.

Table 6-3 First-order transfer-matrix elements from the FS0 reaction target to the focal planes FS1 and FS2 in the high-resolution mode.

		FS1	FS2
$(x\|x)$	$= R_{11}$	-1.65	0.75
$(x\|x')$ [m/rad]	$= R_{12}$	0.05	0.00
$(x'\|x)$ [rad/m]	$= R_{21}$	-0.14	0.63
$(x'\|x')$	$= R_{22}$	-0.60	1.33
$(x\|\delta)$ [m]	$= R_{16}$	-5.76	7.74
$(x'\|\delta)$ [rad]	$= R_{26}$	0.18	1.44
$(y\|y)$	$= R_{33}$	0.00	0.00
$(y\|y')$ [m/rad]	$= R_{34}$	-0.91	2.65
$(y'\|y)$ [rad/m]	$= R_{43}$	1.10	-0.38
$(y'\|y')$	$= R_{44}$	0.00	0.39

As discussed in Section 5.3.3, unreacted-beam rejection can be performed either at FS1 or FS2 when dispersion-matched to either of these two focal planes. Even when the beam is transported in the HTBL in achromatic mode, the beam is focused at these two foci, at which beam rejection can be done although with less precision as in dispersion-matched mode. Combining beam rejection at both foci may increase the efficacy of the rejection rate for some cases. As mentioned above, how the unreacted beam is to be blocked can be optimized for each experiment.

Although the first-order ion-optical description shown in Figure 6.2 and Figure 6.3 are the most important for understanding the concept and main performance parameters of the ion-optical layout of the high-resolution mode, it is also important to model and understand the impact of higher-order contributions to the ion optics. This is particularly important for the Spectrometer Section, because its quadrupole magnets have relatively small aspect (length-to-diameter) ratios. Consequently, the quadrupole fields have virtually no flat region and are dominated by the fringe region. Therefore, ion-optical calculations were performed up to 5th order and effects of higher-order aberrations investigated, as well as the ability to correct for aberrations by hardware using sextupole and octupole coils nested into the quadrupole magnets. The 5th-order transfer maps were calculated in COSY INFINITY using the magnetic field profiles from ANSYS Maxwell analyses of the dipole and quadrupole magnet conceptual designs of Section 9 . The results are shown in Figure 6.4. The higher-order aberrations cause the trajectories to become distorted (see Figure 6.4(a)), although the acceptance losses are relatively small. These losses can be prevented by using the nested sextupole and octupole coils (Figure 6.4(b)).
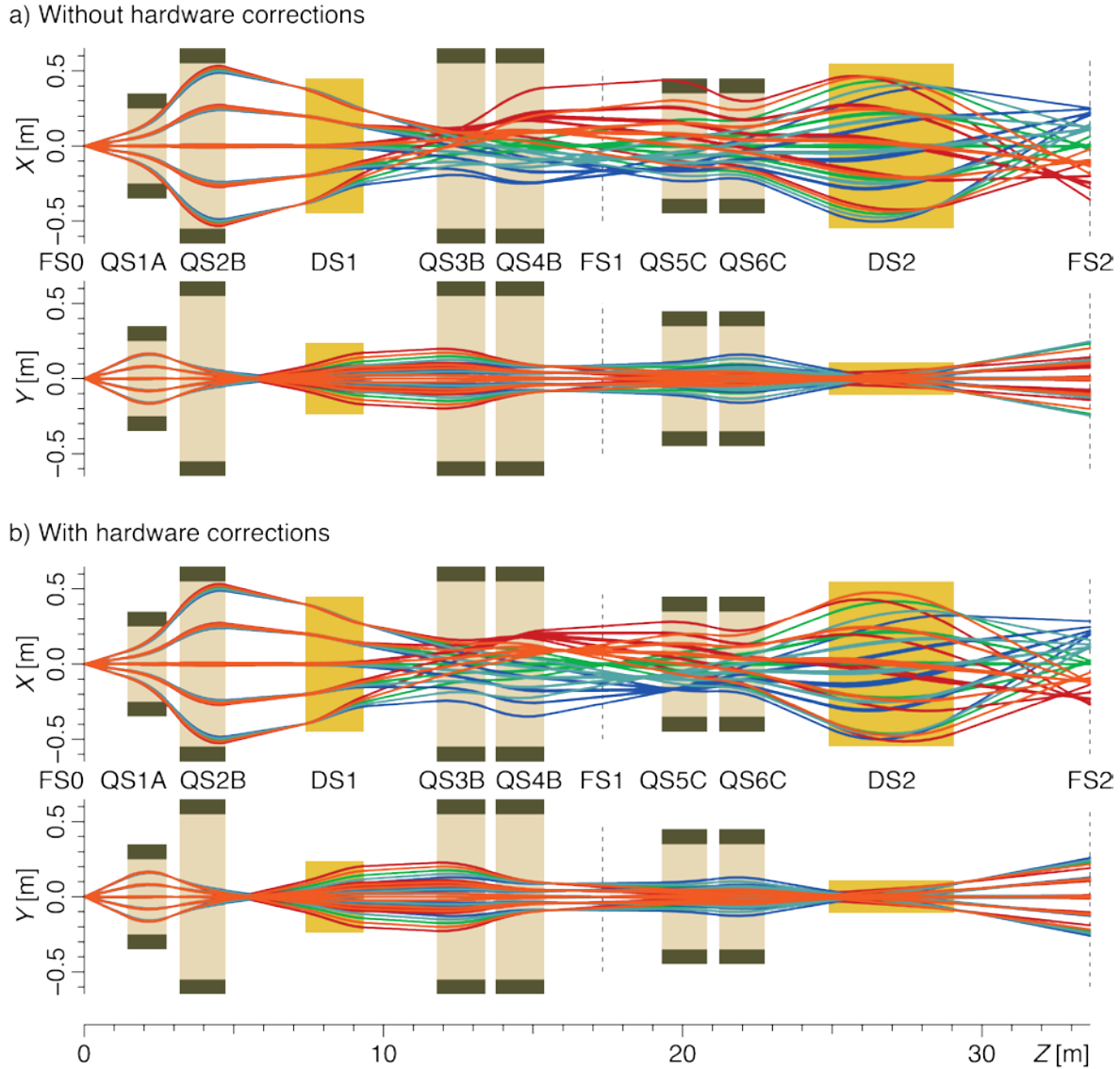
Figure 6.4 Trajectory plots for the high-resolution mode of the Spectrometer Section through 5th order. The ensemble of trajectory are the same as that in Figure 6.3. Panel a) provides the trajectories without hardware corrections (sextupole and octupole coils embedded on the quadrupoles). For panel b) these coils were adjusted to minimize higher-order aberrations. As in the previous figures, the heights of the orange and light-brown boxes represent aperture sizes of the dipole and quadrupole magnets, respectively. The dark boxes on both ends of the quadrupole magnets denote the space where the sextupole and octupole coils are housed.

The incorporation of hardware corrections in the design of the HRS also contributes to maintaining appropriate acceptances of the Spectrometer Section. This is illustrated in Figure 6.5, which shows beam envelopes, and angular and momentum acceptances as simulated in LISE++ by using the transport matrices obtained from COSY INFINITY. Rather than showing the rays for a specific reaction, a flat momentum distribution and isotropic angular distributions were used. In this way, it is easy to get a good overview of the full acceptance of the Spectrometer Section.
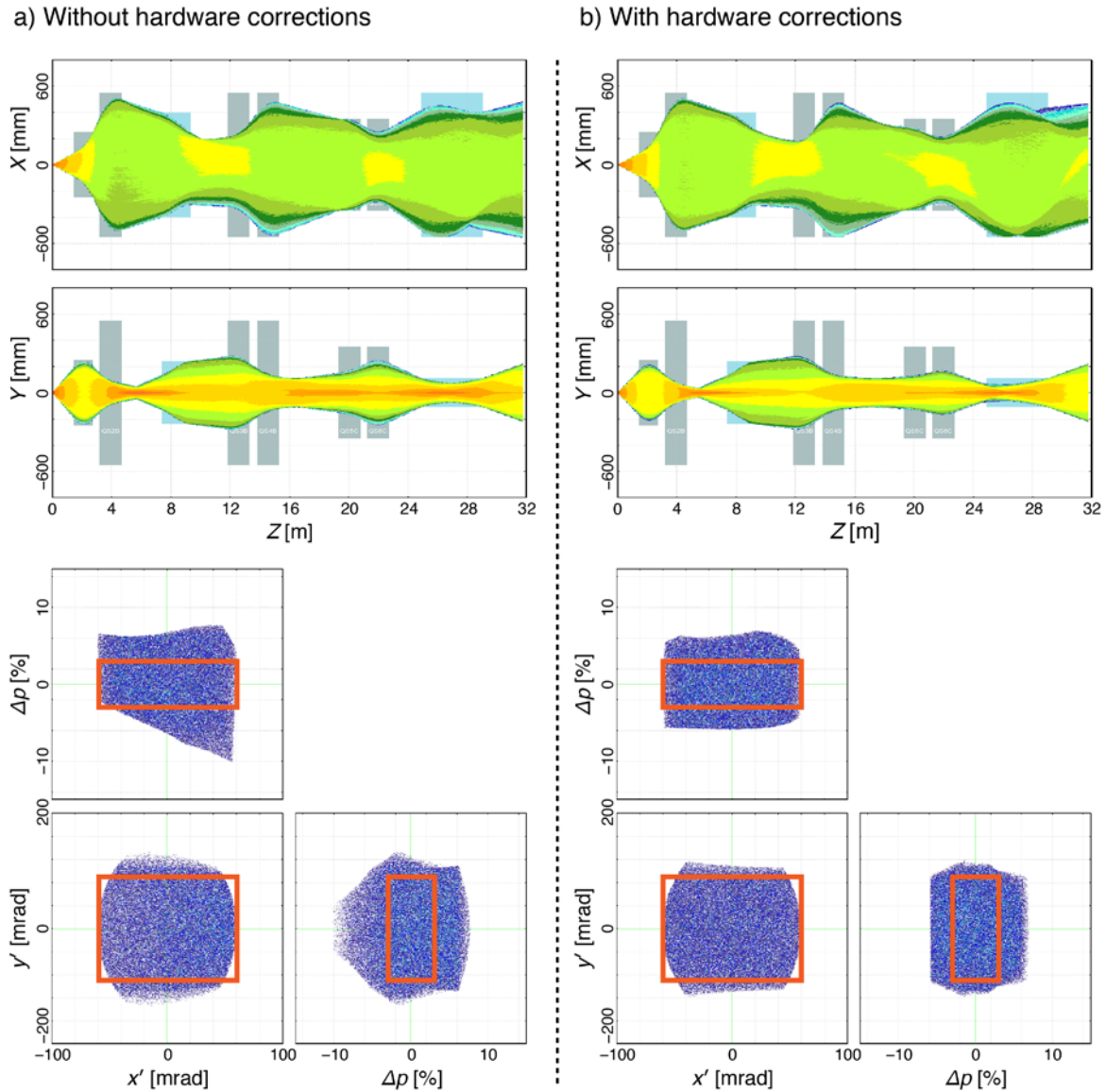
Figure 6.5 Comparison of the envelopes (top), and angular and momentum acceptances (bottom) for the high-resolution mode of the Spectrometer Section, as simulated in LISE⁺⁺, by using transfer matrices obtained from COSY INFINITY. Panel a) shows the envelopes and acceptances without the hardware corrections and panel b) with the hardware corrections. In the acceptance plots, the orange boxes denote ±60 mrad for x', ±90 mrad for y', and ±3% for δp/p.

In these simulation, the warm-bore aperture sizes for the quadrupoles, the good-field regions in the dispersive plane, the vertical gap sizes in the non-dispersive plane for the dipoles, and the assumed focal-plane dimensions (±500 mm [*x*] by ±300 mm [*y*] for FS1 and ±600 mm [*x*] by ±300 mm [*y*] for FS2) were included. Note that the dimensions of the detectors allow for the detection of particles outside the required momentum range of ±2.5%. However, the apertures of the magnets are primarily constrained by the need to meet the angular acceptance requirements. As a

consequence, by using focal plane detectors that cover the apertures in the system (see Figures 6.5 and 6.8), a larger momentum acceptance can be achieved (albeit with a dependence on angle) without increasing the sizes of the magnets or apertures. In other words, the detectors do not restrict the momentum acceptance afforded by the magnets and the large aperture sizes of the magnets (necessary to meet the angular acceptance requirements) can be fully utilized.

These results show that without the hardware corrections, the required acceptances are nearly met with only minor losses at their peripheries. These losses can be recovered by adjusting the sextupole and octupole corrector fields, as described previously. Having these correctors is beneficial for providing the ability to fine-tune the ion optics, especially given the larger sizes of the magnets in the Spectrometer Section.

The hardware corrections provided by the sextupole and octupole coils by themselves are not intended to correct for all the higher-order aberrations. For example, the focal planes at FS1 and FS2 are tilted due to the large second-order matrix elements $(x|x'\delta)$, even after the hardware corrections are applied. Methods aimed at reducing the $(x|x'\delta)$ term affect had detrimental effects on other terms and hence not pursued. Therefore, in the analysis of data taken with the HRS, software corrections based on the inverse raytrace matrix will be employed. Such a technique has been very successfully used for experiments performed at the S800 Spectrometer [BAZ03] at NSCL. An initial study on trajectory reconstruction has been performed for the high-resolution mode of the Spectrometer Section by means of Monte-Carlo simulations. Here, particles were emitted from FS0 and transported through FS2 via the 5th-order transfer maps calculated in COSY INFINITY, using the magnetic field profiles from ANSYS Maxwell analyses of the dipole and quadrupole magnet conceptual designs. At FS2, some disturbance was added to emulate the finite detector resolutions and the effect of straggling in the detector materials (see Section 7). Subsequently, the particles were traced backward to FS0 via the 5th-order inverse maps. By comparing the original trajectories with the reconstructed trajectories, it was found that the uncertainties induced by the detector resolutions and multiple scattering effects were less than 2 mrad (FWHM) and less than 0.1% in momentum.

Along with the further detailed design of the magnets, estimation of acceptable magnetic field quality will be done as next steps. In addition, magnet alignment criteria will be determined.

6.3.2 Neutron invariant-mass mode

The neutron invariant-mass mode is optimized to operate in combination with the MoNA-LISA neutron-detector array, which is placed at forward scattering angles. Because the neutrons emitted in a cone around zero degrees must be able reach MoNA-LISA, sweeper magnet DS1 requires a large gap. The gap size can be made optimal use of by placing the reaction target as close as possible to DS1. Therefore, rather than placing the target at FS0, it is highly preferable to place it in between QS2B and DS1, indicated by FS0′ in Figure 6.6. QS1A and QS2B then serve as extensions of the HTBL and provide the proper beam conditions at FS0′.

In this mode, the final focal plane can be placed at FS1 without using QS5C, QS6C, and DS2, such that the requirements for the momentum resolving power and maximum mass of the particles to be analyzed can be met. Quadrupoles QS3B and QS4B are used to optimize the transport after DS1 at the focal plane FS1. As mentioned in Section 6.3.1, the location of QS3B and the bend

angle provided by DS1 are critical parameters as it is important to ensure that QS3B does not interfere with the path of the neutrons. Since the ion optics is optimized for the target position immediately in front of DS1 without preceding quadrupoles, solutions all the way to FS2 come with strongly reduced angular/momentum acceptances and with compromised ion-optical properties. It should be noted that the requirements for the momentum resolving power and the flight-path length are already satisfied by the ion-optical solution up to FS1.

The exact location of the reaction target is in principle flexible and can be optimized for particular experiments. For the purpose of the ion-optical calculations shown here, we assumed that the target is placed 90 cm from the upstream edge of DS1 as it satisfies the requirement for placing GRETA around the reaction target with its most forward ring of detectors removed (See Section 4.3.1.3). Experiments with MoNA-LISA require a neutron flight path up to 15 m from the reaction target to the detector array, which can be accommodated in the layout shown in Figure 6.6.
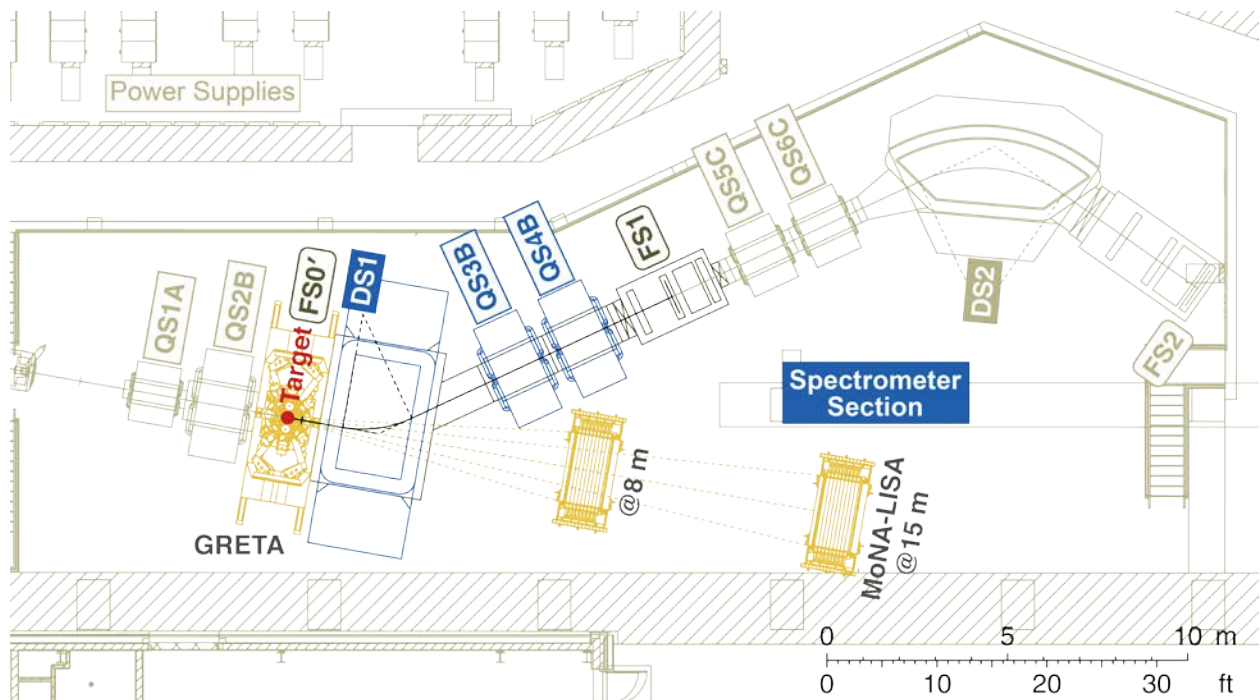
Figure 6.6 Layout of the neutron invariant-mass mode of the Spectrometer Section. The target is located just prior to DS1, downstream of QS1A and QS2B.

The first-order ion-optical beam transport of the Spectrometer Section in the neutron invariant-mass mode is shown in Figure 6.7. The top panel shows the beam transport in the dispersive (x) plane and the middle panel shows the beam transport in the non-dispersive (y) plane.

The downstream edge of DS1 has a defocusing effect on the rays in the dispersive plane. In order to sustain a dispersive-angular acceptance of ±70 mrad over the required momentum acceptance, a large-aperture quadrupole QS3B is necessary. On the other hand, the same edge provides a focusing effect in the non-dispersive plane, and it helps to reduce the vertical envelope size after the dipole. However, since the envelope is expanded by QS3B, a large-aperture quadrupole QS4B

125

is necessary to maintain a sizable non-dispersive-angular acceptance of ±50 mrad. These two quadrupoles are very important in extending the flight path without the need of a very large focal-plane detector system.

Table 6-4 shows the first order ion optical parameters of the neutron invariant mass mode. A point-to-point imaging in the dispersive plane [$(x|x')$=0], in combination with a parallel-to-point imaging in the non-dispersive plane [$(y|y) = 0$] with a large value for $(y|y')$=3.78 is advantageous for achieving high accuracy in the reconstruction of the vertical component of the scattering angle.
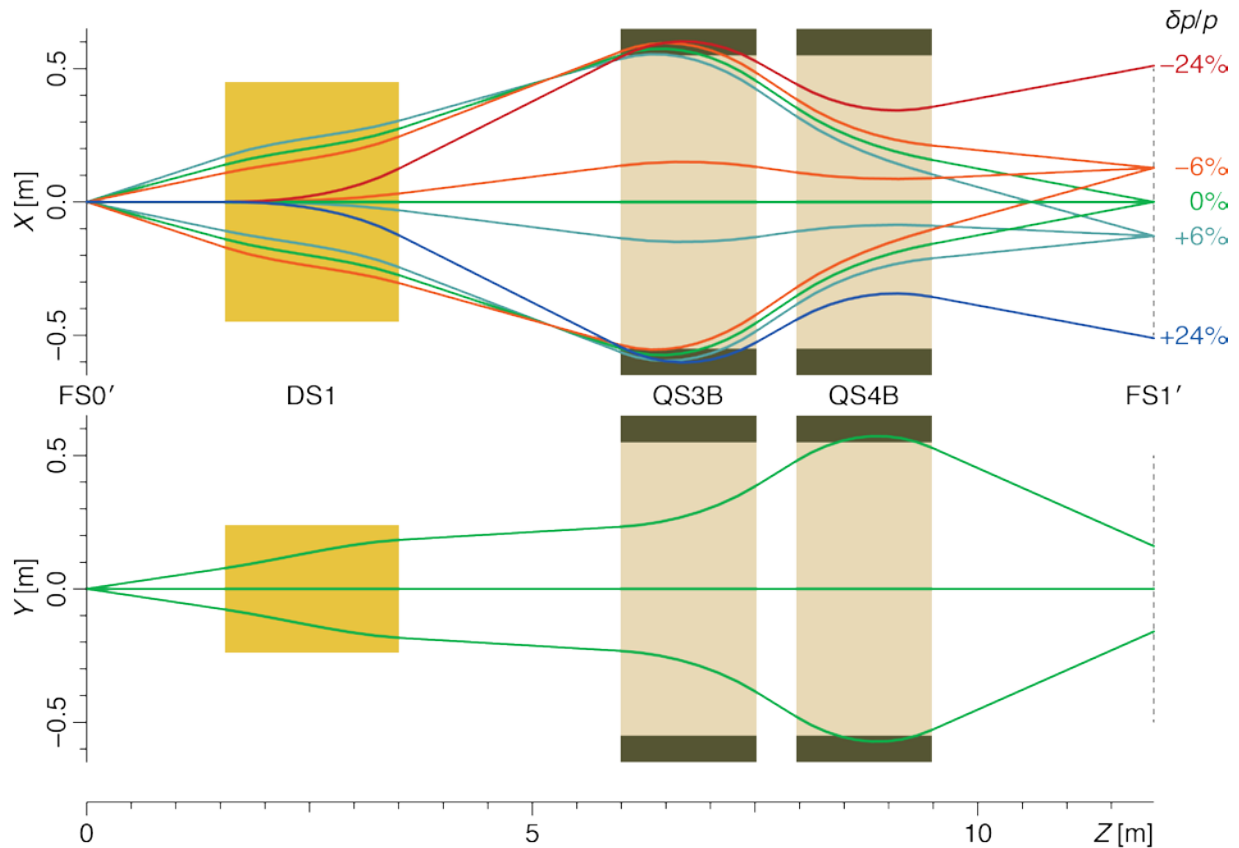
Figure 6.7 Same as Figure 6.3, but for the neutron invariant-mass mode of the Spectrometer Section. For the central momentum (δp/p = 0%, shown in green), trajectories with δx' = -90, 0, 90 mrad in the dispersive plane are shown. Since the angular acceptance strongly depends on momentum, trajectories with δx' = -70, 0, 110 mrad for momentum deviation δp/p = +6% (shown in blue green), and those with δx' = -110, 0, 70 mrad for momentum deviation δp/p = -6% (shown in orange) are drawn. Also drawn are trajectories with larger momentum deviations, δp/p = +24% (blue) and -24% (red), emitted at δx' = 0 mrad. In the non-dispersive plane, trajectories with different momenta coincide, and those with δy' = -50, 0, 50 mrad are depicted. Position divergences at FS0' are not included in this figure. As in the previous figures, the heights of the orange and light-brown boxes represent aperture sizes of the dipole and quadrupole magnets, respectively. The dark boxes on both ends of the quadrupole magnets denote the space where the sextupole and octupole coils are housed.

Higher-order ion-optical simulations were also performed for the neutron invariant-mass mode. Figure 6.8 shows the results of these simulations. Figure 6.8a shows the beam envelopes, and the angular and momentum acceptances without the use of sextupole and octupole coils in the QS3B

and QS4B magnets. The momentum acceptance strongly depends on the angle in the dispersive plane, although the acceptance requirements are met even without the use of the higher-order multipole magnets. In Figure 6.8b, the sextupole and octupole strengths in QS3B and QS4B are optimized and the acceptances are improved and less distorted. Similar to the high-resolution mode, the hardware corrections provided by the sextupole and octupole coils by themselves are not intended to correct for the higher-order aberrations in the focal plane FS1. Therefore, in the analysis of data taken in this mode, software corrections based on the inverse raytrace matrix will be also employed.
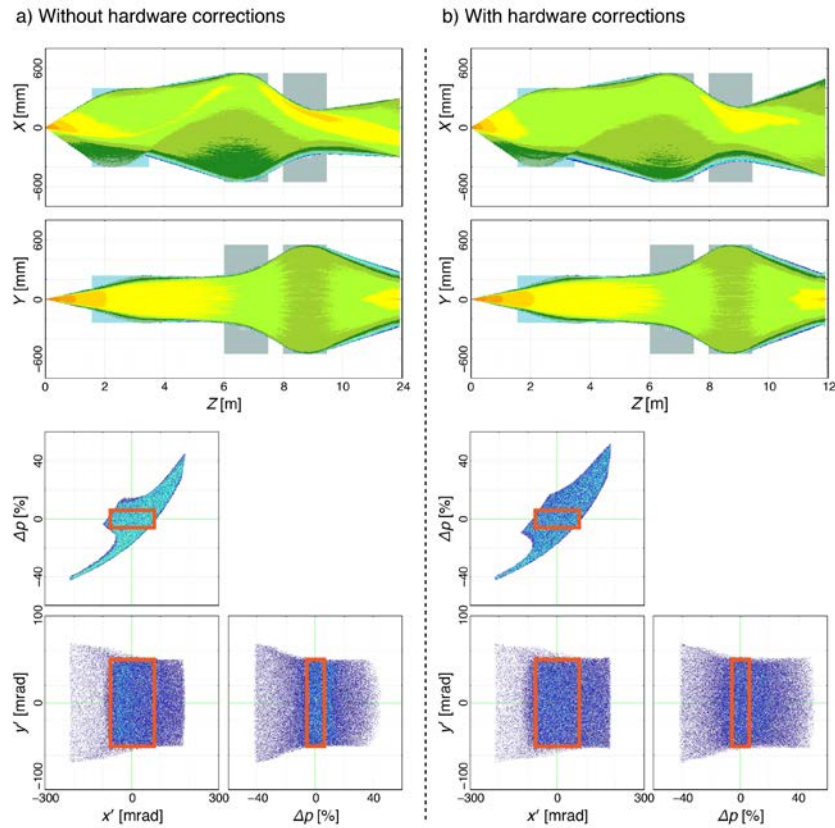
Figure 6.8 Same as Figure 6.5 but for the neutron invariant-mass mode of the Spectrometer Section. In the acceptance plots on the bottom, the limits defined by the scientific requirements (75 mrad for x', 50 mrad for y', and 6% for δp/p) are denoted by the orange boxes.

Table 6-4 First-order transfer matrix elements from the reaction target FS0′ to the focal plane FS1 for the neutron invariant-mass mode.

		FS1
$(x\|x)$	$= R_{11}$	-1.42
$(x\|x')$ [m/rad]	$= R_{12}$	0.00
$(x'\|x)$ [rad/m]	$= R_{21}$	-0.44
$(x'\|x')$	$= R_{22}$	-0.70
$(x\|\delta)$ [m]	$= R_{16}$	-2.13
$(x'\|\delta)$ [rad]	$= R_{26}$	-0.26
$(y\|y)$	$= R_{33}$	0.00
$(y\|y')$ [m/rad]	$= R_{34}$	3.20
$(y'\|y)$ [rad/m]	$= R_{43}$	-0.31
$(y'\|y')$	$= R_{44}$	-2.97

6.3.3   ToF-$B\rho$ mass-measurement mode

The ToF-$B\rho$ mass-measurement mode serves only that particular type of experiment (see Section 4.3.1.5). The Spectrometer Section is operated in the same manner as for the high-resolution mode described in Section 6.3.1 and the HTBL is operated in dispersion-matched beam-transport mode described in Section 5.3.3. No target is placed at FS0. A very long flight path (115 m) is created by combining the Reconfigured A1900 (40.14 m), the HTBL (41.24 m), and the Spectrometer Section (33.63 m) of the HRS, as shown in Figure 6.9. The long flight path is important for reducing the relative uncertainty of the ToF measurement. Because of the use of the dispersion-matched beam-transport mode in the HTBL, the lateral and angular dispersions are matched to those of the Spectrometer Section, and the full beam transport to FS2 is point-to-point in the dispersive direction [$(x/x')=0$] and doubly achromatic [$(x/\delta)=(x'/\delta)=0$]. This ion-optical beam transport is shown in first order in Figure 6.10. Only the transport through the Spectrometer Section is shown, since the transport through the HTBL is identical to that of Figure 5.5. Due to these ion-optical properties, the position and angle at FS2 are independent of the momentum of the particles and the spectrometer's highest resolution can be obtained. The position at FS0 is measured with high precision (0.35 mm FWHM) by using a dedicated tracking detector to determine the rigidity of the isotopes on an event-by-event basis. Timing measurements with small dedicated timing detectors are performed to determine the ToF from the beginning of the ARIS Reconfigured A1900 to FS2 with very high precision (30 ps).
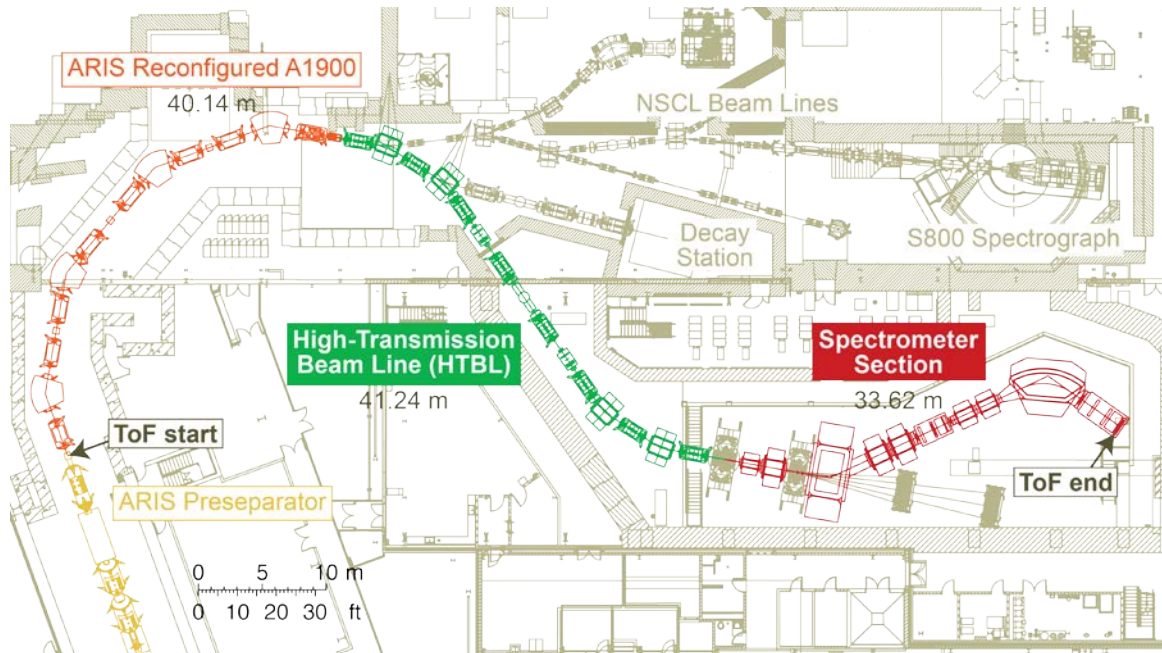
Figure 6.9 Layout of the HTBL and the Spectrometer Section of the HRS, together with the ARIS Fragment Separator. The ToF-Bρ mass-measurements utilize a 115-meter-long flight path which consists of the Reconfigured A1900, the HTBL, and the Spectrometer Section as indicated in the figure.
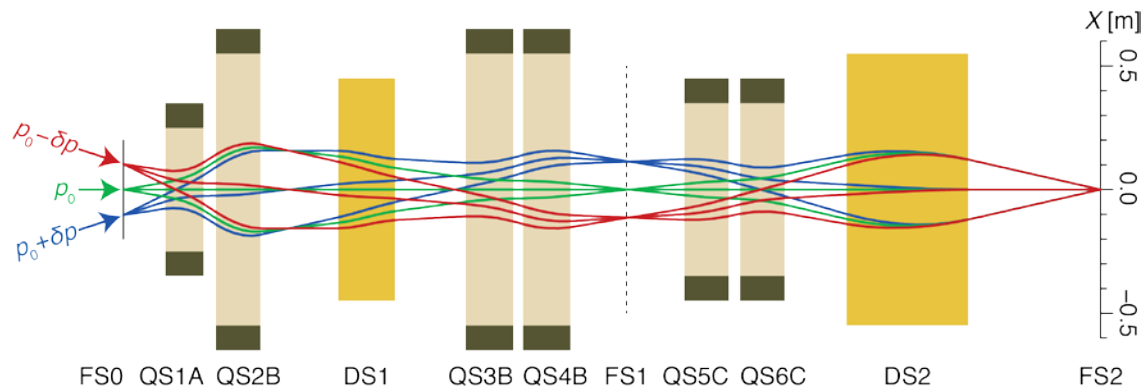
Figure 6.10 Trajectory plot for the high-resolution mode through the Spectrometer Section in the dispersive plane in first order. The spectrometer settings are exactly the same as those in Figure 6.3, but the beam is momentum-dispersed at the target location, by using the HTBL in the dispersion-matched mode (see Figure 5.5). The green trajectories are with the central momentum (p_0), while the blue (red) trajectories denote a high (low) momentum component. They all come into a doubly achromatic focus at FS2 as a consequence of dispersion matching. As in the previous figures, the heights of the orange and light-brown boxes represent aperture sizes of the dipole and quadrupole magnets, respectively. The dark boxes on both ends of the quadrupole magnets denote the space where the sextupole and octupole coils are housed.

6.4 Preferred Spectrometer Section alternative meets requirements

The capabilities of the Spectrometer Section afforded by the preferred ion-optical alternative with regard to the scientific requirements described in Section 6.2 are summarized as follows.

6.4.1 High-resolution mode

The requirements for the high-resolution mode and the capabilities afforded by the preferred ion-optical design are compared as follows and summarized in Table 6-5.

- As shown above, the preferred ion-optical alternative is feasible at the maximum magnetic rigidity of 8 Tm.
- The flight-path length is 33.6 m from the reaction target at FS0 to the final focus at FS2.
- The distance of 125 cm from the target position to the flange of QS1A is available for the placement of auxiliary detectors.
- As shown in Figure 6.3, Figure 6.4, and Figure 6.5 the angular acceptance in the dispersive (non-dispersive) plane is ±60 (90) mrad, corresponding to a solid angle of 22 msr.
- The momentum acceptance of ±% is achieved at all angles, and it is larger at some angles (see Figure 6.5).
- The unreacted beam will be localized in the dispersive direction at the intermediate focus FS1 or at the final focus FS2, which facilitates its rejection at these locations.
- With the horizontal magnification of $M_x = (x|x) = 0.75$ and the dispersion $D_x = (x|\delta) = 7.74$ m, the momentum resolving power is 2000 for a beam spot of $\delta x_i = 5$ mm and the resolution of position determination of $\delta x_f = 1$ mm at FS2.
- The mass resolving power for $E = 160$ MeV/u is 900 for a ToF resolution of 150 ps.
- The charge resolving power is 156 for a resolution in energy loss of 1.3%.
- The angular resolution is 3 mrad (FWHM) as estimated by Monte-Carlo simulations for trajectory reconstruction including up to 5th order

Therefore, the preferred alternative meets or exceeds the requirements imposed by the science program.

Table 6-5 Comparison between the requirements for high-resolution mode of the Spectrometer Section and the capabilities of the preferred ion-optical alternative.

High Resolution Mode	Requirements	Preferred alternative
Maximum Mass	238	238
Mass Resolving Power	400	900
Charge resolving power	156	>156
Time of Flight Resolution (ps)	150	150
Flightpath charged particles (m)	25	33.6
Momentum Resolving power	1500	2000
Spectrometer solid angle (msr)	15	22
Angular resolution (mrad)	5	3
Space around target (cm)	123	125
Momentum acceptance ($\delta p/p$ in %)	±2.5	±3
Unreacted beam rejection	yes	yes
Maximum Rigidity (Tm)	8	8

6.4.2 Neutron invariant-mass mode

The requirements for the neutron invariant-mass mode and the capabilities afforded by the preferred ion-optical alternative are compared as follows and summarized in Table 6-6.

- As shown in Section 6.3.2, the preferred ion-optical alternative is feasible at the maximum magnetic rigidity of 8 Tm.
- The flight-path length is 12.0 m from the reaction target at FS0′ to the final focus at FS1.
- The distance of 90 cm from the target position to the entrance flange of DS1 is available for the placement of auxiliary detectors.
- As shown in Figure 6.7 and Figure 6.8, the angular acceptance in the dispersive (non-dispersive) plane is ±50 (75) mrad, corresponding to a solid angle of 15 msr.
- A momentum acceptance of ±6% is achieved at all angles (see Figure 6.8).
- The neutron solid angle is 32 msr, which effective constrains the vertical angular acceptance for neutrons to ±90 mrad for a distance between the target and the neutron-detector array is 8 m.
- The maximum neutron flight-path length is 15 m.
- The unreacted beam will be localized in the dispersive direction at the focus FS1, which facilitates its rejection at this location.
- With the horizontal magnification of $M_x = (x|x) = -1.42$ and the dispersion $D_x = (x|\delta) = -2.13$ m, the momentum resolving is 300 for a beam spot of 5 mm and the resolution of position determination of 1 mm at FS1.
- At $E = 160$ MeV/u, the mass resolving power is 230 for a ToF resolution of 150 ps.
- The charge resolving power is 156 for a resolution in energy loss of 1.3%.
- The angular resolution is 3 mrad (FWHM) as estimated by Monte-Carlo simulations for trajectory reconstruction including up to 5th order

The preferred alternative meets the requirements.

Table 6-6 Comparison between the requirements for the neutron invariant-mass mode and the capabilities of the preferred ion-optical alternative.

Neutron Invariant-Mass Mode	Requirements	Preferred Alternative
Maximum Mass	132	132
Mass Resolving Power	220	230
Charge Resolving Power	85	156
Time of Flight Resolution (ps)	150	150
Flightpath charged particles (m)	11	12
Momentum Resolving power	290	300
Spectrometer solid angle (msr)	10	15
Angular resolution (mrad)	5	3
Space around target (cm)	90	90
Momentum acceptance (dp/p in %)	±5	±6
Neutron Solid Angle (msr)	32	32
Neutron flight-path length (m)	15	15
Unreacted beam rejection	yes	yes
Maximum Rigidity (Tm)	8	8

6.4.3 ToF-Bρ mass-measurement mode

The requirements for the neutron invariant-mass mode and the capabilities afforded by the preferred ion-optical alternative are compared as follows and summarized in Table 6-7.

- As shown in Section 0, the preferred ion-optical alternative is feasible at the maximum magnetic rigidity of 8 Tm.
- The flight-path length of 115 m is achieved by combining the Reconfigured A1900 (40.14 m), the HTBL (41.24 m), and the Spectrometer Section (33.63 m) of the HRS.
- The angular acceptance is the same as that of the high-resolution mode, ±60 (90) mrad in the dispersive (non-dispersive) plane, corresponding to a solid angle of 22 msr. This is much larger than the 3 msr required for this mode. It is understood that the actual angular acceptance is dependent on the x position at FS0, due to the momentum-dispersed beam spot at this location, which does not negatively impact the ToF-$B\rho$ mass-measurement experiment.
- The momentum acceptance is ±0.5%, which corresponds to a beam-spot size of ±5 cm at FS0.
- With the horizontal magnification of $M_x = (x|x) = -1.00$ and the dispersion $D_x = (x|\delta) = -10.3$ m for the HTBL, the momentum resolving power is 21000 (FWHM) for the resolution of position determination of 0.35 mm (FWHM) at both FB0 and FS0.
- At $E = 160$ MeV/u, the mass resolving power is 14000 (FWHM) for the resolution of the ToF determination of 30 ps (FWHM).

The preferred alternative meets the requirements and can be used to perform highly accurate ToF-$B\rho$ mass measurements.

Table 6-7 shows the comparison between the requirements for the ToF-$B\rho$ mass measurements and the capabilities of the preferred alternative. The preferred alternative meets the requirements and can be used to perform highly accurate ToF-$B\rho$ mass measurements.

Table 6-7 Comparison between the requirements for the ToF-Bρ mass-measurement mode and the capabilities of the preferred ion-optical design. For the calculations, ^{60}Ca at 6.43 Tm was assumed.

ToF-$B\rho$ mass measurement mode	Requirements	Preferred alternative
Maximum Mass	238	238
Mass Resolving Power	10000	14300
Time of Flight Resolution (ps)	30	30
Flightpath charged particles (m)	90	115
Momentum Resolving power	>10000	21000
Spectrometer solid angle (msr)	3	>3
Momentum acceptance ($\delta p/p$ in %)	±0.5	±0.5*
Maximum Rigidity (Tm)	7	8

* This corresponds to a beam-spot size of ±5 cm

6.4.4 Switching between different Spectrometer Section Modes

A relatively large fraction of experiments at FRIB will use the HRS, which means that experiments that run in different modes can run consecutively. It is straightforward to switch between operational modes of the HRS in terms of the fields setting of the HTBL and Spectrometer Section magnets, but a significant amount of set-up and take-down time is associated with the placement of large ancillary experimental systems, such as GRETA, or the switch-over between using focal plane FS1 (in the neutron invariant-mass mode) and FS2 (in the high-resolution or ToF-Bρ mass measurement mode) in the Spectrometer Section of the HRS. Therefore, it will be advantageous to run several experiments with the same ancillary device or the same Spectrometer Section mode one after another in campaigns. Such campaigns are already used for experiments with large ancillary devices at the S800 Spectrometer, for example for experiments in which the S800 spectrometer and GRETINA are combined.

6.5 Technical specifications for the Spectrometer Section

This section described the specifications of technical components to realize the ion-optics solutions of the Spectrometer Section that have been discussed so far. The specifications of the magnetic elements are given in Section 6.5.1, those of the diagnostics and detectors are given in Section 6.5.2, and those of the vacuum systems are given in Section 6.5.3.

6.5.1 Magnetic elements

As shown in Figure 6.1, the Spectrometer Section contains six quadrupole (singlet) magnets and two dipole magnets. The specifications of these magnets as used in the ion-optical simulations of the preferred layout are presented in this section. Conceptual designs of the magnetic elements that

meet these specifications have been developed as presented in Section 9. The 3D magnetic field profiles of these designs were calculated in ANSYS-Maxwell [ANS18] and have been already incorporated in the ion-optical calculations in COSY INFINITY [COS11] that have been presented in this section, with the results meeting the ion-optical design criteria. Later detailed design analyses and associated optimizations will be checked in a similar manner.

6.5.1.1 Quadrupole magnets

The quadrupole magnets in the Spectrometer Section have large bore diameters to accommodate the large envelopes of the particles emerging from the reaction target at FS0 for the high-resolution mode or FS0′ for the neutron invariant-mass mode. Moreover, each quadrupole has sextupole and octupole coils superimposed to be able to correct for higher-order aberrations. There are 3 different types (denoted A, B, and C) of quadrupole magnets, which primarily differ in their bore diameters. The specifications for each magnet type as used in the ion-optical simulations of the preferred layout are provided in Table 6-8. The primary constraint for the iron-dominated quadrupole magnets with superconducting coils was to make them relatively short to optimize the transmission through the Spectrometer Section, while keeping the pole-tip field strength below a sustainable 2.5 T and the field gradients relatively small. Because of their large masses, a warm-iron design is the preferred approach to the quadrupole designs: only the superconducting coils are housed in cryostats.

Initial estimates of the necessary field quality were that an integrated field non-uniformity of better than 1% should be achieved for the purpose of operating the Spectrometer Section in the high-resolution mode. To assess the effects of the field quality on the ion optics, 3D field maps were extracted from the ANSYS Maxwell models of the conceptual designs of the quadrupoles (see Section 9), analyzed in a similar manner as discussed in Ref. [TAK13], and included in the calculations in COSY INFINITY up to 5th order. It was verified by these calculations that the desired ion-optical properties are realized by the quadrupole-magnet designs as presented in Section 9.

Table 6-8 Quadrupole magnet specifications for the Spectrometer Section.

Label	A	B	C
Quantity	1	3	2
Location	QS1	QS2, 3, 4	QS5, 6
Effective field length (m)	1.30	1.50	1.50
Pole-tip radius (m)	0.35	0.65	0.45
Warm-bore radius (m)	0.25	0.55	0.35
Quadrupole maximum field strength (T@poletip)	2.50	2.50	1.50
Quadrupole good-field region radius (m)	0.20	0.44	0.28
Integrated field non-uniformity (%)	1#	1#	1#
Sextupole maximum field gradient (T/m^2)	4.5	2.4	3.2
Octupole maximum field gradient (T/m^3)	8.2	2.5	4.9

Preliminary estimate; defined as the $n=6$ multipole contribution relative to the $n=2$ quadrupole contribution at 80% of the warm-bore radius, at maximum excitation.

6.5.1.2 Dipole magnets

The Spectrometer Section of the HRS contains two large dipoles, the Sweeper Dipole (DS1) and the Spectrometer Dipole (DS2)., A variety of considerations were made in deciding the designs of the dipole magnets in the preferred layout. The specifications for both dipole magnets as used in the ion-optical simulation of the preferred layout are shown in Table 6-9.

The poles of DS1 have a rectangular shape. The length of the magnet was kept as short as possible to enhance the acceptance for neutrons at forward scattering angles in the MoNA-LISA neutron detector array. This gap size (of 48 cm) corresponds to a vertical angular acceptance of ±90 mrad necessary to meet the neutron solid-angle coverage of 32 msr. DS1 provides a bend angle of 35º. The maximum field of DS1 is 2.5 T. The entrance pole face is perpendicular to the beam and the exit pole face has an angle of 35º and is, therefore, vertically focusing.
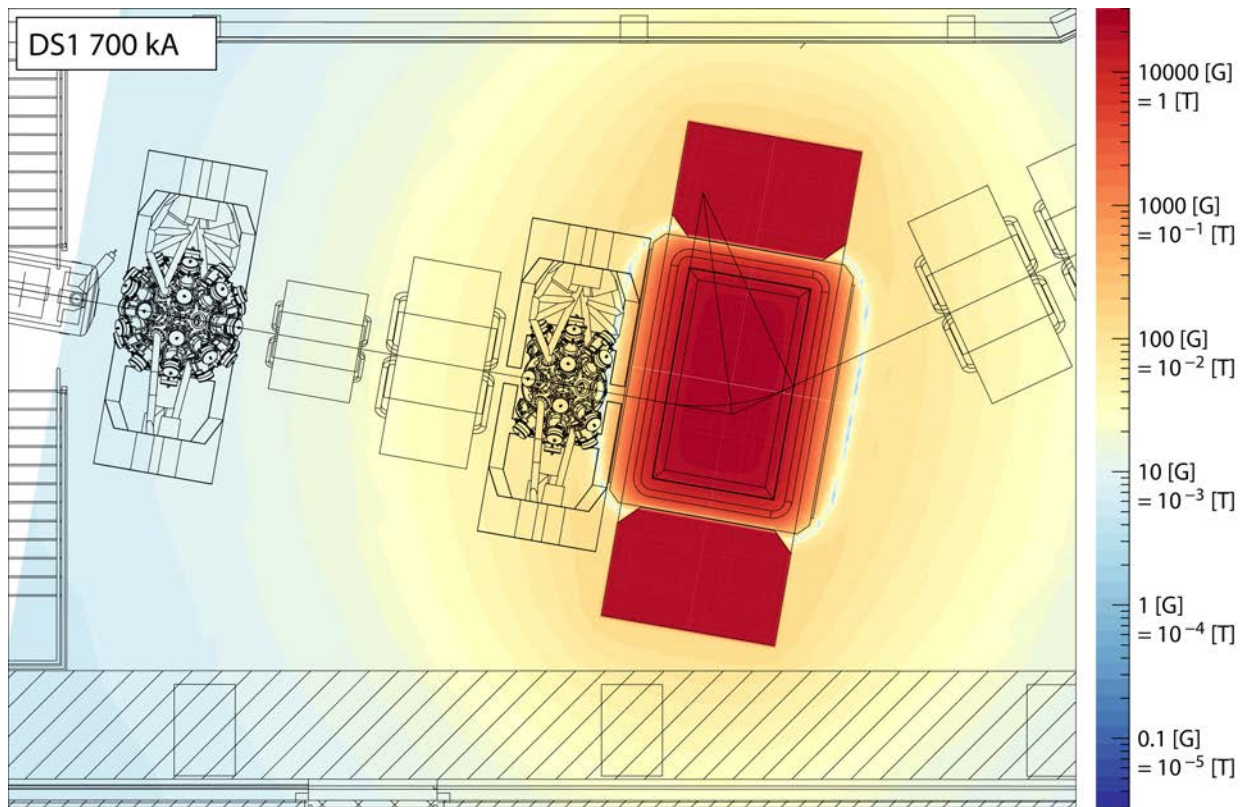
Figure 6.11 Magnetic stray fields around dipole magnet DS1. The magnetic field near the detector modules of the GRETA array placed just in front of DS1 for experiments in the invariant-mass mode is below 100 Gauss.

Stray-field calculations for the preferred Spectrometer Section alternative were performed for the magnets that are placed near detector systems sensitive to such fields. The most constraining specification is that it must be possible to operate GRETA (with its forward and backward rings removed) in front of DS1 (target location FS1). As shown in Figure 6.11, near the GRETA detector modules, the field strength is ~100 Gauss or less, significantly below the limit of 600 Gauss.

Similar stray-field calculations were performed for other magnets near the target areas and found not to pose a problem. Near target location FS0, magnetic fields from all magnets are less than 5 Gauss, allowing for the operation of detector systems that utilize phototubes and other components sensitive to the presence of fields. Therefore, there are no additional specifications for the Spectrometer Section magnets to reduce the fields further.

Spectrometer dipole DS2 is a symmetric sector dipole, which bends the charged-particle trajectories through 60°. It has a maximum field of 2 T and provides a high-quality field for precision analysis of the trajectories. The entrance and exit pole faces have rotations of 20°. They focus horizontally, which eliminates the need for additional quadrupole elements to provide the necessary focusing strength. The pole faces defocus vertically. A node in the center of DS2 improves the transmission through DS2 in the vertical direction, allowing for a relatively narrow gap size. Initial estimates of the necessary field quality were that a field homogeneity of better than 1% should be achieved for the purpose of operating the Spectrometer Section in the high-resolution mode. However, simulations using 5th-order transfer maps calculated in COSY INFINITY using the magnetic field profiles from ANSYS Maxwell analyses of the dipole and quadrupole magnet conceptual designs (See Section 9) were found to have acceptable results though the field homogeneity of the conceptual designs exceeded 1%.

During detailed design, the magnet designs will be optimized with respect to their cost, risk, and ion-optical performance to ensure the science program requirements are met at best value.

Table 6-9 Dipole magnet specifications for the Spectrometer Section.

Label	DS1	DS2
Quantity	1	1
Bending radius (m)	3.2	4.0
Maximum rigidity (Tm)	8.0	8.0
Maximum field (T)	2.5	2.0
Bending angle (deg)	-35	60
Arc length for central ray (m)	1.95	4.19
Vertical gap size (m)	±0.24	±0.11
Good field region width (m)	±0.45	±0.55
Integrated field non-uniformity (%)	1*	1*
Pole-face rotation entrance (deg)	0	-20
Pole-face rotation exit (deg)	35	-20

* Preliminary estimate

6.5.2 Diagnostics and detectors

Similar to the HTBL, the goals of the Spectrometer-Section diagnostics & detector system are defined as follows:

- To facilitate initial commissioning of the HRS
- To facilitate beam tuning and reaction-product identification & characterization

- To provide event-by-event tracking information (momentum, position, angle) & particle identification (energy-loss & total-kinetic-energy measurements) for physics analysis
- To enable long-term stable operation & provide appropriate machine protection

To achieve these goals, the specifications for the diagnostics and detectors have been formulated as described in this section.

As shown in Figure 6.1, the Spectrometer Section has two focal planes, FS1 and FS2. FS1 is primarily used for experiments in the neutron invariant-mass mode (See Section 6.3.2), although tracking detectors at this location can also be used in combination with detectors installed at FS2 to gain additional accuracy for tracking through the full Spectrometer Section to FS2. The trajectory information obtained at FS1 and FS2 is used to reconstruct the trajectories at the FS0 through an event-by-event inverse raytracing procedure. The energy-loss and total-kinetic-energy information is used to identify the isotope species by their mass and atomic numbers on an event-by-event basis. Based on the ion-optical properties of the Spectrometer Section and ample experience with running fast beam experiments with the S800 Spectrograph and Sweeper magnet at NSCL, the suite of detectors installed for neutron invariant-mass mode experiments at FS1 and for high-resolution mode experiments at FS2 must include the following:

- Tracking detectors that provide accurate and high-resolution position (1 mm (FWHM)) and angle information (2 mrad (FWHM)) to determine the trajectories of particles transported through the Spectrometer Section of the HRS on an event-by-event basis. They must be highly efficient (close to 100%), while being thin (less than 6 mg/cm^2) to reduce multiple scattering effects. The horizontal and vertical dimensions of the tracking detectors must be 100×60 cm^2 at FS1 and FS2 to cover the envelope of the beam trajectories. These detectors also need be able to operate at a rate of at least 10 kHz.
- A ΔE energy loss detector with an effective area and rate capability matching the values of the tracking detectors. The ΔE detector must achieve a resolution of $\sigma_{\Delta E}/\Delta E$ of 1.3% (2.3%) (FWHM) to achieve 4σ separation between isotopes that differ in charge number by one for Z=92 (Z=50).
- A timing scintillator with an area matching that of the tracking detectors providing a timing resolution of better than 150 ps. Two thicknesses must be available (100 mg/cm^2 and 300 mg/cm^2). The rate capability of the scintillator must be 1 MHz.
- A total kinetic energy (TKE) detector (hodoscope). It should have a surface and rate capability matching that of the tracking detectors and be sensitive to charged particles (TKE measurement) and γ rays (for isomer tagging and particle identification purposes). The resolution of the hodoscope should be better than 7% for 662 keV γ-rays.

A schematic layout of the detector configuration at FS1 and FS2 is shown in Figure 6.12.
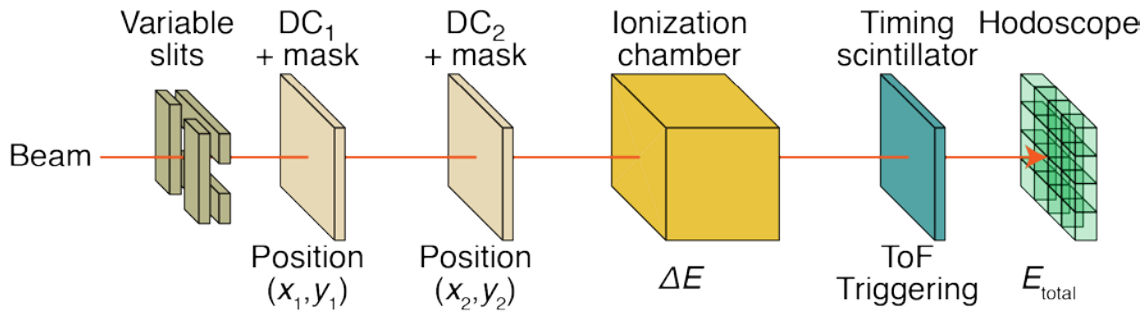
Figure 6.12 Schematic layout of the detector configuration of the diagnostic systems used at FS1 and FS2.

The detector suites are installed in vacuum chambers that are equipped with drives to insert masks in front of the tracking detectors. These masks are inserted for the purposes of the position calibration of the tracking detectors and removed during regular data taking. In addition, the chambers are equipped with a beam blockers/slits that can be inserted and positioned to intercept unreacted beam particles.

All detectors will be read out through data acquisition systems that run Laboratory supported data-acquisition software. The data acquisition system and software must facilitate efficient and high-performance integration with the data acquisition systems of ancillary detector systems.

The detector suite in FS1 must be easily retractable and insertable to accommodate efficient switches between the neutron invariant-mass and high-resolution modes. The tracking detectors at FS1 must be insertable remotely so that they can be activated and used in combination with the detector suite at FS2.

The requirements for the diagnostics and tracking detectors for the Spectrometer Section are summarized in Table 6-10 for general system requirements, Table 6-11 for requirements for the tracking and timing detectors for the Spectrometer Section, and Table 6-12 for requirements for energy-loss detectors in the Spectrometer Section.

Table 6-10 General system requirements for the diagnostics and detector systems of the Spectrometer Section

Parameter	General system requirement
Remotely retractable	Yes (FS1), No (FS2)
Position alignment accuracy	≤ 0.5 mm (transverse to the beam) ≤ 1 mm (long the beam axis)
Accessibility	replacement possible within < 6 hours
Vacuum requirement	10^{-5} Torr vacuum compatible

Table 6-11 Tracking and timing detector requirements for the Spectrometer Section

Parameter	Requirement
Transmission	100%
Single particle detection	Yes
Thickness	Tracking ➔ ≤ 6 mg/cm^2 Timing ➔ 100-300 mg/cm^2
Sensitive area	FS1 ➔ 100x60 cm^2 FS2 ➔ 100x60 cm^2
Resolution (FWHM)	Position ➔ ≤ 1 mm Timing ➔ ≤ 150 ps
Rate capability	Tracking ➔ ≥ 10,000 Hz Timing ➔ ≥ 1 MHz

Table 6-12 Energy-loss detector requirement for the Spectrometer Section

Parameter	Requirement
Transmission	Ion Chamber ➔ 100% Hodoscope ➔ No
Sensitive area	FS1 ➔ 100x60 cm^2 FS2 ➔ 100x60 cm^2
Energy resolution	Ion Chamber ➔ 1.3% Hodoscope ➔ ≤ 7% (662 keV γ-rays)
Rate capability	≥ 10,000 Hz

6.5.3 Vacuum systems

With the lattice design of the Spectrometer Section established, the locations of the magnet are fixed on the floor layout with the conceptual designs of the magnets complete, the dimensions of the vacuum chambers (beam pipes) have been identified. Also, with the standard sets of diagnostic instruments defined, the dimensions of the diagnostic chambers have been identified.

The general requirement for the vacuum systems for the Spectrometer Section is that the systems be able to evacuate to the pressure of 10^{-5} Torr. At this level, the lateral, angular, and energy spreads due to interactions with residual gas in the beam line do not contribute significantly to the uncertainties in the tracking of the particles. At 10^{-5} Torr, the lateral spread can become ~150 μm (FWHM) over the full lengths of the HTBL and Spectrometer Section, which is still much smaller than the position resolutions of the focal plane tracking detectors. At 10^{-4} Torr, the lateral spread increases to ~500 μm (FWHM), which is comparable to the position resolutions of the detector systems. In addition, a pressure of 10^{-5} is required for the operation of cryogenic targets (e.g. a Liquid Hydrogen Target) at FS0. At higher pressures, the residual gas that freezes on the surfaces of the cryogenic systems reduces the ability to reflect heat and the target becomes less stable.

The operation of the Spectrometer Section requires gate valves to isolate diagnostic equipment in beam chambers needed during maintenance. Gate valves separate each section with dedicated pumping station with vacuum gauges. Finally, the locations of bellows necessary to accommodate alignment have been identified.

Turbo-molecular pumping systems are sensitive to the presence of magnetic fields and cannot operate in fields in excess of 50 Gauss. For some of the magnets with significant stray fields, such

as DS1 (see Figure 6.11), this requires that these pumps are placed at appropriate distances from such magnets.

6.6   References

[ANS18] ANSYS® MAXWELL, Release 19.1, ANSYS, Inc.
[BAZ02] D. Bazin et al., Nucl. Instrum. Meth. Phys. Res. A 482, 307 (2002)
[BAZ03] D. Bazin et al., Nucl. Instrum. Meth. Phys. Res. B 204, 629 (2003)
[COS11] M. Berz and K. Makino, MSU Report MSUHEP 101214 (2011), 060804-rev (2013)
[HRS14] HRS Working group, A high Rigidity Spectrometer for FRIB (2014)
[TAK13] H. Takeda et al., Nucl. Instrum. Methods Phys. Res., Sect. B **317**, 798 (2013)
[TAR16] O. B. Tarasov and D. Bazin, Nucl. Instr. and Meth, in Phys. Res. B 376, 185 (2016)
[TAR08] O. B. Tarasov and D. Bazin, Nucl. Instr. and Meth, in Phys. Res. B 266, 4657 (2008)

7 Diagnostics and Detectors

7.1 Introduction and overview

The Diagnostics and Detectors scope includes the materials and manpower needed to acquire, bench test, install, test in situ, and perform the final integrated testing without beam. The scope is visualized in Figure 7.1 and the associated WBS elements are shown in Table 7-1.

Table 7-1. Diagnostics and Detectors WBS.

Experimental Systems - High Rigidity Spectrometer	**HRS.3**
High Transmission Beamline (HTBL)	**HRS.3.01**
High Transmission Beamline Diagnostics and Tracking	**HRS.3.01.02**
HTBL Diagnostic Devices	*HRS.3.01.02.01*
HTBL Tracking Detectors	*HRS.3.01.02.02*
Spectrometer Section	**HRS.3.02**
Spectrometer Section Structural Support and Access to Detector Systems	**HRS.3.02.04**
Spectrometer Section Detector Support and Access at Reaction Target	*HRS.3.02.04.01*
Spectrometer Section Detector Support for MoNA-LISA Detector System	*HRS.3.02.04.02*
Spectrometer Section Detector Access Platforms	*HRS.3.02.04.03*
Spectrometer Section Focal Plane Detector Systems	**HRS.3.02.05**
Spectrometer Section High Resolution Mode Focal Plane Detector Systems	*HRS.3.02.05.01*
Spectrometer Section Invariant Mass Mode Focal Plane Detector Systems	*HRS.3.02.05.02*

To support the diverse scientific program of the HRS described in Section 4, it is important that the HTBL and the Spectrometer Section of the HRS are provided with the necessary diagnostics and detectors for tuning and tracking the rare isotopes. Based on the requirements summarized in Section 5.6.2 for the HTBL and in Section 6.5.2 for the Spectrometer Section, appropriate diagnostics and detector systems were selected as presented in this Section. Figure 7.1 outlines the schematic layout of the detector technologies that meets the scientific requirements of the HRS; the basic concepts, operational conditions and performance optimization of the planned detector technologies are based on the solid experience matured in running the NSCL facility over several decades, including the A1900 Fragment Separator [MOR03], the S800 Spectrograph [YUR99], and the Sweeper Magnet [BIR05] system.

7.1.1 The HTBL diagnostics and tracking systems

The main goals of the HTBL diagnostics and detector systems are to:
- Facilitate initial commissioning of the HRS;
- Facilitate tuning prior and during experiments run with the HRS by providing the necessary characterization of the beam properties. This includes measurements of 2D beam profiles, trajectory angles, and transmission through the HTBL;
- Provide event-by-event tracking information (momentum, position, angle) for the physics analysis of events recorded in the HRS;

- Provide long-term stable beams operations by monitoring service for beam transport and machine protection (see also Section 7.3.5)

As described in Section 5.3, the HTBL accommodates two ion-optical beam-transport modes: the achromatic and dispersion-matched modes. The relationships of these modes to the tracking detector stations in the HTBL are shown in Figure 7.2.

In the achromatic beam-transport mode, the event-by-event measurements of the momentum and angle of the beam particles are required if the momentum and angular resolution of particles detected in the focal plane of the HRS must be better than the momentum and angular spreads in the beam prior to the reaction target at FS0. This can be accomplished by using tracking detectors located at FB1 and/or FB3 (See Section 5.3.2).
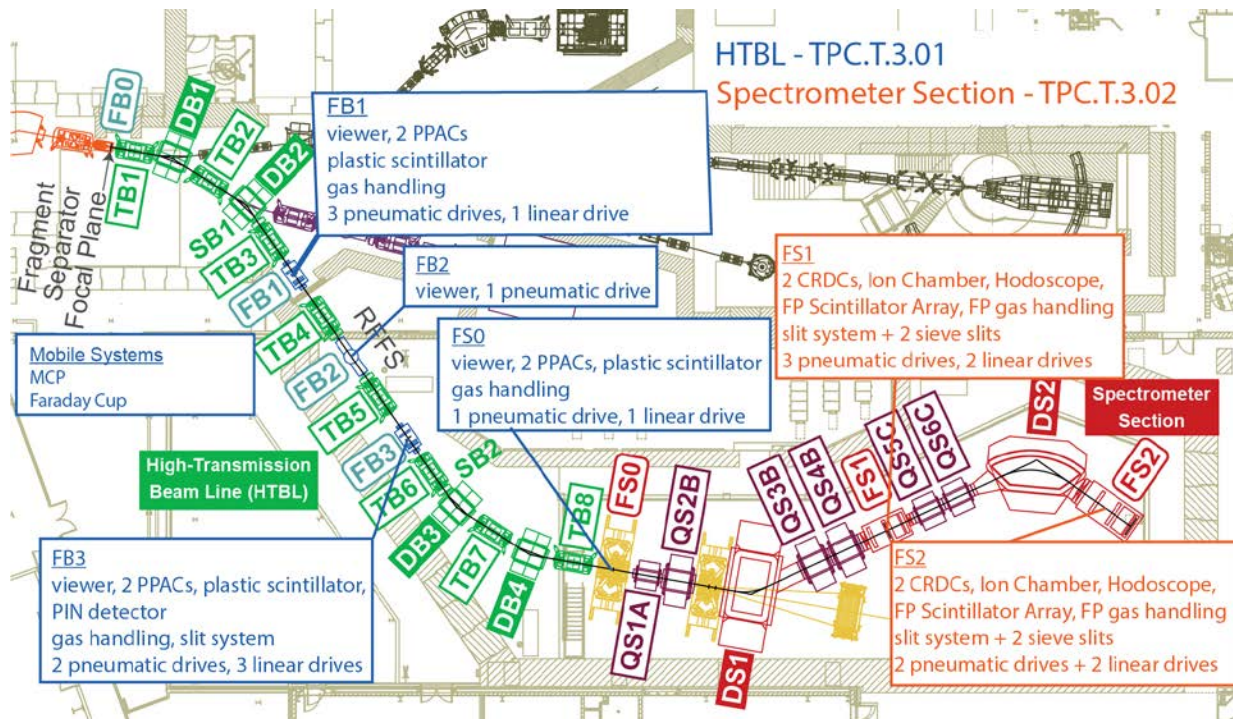
Figure 7.1. Schematic layout of the diagnostics/detector systems for the HRS. Systems at FB1, FB2, FB3, FS0, and mobile systems (blue border) are part of WBS element TPC.T.3.01. Systems at FS1 and FS2 are part of WBS element TPC.T.3.02.

The dispersion-matched mode allows for the measurement of tracks in the Spectrometer Section with momentum resolutions better than the momentum spreads in the beam without the need for event-by-event tracking in the HTBL, as described in Section 5.3.3. However, for TOF-$B\rho$ mass measurements, the momentum of the particles is determined by measuring the position of the beam particles at FS0 (See Section 0). In addition, for some experiments it might be important to know the hit-position and/or angle at an event-by-event basis at the target location FS0 in order to optimize the operation of ancillary detectors. For example, the Doppler reconstruction for in-beam γ-ray spectroscopy with GRETA can benefit from the accurate determination of the hit location on the target, in particular when the dispersion-matched beam optics is employed and the beam spot on the reaction target (FS0) is large.

In both beam transport modes, viewers that can be monitored by camera are very beneficial for beam tuning purposes. Hence, the HTBL must accommodates such viewers at FB1, FB2, FB3, and FS0.
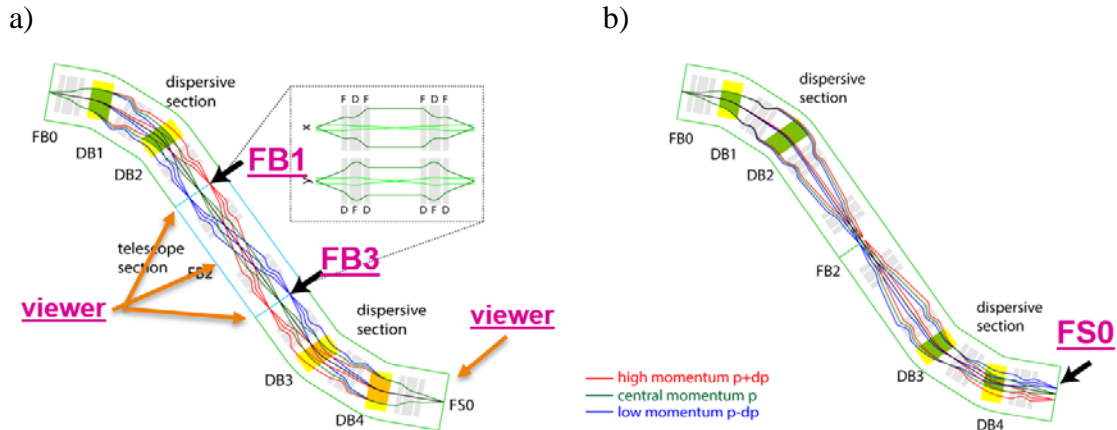
Figure 7.2. Schematic of the basic diagnostic systems configurations along the HTBL, used for the achromatic mode of operation (a) and for the dispersion-matched mode (b).

7.1.2 The Spectrometer Section diagnostics and detectors systems

The main goals of the diagnostics and detector systems of the Spectrometer Section are to:
- Facilitate initial commissioning of the HRS;
- Facilitate beam tuning and reaction-product identification and characterization
- Provide event-by-event tracking information (momentum, position, angle) and identification (energy loss and total energy measurements) for the physics analysis of events recorded in the HRS;
- Provide long-term stable beams operations by monitoring service for beam transport and machine protection.

The conceptual designs of the detector systems for the Spectrometer Section of the HRS are based on existing systems used at NSCL for the S800 spectrograph [YUR99] and Sweeper magnet system [BIR05]. Their use is supported by decades of experience in developing, maintaining and operating these devices [GAD16]. High-resolution identification of reaction products generated in the heavy-ion reactions exploits the dispersion of magnetic spectrometers in conjunction with sophisticated particle detectors. The ion-optical calculations of Section 6.3 imply the need of covering a large surface at the focal planes. From this point of view, gaseous detectors are a convenient solution for providing good tracking capability for event-by-event momentum vector determination. They also deliver good resolution for charge (q) measurements and for energy (E)/energy-loss (ΔE) spectroscopy, which is crucial for an efficient particle identification. As discussed in Section 6, particle trajectories are reconstructed by software using the momentum vectors measured in the focal plane of the Spectrometer Section (either at FS1 or FS2). The timing and energy-loss measurements provide the information to perform particle identification. Furthermore, measurement of the total kinetic energy allows one also to disentangle the

ambiguities in the charge distributions of the reaction products generated in the target for each energy, mass and nuclear charge.

As discussed in Section 6.3, the Spectrometer Section was designed to operate in three basic modes, each of them with specific demands in term of focal-plane detector performance:

- The high-resolution mode of operation, discussed in Section 6.3.1, provides the full spectroscopy capability of the HRS. To achieve the highest mass and momentum resolving powers for heavy rare isotopes, a long flight path is required (in excess of 25 m; the preferred layout achieves 33.6 m) and the focal plane at FS2 is used. The space around the FS0 reaction target station provides the opportunity to install ancillary detectors, including additional tracking detectors

- In the neutron invariant-mass mode, discussed in Section 6.3.2, the momentum vectors of the all reaction products, including the neutrons, need to be measured. The reaction target is placed immediately in front of the sweeper magnet, while the focal plane detector system is placed at the focal plane FS1. In this configuration, only part of the spectrometer is engaged as the transmission through the full Spectrometer Section is compromised by placing the reaction target right in front of the DS1 Sweeper dipole magnet. The fast neutrons emitted within a cone in the forward direction are detected by the MoNA-LISA array [BAU05,MRI09] and their momenta are assessed through a time-of-flight measurement. The required accuracy for the reconstruction of the momentum vector of the charged particles is lower compared to the experiments performed in the high resolution mode.

- For ToF-$B\rho$ mass measurements, discussed in Section 0, the HTBL is operated in dispersed-matched configuration, with no reaction target at FS0. Instead, the position at FS0 is measured with a dedicated high-resolution tracking detector to determine the rigidity of the beam particles on an event-by-event basis. The time-of-flight of the particles is measured with dedicated high-precision timing detectors between the ARIS Fragment Separator and the FS2 focal plane in order to create a very long flight path (of 115 m in the preferred layout).

7.2 Requirements and performance

To meet the scientific specifications discussed in Section 4, the diagnostic systems and tracking detectors for the HRS must satisfy technical requirements discussed in Section 5.6.2 for the HTBL and in Section 6.5.2 for the Spectrometer Section. These are reiterated here, in relation to specific detector technologies that will be employed and discussed in more detail in Section 7.3.

7.2.1 Requirements for the HTBL diagnostics and detector systems

General requirements for the HTBL diagnostic systems are summarized in Table 7-2. All the devices installed in the chambers along the HTBL must be retractable using remotely-controlled linear or pneumatic drives. Typical positioning accuracies of 0.5 mm, in the direction transverse to the beam, and 1 mm, along of the beam axis, are achieved by precise mechanical alignment of the drives. All the instrumentation installed in the HTBL image boxes are accessible through

dedicated access ports and flanges, providing the capability for the repair or replacement of damaged devices within 4 hours. For delicate gas-filled detectors that are equipped with thin vacuum windows, spares must be available. In addition, all the devices mounted inside the chambers are required to be vacuum compatible at a level of 10^{-5} Torr to ensure negligible interference with the operation of all systems and the transport of heavy-ion beams.

Table 7-2 General detector system requirements for the HTBL

Parameter	General Detector System Requirement
Remotely retractable	Yes
Positioning accuracy	≤ 0.5 mm (transverse to the beam) ≤ 1 mm (along the beam axis)
Accessibility	replacement possible within < 4 hours
Vacuum requirement	10^{-5} Torr vacuum compatible

As discussed in Section 7.3, the primary type of particle-tracking detector for the HTBL is the Delay-line Parallel-Plate Avalanche Counter (D-PPAC) [KUM01,KUM13], and the requirements for these detectors are provided in Table 7-3. The tracking detectors provide event-by-event particle detection at FB1, FB3 and FS0, with 100% transmission and a spatial resolution of better than 1 mm (FWHM). Minimum energy loss and low angular straggling require low material budgets: the D-PPACs have thicknesses below 10 mg/cm^2. For applications in which the thickness of the tracking medium must be minimized, the use of position-sensitive micro-channel plate (MCP) detectors [MON05] is an alternative. The rate capabilities of the tracking detectors achieve a few hundred kHz for both D-PPACs and MCPs.

Table 7-3 Tracking and timing detector requirements for the HTBL, satisfied by D-PPAC and plastic scintillators, respectively.

Parameter	Tracking/Timing Detector Requirement
Transmission	100%
Single particle detection	Yes
Thickness	Tracking ➜ ≤ 10 mg/cm^2 Timing ➜ ≤ 100 mg/cm^2
Effective area	Tracking ➜ 20x20 cm^2 Timing ➜ 20x20 cm^2
Resolution (FWHM)	Position ➜ ≤ 1 mm Timing ➜ ≤ 150 ps
Rate capability	Tracking ➜ ≥ a few hundred kHz Timing ➜ ≥ 1 MHz

The principal timing detectors (at FB1, FB3, and FS0) will be plastic scintillators coupled to vacuum photo-multiplier tubes (PMTs) [HOI11], for which the requirements are also listed in Table 7-3. The plastic scintillators for timing measurements can be operated above 1 MHz and have thicknesses below 100 mg/cm^2. Timing resolutions of better than 150 ps should be obtained.

Energy loss measurement for particle identification (PID) at FB3 is achieved using thin ($\leq$500 micron) silicon PIN diode [GRO75], for which the requirements are listed in Table 7-4. Commercially available silicon PIN detector have a maximum area of 5x5 cm^2, which ensures optimum performance in terms of resolution and rate. In order to cover the full dispersive coordinate for the energy-loss measurement at the FB3 chamber, an array of 4 PIN elements of 5x5 cm^2 will be carefully assembled to minimize dead areas in between the elements.

In Table 7-5, the requirements for the viewer systems are provided. These relatively simple systems provide visual feedback for beam-tuning purposes.

Table 7-4 Energy-loss detector requirements for the HTBL, satisfied by the usage of silicon PIN diode detectors.

Parameter	ΔE Detector Requirement
Transmission	100%
Sensitive area	5$\times$5 cm^2 each (with fiducials for calibration) 4 aligned detector for 20$\times$5 cm^2 coverage
Thickness	$\leq$ 500 μm
Energy resolution	$\leq$ 3% (@ 5.5 MeV α-particles)
Rate capability	$\geq$ 1000 Hz

Table 7-5 Viewer system requirements for the HTBL

Parameter	Viewer System Requirement
Single particle detection	No
Transmission	No
Coating	Thin luminescent layer: emits light when exposed to heavy ion beam
Sensitive area	20$\times$20 cm^2 (with fiducials for calibration)

7.2.2   Requirements for the Spectrometer Section diagnostics and detector systems

General requirements for the tracking detectors in the Spectrometer Section are provided in Table 7-6. Typical positioning accuracies of 0.5 mm in the direction transverse to the beam, and 1 mm, in the direction along the beam axis are achieved through precise mechanical alignment. All the instrumentation installed in the focal-plane vacuum chambers are accessible through dedicated access ports and flanges. Expeditious replacement of damaged devices must be achieved within 6 hours and for the relatively delicate gas-filled tracking detector systems with thin exit and entrance foils, spares must be available. All the devices mounted inside the chambers are required to be vacuum compatible at a level of 10^{-5} Torr to ensure negligible interference with the operation of all subsystems and the transport of heavy-ion beams. The tracking detectors at FS1 are primarily used for invariant-mass spectroscopy experiments, but can also serve as additional tracking for experiments in which the full Spectrometer Section up to FS2 is utilized. Hence, these tracking detectors should be retractable. The ionization chamber and hodoscope at FS1 must be easily removable so as not to obstruct particles that are to be transported to FS2. The detector systems mounted at FS2 do not need to be retractable.

Table 7-6 General system requirements for the diagnostics and detector systems of the Spectrometer Section

Parameter	General system requirement
Remotely retractable	Yes (FS1), No (FS2)
Position alignment accuracy	≤ 0.5 mm (transverse to the beam) ≤ 1 mm (long the beam axis)
Accessibility	replacement possible within < 6 hours
Vacuum requirement	10^{-5} Torr vacuum compatible

The requirements for the tracking detectors used in the Spectrometer Section of the HRS are provided in Table 7-7. The tracking detectors at the focal planes provide event-by event particle detection, with 100% transmission. To avoid significant multiple scattering and to minimize energy losses, the thicknesses of the tracking detectors are kept small. The detector system in the focal planes of the Spectrometer Section (FS1 and FS2) must cover large areas. Therefore, for the transverse position and angle tracking, a set of gas-filled Drift Chambers (DCs), located about 1 m apart, are used. They must provide the position with a spatial resolution of 1 mm (FWHM) and be able to handle rates in excess of 10 kHz. A think plastic scintillator must provide the timing signal and cover the same area as the tracking detectors. The timing resolution should be better than 150 ps. The rate capability of the scintillator should exceed 1 MHz.

Table 7-7Tracking and timing detector requirements for the Spectrometer Section

Parameter	Requirement
Transmission	100%
Single particle detection	Yes
Thickness	Tracking ➔ ≤ 6 mg/cm^2 Timing ➔ 100-300 mg/cm^2
Sensitive area	FS1 ➔ 100×60 cm^2 FS2 ➔ 100×60 cm^2
Resolution (FWHM)	Position ➔ ≤ 1 mm Timing ➔ ≤ 150 ps
Rate capability	Tracking ➔ ≥ 10,000 Hz Timing ➔ ≥ 1 MHz

The energy-loss and total kinetic energy of the particles that enter the focal planes at FS1 and FS2 must be determined with good precision. The requirements are provided in Table 7-8. An ion-chamber is needed for an accurate energy-loss measurement with a resolution in energy loss of 1.3% to achieve 4σ separation between isotopes with neighboring charge number up to Z=92. For the total kinetic energy measurement, which is important for separating charge-states that enter the focal planes, the particles are stopped in a hodoscope that must have a resolution of better than 7% for 662-keV γ rays. The sensitivity to γ-rays is helpful for experiments in which isomers are produced that emit photons after being stopped in the focal plane. In this manner events in which isomers are created can be identified. Both the energy-loss and total kinetic-energy measurements should be performed at rates in excess of 10 kHz. It is noted that the plastic scintillator used for

timing purposes also provides an energy-loss signal, but with relatively poor resolutions compared to an ion chamber. The combination of the timing, energy-loss, and total kinetic-energy signals provides the particle identification capability of the Spectrometer Section of the HRS.

Table 7-8 Energy-loss detector requirement for the Spectrometer Section

Parameter	Requirement
Transmission	Ion Chamber ➔ 100% Hodoscope ➔ No
Sensitive area	FS1 ➔ 100×60 cm^2 FS2 ➔ 100×60 cm^2
Energy resolution	Ion Chamber ➔ 1.3% Hodoscope ➔ ≤ 7% (662 keV γ-rays)
Rate capability	≥ 10,000 Hz

7.3 The detector systems of the HRS

The necessary specifications can be met by utilizing designs in use at NSCL that have long-term proven performance and benefit from continuous development and optimization. Therefore, the preferred alternatives of the detector systems of the HRS are based on these existing technologies, which have been vetted against alternative technologies through years of performing experiments with fast beams at NSCL. Therefore, no special development program is required and the systems selected carry low risk with known performance and cost. For some detector systems, upgrades of technologies used at NSCL are ongoing and the preferred alternative benefits from these upgrades, which will be tested with rare-isotope beam prior to the implementation of the HRS. In the following, each of the detector and diagnostics systems are briefly discussed.

7.3.1 The focal planes of the HTBL

As outlined in figure 7.1, the diagnostics system includes several diagnostics stations deployed along the HTBL. The first chamber (FB1) is positioned after the first bending dipole of the ARIS Fragment Separator in the HTBL and is equipped with two delay-line parallel-avalanche counters (D-PPACs) that serve to determine the beam-particle position and angle, and a plastic scintillator for providing a local timing signal. The schematic layout is provided in figure 7.3. This information is recorded on an event-by-event basis so that it can be correlated with measurements in other detector systems.
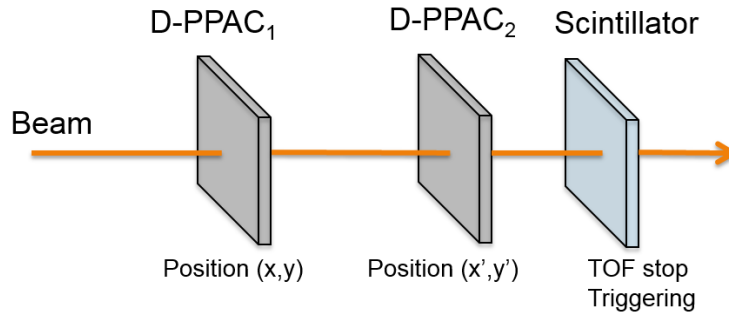
Figure 7.3. Schematic layout of the detector configuration of the diagnostic systems used at FB1 and FS0.

The third diagnostics chamber (FB3) is placed before the bend to the target station (FS0). It has a similar detector layout as the FB1 station, with the addition of a silicon PIN diode for the measurement of energy-loss, as schematically depicted in figure 7.4. The diagnostic chamber at FB3 also includes a variable slit system, which allows for beam shaping and background rejection. In addition, the slit system is necessary for a future insertion of a RF Fragment Separator at FB2, as discussed in Section 4.3.2.7.3.

FB2 is located in between the FB1 and FB3 and will only be equipped with a beam viewer for visual tuning of the beam through the HTBL. FB2 is otherwise reserved as the future location of a RF Fragment Separator.
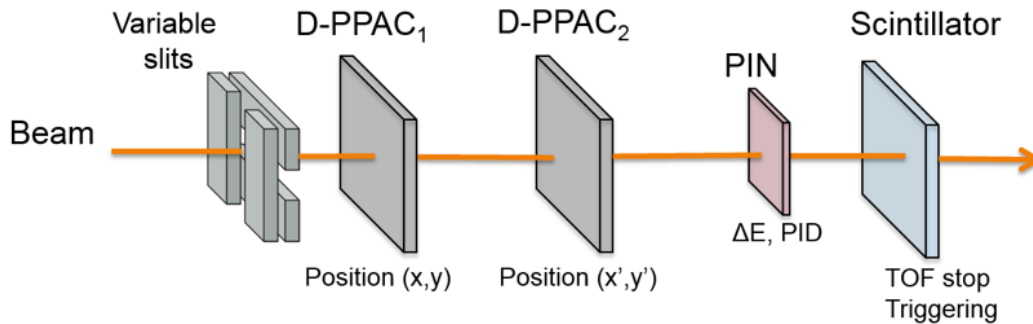
Figure 7.4. Schematic layout of the detector configuration of the third diagnostics station (FB3), which include a tracking system (two D-PPACs), a PIN diode for energy-loss measurement for PID, a plastic scintillator, as well as a system of variable slits for beam tuning and other diagnostic purposes.

The HTBL ends at the reaction target station (FS0), which can, if desirable for the experiment, be equipped with a set of D-PPACs for tracking and a thin plastics scintillator for timing, just like FB1. The detailed configuration of the setup around FS0 will vary from one experiment to another. Often, no tracking or timing detectors will be placed at FS0, but for a subset of experiments, high precision tracking or timing is required at the target. An MCP detection system for accurate position determinations at high rates can also be placed at FS0.

All the diagnostics boxes along the HTBL are equipped with a scintillating viewer plate (red CRT phosphor – Y_2O_2S:Eu) monitored by a ultra-low light bullet-type camera.

Most of the detector systems utilized at stations FB1, FB2, FB3, and FS0 can be inserted with pneumatic drives that move the detectors in or out of the path of the beam. Plastic scintillators are operated with linear drives, as the detectors should be moved by small amounts from time-to-time to prevent excessive localized radiation damage that deteriorates the signal quality. The slit system at FB3 is operated with linear drives as well.

All diagnostics chambers that have PPACs have dedicated gas handling systems. All chambers provide access to the front-end electronics, HV power supplies, and other signal and control system via flanges equipped with appropriate feedthroughs.

7.3.1.1 HTBL diagnostics chamber

The conceptual designs of the chambers FB1, FB3, and FS0 for the HTBL are based on the chamber used at the NSCL A1900 fragment separator focal plane, which is shown in figure 7.5a. The vacuum chamber is a large-volume box of stainless steel, a side of which (perpendicular to the beam trajectory) can be fully opened for easy access to its contents. The top and bottom plates have several ports for mounting the device drives and pumping equipment. The compact, but versatile design of this diagnostic chamber makes it suitable for use in the HTBL.

At FB2, a relatively simple system is required for inserting a viewer and a standard cross chamber (figure 7.5b) presently used at various locations in NSCL for similar purposes serves as the concept for use at the HRS. For all the diagnostic chambers, dedicated flanges are used to mount the drives that move devices into the beam path and to provide electrical/signal feedthroughs or vacuum gauges.
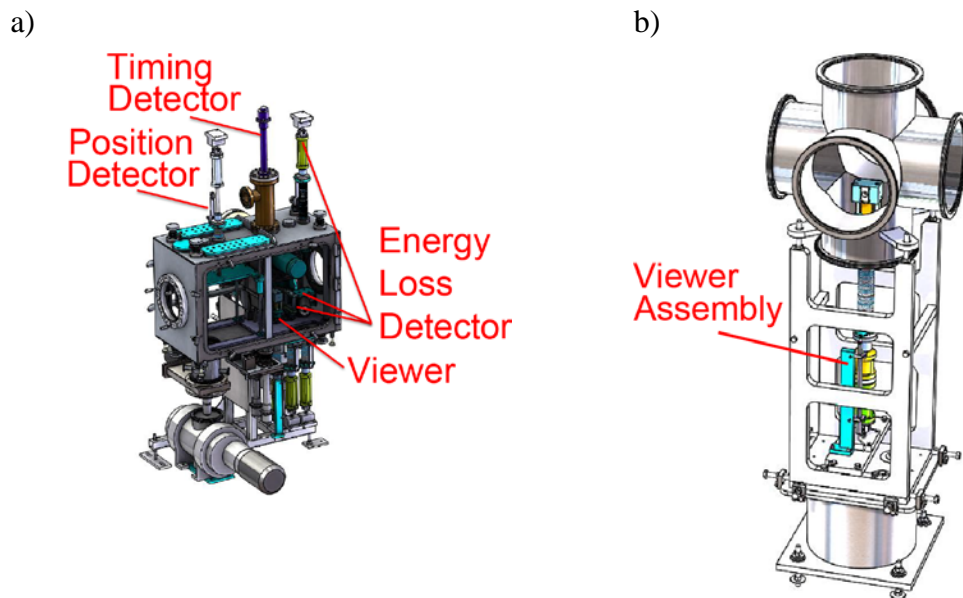
Figure 7.5. a) Design of the Image box of the A1900 Fragment Separator, which serves as the model for the design of the HTBL diagnostics boxes FB1 and FB3. B) Design of a standard cross chamber used to insert viewers and other simple diagnostics and detector system, which serves as model for the box at FB2.

7.3.1.2 The delay-line parallel-plate avalanche counters (D-PPACs)

The positions of the ions transported along the HTBL are measured at stations FB1, FB3, and FS0 by pairs of two-dimensional delay-line parallel plate avalanche counters (D-PPACs) [SWA74,HEM75,PUL02,CAR13,KUM13]. From these position measurements, the trajectory angle can also be determined. In the achromatic beam-transport mode, the momentum of the beam particles can also be determined (see Section 5.6.2). Each D-PPAC has an active area of 20 cm by 20 cm and is filled with isobutane at a typical pressure of 5-6 Torr by using a gas handling system. The detector consists of a cathode foil with a series of aluminum strips oriented in the non-dispersive direction, followed by an anode plate and a second cathode foil with the strips oriented in the dispersive direction. The strips are coupled to a discrete LC delay-line circuit and the position of the impinging particle is derived from the time difference between induced signals propagating along the delay-line circuit. Because the drift direction of the electrons is parallel to the beam direction, the drift-times are short, and high the D-PPACs can operate at high rates without pile-up effects.

The tracking system based on D-PPACs provides:

- A position resolution of about 1 mm (FWHM) over the entire active area (20×20 cm^2)
- A high counting-rate capability of a few hundred kHz
- Energy-losses that are low and independent of hit position for the particles passing through the detector
- Good signal-to-noise ratio for heavy-ions
- Cost-effective production in combination with a relative ease of maintaining and repairing the detectors

7.3.1.3 The plastic scintillator

In order to determine the Time-Of-Flight for the particle identification and to provide trigger signals for other tracking detectors, the HTBL includes plastic scintillators at chambers FB1, FB3, FS0. The detectors (ELJEN plastic scintillator type EJ-230 with a light output of 64% anthracene and a rise time of 0.5 ns [ELJ18]) have an active area that matches that of the tracking detectors (20×20 cm^2). Thinner scintillator detectors are used for heavier ion species. The scintillation light emitted by the scintillator is read out by vacuum photomultipliers (HAMAMATSU type R4998, with TTS 0.16 ns; QE 22 %, assembly H6533).

For high-precision timing measurements, required for ToF-$B\rho$ mass-measurements, specialized systems will be adopted, which are outside of the scope of the HRS, such as small plastic scintillators fitted with two or more photomultipliers (see e.g. [MAT12]). These detectors are relatively inexpensive, but benefit from continuous development specific for particular experiments.

7.3.1.4 The silicon PIN detector

The charge and mass identifications are based on the combined measurements of energy loss and time-of-flight of the beam particles transported along the HTBL. An accurate energy loss spectroscopy for the atomic-number identification is performed with a thin silicon PIN detector [HAR96,TIN08] mounted in chamber FB3. The ability to identify atomic numbers of fission

fragments of known mass and velocity using the energy-loss method depends on the difference in mean energy loss of adjacent atomic numbers, the energy-loss straggling, and the precision of the energy-loss measurement. The limiting factor for atomic-number resolution of the beam particles using the energy-loss method is charge-transfer straggling and electronic energy straggling. Other contributions to the energy-loss width such as absorber path length difference must be kept to a minimum. The energy-loss measurement must be performed in extremely thin and uniform absorbers due to the large stopping powers of heavy-ions.

A large assortment of silicon-based detector technologies for energy-loss measurement are commercially available. Typical energy resolution are within the range of a few percent at 5.5 MeV (α particle), depending of the thickness of the detector effective area, which can range be made as thin as 100 microns. Good resolution is achieved thanks to the excellent thickness uniformity across the detector area, made possible by current advanced silicon production technologies.

7.3.1.5 The position-sensitive multi-channel plate (MCP)

Detectors for heavy-ions based on Micro-Channel Plates (MCP) have been widely used for many years in experimental set-ups for nuclear physics studies at low and intermediate energies [JAG02,ARN14,MEI15,HON16]. These detectors can withstand incident-beam intensities of around 100 kHz at long exposure before degradation in resolution and they are characterized by an extremely low material budget (~70 $\mu g/cm^2$). Such features make MCPs desirable as tracking detectors for experiments requiring high intensity rare-isotope beams and/or when minimum energy loss is required. Accurate position sensitivity (below 1 mm) in one or two directions can be achieved by suitable read-out systems. Although less convenient to utilize and requiring more calibration and service as PPACs for tracking, for specific applications the use of an MCP is desirable. MCP detectors require a vacuum of 10^{-6} Torr. Since this is a more stringent requirement than for the rest of the beam line, it can be addressed by adding local pumping capacity, as is presently done when MCPs are used in combination with the S800 Spectrograph at NSCL.

7.3.2 The focal planes of the Spectrometer Section

The focal planes of the Spectrometer Section are equipped with various detectors for trajectory reconstruction as well as particle identification (PID). The basic detector system configuration planned for the Spectrometer Section is based on the focal plane detector array of the NSCL S800 Spectrometer [YUR99,BAZ03], and was described in section 7.2.2. It consists of a series of two x/y drift chambers, an ionization chamber, a plastic scintillator for timing and a hodoscope, as schematically depicted in figure 7.6.
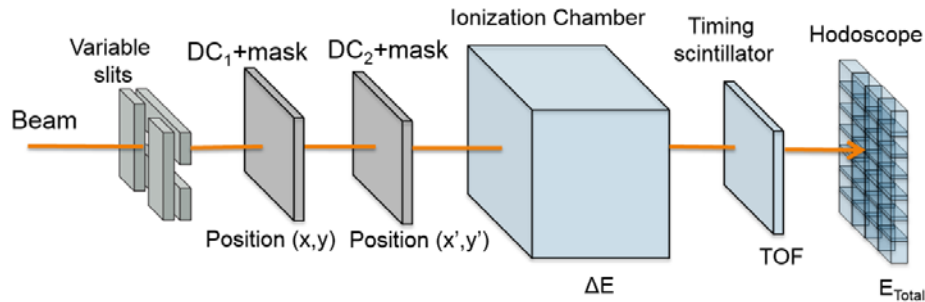
Figure 7.6. Schematic layout of the detector configuration of the focal planes of the Spectrometer Section.

7.3.2.1 Focal plane vacuum chamber

The vacuum chambers for the focal plane detector system of the Spectrometer Section are large and must maintain a vacuum of 10^{-5} Torr. Therefore, they will be constructed from welded stainless-steel plates. The concept for these chambers is similar to the one used for the Sweeper Magnet system at NSCL. The main difference between the existing system (depicted in figure 7.7) and the system required for the HRS is the size of the chamber, as the focal-plane detectors are larger.
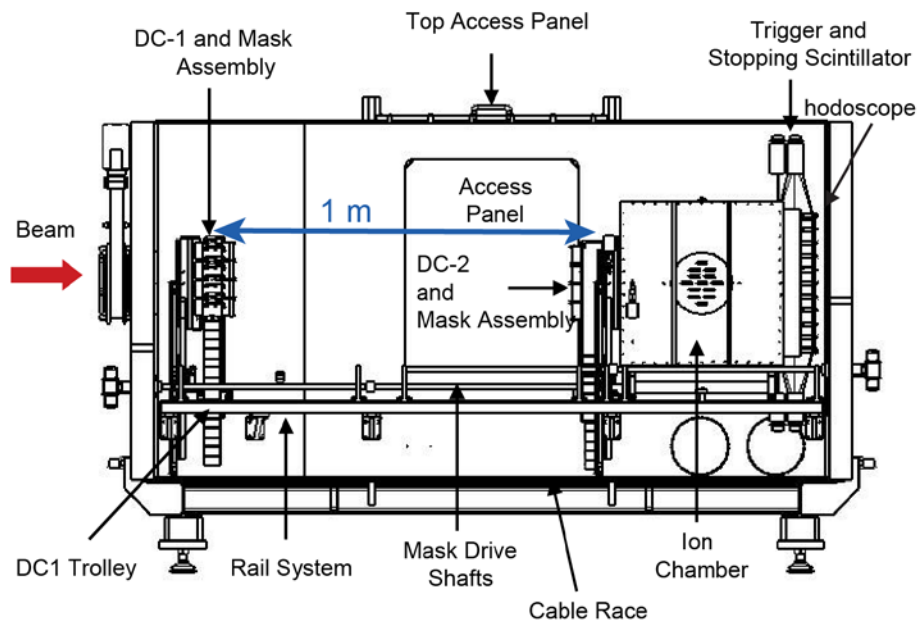
Figure 7.7. Layout of the existing charged-particle detector chamber as presently used for experiments with the Sweeper Magnet at NSCL. The focal-plane detector chambers for the HRS have comparable layout, but are larger in size to accommodate the larger detector systems.

The focal plane vacuum chamber will be equipped with an internal rail system to support and accurately locate the detectors and adjust their positions along the beam axis. The chamber will have a suitable "cable race" at the bottom for the routing of the power cables, cooling, and gas lines needed to operate the detectors. Pneumatically driven rotary actuators are located outside the vacuum chamber for turning the drive shafts attached to the mask assemblies, which allow to raise

and lower the DC masks for position calibration. A linear drive is used to control a blocker for intercepting unreacted beam particles in front of the tracking detectors in case the rigidity of the particles of interest are close to that of the unreacted beam. In addition, the chamber will have several access ports and flanges for the mechanical/turbo vacuum pumps, pressure transducers, the signals and HV bias feedthroughs, and cooling system for the detector front-end electronics; several access panels for installing and removing the instrumentation from the chamber.

7.3.2.2   The drift chamber (DC)

Two large-area Drift Chambers (DCs) that will be placed 1 meter apart are used to measure the positions and derive the angles in each of the focal planes at FS1 and FS2 of the Spectrometer Section. The required position resolution is 1 mm (FWHM), from which the angle of the trajectory can be determined with a resolution of better than 2 mrad, even if multiple scattering effects in the detector planes are considered. This is sufficient for performing an accurate reconstruction of the particle trajectory at the reaction target, as is presently also performed for experiments with the S800 Spectrograph at NSCL [BAZ03]. A schematic depiction of the DC layout is provided in Figure 7.8.

The dimension of the active area of the DCs is ±30 cm in the non-dispersive direction and ±50 cm in the dispersive direction for the FS1 and FS2 focal planes. The DC are filled with standard Ar-based mixtures (e.g. P10) at pressures in the range of 30-50 Torr. The maximum rate is approximately 20 kHz. Above this rate, efficiency losses due to space-charge effects are to be expected, in particular if the beam is concentrated on a small area of the detector. The use of D-PPACs for the Spectrometer Section focal planes is not feasible, as the surface that needs to be covered is relatively large. It is not possible to make such large D-PPACs for which thin foils are used and the gap between the windows is consistent. In addition, when increasing the size of a D-PPAC, the delay lines become long and the signals deteriorate,

The DCs will be based on a design that is presently being constructed for use with the S800 Spectrometer. Instead of the present Cathode-Readout Drift Chamber used at the NSCL S800 spectrometer, the new DC designed for the HRS implements a more advanced hybrid micro-pattern gaseous detector readout; the latter comprises of a multi-layer Thick Gaseous Electron Multiplier (M-THGEM) [COR17] mounted on top of a position-sensitive Micromegas [GIO96] readout, as shown in Figure 7.9. This new position-sensitive hybrid readout configuration, originally developed and currently implemented as charge readout for the Active-Target Time Projection Chamber project [BAZ17], has the advantages of higher gas avalanche gain, excellent position resolution and better reduction of the ion-backflow, leading to overall improvement of the operational stability of the detector. Furthermore, in the conventional CRDC the typical drift times of the electrons to the anode wires are a few hundred ns to around 20 µs, depending on the position of the track in the non-dispersive direction. The relatively long drift times limit the maximum rate that the detector can process properly to around 5-10 kHz. The new detector configuration offers the possibility to increase the field strength on the drift volume with a sizeable increase of the drift velocity of the electrons and thus a better rate capability. The signals from the micromegas readout pads (~2000 channels) are read out and processed by a GET electronics based DAQ system [POL12], characterized by low noise, high data transfer capabilities and multi-hit capability for an efficient digital rejection of pile-up events.
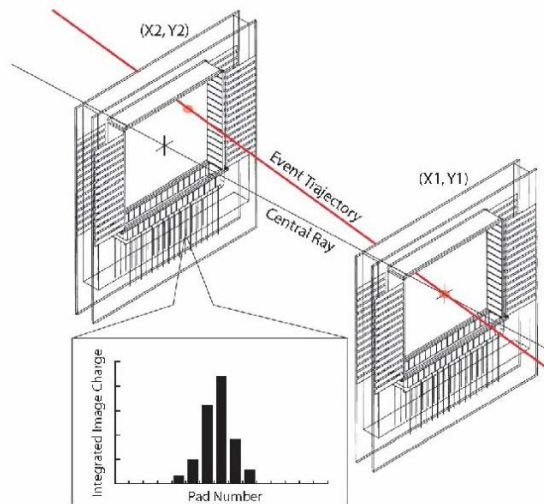
Figure 7.8. Schematic drawing of the tracking system of the spectrometer focal plane as it is presently used in the S800 Spectrograph at NSCL. The focal-plane tracking detectors of the HRS are upgraded versions of these detectors.
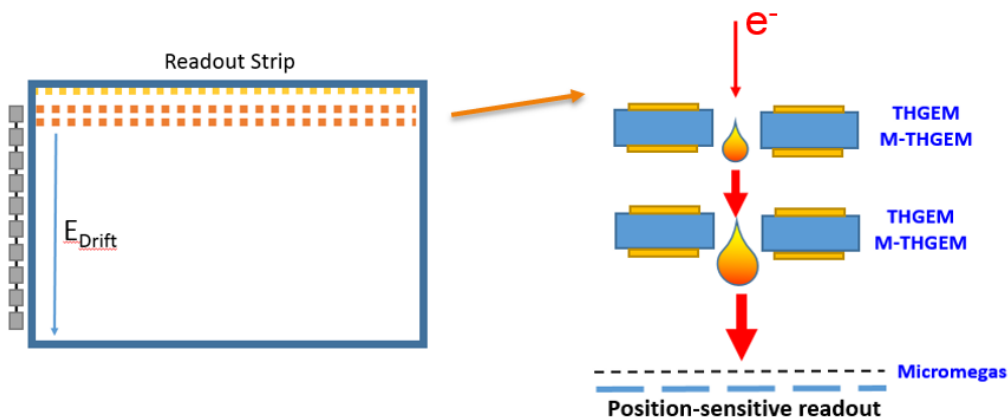
Figure 7.9. Position-sensitive readout of the DC to be implemented for tracking at the spectrometer focal plane.

7.3.2.3 The ionization chamber (IC)

An Ionization Chamber (IC) installed downstream of the DCs is used to identify the atomic number of the transmitted nuclei from their energy loss. The IC detectors have an active area that match the one of the DCs and a depth of approximately 400 mm (16 inches). It is filled with P10 gas (90% argon, 10% methane) at a typical pressure of 300 Torr, although this value can be increased up to 600 Torr for light nuclei. The detector consists of 16 stacked-parallel plate ion chambers with narrow anode-cathode gaps, placed along the detector's central axis, perpendicular to the beam

155

direction. The plates are constructed from 0.7 mg/cm^2 polypropylene with 0.05 µm of aluminum evaporated on each side. The entrance and exit windows of the chamber are made of 14 mg/cm^2 Mylar with an overlay of Kevlar filaments and epoxy.

Figure 7.10. Photograph of the S800 ionization chamber used as a model for the design of the energy-loss detector at the focal plane of the Spectrometer Section.

The basic design of the ICs planned for the spectrometer focal planes is based on the detector currently used at the NSCL S800 spectrometer, shown in figure 7.10.

The electrons and positive ions liberated by the ionization of the gas along the particle trajectory drift towards the closest anode-cathode pair. The drifting electrons and ions absorb the energy stored in the detector capacity and produce a voltage change of the anodes across the resistor. The main advantage of the anode-cathode configuration is that the electrons and ions are collected on a very short distance (about 1.5 cm), thus reducing pile-up and position dependence of the signals. Moreover, dividing the detector into 16 sections reduces the detector capacitance and consequently increase the signal-to-noise ratio. Each anode is attached to a small preamplifier inside the ion chamber; this significantly reduces the electronic noise, although it involves the venting of the whole chamber whenever a malfunctioning preamplifier needs to be replaced. The electronic signals from the preamplifier are sent into a dedicated DAQ system based on the GET electronics [POL12].

7.3.2.4 The plastic scintillator

The scintillation detectors are placed behind the Ionization Chamber and provide energy loss and timing information. The detector consists of a plastic scintillator sheet (~1-mm thick) that will match the areas of the other tracking detectors. The scintillator type is EJ-230 (Light output 64% Anthracene; Rise time 0.5 ns; attenuation length 120 cm), coupled to a series of H6533-assembled HAMAMATSU R4998 PMTs that surround the scintillator area. This configuration allows to reach an optimal photon-collection efficiency and an expected time resolution of the order of 150 ps (FWHM). A similar design is presently being implemented for the S800 Spectrograph at NSCL, for which an illustration is provided in Figure 7.11. The scintillator for the focal-plane detector systems at FS1 and FS2 will have a similar layout but with dimension appropriate for the beam envelope at the HRS.

156
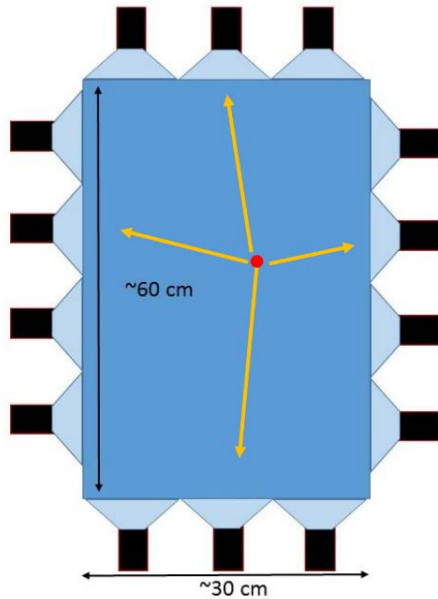
Figure 7.11. Schematic drawing of the scintillator detector used for timing at the S800 spectrograph focal plane. A similar design will be used at focal planes FS1 and FS2 of the Spectrometer Section.

7.3.2.5 The hodoscope

A CsI(Na) hodoscope detector, located downstream of the plastic scintillator, is used to measure the total kinetic energy (TKE) of implanted nuclei, allowing for the identification of different atomic charge states. Additionally, the hodoscope can also be used to detect isomer gamma-rays emitted from the captured nuclei. This type of TKE detector has been successfully implemented at the S800 Spectrograph [MEI11] and is also used for isomer tagging [WIM14].
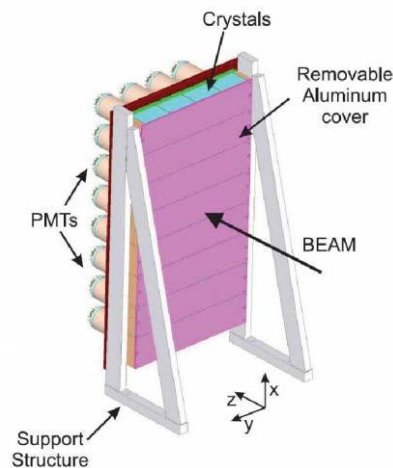
Figure 7.12. Schematic drawing of the hodoscope detector for TKE measurements as presently used in the S800 Spectrograph. The hodoscope that will be used in the focal planes of the Spectrometer Section of the HRS will be similar, but the area covered will be larger to account for the larger beam envelope.

The basic concept of the hodoscope includes a two-dimensional array of closely packed CsI(Na) scintillating crystals, attached to a vacuum photomultiplier (PMT). A good choice for the latter is the Hamamatsu R1307, for its photo-cathodes are made of a bi-alkali material with an responsivity that perfectly matches the scintillation spectra of the CsI(Na) crystals. The crystals are arranged in a 2D array with a total effective area that allows to cover the full envelope of the particle tracks. The frontal and lateral sides of each crystal are covered with two 150-µm thick layers of a reflective material (typically white Teflon) to provide light shielding between the crystals.

157

7.3.2.6   The gas handling system

The spectrometer focal planes include three large-volume gaseous detectors, two drift chambers and one ionization chamber. Their gas handling systems (GHS) are designed to be a high purity gas delivery system to provide up to 50 sccm gas flow to the detectors. The systems are made up of four components: gas supply, the gas handling system control box, the detectors, and the roughing pumps. The GHS have two independent delivery systems for the two types of detectors in each focal plane chamber. One of the delivery system is dedicated to the DCs and the other is dedicated to the Ion Chamber (IC).

7.3.3   Data acquisition systems for the HRS

The detector systems for the HTBL and Spectrometer Section must be read out by appropriate data acquisition system and analyzed by efficient software. The existing NSCL Data acquisition system (NSCLDAQ) is a modular, toolkit, for distributed data acquisition suitable for experimental nuclear physics. It is continuously improved and adapted for new hardware by FRIB Laboratory staff, in close coordination and collaboration with users of the facility. Present developments focus on high-rate data streaming and parallel processing capabilities. Such developments are very beneficial for experiment with the HRS. Therefore, the detector systems of the HRS will also employ this data acquisition framework.

NSCLDAQ features a generalized data flow architecture that supports delivery of data from an arbitrary set of sources to an arbitrary set of consumers on any other system reachable on the network. Consumers can, in turn, be sources for another stage of data flow. Simple proxy objects are used to perform traffic aggregation (data are only sent to a system with consumers once).

The system is open for expansion and is well documented [DAQ18]. Several frameworks have been provided to read out data from what have become standard data source types. These include frameworks for the VMUSB and CCUSB modules from Wiener/JTEC as well as a generic framework that is used both for legacy SBS/Bit3 PCI/VME bus bridges and to readout XIA Digital systems based on the PIXIE-16 module. The ability to acquire data from the Generalized Electronics for TPCs (GET) is being implemented as well, which will, among others, be used to read out the DCs of the Spectrometer Section. Additional frameworks can relatively easily be included, so that NSCL is high adaptable to DAQ systems provided by the users that will operate in coincidence with the detectors of the HRS.

NSCLDAQ features a timestamped generic event builder. It can accept event fragments from segments of the dataflow system, order these data by timestamp and emit events that consist of fragments that are within a user specified coincidence window. These data are submitted back to the NSCLDAQ data flow system where they can be used in later stage event builders. This design allows for the combination of detectors with independent data acquisition systems without modification to each individual component: a procedure routinely done at NSCL and important for the HRS for reasons described above.

The openness of the data distribution system allows users to attach and operate any data analysis framework they choose, including the CERN ROOT system [ROOT97] for online analysis. NSCL provides a general histogramming framework called NSCLSpecTcl. NSCLSpecTcl can be used for online or offline analysis, and like NSCLDAQ, is supported by Laboratory staff. NSCL

SpecTcl, is also well documented [SPEC18]. NSCL SpecTcl's model requires experimenters only to produce parameters of interest from incoming data. The user interface then supports dynamic creation of histograms and gates, and the application of gates to histograms. A rich set of histogram types and gate types allows for very generic analyses.

NSCLDAQ and NSCL SpecTcl are open source projects available for license by the MSU Board of Trustees under the GPLV2 license. SourceForge provides a public facing portal to download either of these systems [SFDAQ18, SFSPEC18].

The integration of multiple devices (both local and external) into the NSCLDAQ framework has been proven to be successful. A good example is the integration of the GRETINA and S800 Spectrograph DAQ systems [FOX18, REC13], which serves as a model for the integration of GRETA and HRS DAQ systems in the future. Since then, the synchronization of data acquisition systems based on timestamping became the default requirement for many of the experimental campaigns. This technique has been developed and optimized for both VME, CAMAC, and DDAS electronics. Additional examples of those are the integration of the S800 Spectrograph DAQ systems with the LENDA neutron detector array [LIP18], CAESAR gamma-detector array [ELM17, LON18], and the ORRUBA charged-particle array [WAL19]. Integration of EPICS into event data streams has also been done, for example for mass measurement experiments [EST11, MAT12, MEI13, MEI15].

For the operation and commissioning of the HRS it is important that the information processed in the DAQ system is immediately processed and available for assessing the quality of the data taking and assessing of the beam transport functionality, including studies of the correlation between beam parameters at different focal planes and the ion-optical transfer matrix elements. Such analysis can conveniently be performed using the above-mentioned NSCLSpecTcl framework. This framework is presently used for the same purposes for the A1900 fragments separator and the S800 spectrograph.

7.3.4   Ancillary detector and support

The Spectrometer Section is equipped with a large, changeable multi-purpose station that precedes the target stations FS0 and FS0′. It can house various ancillary detectors (see Figure 4.17), including those that are large, such as GRETA. Therefore, the scope of the HRS includes platforms around the target stations to mount these detectors, based on existing designs for the placing of GRETINA in front of the S800 Spectrograph. As the Spectrometer Section is situated in a pit due to the large vertical sizes of the magnets, the platforms must be raised to the beam level. A 50-ton crane situated in the HRS high bay will be used to lift heavy items onto these platforms.

Similarly, the components of the MoNA-LISA detector array [BAU05, MRI09] must also be raised to beam height at their location behind the DS1 Sweeper magnet. For that purpose, additional platforms are included in the scope of the HRS. These platforms are simpler than the ones needed for the placement of GRETA, as their sole purpose is to place the MoNA-LISA detectors statically in the correct location, without the need for potentially complex adjustments during experiments. Hence, the main difference with existing detector stands used for the MoNA-LISA detectors is that they need to be raised sufficiently higher.

7.3.5 Alarms and interlocks for equipment protection

The HTBL diagnostics devices and the spectrometer focal plane detectors system will be protected from excessive beam rate by an automatic interlock system, blocking/dumping the beam whenever the pre-set count rate limit is exceeded. The measurement of the count rate will be performed with one of the HTBL PPACs or a dedicated plastic scintillator. The limit will be experiment specific since rate damage, especially in the tracking devices, has been observed to correlate with Z and intensity/area. The shutoff of the beam will be accompanied by a voice/visual alarm in the FRIB control room and in the user data station.

An alarm server will be used to monitor the gas handling system of the HTBL PPACs and of the focal-plane detectors (the drift chambers and the ionization chamber), and to monitor the HV power supply of the focal plane tracking systems, the ion chamber, and the tracking PPACs.

A "voice/visual" alarm in the user data station will be triggered whenever the pressure excursions in the gaseous detectors (PPCAs, Drift Chamber and ion chamber) will be outside an acceptable range, signaling a failure of the gas handling system or a gas leakage along the beam line.

The high voltage of the above-mentioned detectors will be controlled by a dedicated application and an alarm is triggered when the read back value of the power supply does not match the set value: this will interlock the detector power supply and the event will be brought to the attention of the on-shift person immediately. The device or beam physicists provide instructions on the expected response to the possible alarms.

7.4   References

[ARN14] C.W. Arnold et al., "Development of position-sensitive time-of-flight spectrometer for fission fragment research", Nucl. Instr. and Meth. in Phys. Res. A, 764 (2014) 53-58

[BAU05] T. Baumann et al., Nucl. Instr. and Meth. A543, 517 (2005)

[BAZ03] D. Bazin et al., "The S800 spectrograph", Nucl. Instrum. Methods Phys. Sect. B, 204 (2003), pp. 629–633.

[BAZ17] D. Bazin et al., EPJ Web Conf. 163, 4 (2017).

[BIR05] M. D. Bird *et al.*, "System testing and installation of the NHMFL/NSCL sweeper magnet," *IEEE Trans. Appl. Supercond.*, vol. 15, no. 2, pp. 1252–1254, Jun. 2005.

[BRA17] J. Bradt *et al.*, "Commissioning of the Active-Target Time Projection Chamber," *Nucl. Instrum. Methods Phys. Res. Sect. Accel. Spectrometers Detect. Assoc. Equip.*, vol. 875, pp. 65–79, Dec. 2017.

[CAR13] I.P. Carter et al., "An ion beam tracking system based on a parallel plate avalanche counter". EPJ Web of Conferences, 63 (2013), p. 02022

[COR17] M. Cortesi *et al.*, "Multi-layer thick gas electron multiplier (M-THGEM): A new MPGD structure for high-gain operation at low-pressure," *Rev. Sci. Instrum.*, vol. 88, no. 1, p. 013303, Jan. 2017.

[DAQ18] http://docs.nscl.msu.edu/daq/newsite/nscldaq-11.2/index.html; http://docs.nscl.msu.edu/daq/

[ELJ18] https://eljentechnology.com/products/plastic-scintillators/ej-228-ej-230

[ELM17] Elman B., "Quadrupole collectivity beyond N=50 in neutron-rich Se and Kr isotopes", Phys. Rev. C 96, 044332 (2017).

[EST14] A. Estrade et al., Phys. Rev. Lett. 113, 132501 (2014)

[FOX12]   Gretina   User   Documentation,   Ron   Fox,   2012 http://docs.nscl.msu.edu/daq/newsite/gretinauserdocs.pdf

[GAD16] A. Gade and B. M. Sherrill, "NSCL and FRIB at Michigan State University: Nuclear science at the limits of stability," *Phys. Scr.*, vol. 91, no. 5, p. 053003, 2016.

[GIO96] Y. Giomataris, P. Rebourgeard, J. P. Robert, and G. Charpak, "MICROMEGAS: a high-granularity position-sensitive gaseous detector for high particle-flux environments," *Nucl. Instrum. Methods Phys. Res. Sect. Accel. Spectrometers Detect. Assoc. Equip.*, vol. 376, no. 1, pp. 29–35, Jun. 1996.

[GRO75] J. J. Grob, A. Grob, A. Pape, and P. Siffert, "Energy loss of heavy ions in nuclear collisions in silicon," *Phys. Rev. B*, vol. 11, no. 9, p. 3273, 1975.

[HAR96] R. Hartmann et al., "Low energy response of silicon pn-junction detector," Nucl. Instrum. Methods Phys. Res. A, vol. A377, pp. 191–196, 1996.

[HEM75] G. Hempel, F. Hopkins, and G. Schatz, "Development of parallel-plate avalanche counters for the detection of fission fragments," Nucl. Instrum. Methods, 131 (1975), pp. 445–450.

[HOI11] R. Hoischen et al., "Fast timing with plastic scintillators for in-beam heavy-ion spectroscopy," Nucl. Instrum. Methods Phys. Res. Sect. Accel. Spectrometers Detect. Assoc. Equip., vol. 654, no. 1, pp. 354–360, Oct. 2011.

[HON16] R. Hong et al., "High accuracy position response calibration method for a micro-channel plate ion detector" Nucl. Instr. and Meth. in Phys. Res. A, 835 (2016) 42-50

[JAG02] O. Jagutzki, et al., "Position sensitive anodes for MCP read-out using induced charge measurement", Nucl. Instrum. Methods Phys. Res. Sect. A: Accel. Spectrom. Detect. Assoc. Equip. 477 (1–3) (2002) 256–261

[KUM01] H. Kumagai, A. Ozawa, N. Fukuda, K. Sümmerer, and I. Tanihata, "Delay-line PPAC for high-energy light ions," *Nucl. Instrum. Methods Phys. Res. Sect. Accel. Spectrometers Detect. Assoc. Equip.*, vol. 470, no. 3, pp. 562–570, 2001.

[KUM03] H. Kumagai et al., "Development of Parallel Plate Avalanche Counter (PPAC) for BigRIPS fragment separator," Nucl. Instrum. Methods Phys. Sect. B, 317 (2013), pp. 717–727.

[KUM13] H. Kumagai *et al.*, "Development of Parallel Plate Avalanche Counter (PPAC) for BigRIPS fragment separator," *Nucl. Instrum. Methods Phys. Res. Sect. B Beam Interact. Mater. At.*, vol. 317, pp. 717–727, 2013

[LIP18] S. I. Lipschutz, Ph.D. Thesis, Michigan State University (2018); S. I. Lipschutz et al., submitted for publication

[LON18] Longfellow B., "Measurements of key resonances for the ^{24}Al(p,γ)^{25}Si reaction rate using in-beam gamma-ray spectroscopy", Phys. Rev. C 97, 054307 (2018)

[MAT12] M. Matoš *et al.*, "Time-of-flight mass measurements of exotic nuclei," *Nucl. Instrum. Methods Phys. Res. Sect. Accel. Spectrometers Detect. Assoc. Equip.*, vol. 696, pp. 171–179, Dec. 2012.

[MEI13] Z. Meisel and S. George, IJMS 349, 145 (2013)

[MEI15] Z. Meisel et al., Phys. Rev. Lett. 114, 022501 (2015)

[MOR03] D. J. Morrissey *et al.*, "Commissioning the A1900 projectile fragment separator", *Nucl. Instrum. Methods Phys. Res. Sect. B Beam Interact. Mater. At.*, vol. 204, pp. 90–96, 2003.

[MRI09] MRI-Consortium: Development of a Neutron Detector Array by Undergraduate Research Students for Studies of Exotic Nuclei, NSF grants 0922335, 0922409, 0922446, 0922462, 0922473, 0922537, 0922559, 0922622, and 0922794

[POL12] E. Pollacco *et al.,* "GET: A Generic Electronic System for TPCs for Nuclear Physics Experiments", Physics Procedia 37, 1799 (2012)

[PUL02] A. Pullia, W. F. J. Muller, C. Boiano, and R. Bassini, "Resistive or capacitive charge-division readout for position-sensitive detectors," IEEE Trans. Nucl. Sci., 49 (2002), pp. 3269–3277.

[ROOT97] ROOT - An Object Oriented Data Analysis Framework,Proceedings AIHENP'96 Workshop, Lausanne, Sep. 1996, Nucl. Inst. & Meth. Phys. Res. A 389 (1997) 81-86. See also http://root.cern.ch/

[REC13] Recchia F., "Configuration mixing and relative transition rates between low-spin states in ^{68}Ni", Phys. Rev. C 88, 041302(R) (2013)

[SCH07]

[SFDAQ18] http://sf.net/projects/nscldaq

[SFSPEC18] http://sf.net/projects/nsclspectcl

[SPEC18] http://docs.nscl.msu.edu/daq/

[SWA75] D. Swan, J. Yurkon, and D. J. Morrissey, "A simple two-dimensional PPAC," Nucl. Instrum. Methods Sect. A, 348 (1974), pp. 314–317.

[TIN08] C.S. Tindall et al., "Silicon Detectors for Low Energy Particle Detection", IEEE trans. On Nuclear Science, Vol. 55, No. 2, April 2008.

[WAL19] D. Walter et al., to be published

[WIM14] K. Wimmer et al., Nucl. Instr. And Meth, in Phys. Res. A 769, 65 (2014)

[YUR99] J. Yurkon *et al.*, "Focal plane detector for the S800 high-resolution spectrometer," *Nucl. Instrum. Methods Phys. Res. Sect. Accel. Spectrometers Detect. Assoc. Equip.*, vol. 422, no. 1, pp. 291–295, Feb. 1999.

8 Commissioning Plan

The commissioning plan for the HRS assumes that magnets, diagnostics systems, and auxiliary systems have been installed and that those subsystems have been verified to operate within design specifications. While commissioning will allow to demonstrate the key performance parameters (KPPs; see Section 3.4), the commissioning scope extends beyond the bare demonstration of KPPs.

The initial beam properties for commissioning purposes will be characterized at the ARIS fragment separator focal plane diagnostic box. Tracking detectors and slit systems in the HTBL and the spectrometer section are assumed to be calibrated with sources and masks before actual commissioning starts. The calibration of the drift-chamber tracking detectors in the Spectrometer Section can be verified with masks that can be inserted during beam operation.

With tracking detectors installed at each focal plane, the actual ion-optical transfer matrix elements by analyzing the correlation of variables at the initial and final focal plane will be measured. Commissioning will make use of the inverted response matrix method for the quadrupole elements in the beam line. An ion-optical calculation with COSY INFINITY based on the measured field maps will yield the matrix elements at the focal planes in the beam line and spectrometer. Using a linear approximation, the change of the ion optical matrix elements as a function of the deviation of quadrupole fields can be calculated as a response matrix. After measurement of the beam trajectories with tracking detectors, optimized values of the quadrupole fields can be calculated by inversion of the response matrix.

For the HTBL, commissioning will start with the achromatic beam transport mode. The two tracking detectors at FB1 will be used to measure horizontal and vertical positions and angles for different beam momenta. The inverted response matrix method [UES12] will be used to optimize the quadrupole elements to simultaneously satisfy the focus condition [$(x|x') = (y|y') = 0$], as well as nominal position and angle dispersion [$(x|\delta)$, $(x'|\delta)$] and position magnifications. Similar approaches will be subsequently applied to FB3 and FS0. The pair of tracking detectors will be used to evaluate focus condition and achromaticity [$(x|\delta) = (x'|\delta) = 0$] at FS0 while maintaining nominal magnifications. Symmetry considerations can be used in cases with more available tuning parameters than ion-optical boundary conditions. The tuning of higher-order magnetic elements (sextupole and octupole corrector coils) can be optimized by minimization of the inclination of the dispersive focal planes at FB1 and FB3 using the tracking detectors at those positions. The transmission efficiency will be evaluated by comparing beam rates at FB1, FB3, and FS0 as a function of beam emittance and momentum deviation, characterized at the ARIS focal plane. In addition, it will be confirmed that the requirements for the reconstruction of the momentum (momentum resolving power of 1500) and angle (resolution of 5 mrad) at FS0 from the position and angle measurements at FB1 and FB3 (see Section 5.2) are met.

The commissioning of the high-resolution mode of the spectrometer section will commence with the optimization of the first four quadrupole elements to satisfy position focus conditions and to achieve nominal position and angle dispersion by application of the inverted matrix method. Tracking detectors at FS1 will be used to correlate the beam property measurements. The last two quadrupole elements will be tuned to achieve focus condition at the FS2 tracking detectors. The

higher-order ion-optical aberrations will tilt the focal planes at FS1 and FS2 even with the sextupole and octupole corrections applied and an iterative process will be used to optimize transmission rather than the position of the focal plane.

For the commissioning of the dispersion-matched beam transport mode through the HTBL a similar approach as for the achromatic beam transport mode will be chosen. Foci, dispersion, and magnification at FS0, as well as vertical foci at FB1 and FB3 will be optimized with the tracking detectors at FB1, FB3, and FS0. The correct dispersion at FB2 can be verified with the viewer plate. If found necessary, a pair of smaller NSCL-type PPAC detectors could be installed temporarily in the FB2 beam line cross to verify focus conditions as well. Dispersion-matching into the spectrometer section, using the high-resolution spectrometer mode, will be optimized by achieving position focus and achromaticity at FS2. Tracking detectors at FS0, FS1, and FS2 will be used for this part of commissioning. The acceptance of the spectrometer section for both beam transports mode will be characterized by measuring the beam transport of a high emittance beam with a variable momentum spread to FS1 and FS2. This also commissions the HRS for the ToF-$B\rho$ mass-measurement mode, which uses the HTBL in dispersion-matched mode together with a high-resolution spectrometer mode.

The neutron invariant-mass mode of the spectrometer section can be commissioned with the FS1 detector setup. Higher order correction elements will be tuned to optimize acceptance.

Event-by-event particle identification detector setups at FS1 and FS2 (ionization chamber, timing scintillator, hodoscope) will be commissioned during the commissioning of the spectrometer section. Initial standard modes for particle identification including momentum corrections will be developed with a reaction target at FS0. This will then allow to demonstrate the key performance parameters by measuring a neutron knockout reaction. Through the above measurements of the Spectrometer Section, it will be confirmed that the scientific requirements (See Section 6.2) are met.

8.1 References

[UES12] T. Uesaka, S. Shimoura, and H. Sakai (for the SHARAQ Collaboration), "The SHARAQ spectrometer", Prog. Theor. Exp. Phys. 2012, 03C007 (2012).

9 Magnets

9.1 Introduction and overview

The Magnet scope includes the materials and manpower needed for acquiring, bench testing, installing, in-situ testing, and final integrated testing without beam of the magnetic elements of the Magnet system WBS (See Table 9-1). This includes the nuclear magnetic resonance (NMR) probes used to measure the magnetic fields in the dipole magnets.

Table 9-1. Magnet system WBS.

Experimental Systems - High Rigidity Spectrometer	HRS.3
High Transmission Beamline (HTBL)	**HRS.3.01**
High Transmission Beamline Magnets	**HRS.3.01.03**
HTBL Dipole Magnets	*HRS.3.01.03.01*
HTBL Quadrupole & Multipole Magnets	*HRS.3.01.03.02*
HTBL Installation, Testing, and Magnet Mapping	*HRS.3.01.03.03*
High Transmission Beamline Alignment	**HRS.3.01.08**
Spectrometer Section	**HRS.3.02**
Spectrometer Section Magnets	**HRS.3.02.03**
Spectrometer Section Dipole Magnets	*HRS.3.02.03.01*
Spectrometer Section Quadrupole & Multipole Magnets	*HRS.3.02.03.02*
Spectrometer Section Installation, Testing and Magnet Mapping	*HRS.3.02.03.03*
Spectrometer Section Alignment	**HRS.3.02.10**

9.2 Requirements

The magnetic-element layout is shown in Figure 9.1. The requirements of the magnetic elements originate from the lattice design meeting the physics requirements (See Section 4) for the HTBL (See Section 5) and for the Spectrometer section (See Section 6).

9.2.1 High Transmission Beam Line (HTBL) magnets requirements

The HTBL consists of eight quadrupole triplets, four bending dipoles, and two steerer dipole magnets. The quadrupole triplet design is the same as the T2 triplet with a FSQB-FSQC-FSQB configuration as presently used at NSCL in the A1900 Fragment Separator with each quadrupole having sextupole and octupole coils to correct for higher-order aberrations. The magnet specifications are provided in Table 9-2.

The four dipole (DB1-DB4) magnets are a larger version of an existing NSCL XPF 6 Tm dipole design to accommodate a rigidity of 8 Tm. The magnet specifications are provided in Table 9-3. The two steerer dipole magnets (SB1, SB2) requirements are given in Table 9-4.
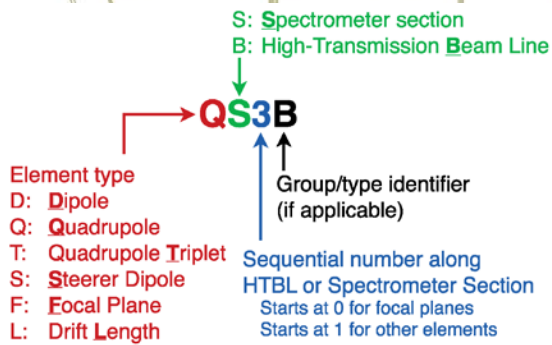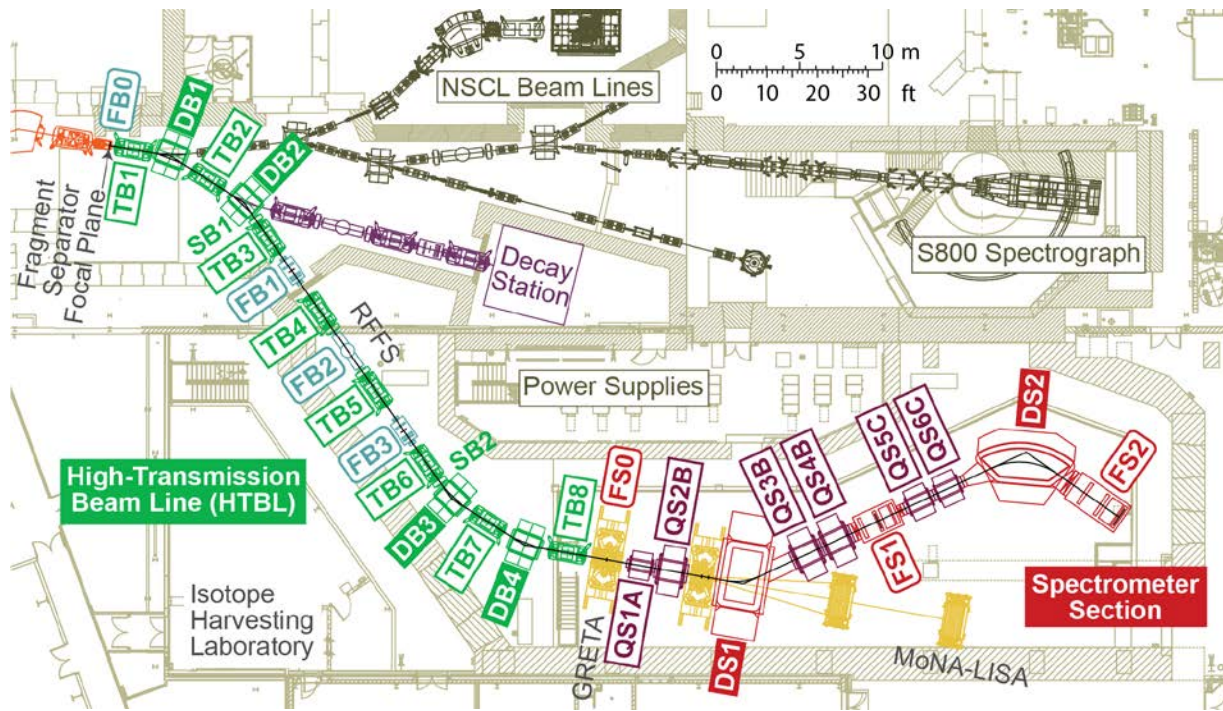
Figure 9.1 (Top) Overview of the magnetic elements of the HRS, with the nomenclature as shown on the left. The HTBL magnetic elements include triplets (TBx, x=1..8), dipoles (DBx, x=1..4), and steering magnets (SB1, SB2). The Spectrometer Section magnets include six single quadrupoles (type A = QS1A, type B = QS2B, QS3B, QS4B, ant type C = QS5C, QS6C) and two dipoles (DS1, DS2).

Table 9-2. High-Transmission Beam Line (HTBL) quadrupole magnet requirements for 8 triplets labeled TB1-TB8 in Figure 9.1. Each triplet has three quadrupole magnet elements: FSQB, FSQC, and FSQB. Each quadrupole segment includes sextupole and octupole windings.

Label	FSQB	FSQC
Quantity (in 8 quadrupole triplets)	16	8
Effective field length (nominal) (m)	0.40	0.79
Pole-tip radius (m)	0.15	0.15
Warm-bore radius (m)	0.10	0.10
Quadrupole maximum field strength (T@poletip)	2.50	2.50
Quadrupole good-field region radius (m)	0.10	0.10
Field quality (% not quadrupole)	1%[#]	1%[#]
Sextupole maximum field gradient (T/m^2)	10	10
Octupole maximum field gradient (T/m^3)	50	50

 # sum of all non-quadrupole components, relative to the n=2 quadrupole amplitude, obtained by measuring the field map at 50A excitation at a radius of 81 mm.

Table 9-3. High-Transmission Beam Line (HTBL) dipole magnet requirements for dipoles labeled DBx in Figure 9.1 compared to extant NSCL XFP dipole magnets.

Label	NSCL XFP	DBx (x = 1, 2, 3, 4)
Quantity	N/A	4
Bending radius (m)	3.1	4.10
Maximum rigidity (Tm)	5.3	8.0
Maximum field (T)	1.7	2.0
Bending angle (deg)	±22.5	22.5
Arc length for central ray (m)		1.61
Vertical gap size (m)	±0.035	±0.05
Good field region (m)		±0.10
Field quality (% not dipole)		0.5[#]
Pole-face rotation entrance (deg)		11.25
Pole-face rotation exit (deg)		11.25

Preliminary estimate

Table 9-4. High-Transmission Beam Line (HTBL) steerer dipole magnet requirements for steerers labeled SB1, SB2 in Figure 9.1.

Label	SBx (x = 1, 2)
Quantity	2
Length	0.40
Gap size (m)	±0.10
Maximum rigidity (Tm)	8
Maximum deflection angle (mrad)	10
Maximum field (T)	0.20

9.2.2 Spectrometer Section magnets requirements

The Spectrometer Section magnets include six quadrupole singlet magnets and two dipoles. Each quadrupole has sextupole and octupole coils superimposed to correct for higher-order aberrations. There are 3 different types: QS1A is the only quadrupole magnet of type A and has the smallest bore size; QS2B, QS3B, QS4B are of type B and have the largest bore sizes; and QS5C, QS6C are of type C. The quadrupole magnet specifications for each type are given in Table 9-5. The Spectrometer Section of the HRS contains two large dipoles, the Sweeper Dipole (DS1) and the Spectrometer Dipole (DS2), with specifications provided in Table 9-6.

Table 9-5 Quadrupole magnet requirements for the Spectrometer section of the HRS.

Label	A	B	C
Quantity	1	3	2
Location	QS1	QS2, 3, 4	QS5, 6
Effective field length (m)	1.30	1.50	1.50
Pole-tip radius (m)	0.35	0.65	0.45
Warm-bore radius (m)	0.25	0.55	0.35
Quadrupole maximum field strength (T@poletip)	2.50	2.50	1.50
Quadrupole good-field region (m)	0.20	0.44	0.28
Field quality (% not quadrupole)	1#	1#	1#
Sextupole maximum field gradient (T/m^2)	4.5	2.4	3.2
Octupole maximum field gradient (T/m^3)	8.2	2.5	4.9

Preliminary estimate; defined as the n=6 multipole contribution relative to the n=2 multipole contribution at the warm-bore radius, at maximum excitation

Table 9-6. Dipole magnet requirements for Spectrometer Section of the HRS.

Label	DS1	DS2
Quantity	1	1
Bending radius (m)	3.2	4.0
Maximum rigidity (Tm)	8.0	8.0
Maximum field (T)	2.5	2.0
Bending angle (deg)	-35	60
Arc length for central ray (m)	1.95	4.19
Vertical gap size (m)	±0.24	±0.11
Good field region width (m)	±0.45	±0.55
Field inhomogeneity (% not dipole)	1*	1*
Pole-face rotation entrance (deg)	0	-20
Pole-face rotation exit (deg)	35	-20

*Preliminary Estimate

9.3 Design approach

The requirements for the HTBL (Section 5) and Spectrometer Section (Section 6) that are derived from the HRS experimental program (Section 4) includes the use of ion beams of relatively high

rigidity (up to 8 Tm) and the necessity to transport beams of large three-dimensional phase space, which requires that the magnets have substantial apertures, especially in the Spectrometer Section. Iron-dominated magnetic elements using superconducting coils have been used at the NSCL for decades for similar purposes and have shown their efficacy in this application. Alternative approaches like current-dominated magnetic elements would require R&D, have higher risk and higher cost, and provide no particular performance benefit.

As a consequence, the preferred alternative approach for large aperture magnetic elements is based on iron-dominated magnetic elements using superconducting coils. An exception are the steering dipoles that only need to bend the beams with an angle of ± 10 mrad. Consequently, for these magnets, iron-dominated, normal-conducting designs will be pursued.

9.4 Preferred alternative

As described below, a conceptual design for each magnetic element has been developed. Though not discussed in detail, magnet stand conceptual designs and costs have been developed and are shown in some of the magnet figures following with most typical of extant NSCL systems. The design model magnetic fields from MAXWELL [ANS18] were used in ion-optical simulations (Sections 5 and 6) to verify that the conceptual design provides appropriate performance. In addition, these designs provided a good basis for estimating the cost. Further detailed analyses will be used to optimize the designs relative to cost, risk, and performance, including the usual iterations with concomitant ion optical performance compared to science-driven requirements.

9.4.1 HTBL quadrupole magnets

The quadrupole triplet design meeting the magnet requirements provided in Table 9-2 is the NSCL T2 triplet with a FSQB-FSQC-FSQB configuration presently used in the A1900 Fragment Separator (See Figure 9.2) with each quadrupole having sextupole and octupole coils to correct for higher-order aberrations. The design values for the quadruple triples are provided in Table 9-7. The field quality from magnetic measurements of these magnets was included in the ion-optical simulations and found to be appropriate. In the detail design phase, lessons learned from the A1900 magnet fabrication as well as the more recent FRIB magnet experience will be incorporated.

a)   b)
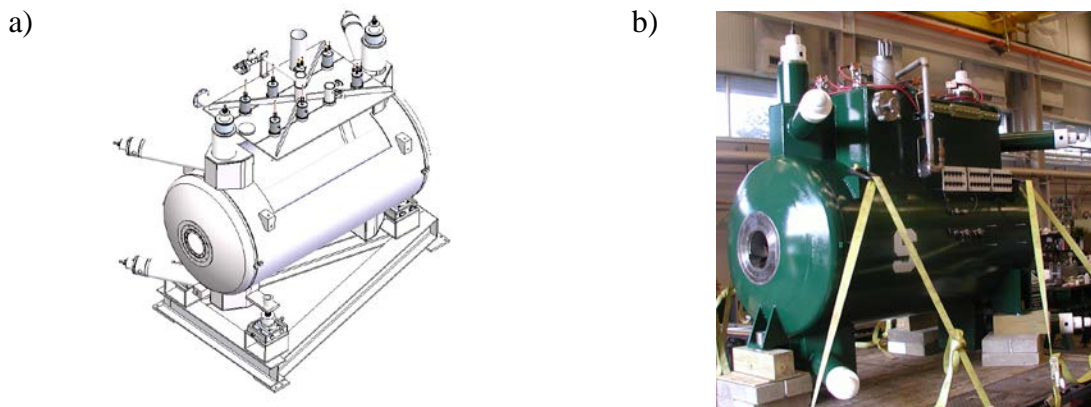
Figure 9.2 a) Mechanical layout and b) picture of the Quadrupole Triplet used for TBx in the HTBL. The same quadrupole design is used in the NSCL A1900 Fragment Separator.

Table 9-7 HTBL quadrupole triplet design values meeting requirements provided in Table 9-2.

Label	FSQB	FSQC
Quantity (in 8 quadrupole triplets)	16	8
Quadrupole Specifications		
Steel length / quadrupole effective length (m)	0.325 / 0.400	0.715 / 0.790
Steel mass (kg)	821	1806
Steel pole radius (cm)	15	15
Wire diameter bare / insulated (mm)	0.80 / 0.86	0.95 / 1.01
Length of wire per coil (m, approximate)	3658	4258
Coil cross section (mm^2)	2710	2710
Coil type:	potted – random wound – self protecting	
Peak gradient (T/m) / peak I (A)	15.8 / 65	16.2 / 85
Stored energy at peak field (kJ)	88	172
kA-turns	185	174
Inductance (H)	41.5	47.7
Power supply A / V bipolar	70 / 6	90 / 6
Sextupole Specifications		
Wire diameter bare / insulated (mm)	0.648 / 0.698	0.648 / 0.698
Peak gradient (T/m^2) / Peak I (A)	11.1 / 40	11.1 / 40
kA-turns	11.2	11.2
Inductance (H)	1.23	1.23
Power supply A / V bipolar	45 / 6	45 / 6
Octupole Specifications		
Wire diameter bare / insulated (mm)	0.648 / 0.698	0.648 / 0.698
Peak gradient (T/m^3) / peak I (A)	48.8 / 20	48.7 / 20
kA-turns	5.4	5.4
Inductance (H)	0.54	0.54
Power supply A / V bipolar	20 / 6	20 / 6
Cryostat Specifications		
Cryogenic load	See Section 11	
Warm bore radius (cm)	10	
Magnet steel separation distance (m)	0.237	
Flange-to-flange overall length (m)	2.267	
Assembled mass (kg)	5610	

9.4.2 HTBL dipole magnets

The four dipole (DB1-DB4) magnets are a larger version of an existing NSCL XPF 6-Tm dipole, shown in Figure 9.3. A conceptual design of DBx meeting the requirements of Table 9-3 is shown next to the NSCL XPF dipole in Figure 9.4, with design values as specified in Table 9-8. The

magnetic field analysis is shown in Figure 9.5. These magnets are comparable in size, field magnitude and stored energy to other NSCL dipoles, so there are no concerns with respect to the design (forces, critical current, quench protection, etc.). As shown in the bottom panel of Figure 9.5, the magnetic field at the outside of the steel does not exceed the saturation level. This ensures that the fringe fields will not be excessive.
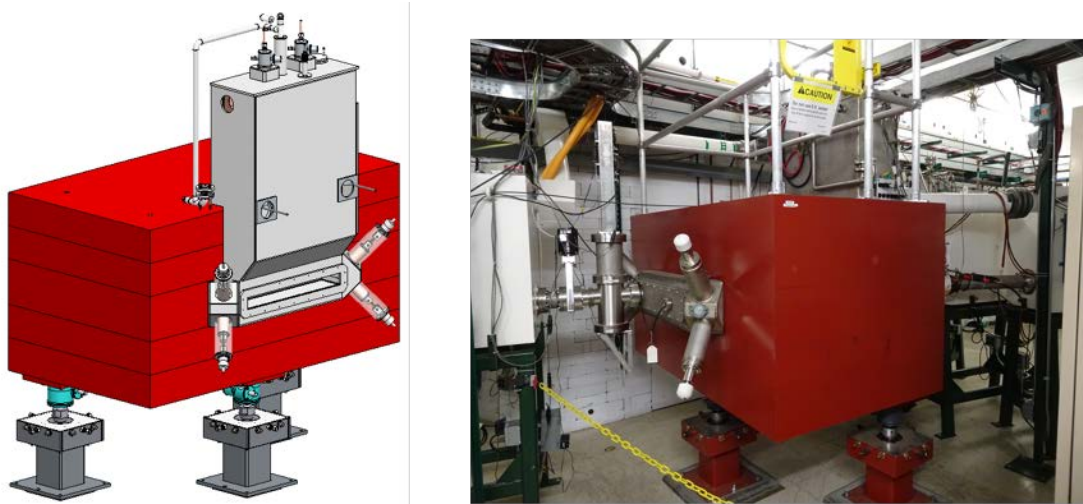
Figure 9.3 Mechanical design layout (left) and image (right) of an existing XPF 6-Tm dipole magnet used in the NSCL A1900 Fragment Separator. This magnet forms the basis of the dipole magnets used in the HTBL, which are scaled up to accommodate operation at rigidities of up to 8 Tm.
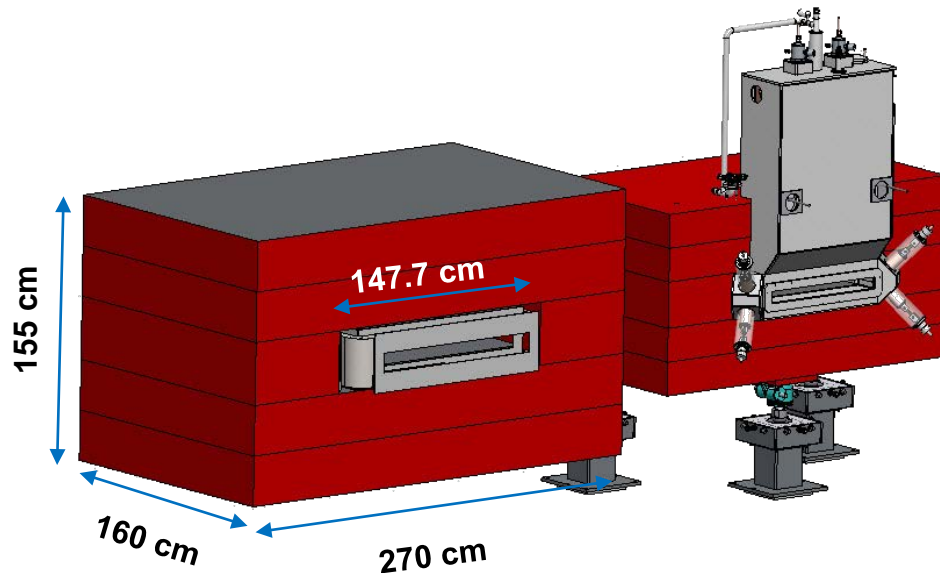
Figure 9.4 HTBL dipole magnet (DB1-DB4) layout with a length of 160 cm, a width of 270 cm, a height of 155 cm, a gap size of 10 cm, a gap width of 147.7 cm, necessary to accommodate a pole width of 119.4 cm. The magnet is shown next to an NSCL XFP dipole for comparison.

Table 9-8 HTBL DBx dipole design values meeting the requirements of Table 9-3. Note that the conceptual design field non-uniformity (0.13%) is better than the preliminary requirement (0.5%).

Parameter	Value
Quantity	4
Steel length/width/height/gap (m)	1.6,2.7,1.55,0.10
Steel mass (metric tons)	49.88
SC wire cross section (mm^2)/kA-turns	34x34, 117.5
B_{max} (T) gap	2.01
Integrated field non-uniformity (%)	0.13
B_{max} on outside of yoke (T)	<2.1
B_{max} in coil (T)	1.80
Stored energy (kJ)	376
Effective magnetic length (m)	1.65
∫B·dl (T m)	3.30
J_c with 3.21T & 4.2K (A/mm^2) for FRIB FSD1 wire	277
J_{op} - operating current density (A/mm^2)	107
J_{op}/J_c	0.39
Power supply A,V, uni or bipolar	214, 6, 2 quadrant (+I, ±V)
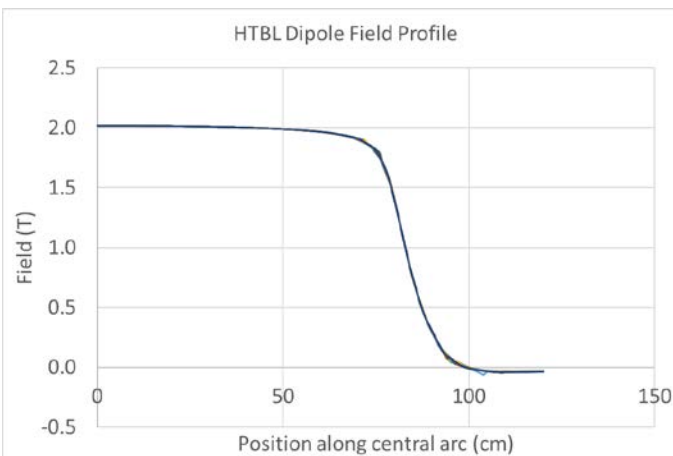
Figure 9.5 Magnetic field analysis of the DBx dipole magnets of the HTBL. (top) HTBL dipole field profile as a function of position along the central arc. (bottom) Analysis of the magnetic field outside of the steel, which is below the saturation level. This ensures that the fringe fields will not be excessive.

172
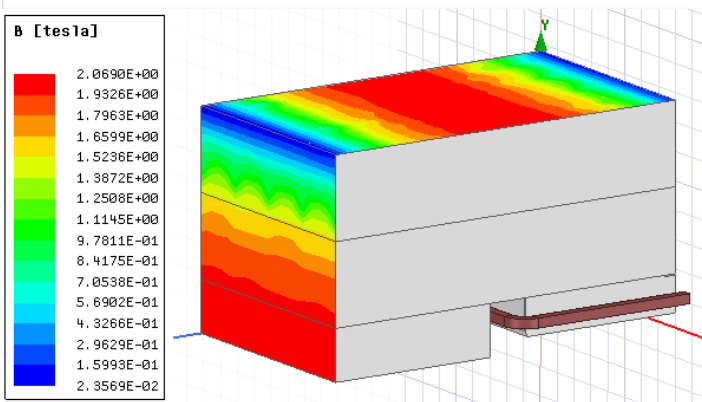
The structural analysis of two conceptual designs of the coil bobbin for the HTBL dipole magnet has been performed. One design has an additional compression link added to the long straight section of the coil. The resulting stress and deformations are shown in Figure 9.6. The addition of the compression link reduces the displacement of the long straight section from 1.76 mm to 0.95 mm, which will help ensure the bobbin fits within the cryostat.

a)

b)

c)

d)

Displacement 0.66 mm   Displacement 1.76 mm   Displacement 0.49 mm   Displacement 0.95 mm
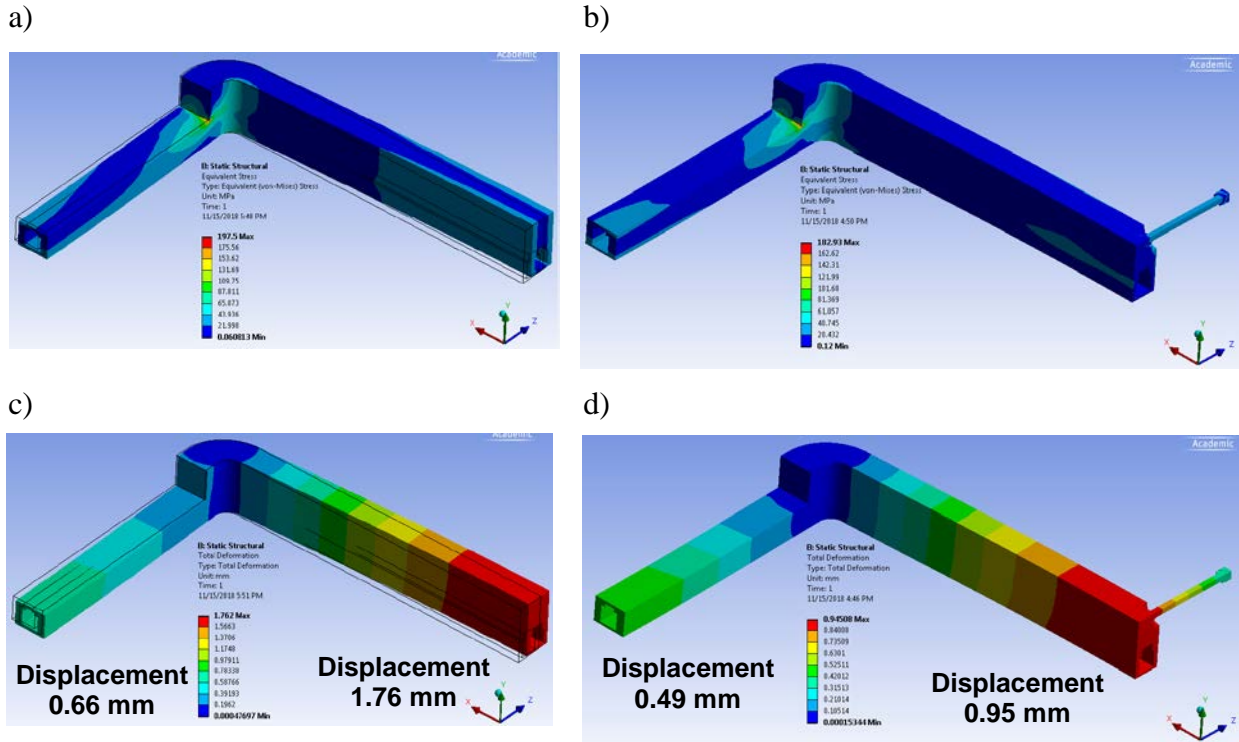
Figure 9.6 Stress (a and b) and deformation (c and d) calculations for the coil bobbin of the HTBL dipoles before (a and c) and after (b and d) the inclusion of an additional compression link. The displacement along the long straight section has been reduced from 1.76 mm to 0.95 mm.

9.4.3 HTBL steering magnets

A conceptual design of the steering magnets (SB1,SB2) that meets the requirements of Table 9-4 is shown in Figure 9.7(a). The design values are shown in Table 9-9 and the derived magnetic-field analysis, calculated in MAXWELL, is shown Figure 9.7(b).

The copper conductor of the steerer magnets will be Luvata #8581 (with a 1/4"×1/4" cross section and with a 0.143" cooling channel) in 7 double pancakes with 24 turns per double-pancake giving 168 turns per coil (7x24) or 37.0 kA-turns per coil with a current of 220.2 A. Given the voltage of 77 V, the power is about 16.9 kW. These magnets are comparable in size and field magnitude to common accelerator-based steering magnets, so there are no concerns with respect to the design challenges.
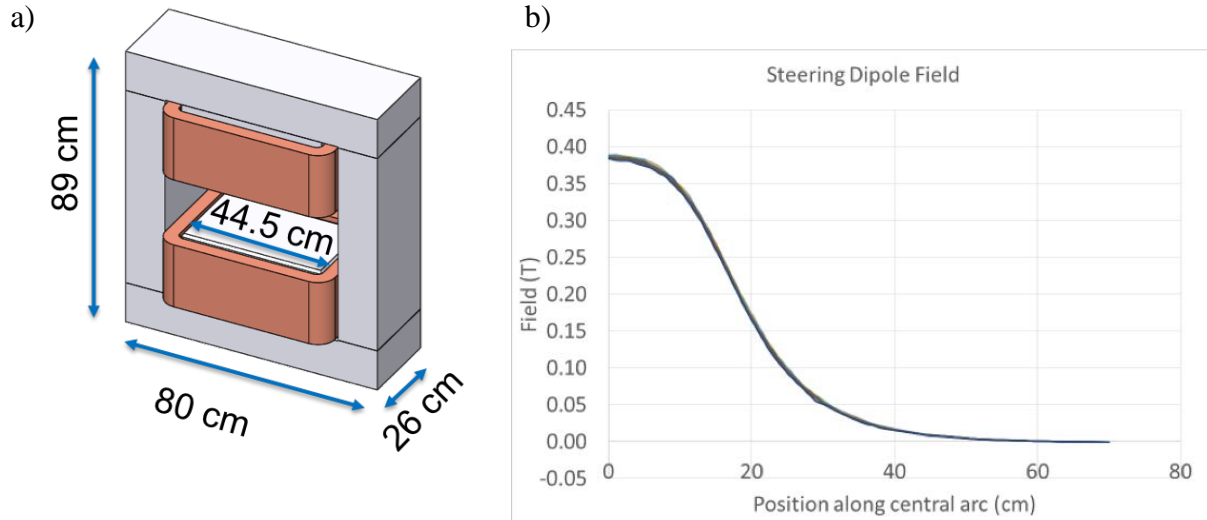
Figure 9.7 (a) HTBL steerer (SB1-SB2) layout with a length of 26 cm, a width of 80 cm, a height of 89 cm, a gap of 21 cm, and a pole width of 44.5 cm. (b) SBx magnetic dipole field as a function of the position along the central arc, as calculated in MAXWELL.

Table 9-9. HTBL SBx steerer design values that meet the requirements of Table 9-4.

Parameter	Value
Quantity	2
Steel length/width/height/gap (m)	0.26,0.80,0.89,0.21
Pole width (m)	0.445
Steel mass (kg)	1400
SC wire cross section(inch^2)/kA-turns	0.25x0.25,37.0
Bmax (T) gap	0.39
Integrated field non-uniformity (%)	$\pm$1.5
Effective magnetic length (m)	0.21
$\int$B·dl (T m)	0.081
Power supply A,V, uni or bipolar	250,100,bipolar

9.4.4 Spectrometer Section quadrupoles

The quadrupoles in the spectrometer section are all warm-iron quadrupoles, i.e., the superconducting coils are in liquid helium ("cold") and the yoke and pole tips are at room-temperature ("warm"). These quadrupoles are similar to the warm-iron quadrupoles of the new ARIS Fragment Separator and lessons learned from the design and construction of these magnets will be applied to the Spectrometer Section quadrupoles. The warm-iron quadrupole designs that meet the magnet requirements provided in Table 9-5 are shown in Figure 9.9(a-c), accompanied by the magnetic fields calculated in MAXWELL. These fields were used in the ion-optical simulations of Section 6 and the field quality was found to be acceptable. The parameters for the quadrupole magnets are given in Table 9-10 and for the sextupole and octupole coils in Table 9-11. Although these warm iron quadrupoles are similar in design to FRIB quadrupoles, the forces and stored energy are considerably larger. For these quadrupoles, the field at the pole tip is comparable

174

to FRIB quadrupoles (2.5 T for QA and QB vs. 2.0 T for FRIB FSQ5), so the forces scale approximately linearly, i.e., the amp-turns in the coils increase approximately linearly relative to the pole-tip radius to achieve the required field gradient. An initial analysis has been performed on a conceptual helium-vessel design for the most-challenging, largest-bore quadrupole QSB, which showed that there is sufficient space between the coils and yoke pole tips for a helium vessel that is sufficiently stiff, as shown in Figure 9.8. Both the stress and displacement in the helium-vessel are within acceptable limits. Also, a preliminary quench analysis has been performed to ensure that the quench protection of the magnets is achievable.

a)
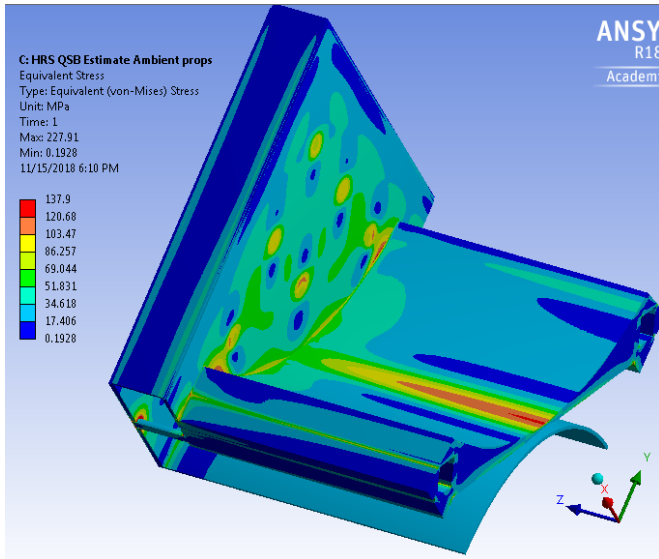
Figure 9.8 Stress analysis (a) and deformations (b) of the liquid helium vessel of QSB due to vacuum and coil forces. The peak stress value is within acceptable limits. The center of the panel moves slightly more than 1 mm, but the movement at the coil locations in negligible.

b)
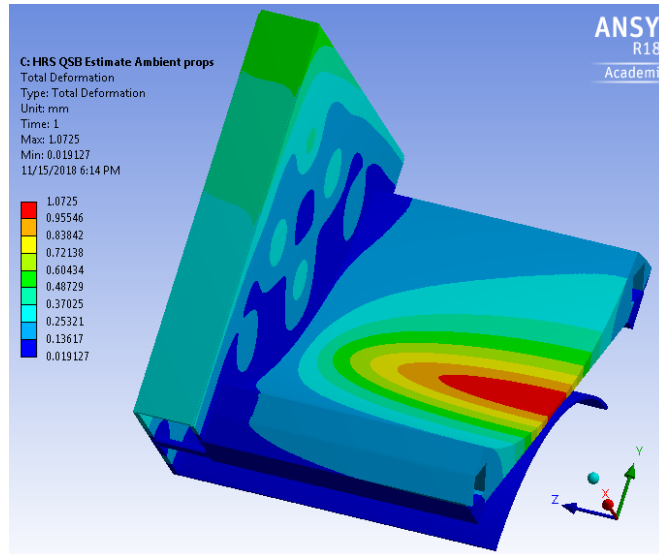
Table 9-10 Spectrometer Section quadrupole design values that meet the requirements of Table 9-5. Note that the initial ion-optical simulations have found the integrated field non-uniformities to be acceptable. The non-uniformity values shown are the values calculated from the magnetostatic models and are

175

similar to the preliminary estimates (1%). The field values from the MAXWELL model were found to achieve acceptable performance providing a sound basis for detailed design and optimization.

Label	QSA	QSB	QSC
Quantity	1	3	2
Steel length (cm)	123	132	134
Steel mass (metric tons)	13.86	49.35	20.62
Quadrupole SC coil cross section(mm^2)/ kA-turns	50×50, 400	84×84, 1000	45×45, 270
Quadrupole power supply A,V, uni or bipolar	415 A, 6 V, 4 quad. (±I, ±V)	449 A, 40 V, 4 quad. (±I, ±V)	345 A, 6 V, 4 quad. (±I, ±V)
Integrated field non-uniformity	0.88%	1.17%	0.36%
B_{max} on outside of yoke (T)	2.26	2.53	1.34
B_{max} in quadrupole coils (T)	4.77	6.37	3.34
Stored energy in quadrupole (kJ)	1374	9965	830
L_{eff} of quadrupole (m)	1.38	1.50	1.51
$\int G \cdot dl$ (T)	9.33	5.94	5.04
J_c (B_{max} in quad, 4.2 K) (A/mm^2)	950	557	1301
J_{op} (A/mm^2)	255	223	212
J_{op}/J_c	26.8%	40%	16%

* For FRIB FSQ5 wire
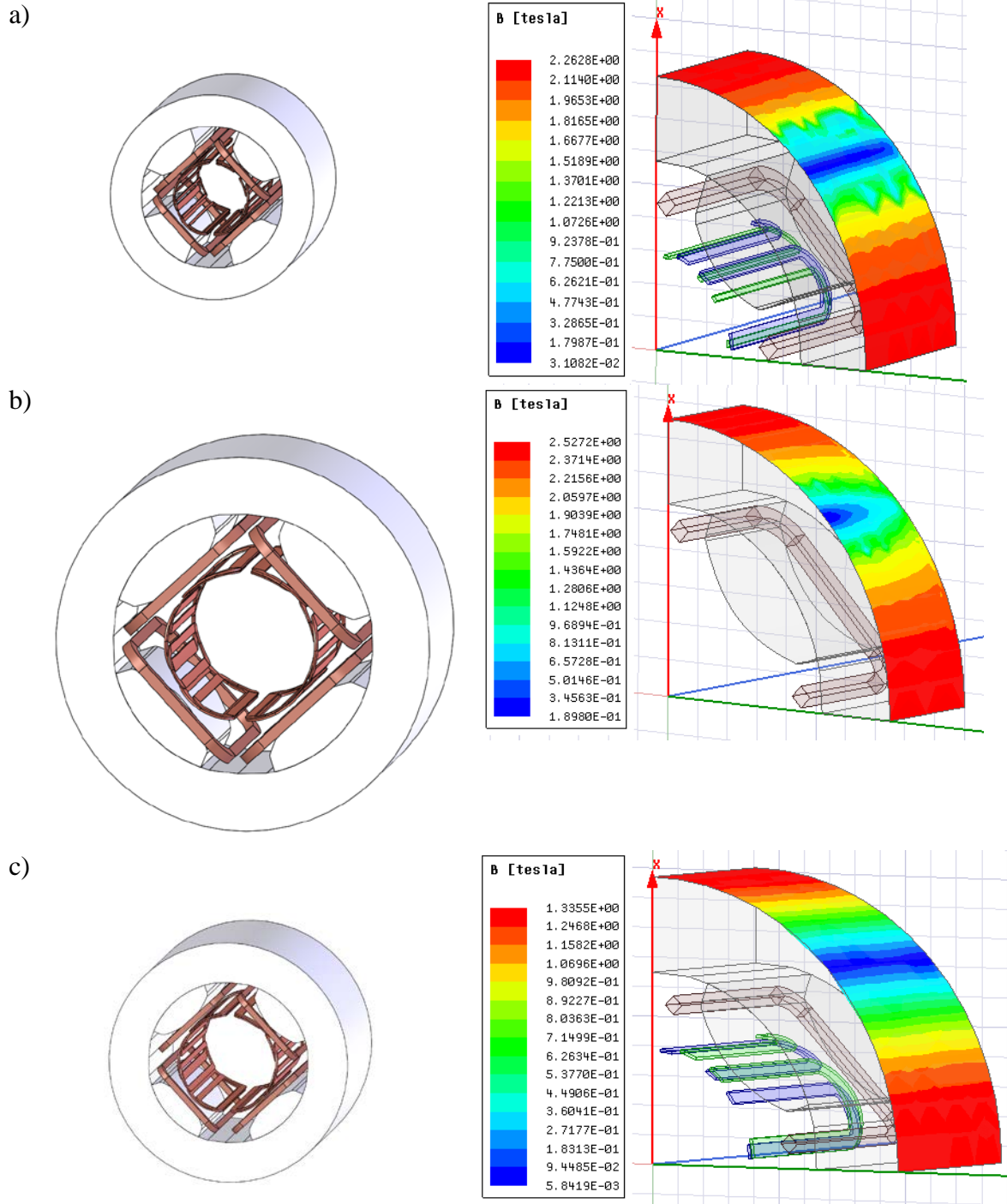
Figure 9.9 Layout and magnetic-field analysis of the quadrupole magnet types of the Spectrometer Section. (a) Type A with a length of 130 cm, a diameter of 165 cm, and a warm-bore radius of 25 cm; (b) Type B with a length of 150 cm, a diameter of 300 cm, and a warm-bore radius of 55 cm; and (c) Type C with a length of 150 cm, diameter of 194 cm, and a warm-bore radius of 35 cm

Similarly, the sextupole and octupole packages (Table 9-11) have been evaluated following experience with similar implementations in the A1900 T2 quadrupoles and the FRIB warm-iron quadrupoles. The resulting magnetic fields, coil package evaluations for clearances, forces, critical currents, and stored energy were found to meet requirements.

Table 9-11 Spectrometer Section sextupole and octupole design values that meet the requirements of Table 9-5.

Label	QSA	QSB	QSC
Sextupole			
Sextupole SC coil cross section(mm²)/ Amp-turns	492, 48	1530, 210	666, 90
Sextupole power supply A,V, uni or bipolar	63 A, 6 V 4 quadrant (±I, ±V)	228 A, 6 V 4 quadrant (±I, ±V)	87 A, 6 V 4 quadrant (±I, ±V)
B_{max} in sextupole coils (T)	2.86	4.83	3.22
Stored energy in sextupole (kJ)	14.9	346	58.0
L_{eff} of sextupole (m)	1.32	1.45	1.39
$\int G \cdot \mathrm{d}l$ (T/m)	5.88	3.75	5.08
Octupole			
Octupole SC coil cross section (mm²) / Amp-turns	193, 18	735, 100	474, 40
Octupole power supply A,V, uni or bipolar	60 A, 6 V 4 quadrant (±I, ±V)	225 A, 6 V 4 quadrant (±I, ±V)	51 A, 6 V 4 quadrant (±I, ±V)
B_{max} in octupole coils (T)	2.91	4.52	3.03
Stored energy in octupole (kJ)	2.77	90.4	13.0
L_{eff} of octupole (m)	1.38	1.48	1.40
$\int G \cdot \mathrm{d}l$ (T/m²)	10.78	3.89	7.57

9.4.5 Spectrometer Section dipole magnets

As discussed in Section 6, the Spectrometer Section contains two large dipole magnets. The first dipole magnet, DS1, has a large vertical gap to allow neutrons emitted in the forward direction to reach the neutron detectors placed as forward scattering angle. The conceptual design for DS1 is shown in Figure 9.10. An analysis of the magnetic field for DS1 was performed in MAWELL. The magnetic field at the highest operating current on the outside of the magnet yoke is shown in Figure 9.11. The magnetic fields are below the saturation level, which ensures that the fringe fields do not become excessively large. In Figure 9.12, the dipole field uniformity as a function of radial position is shown for different operating currents. The non-uniformity ranges from +1.6% to -2.5%, but is almost independent of the operating current. Since the MAXWELL fields from this design were used in the ion-optical simulations presented in Section 6 and the required ion-optical properties of the Spectrometer Section were achieved, these levels of non-uniformity may be acceptable for DS1 though the preliminary homogeneity requirements were set at 1%. During the

detailed design of DS1 optimization with respect to the cost, risk, and performance will be done in conjunction with further evaluation of the ion-optical performance under DS1 design assumptions.

Initial engineering studies have been done to ensure that the 650 metric ton magnet can be supported by a three-dimensional alignment system (see Figure 9.13) and can be constructed of steel segments of less than the overhead vault crane limit of 100,000 pounds while maintaining the necessary mechanical and magnetic integrity, as shown in Figure 9.14. The displacement of the yoke and pole tips are both less than 0.001", which is less than the fabrication tolerance of the parts. Note that the vault will have the floor recessed by 6 feet to position the magnet gap center at the same height as the rest of NSCL beam lines. A conceptual design of the helium vessel has been analyzed to ensure that the large Lorentz forces in the coils are manageable. The forces on the coils, both along the straight section in the yoke and along the ends, have been studied and sufficient space between the coils and yoke pole tips exists. The results of the structural analysis are shown in Figure 9.15. Both the stress and deformation are within tolerable limits.

The stored energy in this magnet is significantly larger than other magnets at FRIB/NSCL. As a result, the quench-protection scheme will be different than previously built and operated magnets. The SAMURAI dipole magnet at RIKEN [SAT13,KOB13] has comparable dimensions as the DS1 magnet and its quench protection scheme will be evaluated as a candidate for DS1.

During the detailed design phase, the magnet design will be optimized to minimize cost and to reduce risk while meeting the ion optical performance requirements. Table 9-12 is a summary of the conceptual design for DS1.
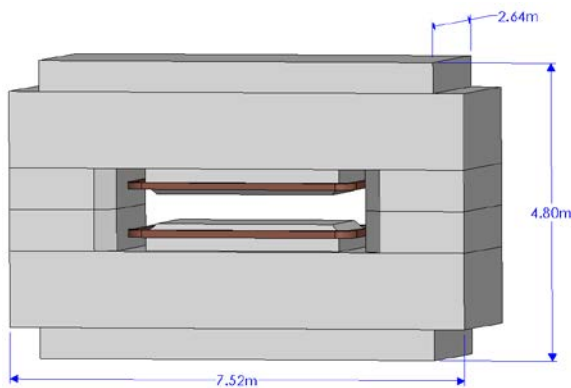
Figure 9.10 Conceptual layout of the DS1 dipole magnet, with dimension as specified.
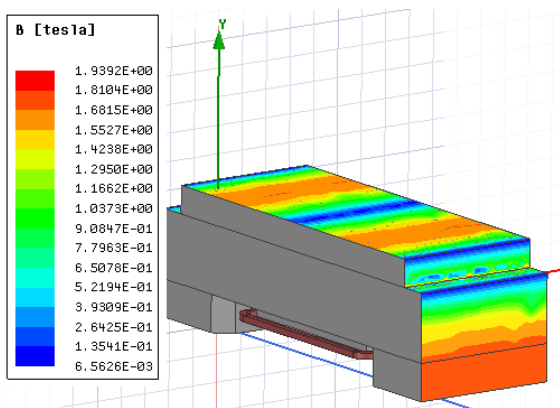
Figure 9.11 Magnetic field on the outside of the yoke for the DS1 magnet.
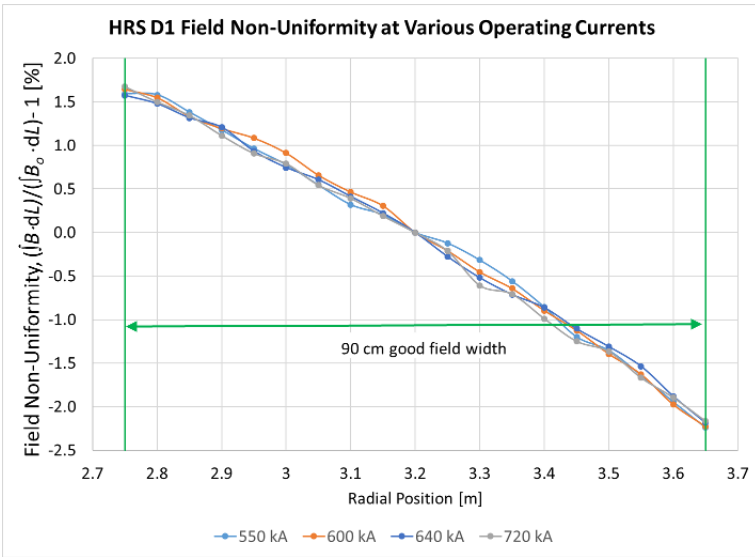
Figure 9.12 Field non-uniformity of spectrometer section DS1 dipole as a function of the radial position and at various operating currents. Note that ion-optical simulations have so far found this to be acceptable though preliminary specification of 1% non-uniformity was provided.
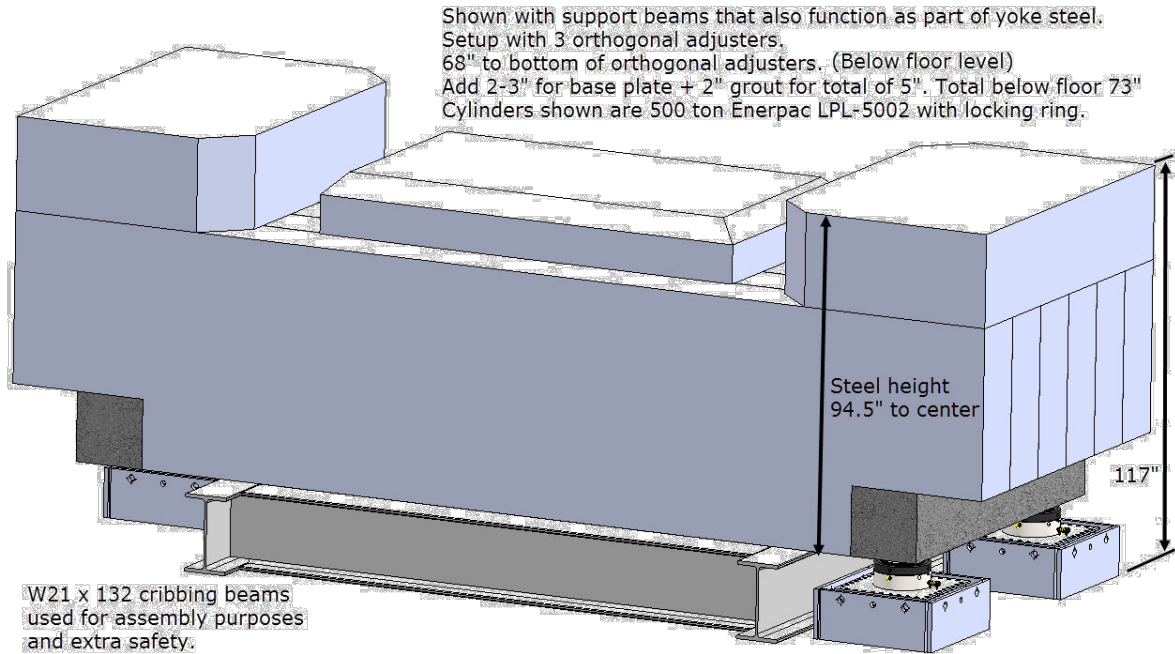
Figure 9.13 Bottom half of yoke for DS1 shown on support stand.

a)
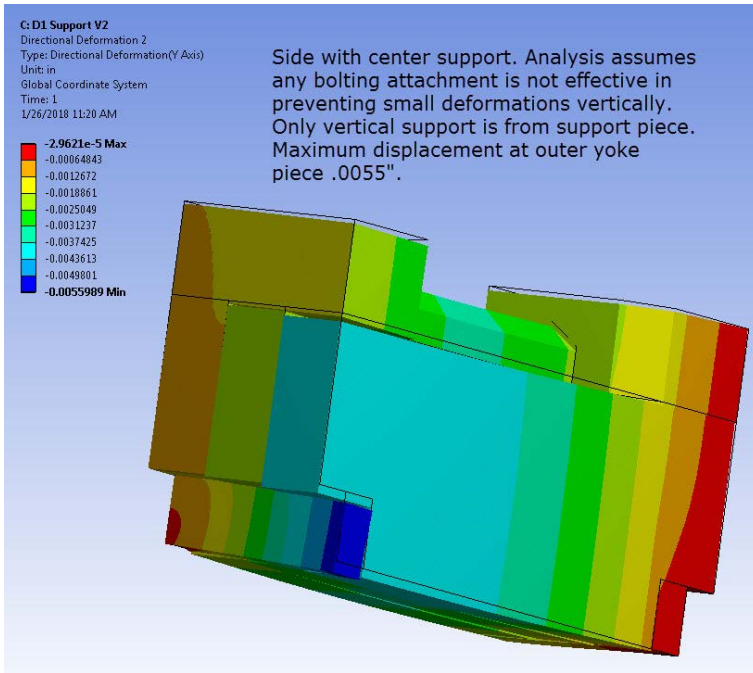
Figure 9.14 a) Deformation of the DS1 support stand. The maximum displacement if 0.0055" at the outer yoke piece; b) The pole piece for DS1 stays flat within 0.0005" when placed on the support stand.

b)

a) b)
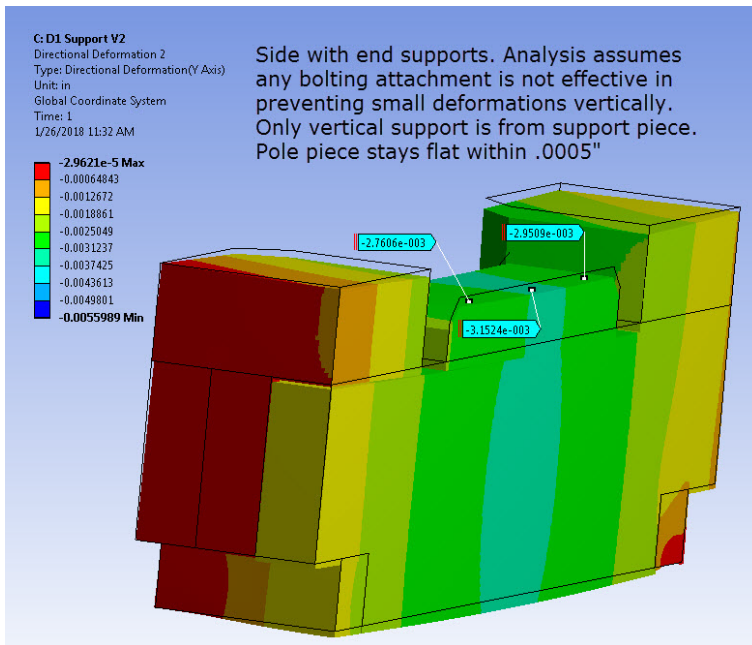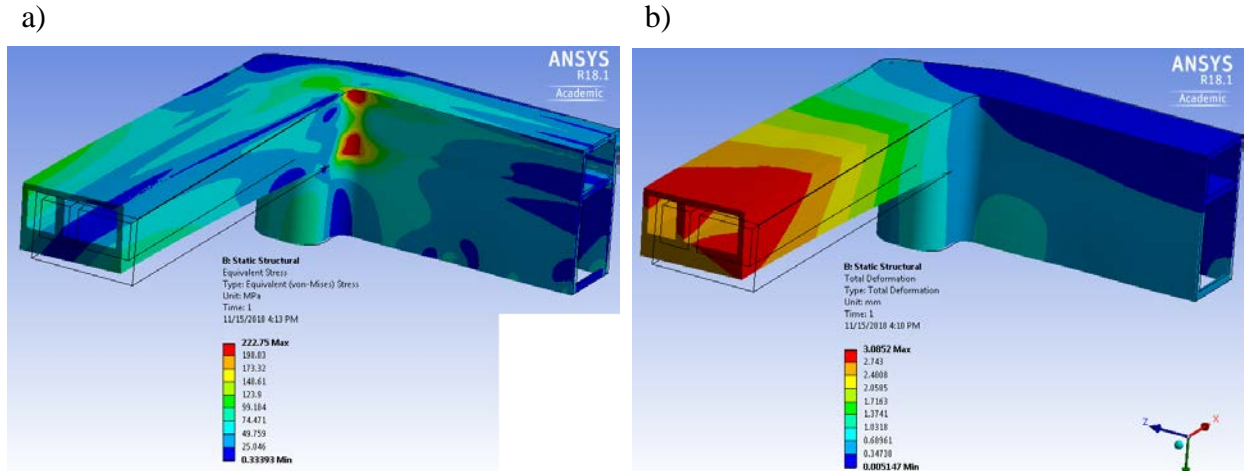
Figure 9.15 Stress (a) and deformation (b) in the coil bobbin for DS1. The peak stress is below the maximum allowable stress and the maximum displacement is 3 mm on the end of the coil. For a coil as large as DS1, this is well within the acceptable range.

Table 9-12 Spectrometer section DS1 dipole design values that meet the requirements of Table 9-6. The non-uniformity values shown are the values calculated from the magnetostatic models, and are similar to the preliminary estimates (1%). The field values from the MAXWELL model where found to achieve acceptable performance providing a sound basis for detailed design and optimization.

Parameter	Value
Quantity	1
Steel length/width/height/gap (m)	2.635, 7.52, 4.80
Steel mass (metric tons)	649.4
SC wire cross section (mm^2)/kA-turns	110×110, 550
B_{max} (T) gap	2.24
Integrated field non-uniformity (%)	+1.6 / -2.2
B_{max} on outside of yoke (T)	1.94
B_{max} in coil (T)	2.76
Stored energy @ 550 kA-turns (kJ)	7712.6
L_{eff} @ 550 kA-turns (m)	2.205
$\int B \cdot dl$ (T-m)	4.941
J_c (B_{max} in quad, 4.2 K) (A/mm^2)*	299.3
J_{op} - operating current density (A/mm^2)	60.6
J_{op}/J_c	20.2%
Power supply A,V, uni or bipolar	364 A, 40 V 2 quadrant (+I, ±V)

* Based on FRIB FSD1 wire

The conceptual design for DS2 is shown in Figure 9.16. In Figure 9.17, the dipole field non uniformity is shown as a function of the radial position, with levels ranging from -1.0% to +1.3% within the good field region. Since the MAXWELL fields from this design were used in the ion-

optical simulations presented in Section 6 and the required ion-optical properties of the Spectrometer Section were achieved, these levels of non-uniformity may be acceptable for DS2 though the preliminary homogeneity requirements were set at 1%. During the detailed design of DS2 optimization with respect to the cost, risk, and performance will done in conjunction to further evaluation of the ion-optical performance under DS1 design assumptions. Table 9-13 is a summary of the design details.

Engineering analyses for DS2 has not progressed to the level of that for DS1. However, the DS2 design follows design approaches based on NSCL/FRIB experience and engineering evaluations of the DS1 dipole. As a consequence, the conceptual design provides a sound basis for costing and further detailed analyses.
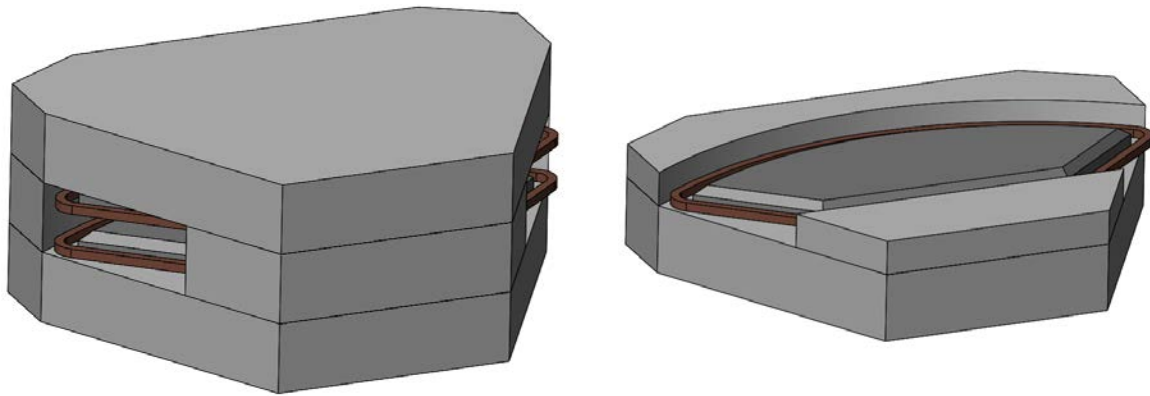
Figure 9.16 DS2 dipole layout, including a cut-away view showing the pole-tip and coil details. The length of DS2 is 5.87 m, the width is 4.21 m, and the height is 2.40 m.
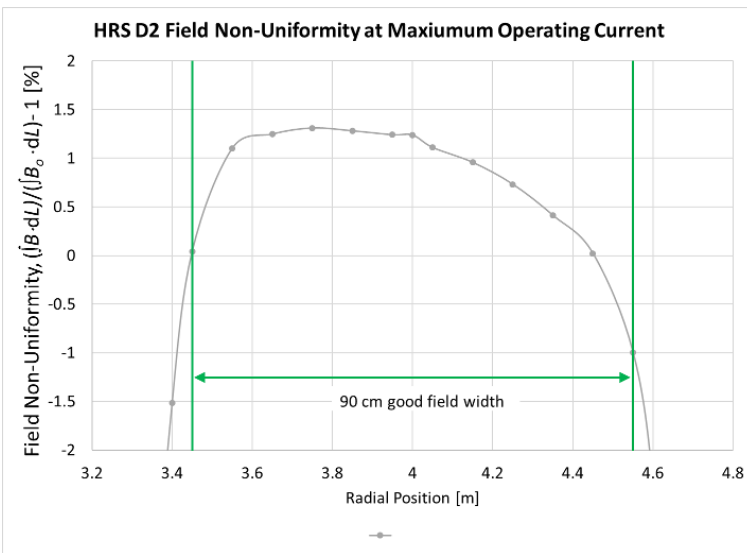
Figure 9.17 DS2 field non-uniformity as a function of the radial position. A non-uniformity ranging from +1.3% to -1.0% is achieved over the good field region in the conceptual design. Note that the ion-optical simulations have found this level of non-uniformity to be acceptable although a preliminary specification of 1% non-uniformity was provided.

Table 9-13 Spectrometer section DS2 dipole design values that meet the requirements of Table 9-6. Note that ion optical simulations have so far found this to be acceptable though preliminary specification of 1% non-uniformity was provided.

Parameter	Value
Quantity	1
Steel length/width/height/gap (m)	5.87 / 4.21 / 2.40
Steel mass (metric tons)	303.9
SC wire cross section (mm²)/kA-turns	100×100 / 720
B_{max} (T) gap	1.99
Integrated field non-uniformity (%)	+1.3 / -1.0
B_{max} on outside of yoke (T)	1.92
B_{max} in coil (T)	1.10
Stored energy (kJ)	2578
Effective magnetic length at R = 4 m (m)	4.27
∫B·dl (T m)	8.476
J_c with 3.21T & 4.2K (A/mm²) - for FRIB FSD1 wire	988.9
J_{op} - operating current density (A/mm²)	100.8
J_{op}/J_c	0.102
Power supply A,V, uni or bipolar	455 A, 6 V 2 quadrant (+I, ±V)

9.5 Quench protection

A quench analysis has been performed for the HTBL dipole and all magnets in the Spectrometer Section. The HTBL quadrupoles were not analyzed since they are copies of an existing design. Three types of magnet quench-protection methods are identified:

1. Self-protecting. Some magnets do not require quench detection. In the event of a quench, the power supply will detect the quench and ramp to 0 A. The current will then decay through the magnet and slow dump resistor. The corresponding circuit diagram is shown in Figure 9.18.
2. Quench heating. Some magnets require quench heaters to ensure all coils quench. In this case, a switch (see Figure 9.19) is opened after detecting the quench. The current will then go through the quench heater (R_QPH) and fast dump (R_fast) resistors. The voltage across R_QPH is used to power the quench protection heaters (QPH) on each coil. This will limit the peak voltage to ground during the quench.
3. Quench protection similar to the SAMURAI magnet at RIKEN [KOB13,SAT13]. In this scheme, the heaters are used to quench the entire outer layers of the coils.

In Table 9-14, the quenching-protecting method for each of the magnets is identified. The preliminary estimated peak voltage and temperature during the quench are also provided.
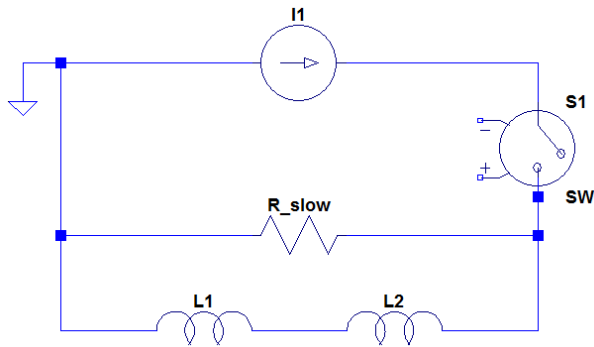
Figure 9.18 Circuit diagram for self-protecting magnets.
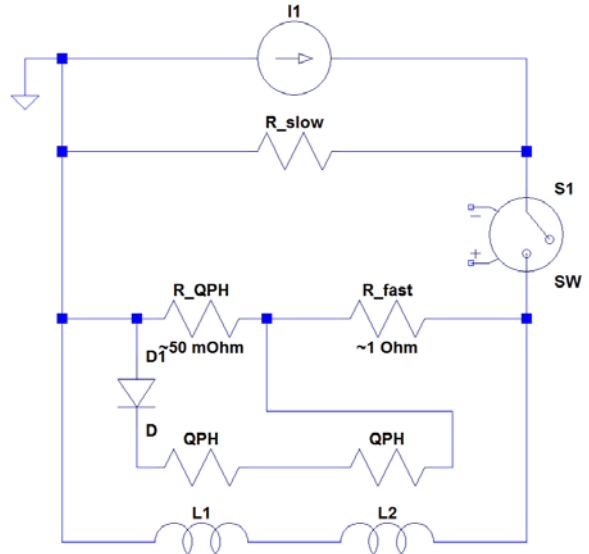
Figure 9.19 Example of quench circuit for magnets with quench heaters on all coils.

Table 9-14 Quench protection methods used for each magnet and preliminary estimated quench results.

Magnet	Quench Protection Method	Peak Voltage (V)	Peak Temperature (K)
QSA quadrupole	QPH	178	116
QSA sextupole	Self-protecting	89	79
QSA octupole	Self-protecting	41	36
QSB quadrupole	QPH	527	159
QSB sextupole	QPH	102	89
QSB octupole	Self-protecting	46	122
QSC quadrupole	QPH	520	159
QSC sextupole	Self-protecting	481	122
QSC octupole	Self-protecting	101	57
DS1 dipole	Samurai	TBD	TBD
DS2 dipole	Samurai	TBD	TBD
HTBL dipole	Self-protecting	214	179

9.6 References

[ANS18] ANSYS® MAXWELL, Release 19.1, ANSYS, Inc.

[KOB13] T. Kobayashi et al., "SAMURAI Spectrometer for RI Beam Experiments," Nuclear Instruments in Physics Research B 317, pp. 294-304 (2013)

[SAT13] H. Sato et al., "Superconducting Dipole Magnet for SAMURAI Spectrometer," *IEEE Transactions on Applied Superconductivity*, vol. 23, no. 3, 4500308 (June 2013)

10 Power Supplies

10.1 Introduction and overview

The Power Supplies (PS) scope includes the materials and manpower needed for designing, acquiring, bench testing, installing, in-situ testing, and final integrated testing without beam of the power supplies, power connection to the loads, and technical utilities, as specified by the WBS provided in Table 10-1.

Table 10-1 Power Supply WBS

Experimental Systems - High Rigidity Spectrometer	HRS.3
High Transmission Beamline (HTBL)	HRS.3.01
High Transmission Beamline Power Supplies	HRS.3.01.05
Spectrometer Section	HRS.3.02
Spectrometer Section Power Supplies	HRS.3.02.07
Central Systems	HRS.3.03
Technical Utilities and Infrastructure	HRS.3.03.04

10.2 Requirements

The requirements of the power supplies (PS) originate from the lattice design meeting the physics requirements (See Section 4) for the HTBL (See Section 5) and for the Spectrometer section (See Section 6) with concomitant hardware for the magnets (See Section 9). These requirements are summarized in Tables Table 10-2 and Table 10-3 in Section 10.4.1. The general power supply requirements are as follows:

- All superconducting magnet (SCM) PS will operate continuously in DC mode, i.e., there are no superconducting persistent switches.
- All PS are remotely programmable.
- In order to ramp the magnet current up (source) and down (sink), the dipole magnets require 2 quadrant (+I, ±V) SCM PS, and the multipoles require 4 quadrant (±I, ±V) SCM PS. Most magnets require the SCM PS to source and sink at ±6 V (or at a lower programmable voltage limits). However the QSB quadrupole and DS1 dipole magnets require the power supplies to source and sink at ±40 V in order to minimize the time required to ramp the magnets to field.
- During ramp up and ramp down, the PS ramps at the programmable voltage limit. Once the current set point is reached, the voltage will drop (to the voltage drop on the resistive DC leads) and the PS will regulate current.
- The SCM PS will supply power to a superconducting magnet, which is a purely inductive load, through a series DC lead resistance. Every SC magnet will have a dump resistor in parallel, located at the PS, to protect the magnet and PS from open circuit and to provide a safe path to discharge stored energy in the magnet. The dump resistor must be rated to dissipate the stored energy in the magnet plus margin, after a ramp at full voltage to full current. The current feedback measurement must be taken after the dump resistor (shown in Figure 10.2 and Figure 10.3), so that the magnet current is the regulated parameter. The dump resistor is included in

the PS scope. If the current measurement device fails or becomes disconnected, the PS shall interlock off.

- If the PS shuts off (for any reason, AC power, operator command, PS failure, external interlock, etc.), most magnets will slow dump at a maximum of 80 V. The dump resistance is based on 80V at maximum supply current. For example, a 0.8-Ohm dump resistor is used for a 100-A maximum-current supply). The QSB quadrupole and DS1 dipole magnets may slow dump at a higher voltage.

- All of the HTBL magnets and several Spectrometer Section magnets are self-protecting and no special circuits are needed other than the 80-V slow dump resistor. Per Table 9-14, the two HRS dipoles, six HRS quadrupoles, and three HRS sextupoles will require fast dump circuits as shown in Figure 9.19. The fast dump resistors (R_slow, R_fast, and R_QPH) and switches (S1), will be included in the PS scope. The maximum fast dump voltage is 200 V. The magnet scope will include the diode (D1) and quench protection heaters (QPH). The diode turn-on voltage will be sized so that the 80-V slow dump will not trigger the quench-protection heater resistors. However a ~100 V to 200 V fast dump will trigger the heaters. The fast dump switch will only be opened for magnet emergencies (i.e. the coil voltage difference exceeds 100 mV). Both the SAUMRAI and QPH quench-protection methods will require the same fast dump switch and a similar fast dump resistor topology. The QSB quadrupole and DS1 dipole magnets may fast dump at a higher voltage.

- The fast dump switch must be rated to open at full current, and rated for the dump voltage. The dump switch shall be normally open (fail-safe), such that if the controls are disconnected, the switch opens and the magnet quickly discharges. The response time of the switch to open from the time a signal is received shall be less than 100 ms. The control signal shall react within 15 ms from the event requiring a fast dump. The total delay shall be less than 115 ms. The PS with fast dump switches shall have separate inputs for the external interlock and for control of the fast dump switch. The 100 ms fast dump switch opening response time is the time defined as the time from the start of when the control input from the PLC changes state, to when the switch is open. When the switch is open, the circuit is in the fast dump state.

- The magnets shall not fast dump if the power supply turns off. The purpose of the slow dump is to discharge the magnets in case the power goes off or the power supply turns off for any reason. The capability to power the dump switch from UPS power is needed (UPS is provided by HRS conventional facilities). Therefore, the fast dump switch shall have a separate AC power connection to enable a connection of the fast dump switch to UPS power if necessary.

- All PS will have sufficient internal and hardwired external PLC (controls scope) interlocks to prevent damage to either the PS or magnet due to changes in cooling conditions, AC power disturbances, and out-of-range set-points. Room-temperature corrector magnet (RTM) coils will have a water-flow interlock, and an over-temperature interlock to provide redundant protection against damage from overheating. All superconducting magnets (SCM) will be protected by having helium-level, helium-pressure, and lead-voltage interlocks.

- HRS controls and magnets will provide magnet-quench detection. The main method for quench detection is by measuring the voltage difference between different coils. In addition, the current leads are protected against excessive temperatures by continuously monitoring lead voltage drops. The measurements are taken across the leads (not across the magnet) inside of the cryo-

vessel, from the room temperature feedthrough to the superconducting magnet connections. The leads typically are set to have a voltage drop of 70 mV at maximum current. If the lead voltage increases to 100 mV the PS is interlocked off. The power supply shall shut off its output within 50 ms, measured from the time the external interlock signal is received to the time the supply switches off.

- SCM PS operates in either two or four quadrants. A two quadrant SCM PS sources or sinks power with one polarity of current [(+V, +I), (-V, +I)]. A four quadrant (or bipolar) SCM PS, sources or sinks power in any polarity [(+V, +I), (+V, -I), (-V, +I), (-V, -I)], and cross through zero current smoothly. Dipole PS require two-quadrant operation, all others require four-quadrant operation. However, it may be advantageous to use a four-quadrant SCM PS, even if only two quadrants are required. This would simplify the overall system, and reduce the types of spares required.

- All PS will use Ethernet Digital control with EPICS interface capability, by using the Modbus TCP communication protocol. The current and/or voltage set points, read backs, limits, and digital commands, and statuses (other than external interlock and on/off status) shall be made over the network. All PS shall have a hardwired on/off status output. The response time of this output shall be 50 ms or less. The on/off status output shall be a 24-V signal, with 24 V signifies "on", and 0 V or disconnected signifies "off". The external interlock and fast dump-switch control signals shall always be hardwired, and designed to be fail-safe. Hence, if the signal becomes disconnected, the PS shall shut off, or the switch shall open. These signals shall operate using an isolated 24-V signal: a 24-V level allows operation while 0-V or a disconnected status disables the PS or opens the switch.

- The long-term current stability requirements (defined as parts per full scale current, over 8 hours with fixed line, load, and ambient temperature) match those from the FRIB Experimental Systems Division [FRIB-T31209-SP-000152] pre-separator: ±20 ppm (long term stability and temperature coefficient) class for the dipoles, ±280 ppm class for quadrupoles, and ±500 ppm for the multipoles. The dipole PS will be located in the lower level of the PS area, where the air-temperature stability will be tightest at 24 °C ± 2.8 °C. The calculated worst-case long-term dipole PS current stability equals ±130 ppm full scale (20 ppm/°C temperature coefficient, assuming constant line and load, and worst case air temperature stability). The worst-case air-temperature stability on the mezzanine will be 24 °C ± 5.6 °C. Therefore, the calculated worst-case long-term quadrupole-current stability equals ±1850ppm (140 ppm/ °C temperature coefficient), and the calculated worst-case long-term multipole current stability equals ±2740ppm (200 ppm / °C temperature coefficient). These calculated worst-case long-term current stabilities meet the required PS stability in Table 10-2 and Table 10-3. Testing of similar systems at FRIB and NSCL have shown the measured long-term current stability to be well within the calculated values.

- DC leads are cables required to connect the PS to the magnets. The DC leads from the PS to the magnet will be approximately 100 ft. each. Extra flex UL tray-rated cable will be used because of its flexibility and durability. The number of conduits to exit the rack area and route to the magnets has been calculated and incorporated into the building design. The conduits are based on the number of DC leads, lead gauge, and lead length of the HRS DC leads, with additional conduits for all other signal types and spare conduits. The DC leads will be routed

between the racks and beamline vault, will be routed in cable trays, and through conduits between the areas. The DC leads are required to be UL listed for use in cable tray, and follow NEC guidelines for use in conduits, terminations, connections, etc. The DC leads are also sized to minimize the voltage drop to ~1 V, in order to minimize the time to ramp the magnet to field.
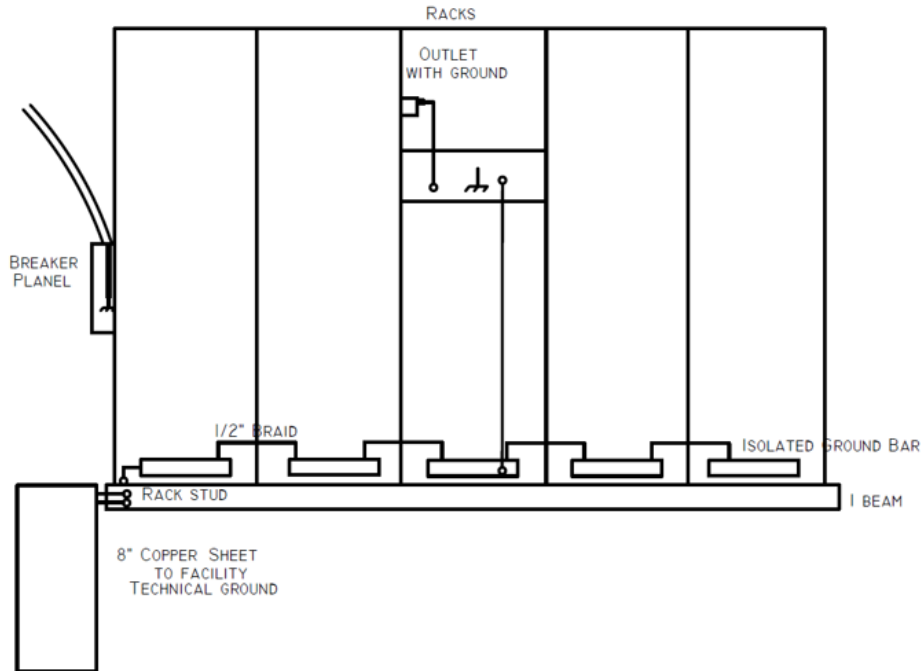
Figure 10.1 Typical rack row and device grounding block diagram.

10.3 Design approach and alternative analyses

Switch-mode regulated PS technology is preferred over linearly-regulated PS technology because of the higher efficiency and the smaller physical size. Switch-mode technology is a proven technology at NSCL and FRIB. One drawback of the switch-mode topology is the presence of high-frequency noise, which can be mitigated by high-frequency grounding. Like most electrical equipment, the FRIB Power Supply (PS) systems must be grounded to a facility ground to comply with electrical codes. This is typically achieved through the main electrical ground from the 60-Hz supply. But while this type of grounding is sufficient for safety purposes, it is inadequate for high-frequency currents, which require a very low impedance path. The high-frequency grounding of HRS power supplies will follow standard practices and suggestions [FRIB-T31209-PR-000444, FRIB-T10503-VS-000001], and as shown in Figure 10.1.

Standard "off-the-shelf" single-quadrant PS with external polarity reversal will be used for the Room-Temperature (RT) steerer magnet PS. The polarity reversal will have a zero-crossing delay of around 2 seconds. The SCM PS will utilize FRIB type PS or similar custom build-to-specification PS. Alternative approaches such as build-in-house, and build-to-print have been considered but are not practical as the SCM PS use standard technology available at several specialty power-supply suppliers. Technical utilities use off-the-shelf equipment and standard

industrial practices. Examples of FRIB SCM PS and interfaces [FRIB-T31209-CM-000111] are shown in Figure 10.2 and Figure 10.3.
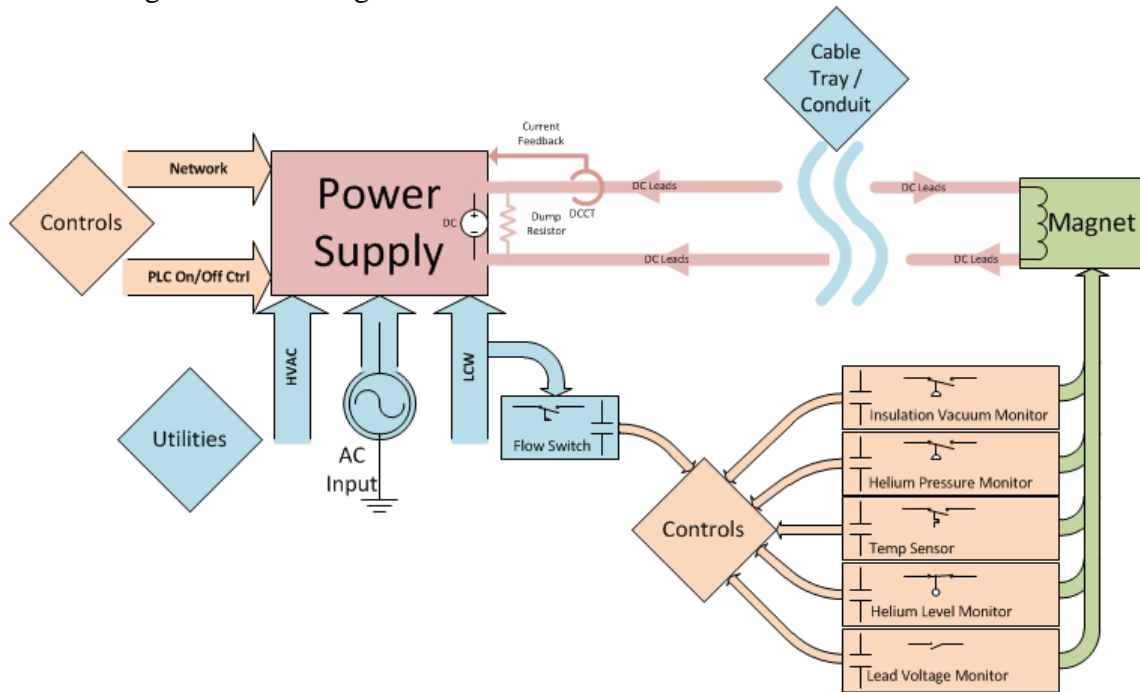
Figure 10.2 Typical SCM PS block diagram
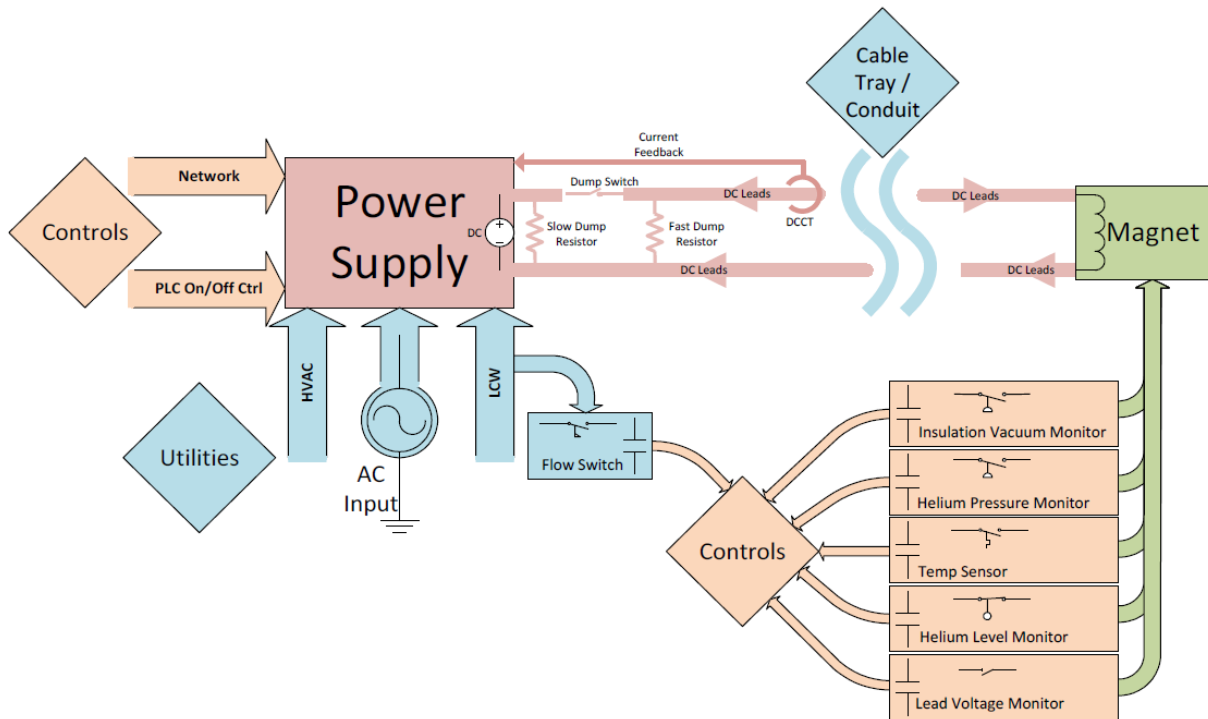
Figure 10.3 Typical SCM PS block diagram with fast dump circuit.

10.4 Preferred alternative

The hardware including power supplies and associated infrastructure will be similar to recent FRIB procurements. Technical utilities use off-the-shelf equipment and follow standard industrial practices.

10.4.1 Power supplies

10.4.1.1 HTBL power supplies

Table 10-2 contains the HTBL magnet name, quantity, maximum magnet current required, PS current, PS voltage, stability requirement, and PS stability. These requirements originate from the lattice design meeting the physics requirements (See Section 4) for the HTBL (See Section 5) with concomitant magnet hardware (See Section 9).

Table 10-2 HTBL PS requirements

Magnet type	Magnet Description	Current (A)	PS stability ppm_fs*	Required PS stability ppm_fs**	Voltage (V)	Number of Quadrants	E_stored (J)	L (H)	Total PS needed	80 V Slow Dump Circuit Required	200V Fast Dump Circuit Required	Delta V Circuit Required	Quench Protection Topology
HTBL-D	Dipole	214.	20	150	6	2 (or 4)	3.76E+05	16.40	4	yes	no	no	Self-protecting
HTBL-QB(Q)	Quad	70.0	300	2000	6	4	8.80E+04	41.5	16	yes	no	no	Self-protecting
HTBL-QB(S)	Sextupole	45.0	300	2000	6	4	9.60E+02	1.2	16	yes	no	no	Self-protecting
HTBL-QB(O)	Octupole	20.0	500	3000	6	4	1.00E+02	0.5	16	yes	no	no	Self-protecting
HTBL-QC(Q)	Quad	90.0	300	2000	6	4	1.72E+05	47.7	8	yes	no	no	Self-protecting
HTBL-QC(S)	Sextupole	45.0	300	2000	6	4	9.60E+02	1.2	8	yes	no	no	Self-protecting
HTBL-QC(O)	Octupole	20.0	500	3000	6	4	1.00E+02	0.5	8	yes	no	no	Self-protecting
C1	RT Corrector	250	500	3000	100	2	4.43E+03	0.16	2	NA	NA	NA	NA

* Parts per million of full scale (ppm_fs) assuming constant line, load, and ambient temperature
** ppm fs assuming constant line, load, and worst case ambient temperature change

10.4.1.2 Spectrometer Section power supplies

Table 10-3 contains the HTBL magnet name, quantity, maximum magnet current required, PS current, PS voltage, stability requirement, and PS stability. These requirements originate from the lattice design meeting the physics requirements (See Section 4) for the Spectrometer Section (See Section 6) with concomitant magnet hardware (See Section 9).

Table 10-3 Spectrometer Section PS requirements.

Magnet type	Magnet Description	Current (A)	PS stability ppm_fs*	Required PS stability ppm_fs**	Voltage (V)	Number of Quadrants	E_stored (J)	L (H)	Total PS needed	80 V Slow Dump Circuit Required***	200V Fast Dump Circuit Required****	Delta V Circuit Required	Quench Protection Topology
QSA	Quad	414.9	300	2000	6	4	1.37E+06	15.96	1	yes	yes	yes	QPH
	Sextupole	62.5	300	2000	6	4	1.49E+04	7.63	1	yes	no	no	Self-protecting
	Octupole	59.8	300	2000	6	4	2.77E+03	1.55	1	yes	no	no	Self-protecting
QSB	Quad	448.8	300	2000	40	4	9.96E+06	98.93	3	yes	yes	yes	QPH
	Sextupole	227.3	300	2000	6	4	3.46E+05	13.41	3	yes	yes	yes	QPH
	Octupole	225.2	300	2000	6	4	9.04E+04	3.56	3	yes	no	no	Self-protecting
QSC	Quad	345.7	300	2000	6	4	8.28E+05	13.86	2	yes	yes	yes	QPH
	Sextupole	86.5	300	2000	6	4	5.80E+04	15.48	2	yes	no	no	Self-protecting
	Octupole	50.3	300	2000	6	4	1.30E+04	10.28	2	yes	no	no	Self-protecting
DS1	Dipole	363.8	20	150	40	2 (or 4)	7.71E+06	162.23	1	yes	yes	yes	SAMURAI
DS2	Dipole	454.3	20	150	6	2 (or 4)	2.54E+06	24.61	1	yes	yes	yes	SAMURAI

* ppm_fs assuming constant line, load, and ambient temperature

** ppm_fs assuming constant line, load, and worst case ambient temperature change

*** QSB quadrupole and DS1 dipole magnets may slow dump at a higher voltage

**** QSB quadrupole and DS1 dipole magnets may fast dump at a higher voltage

10.4.2 Technical utilities and infrastructure

HRS technical-equipment racks are part of the technical utilities. Rack space calculations have been made and include the following specifications. To keep the temperature of the PS well below the maximum operating temperature, the use of exhaust fans may be incorporated in racks which contain air-cooled PS. One rack unit (1.75 in) is the recommended spacing between power supplies and is accounted for in the calculations. Blank panels will be installed in the 1 U spaces between power supplies to help prevent dust from settling inside the PS. Water cooled PS (SCM PS) will be located in the bottom of the rack to keep them out of the exhaust path, to help prevent equipment damage in case of a water leak, and to keep them from heating unnecessarily. Rack space calculations include a maximum 80% fill factor. This provides an opening for the air to flow above the SCM PS and around the air cooled supplies. Physical space is available for additional and upgrade racks if necessary. Forty-two racks are foreseen for HRS PS (32) and controls (10). Five

racks are foreseen and reserved for the future 120 kW RF separator electronics. Space for 63 racks is available on the mezzanine and ground levels of the PS area as shown in Figure 10.4.
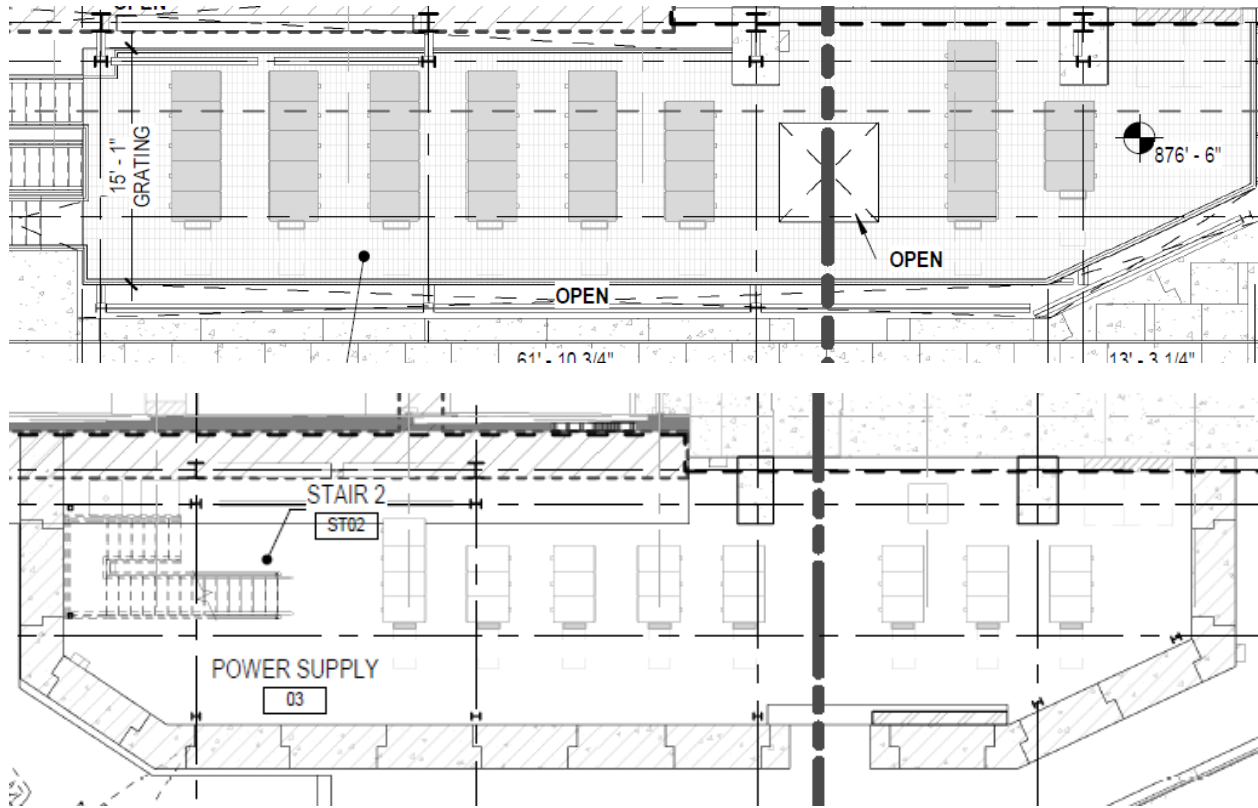
Figure 10.4 (top) Rack layout at the mezzanine level, providing space for 38 racks. (bottom) Rack layout at the ground floor level, providing space for 25 racks.

- Utilities for PS include AC power (330 kW total with upgrades), treated filtered Process Water (PW) for SCM PS (360 GPM total with upgrades), and HVAC (7.8 tons total with upgrades). The capacities have been calculated and provided through the conventional facilities scope (outside of the HRS scope). The final distribution of AC power (from the AC panels to the racks) and PW (from main header to devices in the racks) is part of technical utilities.
- All SCM PS will be fed from 208 VAC 3-phase AC power, or standard 120 VAC. RT corrector magnets will use standard 208 VAC 3-phase AC power. Each rack row will have a 400-A panelboard mounted on the end of the row. Installation of 240 kW at 480 VAC 3-phase power for a future 120-kW RF separator has been foreseen and physical space has been reserved. A UPS panel will be provided by conventional facilities and the technical utilities scope will cover the distribution from the UPS panel to the controls racks where UPS is required for cryogenic PLCs and magnet fast dump switches. Six clean-power AC panels, clean-power transformers, and related equipment will be provided by conventional facilities. Technical utilities scope will cover the clean-power distribution from the 6 panels in the vault to the diagnostics and detectors on the HTBL and Spectrometer Section.
- Calculations have been made for water-cooled SCM PS HVAC and PW flow requirements. Conventional facilities will provide the PW system used to cool power supply racks. The PW

system shall be cooled with a dedicated cooling-tower water system. Process Water (PW) will be sized to be at least a 150-lb. rated system. Process Water temperature rise through equipment is assumed to be similar to the RF rack facility at FRIB. This assumption results in an average temperature rise through the equipment of approximately 7 °F. The Process water loop will be designed to provide water with a temperature of 90 °F ± 2 °F to the technical equipment. Process Water systems will be normal-quality cooling water, not Low Conductivity Water (LCW). There are no known special quality requirements. A 5-Micron Side-Stream filter is included for the closed loop PW system. The process-water pressure drop across each Power Supply has been measured to be approximately 80 psig.

- Low-conductivity water is only required for the RT steerer magnets in the vault. The two magnets require 5 GPM each. An additional 5 GPM has been reserved in case the large roughing pump will be water cooled. Space will be reserved for the future RF separator, which will require 28 GPM of PW on the rack mezzanine, 120 GPM of LCW to the transmitter (72 GPM) and cavity (48 GPM), and 5 GPM each for the RT kicker magnets.

- Waste heat from DC cables and air-cooled RT steerer magnet PS are included in HVAC requirements. The High bay Air Handling Unit will maintain the air temperature at 75 °F ± 10 °F throughout the high bay, but will control to the thermostat furthest from set point. The thermostats will be located near the mezzanine. The lower level of the rack area will be controlled to a space temperature of 75 °F ± 5 °F. Space relative humidity will vary from 10% to 60 %. The dipole PS will be located in the lower level rack area due to the tighter air temperature stability.

- The DC leads from the PS to the magnet will be routed between the equipment racks and the magnets in the vaults. The DC cables will be routed in cable trays, and through conduit between the areas. The conduits are part of the conventional facilities scope (outside of the HRS scope). The cable trays from the racks to the conduits and cable trays along the beamline are part of technical utilities scope. The number of conduits has been calculated, and the calculations of the number of conduits include a 50% fill factor versus the National Electric Code. The voltage drop on the cables have been calculated to be approximately 1 V for the superconducting magnet PS and is well within the acceptable range. Sixty-one six-inch conduits for DC and controls are foreseen. The building design includes 71 six-inch conduits, as shown in Figure 10.5, plus an alternate route with 16 four-inch conduits. Additionally, an alternate route through the existing NSCL wall and through conduits in a future roof-beam ledge has been identified.
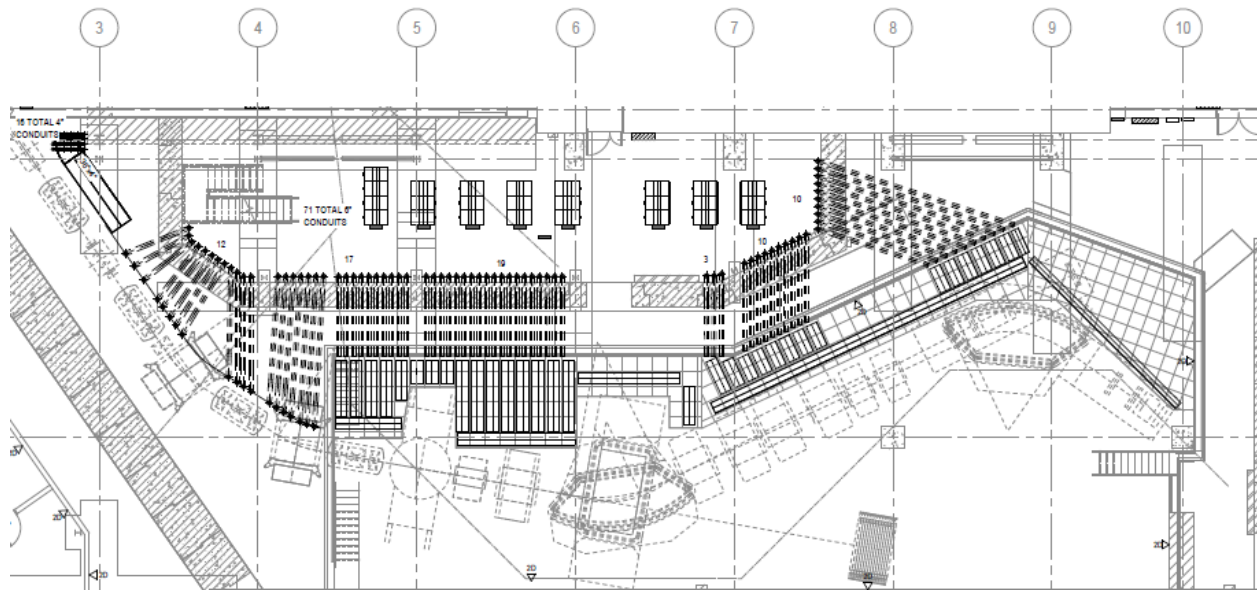
Figure 10.5 Layout of conduits from equipment racks to the HTBL and Spectrometer Section of the HRS.

Compressed-air and dry-nitrogen distribution along the HRS beamlines are part of technical utilities scope. Conventional facilities will provide the compressed air capacity and main distribution. The existing NSCL dry-nitrogen supply will be the primary source for HRS, along with N_2 bottles and/or boil-off Dewars, if additional capacity is required.

Possible future upgrades have been considered for the worst-case upgrade as far as rack space, conduit, and utilities are concerned. Physical room for racks will be available, conduits will be in place, and utilities will have adequate infrastructure in place for future upgrades. Future upgrades include an RF Separator along with 2 kicker magnets (identical to the RT corrector magnets), and some rack space is reserved for other future possibilities.

10.5 References

[FRIB-T31209-SP-000152] Superconducting Magnet Power Supplies Specifications
[FRIB-T31209-PR-000444] FRIB Power Supplies High Frequency Grounding Installation Procedure
[FRIB-T10503-VS-000001] Using the FRIB Facility Grounding Mesh System Effectively
[FRIB-T31209-CM-000111] FRIB Power Supply Interface Control Document

11 Cryogenic Systems

11.1 Introduction and overview

The HRS requires cryogenic capacity in the form of liquid helium and liquid nitrogen for cooling of the superconducting magnets. The Work Breakdown Structure (WBS) is given in Table 11-1. The cryogenic mode of operation is patterned after the existing refrigeration system presently supplying the magnets of the NSCL A1900 fragment separator. The system design assumes the magnetic coils are bath cooled with helium supplied directly as liquid from a pressurized Dewar. The thermal shield is assumed to be cooled with liquid nitrogen.

Table 11-1. Work Breakdown Structure (WBS) for HRS cryogenic system.

Experimental Systems - High Rigidity Spectrometer	**HRS.3**
High Transmission Beamline (HTBL)	**HRS.3.01**
High Transmission Beamline Power Cryogenics	**HRS.3.01.06**
Spectrometer Section	**HRS.3.02**
Spectrometer Section Cryogenics	**HRS.3.02.08**

There are several possible cryogenic plants that may be used to supply cryogenics to the HRS, including the existing NSCL plant, the existing FRIB plant, or a new cryogenic plant. It is not foreseen that the costs incurred in providing service to the HRS system will change significantly as long as a welded line type (not U-tube) design for local magnet connections is used.

All new magnet designs will comply with FRIB cryogenic plant requirements. Since the HTBL quadrupole triplet is based on the existing design of the A1900 triplet, its design will be reviewed and any necessary modifications made to comply with these requirements. For example, the FRIB system returns cold helium to the refrigerator at a lower pressure than in the NSCL system. This results in a smaller pressure difference to drive lead flow. Therefore, the triplet current lead design will need to be modified to be compatible with the lower pressure difference.

11.2 Requirements

Requirements for cryogenic capacity of the HTBL and Spectrometer Section are as shown in Table 11-2. The cryogenic loads are based on known loads of similar operational equipment. For example, the existing A1900 system loads are known and almost identical to the HTBL system design. NSCL and FRIB have many large superconducting magnets of unique types in operation providing a good basis for accurate estimates of the spectrometer magnets cryogenic loads. Refrigeration loads due to current lead mass flow requirements that return gas warm require additional capacity from liquid nitrogen temperature to the 4.5K gas phase. The refrigeration loads due to both static loads returned cold and those for lead flow requirement (at maximum current requirement) of these devices are shown in Table 11-2.

For present operation of the NSCL coupled cyclotron accelerator system, most of the cryogenic capacity of the existing plant is required. Upon commissioning of the new FRIB accelerator,

however, some devices will be removed from the system and that capacity as given in Table 11-3 becomes available. There is a shortfall of about 208W between the new cryogenic loads and those decommissioned, much of that being due to the increased current lead requirement due to larger total current requirement from an increased number of magnets. One possible option being explored is the operation of the reconfigured A1900 off the FRIB cryogenic plant. The loads of the A1900 are equivalent to that shown for the HTBL magnets, close to being equal to the shortfall. This would therefore leave enough capacity in the present NSCL plant to fully handle the HRS total cryogenic load in addition to its other remaining loads. Importantly, no additional cryogenic plant capacity will be required. The cryogenic capacity necessary for the HRS will be available from a combination of extant FRIB and NSCL cryogenic plants.

Table 11-2. HTBL, Spectrometer Section, and distribution cryogenic loads at 4.5K.

HTBL and HRS Cryogenic Loads		Load/ unit @ 4.5 K (W)	Total load @ 4.5 K (W)	Total load for leads, from 80 K (W)	Total (W)
Device	Quantity				
HTBL Valve Boxes	12	6.5	78		
HTBL Magnets	12	5	60	151	
Spectrometer Valve Boxes	8	6.5	52		
Spectrometer Dipoles	2	20	40	32	
QS1A Quad	1	11	11	21	
QS2B-QS4B Quads	3	16	48	104	
QS5C - QS6C Quads	2	13	26	37	
Branch Box 1 System	1	16	16		
Branch Box 2	1	16	16		
Transfer Line, 300 ft	300	0.1	30		
Total			**377**	**345**	**722**

Table 11-3. Cryogenic load reduction from decommissioned coupled cyclotron elements.

Loads Removed Upon FRIB Operation		Total load for leads, from 80 K (W)	Total (W)
Device	He load (W)		
K1200 Coil	144	61.8	
K1200 Cryopanels	45		
K500 Coil	62	38.6	
K500 Cryopanels	40		
SC ECR	48	52.1	
Coupling Line	15	7.3	
Total	**354**	**160**	**514**

11.3 Design approach and alternative analyses

The design approach for the cryogenic system is based on a system similar to the cryogenics of the current A1900 and assumes branching from an existing cryogenic transfer line as is shown in Figure 11.1. This line has proven cryogenic capacity since it is part of the system supplying equipment of similar loads to be later decommissioned. If another cryogenic plant is used as the source, the existing cryogenic header of Figure 11.1 will be appropriately modified.

A branch box (HRS Branch Box 1 in Figure 11.1) from the existing main transfer line serviced by U-Tube connections is included in the design. A directional control box (HRS Branch Box 2 in Figure 11.1) separating upstream and downstream section sections of the HTBL is included and has valves to isolate one direction of the transfer line. HRS Branch Box 2 is assumed to be a welded-line construction without U-tube disconnects, similar to the extant NSCL cryogenic Box 23 shown in Figure 11.2(a).
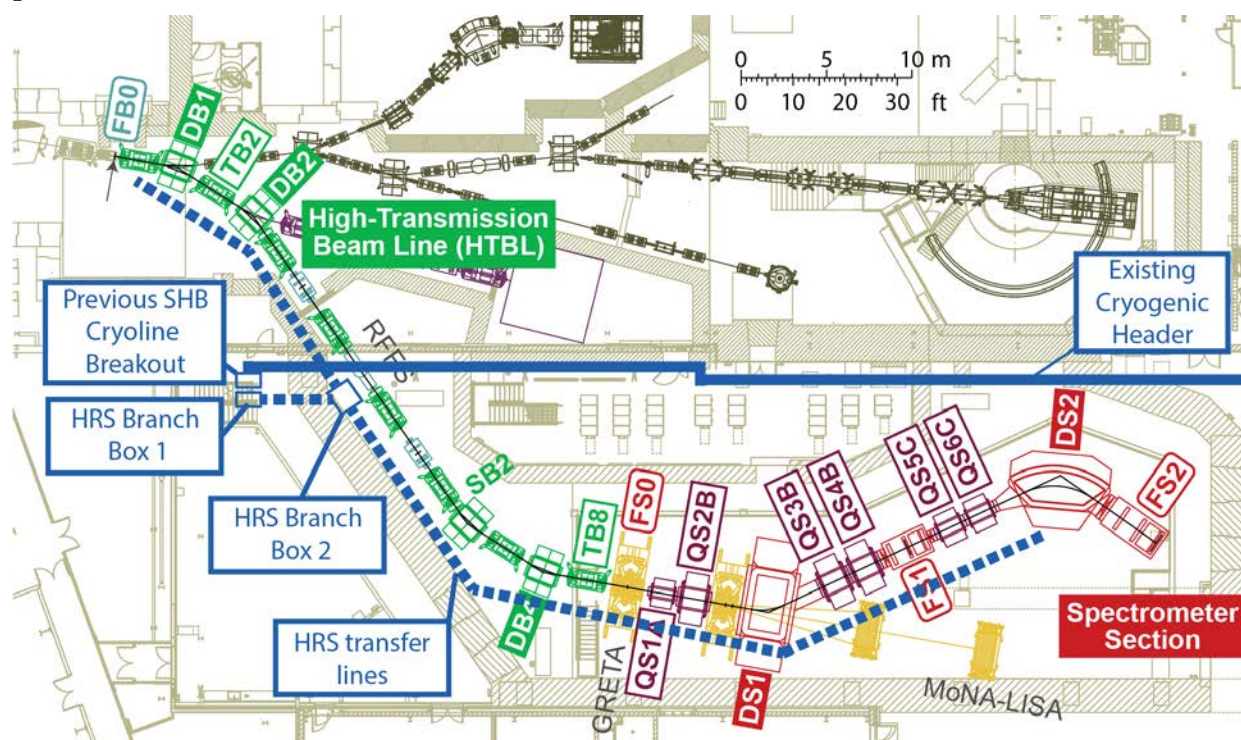
Figure 11.1 Cryogenic system layout conceptual design.

For each of the 20 cryostats (12 in the HTBL and 8 in the Spectrometer Section), there will be local valve boxes of the same design as those used for the A1900 magnets. Each valve box will have the capability of switching return helium to a warm (>20K) or cold return with the capability of supplying cold gas or LHe during cooling down. Liquid nitrogen supply and return switching for the thermal shield is also present in the local box. Similar to NSCL local distribution shown in Figure 11.2(b), welded connections to the magnets are assumed with no U-Tubes at the magnets. See references [NSCL09], [VIN09], and [LAU98].

Figure 11.2 (a) NSCL Box 23 similar to proposed HRS Branch Box 2; (b) NSCL local valve box and transfer line section similar to proposed local HRS cryogenic boxes and transfer line

The initial implementation will include a cryogenic line from the main transfer line, all branch boxes and the entire section of the transfer line including local valve boxes for 1st half of the HTBL. The further implementation will include the extension of the cryogenic head and local valve boxes needed to service the additional devices.

In the future, there may also be plans for an improved method of supplying cryogens to the newly reconfigured A1900 and also to incorporate a new, more modern helium plant. Besides having higher efficiency, this may increase cryogenic capacity. Even though the existing system and possibly the existing main cryogenic header may be replaced, it is not foreseen that the costs incurred in providing service to the HRS system will change significantly as long as a welded line type design for local magnet connections is used.

11.4 References

[NSCL09] NSCL Cryoplant Upgrade Recommendation Report, NSCL Meeting, 6/26/2009
[VIN09] Cryoplant Options and Operation Report, John Vincent, 6/2/2009
[LAU98] Review of Liquid Helium Production System, H. Laumer, 1/29/1998

12 Control Systems

12.1 Introduction and overview

The Controls scope includes the materials and labor needed to design, procure, assemble, bench test, install, test in situ, and to perform final integrated testing without beam as specified by the WBS provided in Table 12-1. The main areas of scope include Protection Systems, Controls, and Network & IT.

Low Level Control Systems include Low level controls for both the High Transmission Beamline and Spectrometer Section and is based on Experimental Physics and Industrial Control (EPICS) framework.

Protection systems include both Personnel Protection Systems (PPS), and Machine Protection Systems (MPS). The PPS provides protection to personnel from radiation hazards through access control and radiation monitoring. It also provides monitoring and alarming for low oxygen or flammable gas conditions. The MPS monitors relevant beam parameters and stops beam when conditions are no longer satisfied.

The Network and IT systems provide a high-bandwidth, high reliability network and computing platform to support control system operation.

High Level controls provide CS-Studio Operation screens, and applications such as Chart recorders, Save/Restore Utility, Archiver, alarm server, logging applications, high level EPICS IOCs, and controls for the beamline commissioning.

Table 12-1 WBS for the control systems of the HRS

Experimental Systems - High Rigidity Spectrometer	**HRS.3**
High Transmission Beamline (HTBL)	**HRS.3.01**
High Transmission Beamline Low Level Controls	HRS.3.01.07
Spectrometer Section	**HRS.3.02**
Spectrometer Section Low Level Controls	HRS.3.02.09
Central Systems	**HRS.3.03**
Protection Systems	HRS.3.03.01
Personnel Protection Systems	*HRS.3.03.01.01*
Machine Protection Systems	*HRS.3.03.01.02*
Network & IT	HRS.3.03.02
High Level Controls	HRS.3.03.03

12.2 Requirements

The requirements for controls originate from the lattice design meeting the physics requirements (see Section 4) for the HTBL (see Section 5) and for the Spectrometer section (see Section 6) with concomitant hardware (see Sections 7, 9, 10, 11, and 13).

12.2.1 Controls requirements

The resulting hardware to support the design used for magnets, power supplies, diagnostic systems, vacuum systems and cryogenics drive the signal requirements for control systems. These requirements are captured in tables for each device. An example is given for the HTBL quadrupole triplets in Table 12-2. These tables are used to determine the number of analog inputs (AI), analog outputs (AO), digital inputs (DI), digital output (DO) points, and instrumentation such as temperature controller points (Temp), 5B style signal conditioning modules, serial/ethernet connections, and motor controls (Motor Ctrl).

Table 12-2 Signal list for the HTBL quadrupole triplets used to determine the controls I/O requirements.

TBn Quad Triplet - Cryoload PLC									
Signal	AI	AO	DI	DO	Temp	5B	Serial	Ethernet	Motor Ctrl
Helium Vessel Pressure Transducer	1					1			
Helium Level Sensor	1								
Heat Shield Temperature Sensor			1		1		0.125		
Helium Vessel Temperature Sensor			1		1		0.125		
Heat Shield Temperature Sensor			1		1		0.125		
Helium Vessel Temperature Sensor			1		1		0.125		
Cryostat Vacuum Indicator	1		2				1		
Helium Vessel Rupture Disc/Popoff	1					1			
4-20 mA I to P	1	1							
4-20 mA I to P	1	1							
Solenoid Valve				1					
Solenoid Valve				1					
Solenoid Valve				1					
Insulating Vacuum Turbo Gate Valve			2	1					
Insulating Vacuum Roughing Pirani	1		2						
Insulating Vacuum Pirani	1		2						
Insulating Vacuum Cold Cathode	1		2				1		
Insulating Vacuum Turbo Pump	1		2	2			1		
Helium Vessel Pressure Transducer	1					1			
Heat Shield Temperature Sensor			1		1		0.125		
Helium Vessel Temperature Sensor			1		1		0.125		
PLC Interconnect			3	3					
TBn Quad Triplet Cryoload PLC Total:	11	2	21	9	6	3	3.75	0	0

Based on these tables, the device requirements are then summarized by portions of the project as shown in Table 12-3 for the HTBL and in Table 12-4 for the Spectrometer Section.

All of the HTBL magnets and several Spectrometer Section magnets are self-protecting and require lead-voltage, helium-level, and helium-pressure monitors for quench detection. Per Table 9-14 and

Table 10-3, the two HRS dipoles, six HRS quadrupoles, and three HRS sextupoles will require fast dump circuits as shown in Figure 9.19. The fast dump switch will only be opened for magnet emergencies. Controls will provide the Delta-V circuit to monitor the coil voltages and trigger the fast dump switch to open if the output exceeds a threshold (i.e. the coil voltage difference exceeds 100 mV). Both the SAUMRAI and QPH quench-protection methods will require the same fast dump switch and a similar fast dump resistor topology.

The dump switch shall be normally open (fail-safe), such that if the controls are disconnected, the switch opens and the magnet quickly discharges. The response time of the switch to open from the time a signal is received shall be less than 100 ms. The control signal shall react within 15 ms from the event requiring a fast dump. The total delay shall be less than 115 ms. The PS with fast dump switches shall have separate inputs for the external interlock and for control of the fast dump switch. The 100 ms fast dump switch opening response time is the time defined as the time from the start of when the control input from the PLC changes state, to when the switch is open. When the switch is open, the circuit is in the fast dump state.

High-level controls requirements flow from higher-level systems requirements and will utilize systems similar to those used at the FRIB Laboratory at present. High level control screens for use by Operations will be required, driven by CS-Studio. Applications already utilized by the FRIB Laboratory will be extended for use for the HRS, such as EPICS archivers, alarm servers, CS-Studio for screen creation and an Electronic Logbook.

Table 12-3 Device I/O Summary for the HTBL, separated into beamline, vacuum and cryoload control systems used to determine the controls I/O requirements.

System	Device	AI	AO	DI	DO	TEMP	5B	Serial	Ethernet	Motor Ctrl	EPICS IOC
HTBL – beam line	TB1	27	9	12	21	0	27	0	9	0	540
	DB1	4	2	4	6	0	4	0	1	0	91
	TB2	27	9	12	21	0	27	0	9	0	540
	DB2	4	2	4	6	0	4	0	1	0	91
	SB1	1	0	4	2	0	0	0	2	0	74
	TB3	27	9	12	21	0	27	0	9	0	540
	FB1	10	2	14	29	0	0	0	1	1	251
	TB4	27	9	12	21	0	27	0	9	0	540
	FB2	1	0	2	3	0	0	0	0	0	21
	TB5	27	9	12	21	0	27	0	9	0	540
	FB3	12	2	16	36	0	0	0	1	3	340
	TB6	0	0	4	3	0	0	0	0	0	21
	SB2	27	9	12	21	0	27	0	9	0	540
	DB3	1	0	4	2	0	0	0	2	0	74
	TB7	4	2	4	6	0	4	0	1	0	91
	DB4	27	9	12	21	0	27	0	9	0	540
	TB8	4	2	4	6	0	4	0	1	0	91
	Total	27	9	12	21	0	27	0	9	0	540
HTBL - Vacuum	Vacuum	34	0	93	25	0	0	17	0	0	983
	Total	34	0	93	25	0	0	17	0	0	983
HTBL - cryoload	TB1	11	2	21	9	6	3	3.75	0	0	298
	DB1	12	2	21	8	6	3	3.75	0	0	301
	TB2	11	2	21	9	6	3	3.75	0	0	298
	DB2	12	2	21	8	6	3	3.75	0	0	301
	TB3	11	2	21	9	6	3	3.75	0	0	298
	TB4	11	2	21	9	6	3	3.75	0	0	298
	TB5	11	2	21	9	6	3	3.75	0	0	298
	FB3	0	0	0	0	0	0	0	0	0	0
	TB6	11	2	21	9	6	3	3.75	0	0	298
	DB3	12	2	21	8	6	3	3.75	0	0	301
	TB7	11	2	21	9	6	3	3.75	0	0	298
	DB4	12	2	21	8	6	3	3.75	0	0	301
	TB8	11	2	21	9	6	3	3.75	0	0	298
	Total	136	24	252	104	72	36	45	0	0	3585

Table 12-4 Device I/O Summary for the Spectrometer Section, separated into beamline and cryoload control systems used to determine I/O requirements.

Beamline Section	Device	AI	AO	DI	DO	TEMP	5B	Serial	Ethernet	Motor Ctrl	EPICS IOC
Spectrometer Section - Beamline	FS0	10	2	10	27	0	0	0	1	1	233
	QS1A	9	3	8	11	0	9	0	3	0	204
	QS2B	9	3	10	12	0	9	0	3	0	213
	DS1	18	2	6	9	0	2	0	1	0	190
	FS1	13	2	18	41	0	0	0	1	2	342
	QS3B	9	3	10	12	0	9	0	3	0	213
	QS4B	9	3	10	12	0	9	0	3	0	213
	QS5C	9	3	8	11	0	9	0	3	0	204
	QS6C	9	3	8	11	0	9	0	3	0	204
	DS2	18	2	6	9	0	2	0	1	0	190
	FS2	11	2	14	39	0	0	0	1	2	312
	Total	124	28	108	194	0	58	0	23	5	2518
Spectrometer Section - Vacuum	Vacuum	18	0	74	26	0	0	12	0	0	708
	Total	18	0	74	26	0	0	12	0	0	708
Spectrometer Section – Cryoload	QS1A	11	2	21	9	6	3	3.75	0	0	298
	QS2B	11	2	21	9	6	3	3.75	0	0	298
	DS1	12	2	28	10	15	1	3.75	0	0	382
	QS3B	11	2	21	9	6	3	3.75	0	0	298
	QS4B	11	2	21	9	6	3	3.75	0	0	298
	QS5C	11	2	21	9	6	3	3.75	0	0	298
	QS6C	11	2	21	9	6	3	3.75	0	0	298
	DS2	12	2	28	10	15	1	3.75	0	0	382
	Total	90	16	182	74	66	20	30	0	0	2551

12.2.2 Protection systems requirements

The requirements for protection systems are derived from the hardware used to support the design of the HRS and fall into two categories, personnel protection and machine protection. The use of superconducting magnets requires an oxygen deficiency hazard monitoring system. Prompt radiation produced by the beam requires a radiation safety system. Possible damage from the beam to equipment and detectors in the vault determine the requirement for a machine protection system. The requirements for Personnel Protection Systems (PPS) include monitoring radiation levels, providing warnings and triggering beam shutdown when levels exceed thresholds. It also includes providing access control to the vault to prevent personnel from being present when beam is present in the vault. It provides low-oxygen monitoring and flammable-gas detection and alarming using both visual and audio systems upon detection. If oxygen concentration levels below 19.5% are detected, both audible and visual alarms will be triggered signaling for evacuation from the vault. Additionally, flammable gasses will be used in some detector systems used with the HRS, requiring monitoring for such flammable gases in the vault. If unsafe levels are detected this system will also signal evacuations using both audible and visual alarms.

The PPS is to be compatible with existing Laboratory personnel protection systems, using similar hardware for both the PLCs, monitoring, and miscellaneous hardware to minimize the total cost of ownership across the Laboratory.

The Machine Protection Systems (MPS) are to provide a hardware interface for diagnostics which will shut down beam delivery within 500 ms if an unsafe beam condition is detected for the hardware based on the current diagnostics.

In Table 12-5, an example of safety devices for the proposed design for the Radiation Safety portion of PPS is provided as an example of how I/O requirements for the personnel protection system are determined, adding up digital inputs (DI) and digital output (DO) points.

Table 12-5 Radiation Safety System Hardware and I/O List used to determine I/O requirements

Device	Qty	DI	DO
Door Switch	4	8	4
Gate Switch	2	4	2
E-Stop	5	10	5
Light Stack	5		15
Gamma Detector	2	6	
Neutron Detector	4	12	
Rad Monitor	3	3	
Wall Plug	1	2	1
Beacon	7		7
Arm Button	6	12	6
I/O Count Totals		57	40

12.2.3 Network and IT requirements

The requirements for network connections flow from the hardware used in the beamline design. Power supplies, vacuum controllers, low level controls require Ethernet or serial connections. The overall design is an extension of existing Laboratory design, utilizing standardized hardware and providing similar bandwidth to existing systems. IT will utilize existing file servers, file storage, and archivers, and will expand capabilities for the additional signals being added to the control system.

12.3 Design approach

The requirements are readily achieved using systems that are the same or similar as those that have been in use at NSCL and/or were more recently implemented at FRIB. This approach minimizes both cost and performance risk and does not require an R&D program. This also reduces the overall cost of ownership in expertise required to support similar systems and in spare parts costs.

12.3.1 Low-level control systems design approach

While the control system is based on EPICS, hardwired inputs will be wired into separate PLCs for beamline, vacuum, and cryogenic signals. Requirements from assessments in Table 12-3 and Table 12-4 are used to determine the PLC I/O modules required and associated hardware to support

the system. The I/O modules and PLC drops are tallied in Table 12-6 for the HTBL and in Table 12-7 for the Spectrometer Section.

Cryogenic control systems require a higher level of reliability and will tie into cryo-plant controls. Redundant power supplies and uninterruptable power supplies (UPS) will be utilized for those systems.

Table 12-6 PLC hardware design summary for the HTBL.

		AI	AO	DI	DO	TEMP	5B	Serial	Ethernet	Motor Ctrl	EPICS Signals
Beamline PLC	Signals	257	84	156	267	0	232	0	82	4	5465
	I/O Modules	17	11	10	17	0	15	0		1	
	Module Total			55							
	Drops Required			7							
Vacuum PLC	Signals	34	0	93	25	0	0	17	0	0	983
	I/O Modules	3	0	6	2	0	0	2		0	
	Module Total			11							
	Drops Required			2							
Cryoload PLC	Signals	136	24	252	104	72	36	45	0	0	3585
	I/O Modules	9	3	16	7	9	3	3		0	
	Module Total			35							
	Drops Required			4							

Table 12-7 PLC hardware design summary for the Spectrometer Section.

		AI	AO	DI	DO	TEMP	5B	Serial	Ethernet	Motor Ctrl	EPICS Signals
Beamline PLC	Signals	124	28	108	194	0	58	0	23	5	2518
	I/O Modules	8	4	7	13	0	4	0		1	
	Module Total			32							
	Drops Required			4							
Vacuum PLC	Signals	18	0	74	26	0	0	12	0	0	708
	I/O Modules	2	0	5	2	0	0	1		0	
	Module Total			9							
	Drops Required			1							
Cryoload PLC	Signals	90	16	182	74	66	20	30	0	0	2551
	I/O Modules	6	2	12	5	9	2	2		0	
	Module Total			25							
	Drops Required			3							

12.4 Preferred alternative

12.4.1 Controls systems preferred alternative/hardware

The PLC proposed for the HRS is based on the Allen Bradley ControlLogix Family. This was originally selected for NSCL and FRIB due to several factors. It has the largest installed market share in industrial settings in North America and is used at other national laboratories such as JLab and ORNL. There is existing in-house expertise and the manufacturer provides excellent local support. The I/O cards provide the direct interface to the process devices via modular I/O. Digital I/O interfaces with discrete logic signals via 24 VDC. Analog I/O interfaces for devices will use 4-20 mA current loops or ±10 VDC signal levels. Other signaling levels can be translated through appropriate signal conditioning. An example of a PLC system in shown in Figure 12.1(a) and I/O wiring installation in racks is shown in Figure 12.1(d).

Interface modules (IFMs) will be used as the connection point between the 1756 ControlLogix PLC Input and Output modules and the signals from the operational devices. This significantly reduces the amount of labor and possible errors involved in wiring terminal blocks to the PLC I/O modules.

a)

b)

c)

d)
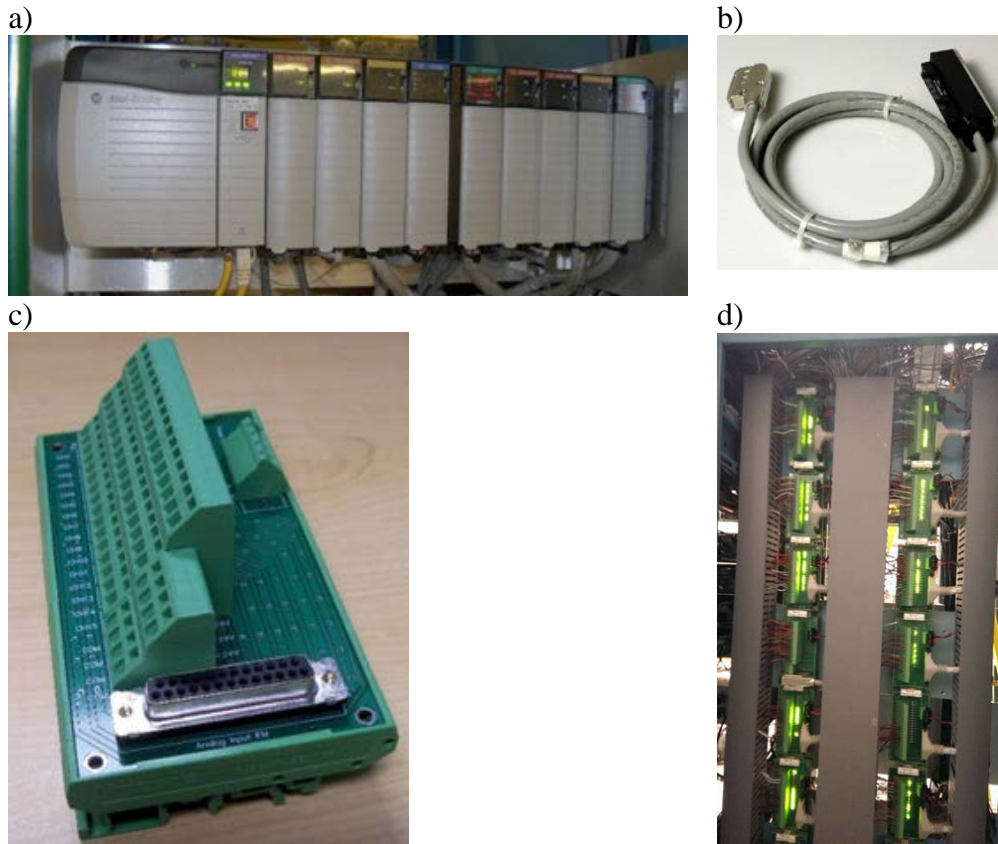
Figure 12.1 a) PLC installed in rack; b) Commercial cable; c) Sample IFM; d) 19" racks installed at the Laboratory

The IFMs were designed in house (see Figure 12.1(c)) to interface with specific Allen Bradley I/O modules. Unlike commercial versions, they have added 24VDC or Com connections for every signal (module-type dependent) through the use of multi-level terminal. The IFMs use one module for each IO type, analog input and output, digital inputs and outputs, and utilize a commercial pre-

wired cable (see Figure 12.1(b)) from the I/O module to the IFM to reduce the amount of customized wiring.

While many devices such as power supplies, vacuum controllers, and motor controllers have intelligent Ethernet interfaces where signals can be read directly into EPICS, any signals that will use interlocks will be hardwired from the devices to a PLC.

All of the PLCs will have the ability to interface directly with EPICS Input Output Controllers. The EPICS IOCs convert PLC tag names into EPICS control system names that can be accessed across the control system network and allows users the ability to control and monitor devices connected through the PLCs. The number of EPICS channels required by the project will determine the number of EPICS IOCs.

High level controls design will include operations screens, high level EPICS IOCs, channel archivers and logbooks similar to the existing facility.

Instrumentation signals requiring a transducer or signal-level conditioning will use a subset of commercially available hardware utilized in NSCL and FRIB. All controls instrumentation is located in racks placed outside of the experimental vault to protect against any radiation damage. In addition, this provides access to the instrumentation without the need for entering the vault during experiments.

Cryogenic temperatures will be read utilizing Lakeshore Monitors hardware as is used for FRIB. This provides the advantage of utilizing the same manufacturer for sensor and instrumentation interfaces, reducing possible future incompatibilities between equipment obtained from different vendors. Most temperature readings will be read over the serial interface by the EPICS control system. When temperatures are needed in a control loop within the PLC, they will be wired directly to the PLC as an analog input from the Lakeshore Monitor.

Cryogenic helium levels will be read through American Magnetics level monitors which also provide burnout protection to the sensor. Lakeshore temperature monitors and the American Magnetics level monitors provide digital outputs for use with interlocks, and provide local displays independent of the control system. Analog readings are also provided and hardwired into the PLC. Lead drops and pressure sensors will utilize a commercially available Isolated Signal conditioning Module called a 5B module to convert from low-level signals to standard analog input values of ±5 V wired to the PLC.

Delta V and quench detection for the 11 magnets mentioned in the controls requirements section will utilize Danfysik commercial 4-channel quench-detector hardware, which will monitor up to 4 magnets. The quench outputs will provide digital inputs to the PLC to interlock off the PS and fire the fast dump switch.

12.4.2 Protection systems preferred alternative and hardware

Personnel Protection Systems (PPS) are separated into two systems: Radiation Safety System (RSS) and Oxygen Deficiency Hazard (ODH), as shown in Figure 12.2.
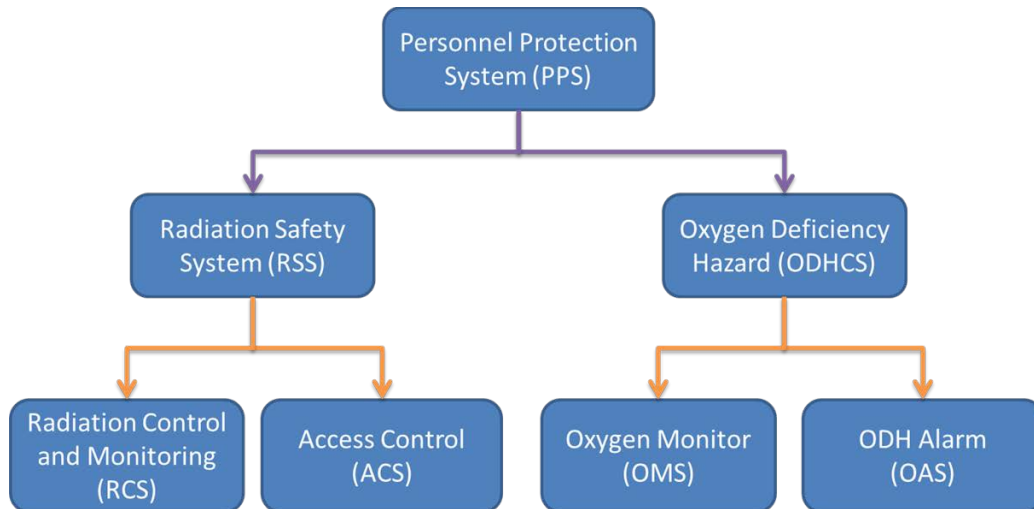
Figure 12.2 Personnel Protection System Architecture

Radiation Safety PPS includes radiation control and monitoring, access control, and beam intercepting devices. Oxygen Deficiency PPS includes monitoring and alarming functions.

The personnel protection system will be an extension of the Laboratory's existing experimental radiation safety system and Oxygen Deficiency Hazard Control System (ODHCS). It will utilize a safety rated Allen Bradley GuardLogix PLC. The safety PLC monitors inputs from door switches, E-stops, arm buttons, radiation monitors, and oxygen monitors to either trigger the interruption of beam, or to trigger warning alarms using both lights, and audible systems. A conceptual layout of the PPS for the HRS is shown in Figure 12.3. It illustrates the placement of safety hardware, monitors and detectors. The system also includes a wall plug, beam stop and faraday cup.

While experiments in the HRS vault are ongoing, the vault is secured by using an access control system. Radiation levels are monitored in and around the experimental areas as seen in Figure 12.3. Neutron Radiation levels above an initial threshold of 0.5 mR/hr for public areas, and 2 mR/hr within the radiation level 2 areas of the lab, will trigger a magenta radiation warning light. Higher radiation levels (2 mR/hr for public areas, 5 mR/hr within the radiation level 2 areas in the lab) will shut off the beam. Access control violations into the HRS Vault while running beam into the vault will also terminate the beam. The ODH system will have sensors that measure oxygen concentrations and the presence of flammable/explosive gases. Appropriate warning lights and audible systems will be utilized for both radiation safety and ODH safety systems, posted within the vault and at entrances as seen in Figure 12.3.

MPS will provide a Fast Protection System slave node in the HRS rack room. This will interface to the FRIB machine protection system Fast Protection System Master via a fiber connection. The overall architecture is shown in Figure 12.4. Diagnostic devices requiring a beam shut off can be hardwired to the HRS MPS slave using either a fiber or copper connection and will provide one of two signals ("Not OK" and "Not OK latch") to the MPS slave. If the "Not OK" signal is detected by the MPS slave from the diagnostic electronics, the signal will be relayed to the FRIB MPS master, which in turn will terminate the beam through mitigation devices in the FRIB Front End.
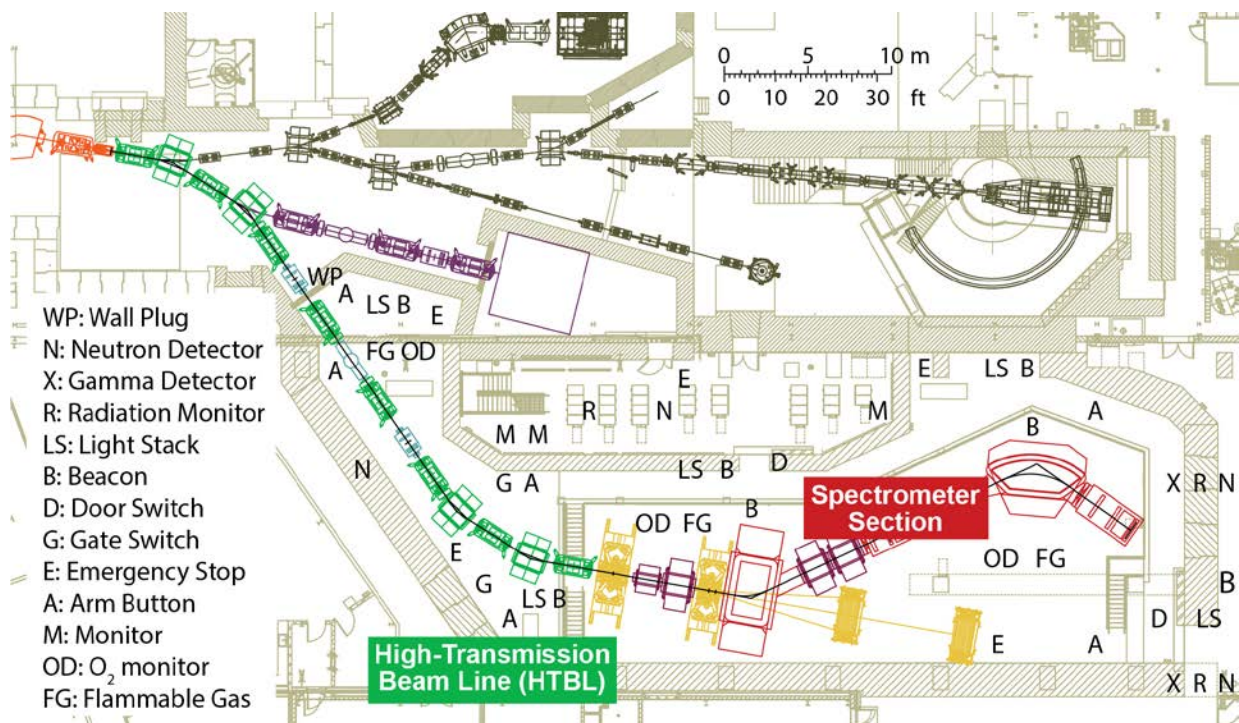
Figure 12.3 Conceptual layout of the Personnel Protection Systems for the HRS.

WP: Wall Plug
N: Neutron Detector
X: Gamma Detector
R: Radiation Monitor
LS: Light Stack
B: Beacon
D: Door Switch
G: Gate Switch
E: Emergency Stop
A: Arm Button
M: Monitor
OD: O_2 monitor
FG: Flammable Gas

High-Transmission Beam Line (HTBL)

Spectrometer Section
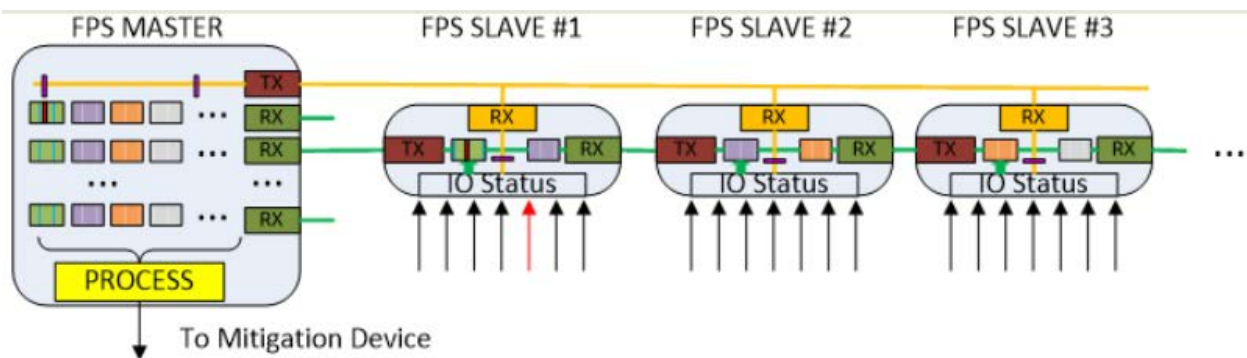
Figure 12.4 MPS Fast Protection System architecture

12.4.3 Network and IT preferred alternative/hardware

The Network design will extend the existing experimental controls network utilizing Juniper series smart switches. Juniper switches are an MSU/FRIB/NSCL standard and provide the best performance/price ratio. The expected number of ports based on the requirements demonstrated in the Table 12-3 and Table 12-4. The total number of connections for the project will be covered by the use of a pair of fiber-uplinked aggregation switches and six edge switches. The controls network architecture is shown in Figure 12.5. IT will utilize existing file servers, file storage, and archivers, and will expand capabilities for the additional signals being added to the control system.
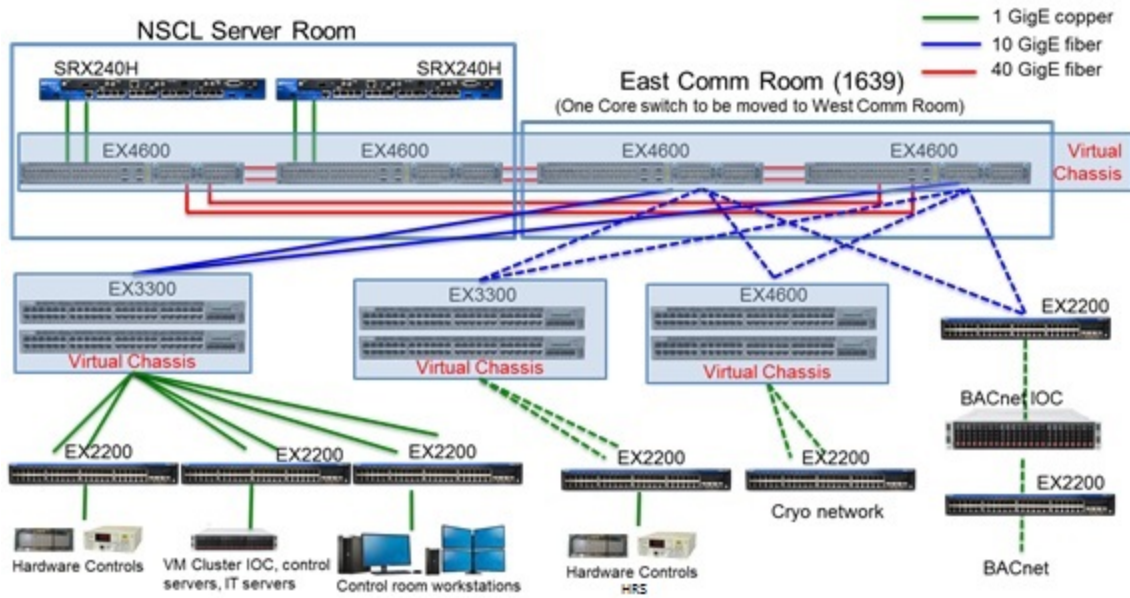
Figure 12.5 Controls Network Architecture

13 Vacuum Systems

13.1 Introduction and overview

In Table 13-1, the WBS entries of relevance for the vacuum systems of the HRS are provided, which include the vacuum systems for the HTBL and the Spectrometer Section. In Figure 13.1, the scope of the vacuum systems is shown. It includes the diagnostic and detector boxes, gate valves, bellows, flanges, and beam-line chambers that connect the ion-optical elements. However, the vacuum chambers inside the magnetic elements (e.g. dipoles, quadrupoles) are not included, as they are included as part of the scope of the magnets.

Table 13-1 WBS for the vacuum systems for the HRS

Experimental Systems - High Rigidity Spectrometer	HRS.3
High Transmission Beamline (HTBL)	HRS.3.01
High Transmission Beamline Vacuum	HRS.3.01.04
Spectrometer Section	HRS.3.02
Spectrometer Section Vacuum	HRS.3.02.06
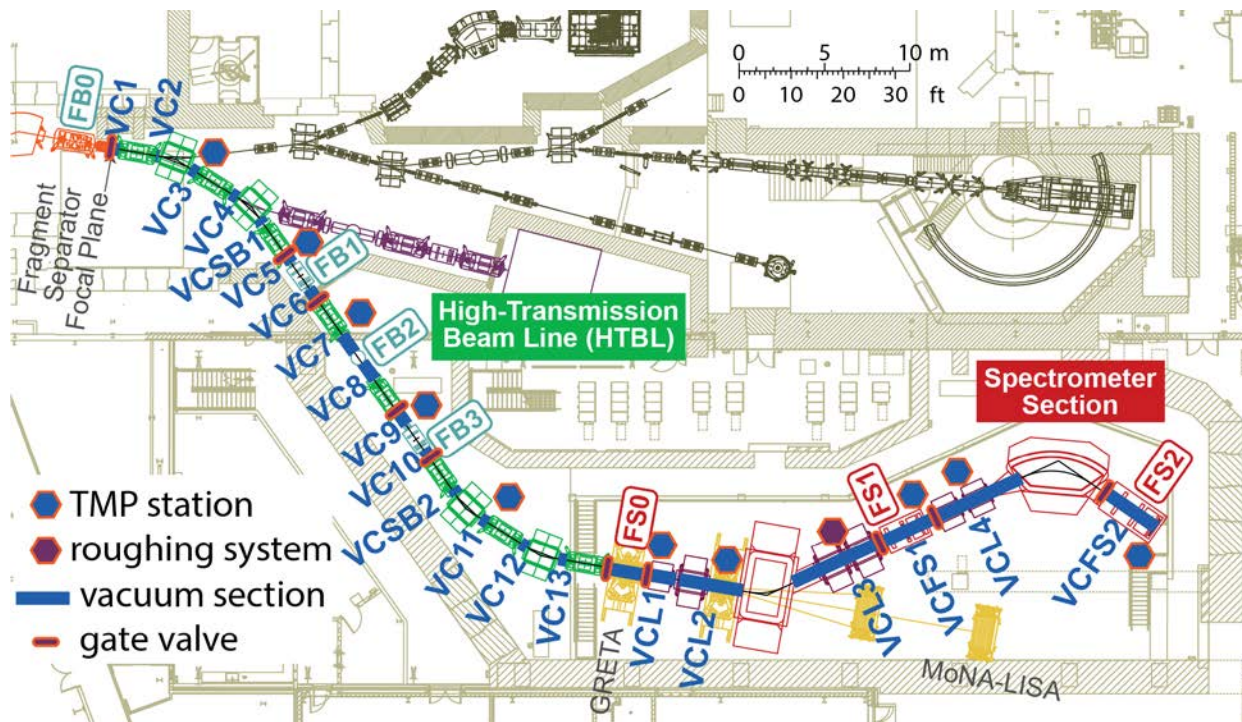
Figure 13.1 Overview of the vacuum elements and pumping systems of the HRS.

13.2 Requirements

The requirements of vacuum system originate from the lattice design that meets the scientific requirements (see Section 4) for the HTBL (See Section 5.6.3), the Spectrometer Section (See Section 6.5.3), and their detector and diagnostic systems (See Section 7). The required pressures for the HTBL and the Spectrometer Section of the HRS are 1.0×10^{-5} Torr, based on experience

with running experiments with fast beams in the S800 Spectrograph and the sweeper magnet system. This level of vacuum is sufficient to operate all detector systems except for the Multi-Channel Plates (MCPs; see Section 7.3.1.5), which requires a pressure of ~1.0×10^{-6} Torr. When that system is used, that pressure will be achieved by adding pumping capacity locally, as is presently done for the operation of MCP detectors in the beam line to the S800 Spectrograph.

Gate valves must be included in the design of the vacuum system to enable the isolation of beam line sections and diagnostic chambers for servicing specific items without the need for venting the entire beam line. The beam chambers must have sufficient diameters to allow for the transmission of the rare isotope beams from the ARIS Fragment Separator to the target station of the HRS and for the transport of reaction products to the focal planes of the Spectrometer Section.

Turbo-molecular pumping systems must be placed outside of magnetic fields in excess of 50 Gauss. This limits the location where they can placed, especially for the large sweeper dipole DS1, as shown in Figure 6.11

13.3 Design approach and alternative analyses

The design approach was largely based upon decades of experience with beam-line and spectrometer systems at NSCL, as well as the more recent FRIB vacuum system experience. Since these approaches have proven to have appropriate performance and are cost-effective both in terms of initial procurements and life-cycle costs, no viable alternatives were identified.

13.4 Preferred alternative

As shown in Figure 13.1, the HRS vacuum system contains twenty-five vacuum chambers, six of which contain diagnostic devices and detectors along the beamline (FB1, FB2, FB3, FS0, FS1, and FS2). The beam pipes in the HTBL section have a nominal diameter of 0.2 meters. In the Spectrometer Section (downstream of FS0), larger beam profiles require chambers and beam pipes with apertures of more than one meter in diameter. The vacuum elements for the HTBL are provided in Table 13-2 and for the Spectrometer Section in Table 13-3. They include the dimensions of each section, which are designed to accommodate the trajectories of rare isotope beams based on the ion-optical studies presented in Section 5 for the HTBL and Section 6 for the Spectrometer Section. There is sufficient space around the magnets to place turbo-molecular pumps outside of regions where magnetic fields in excess of 50 Gauss are present.

Ten in-line gate valves are included to allow independent pump-down of beamline segments, and removal of diagnostic chambers without the need to vent the entire beamline. Additionally, gate valves are located on each of the ten turbo-molecular pumping stations installed along the beamline for machine protection and ease of maintenance. The HTBL section of the HRS beamline is very similar in design to the existing A1900 beamline, currently in operation at NSCL. Due to their design similarities, five turbo pumping stations with similar capacity to those used in A1900 (~500 l/s nominal pumping speed) were selected for the HTBL. The significantly larger chamber volumes in the spectrometer section require higher-capacity pumps. Therefore, five 2000 l/s turbo pumping stations were selected. To supplement these pumping stations, a large roots pumping system was specified to aid in the evacuation of the large volume spectrometer section vacuum vessels.

Table 13-2 Vacuum elements of the HTBL.

Item	Description	Flange Size
GV10	Gate Valve 10" CFF	CFF 10"
VC1	Vacuum chamber ~0.47m long, 0.2m bore, 10" CFF; 2.75" CFF ports for gauges	CFF 10"
TB1	Magnetic element	
VC2	Vacuum chamber ~0.46m long, 0.2m bore, 10" CFF ends; 2.75" CFF ports for gauges	CFF 10"
DB1	Magnetic element	
VC3	Vacuum chamber ~0.45m long, 0.2m bore, 10" CFF ends; 10" CFF side port for pumping; 2.75" CFF ports for gauges	CFF 10"
TB2	Magnetic element	
VC4	Vacuum chamber ~0.45m long, 0.2m bore, 10" CFF ends; 2.75" CFF ports for gauges	CFF 10"
DB2	Magnetic element	
VCSB1	Vacuum chamber ~0.46m long, 0.2m bore, 10" CFF ends; 2.75" CFF ports for gauges	CFF 10"
TB3	Magnetic element	
GV10	Gate Valve 10" CFF	CFF 10"
VC5	Vacuum chamber ~0.49m long, 0.2m bore, 10" CFF ends; 10" CFF side port for pumping; 2.75" CFF ports for gauges	CFF 10"
FB1	Diagnostic Chamber (Viewer system, position detector x2, timing detector)	CFF 10"
VC6	Vacuum chamber ~0.49m long, 0.2m bore, 10" CFF ends; 2.75" CFF ports for gauges	CFF 10"
GV10	Gate Valve 10" CFF	CFF 10"
TB4	Magnetic element	
VC7	Vacuum chamber ~1.32m long, 0.2m bore, 10" CFF ends; 10" CFF side port for pumping; 2.75" CFF ports for gauges	CFF 10"
FB2	Diagnostic Chamber - 6 way cross (retractable viewer system)	CFF 10"
VC8	Vacuum chamber ~1.32m long, 0.2m bore, 10" CFF ends; 2.75" CFF ports for gauges	CFF 10"
TB5	Magnetic element	
GV10	Gate Valve 10" CFF	CFF 10"
VC9	Vacuum chamber ~0.9m long, 0.2m bore, 10" CFF ends; 10" CFF side port for pumping; 2.75" CFF ports for gauges	CFF 10"
FB3	Diagnostic Chamber (Viewer system, position detector, timing detector, energy-loss detector & slit system)	CFF 10"
VC10	Vacuum chamber ~0.9m long, 0.2m bore, 10" CFF ends; 2.75" CFF ports for gauges	CFF 10"
GV10	Gate Valve 10" CFF	CFF 10"
TB6	Magnetic element	
VCSB2	Vacuum chamber ~0.46m long, 0.2m bore, 10" CFF ends; 2.75" CFF ports for gauges	CFF 10"
DB3	Magnetic element	
VC11	Vacuum chamber ~0.45m long, 0.2m bore, 10" CFF ends; 2.75" CFF ports for gauges	CFF 10"
TB7	Magnetic element	
VC12	Vacuum chamber ~0.45m long, 0.2m bore, 10" CFF ends; 10" CFF side port for pumping; 2.75" CFF ports for gauges	CFF 10"
DB4	Magnetic element	
VC13	Vacuum chamber ~0.45m long, 0.2m bore, 10" CFF ends; 2.75" CFF ports for gauges	CFF 10"
TB8	Magnetic element	

Table 13-3 Vacuum elements of the Spectrometer Section

Item	Description	Flange Size
GV10	Gate Valve 10" CFF	CFF 10"
FS0	HRS Target (Viewer system, position detector, timing detector)	CFF 10"
GVL	Gate Valve 1.1m diameter	O-ring seal
VCL1	Vacuum chamber ~2m long, 0.5m bore, 12" CFF port for pumping, 2x 2.75" CFF ports for gauges	O-ring seal
VCL2	Vacuum chamber ~3m long, 1.1m bore; 12" CFF port for pumping, 2x 2.75" CFF ports for gauges	O-ring seal
DS1	SWEEPER MAGNET	
VCL3	Vacuum chamber ~6m long, 1.1m bore; 12" CFF port for pumping, 2x 2.75" CFF ports for gauges	O-ring seal
GVL	Gate Valve 1.1m diameter	O-ring seal
FS1	Vacuum chamber 1.5m x 1.5m x 3.0m	O-ring seal
GVL	Gate Valve 0.7m diameter	O-ring seal
VCL4	Vacuum chamber ~6m long, 0.7m bore; 12" CFF port for pumping, 2x 2.75" CFF ports for gauges	O-ring seal
DS2	SPECTROMETER DIPOLE MAGNET	
GVR	Gate Valve 1.1m x 0.22m rectangular	Custom O-ring
FS2	Vacuum chamber 1.5m x 1.5m x 5.0m	O-ring seal

14 Conventional Facilities

14.1 Introduction

The Conventional Facilities will be provided by Michigan State University at a cost of ~$23M. The construction of the 31000-square-foot High Rigidity Spectrometer and Isotope Harvesting vault began mid-calendar year 2018 with beneficial occupancy provided at the beginning of calendar year 2020. The new vault is located in the center of the FRIB complex as shown in Figure 14.1.
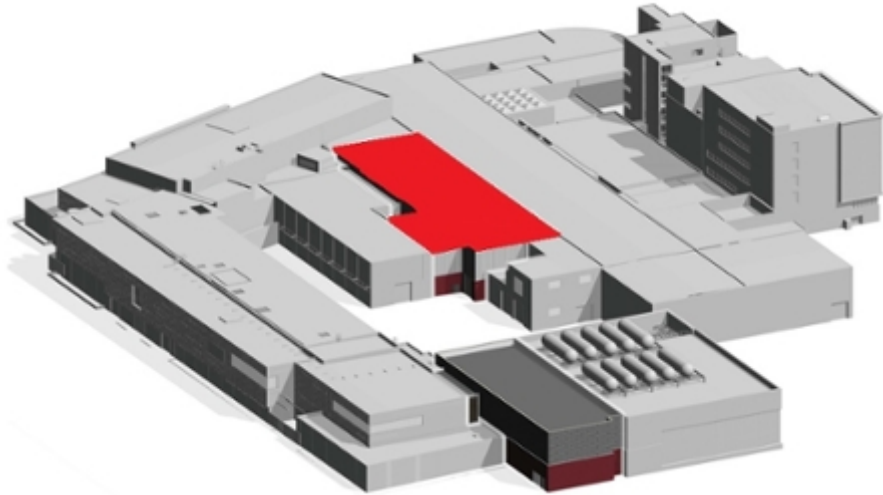
Figure 14.1 The location of the High Rigidity Spectrometer and Isotope Harvesting vault (indicated in red) within the FRIB complex on the campus of Michigan State University.

The layout of the HRS, consisting of the HTBL and the Spectrometer Section are provided in Figure 14.2. Note that the initial section of the HTBL, from FB0 (the final focal plane of the ARIS fragment separator) to FB2 will be situated inside the existing building infrastructure. An internal wall between FB1 and quadrupole triplet TB4 separates the FRIB Laboratory beam delivery system from the experiment area that houses the HRS. The high bay that houses the HRS also houses the Isotope Harvesting Laboratory (on the west side), which will be separated from the HRS area by a radiation shielding wall.
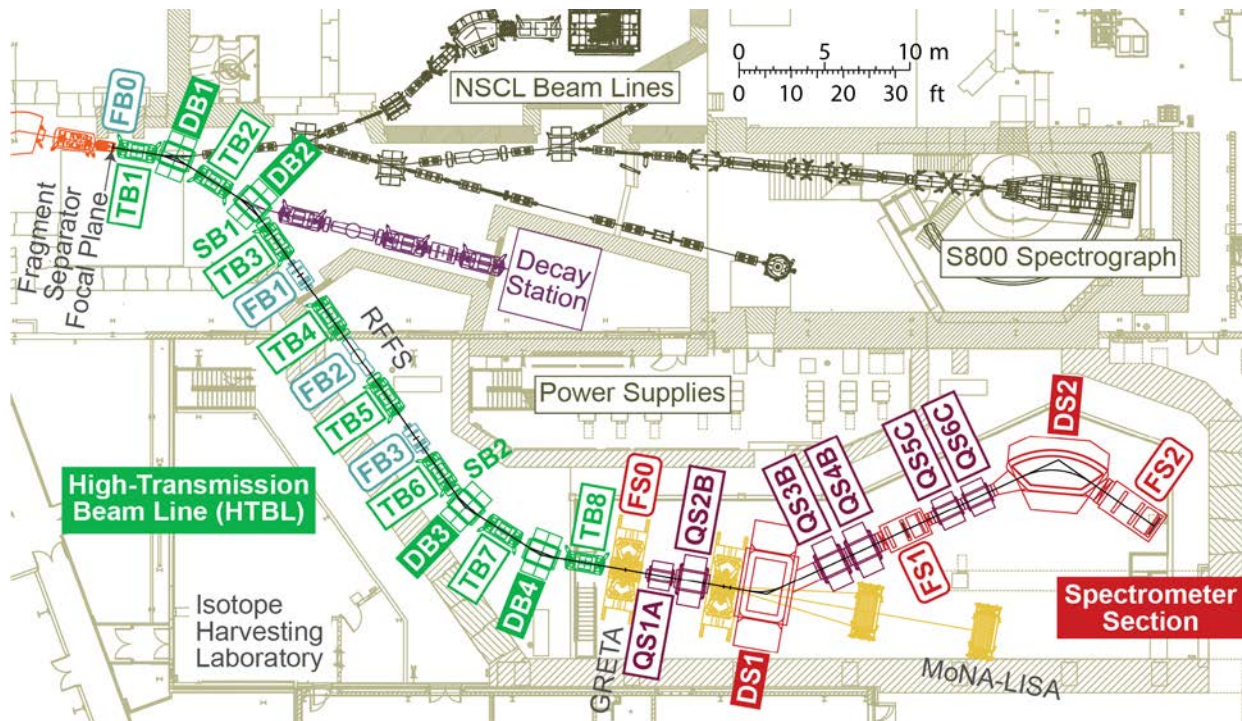
Figure 14.2 Layout of the High-Transmission Beam Line (HTBL) and the Spectrometer Section of the HRS.

14.2 Radiation transport and safety

14.2.1 Requirements

The radiation shielding for the High Rigidity Spectrometer (HRS) experimental area has been analyzed [GEO18] to ensure that it will achieve radiation dose levels external to the shielding compatible with requirements for controlled areas (<2 mrem/h) and for public areas (<2 mrem in any hour and <100 mrem in a year) [GRI18].

14.2.2 Radiation transport analysis

A Monte-Carlo radiation transport code PHITS [SAT13] was used to evaluate radiation environment in the HRS experimental area to ensure the adequacy of the proposed shielding. The effect of penetrations in the shielding was evaluated using PHITS and a labyrinth formalism using a semi-empirical method outlined in [COS14]. To cover the range of possible conditions, a light (^{18}O), a medium (^{132}Sn), or a heavy (^{238}U) beam with an energy of 250 MeV/u and an intensity of 10^7 particles per second (pps) was stopped in a beryllium target at one of three possible locations labeled S1, S2, and S3 (see Figure 14.3). To perform failure mode analysis, another set of points labeled F1, F2, and F3 was identified as failure locations to mimic scenarios where a dipole fails and a beam goes straight into concrete walls instead of being bent by a dipole (see also Figure 14.3). The resulting radiation fields are linearly proportional to beam intensity; maximum beam intensities compatible with radiation requirements were determined.

A simplified radiation transport geometry was used that has a realistic shielding layout and includes beamline magnet iron parts, but not other items in the vault inconsequential to radiation shielding such as vacuum chambers, detectors etc.

The radiation outside the vault at locations where personnel can be present, labelled L3, L4, L6-9, and above the roof beams, as well as sky shine and at the closest public area was evaluated (see Figure 14.3). Dose equivalent rates were estimated 30 cm away from nearest walls. Vertical integration was performed according to NASA "human torso" definition, approximately 61 cm to 190 cm above the ground surface [NAS95]. The radiation levels at L6, the exhaust air labyrinth used to mitigate oxygen deficiency hazard conditions, were evaluated by using PHITS and by using the above-mentioned semi-empirical method [COS14]. The latter method was found to overestimate radiation levels several times compared to PHITS. Other penetrations were evaluated by using the semi-empirical method.
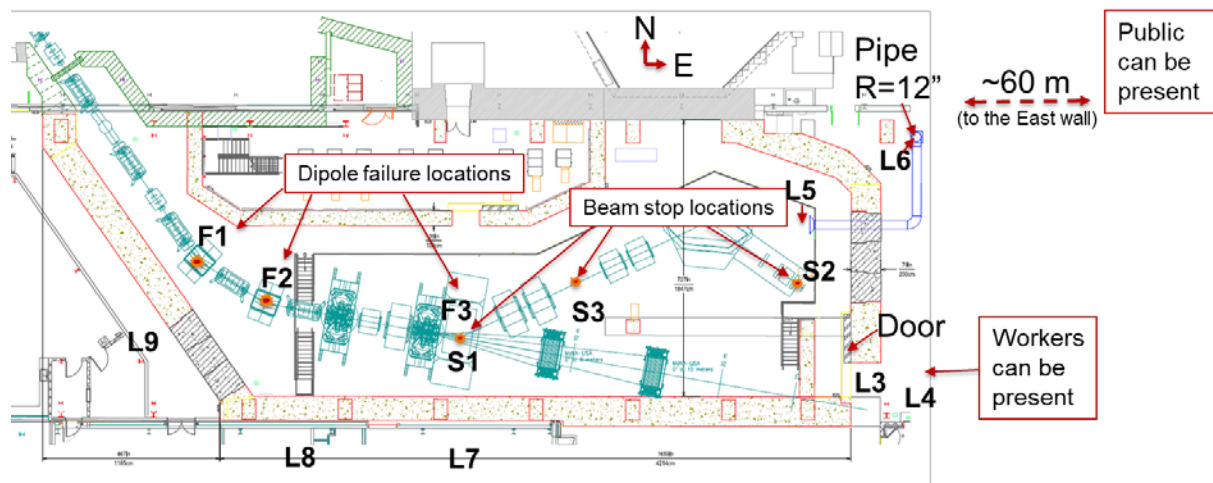
Figure 14.3 HRS layout showing three possible beam loss locations (S1, S2, and S3), dipole failure locations (F1, F2, and F3) and radiation dose evaluation points (tallies) L3 (30 cm from door), L4 (30 cm from wall), L6 (60 cm cube at exit of 12" pipe), L7,L8, and L9 (30 cm from nearest walls). Labeled "Door", the main vault entrance door consists of 18-inch thick steel backed by 6 inches of polyethylene. The closest public area is also shown.

14.2.3 Radiation analysis results

The dose equivalent rates (in mrem/h) calculated for tally points L3, L4, L6, L7, L8, and L9 for ^{18}O, ^{132}Sn, and ^{238}U beams at 250 MeV/u stopped at loss points S1, S2, and S3, or passing through a failed dipole magnet at F1, F2, and F3, were converted to beam intensities (in particles per second, or pps) meeting the 2 mrem/h requirement are presented in Table 14-1 and Table 14-2 . These beam intensities are compatible with the HRS Science program. Experiments with beam intensities of 10^6 pps are possible across the chart of nuclei and for many beams intensities of 10^7 pps or higher are feasible, especially if shielding is added locally to further reduce dose rates.

Table 14-1. Beam intensities in particles per second (pps) that satisfy the 2 mrem/h requirement for 250 MeV/u ^{18}O, ^{132}Sn, and ^{238}U stopped at beam loss locations S1, S2, and S3 and tally locations L3, L4, L6, L7, L8, and L9. (see Figure 14.3).

Beam Loss Point	S1			S2			S3		
Beam	^{18}O	^{132}Sn	^{238}U	^{18}O	^{132}Sn	^{238}U	^{18}O	^{132}Sn	^{238}U
Tally Location	Beam intensity (pps) for which the dose rate is less than 2 mrem/h								
L3	2.3E+08	5.2E+07	4.7E+07	1.3E+07	4.9E+06	4.6E+06	7.7E+09	4.1E+09	3.7E+09
L4	6.7E+08	1.5E+08	1.4E+08	3.5E+07	1.1E+07	9.8E+06	1.7E+10	5.7E+09	7.3E+09
L6	1.4E+11	6.7E+10	1.8E+10	1.7E+10	7.6E+09	1.1E+10	5.1E+09	3.5E+09	1.5E+09
L7	2.5E+11	7.7E+11	3.0E+12	4.5E+11	2.0E+12	4.8E+10	4.0E+13	3.3E+12	3.4E+12
L8	4.2E+11	4.7E+11	5.5E+12	7.1E+11	6.0E+11	9.4E+10	3.2E+12	3.6E+11	3.1E+12
L9	1.3E+12	3.4E+11	3.0E+13	1.7E+12	3.6E+11	2.0E+12	1.7E+12	1.9E+11	2.8E+12

Table 14-2 Beam intensities in particles per second (pps) that satisfy the 2 mrem/h requirement for 250 MeV/u ^{18}O, ^{132}Sn, and ^{238}U passing through dipole failure locations F1, F2, and F3 and tally locations L3, L4, L6, L7, L8, L9 (see Figure 14.3).

Dipole Failure Point	F1			F2			F3		
Beam	^{18}O	^{132}Sn	^{238}U	^{18}O	^{132}Sn	^{238}U	^{18}O	^{132}Sn	^{238}U
Tally Location	Beam intensity (pps) for which the dose rate is less than 2 mrem/h								
L3	4.1E+11	1.1E+11	9.1E+10	1.9E+10	5.3E+09	4.2E+09	4.9E+07	1.4E+07	1.1E+07
L4	1.1E+12	3.2E+11	2.5E+11	6.8E+10	1.9E+10	1.5E+10	2.2E+08	6.2E+07	4.9E+07
L6	5.4E+13	1.5E+13	1.2E+13	2.1E+11	5.8E+10	4.6E+10	6.0E+10	1.7E+10	1.3E+10
L7	1.2E+10	3.4E+09	2.7E+09	9.6E+07	2.7E+07	2.1E+07	2.9E+11	8.1E+10	6.4E+10
L8	2.3E+07	6.3E+06	5.0E+06	1.7E+09	4.8E+08	3.8E+08	7.2E+11	2.0E+11	1.6E+11
L9	2.3E+12	6.4E+11	5.1E+11	1.1E+12	3.2E+11	2.5E+11	3.4E+12	9.4E+11	7.4E+11

Dose rates in other key areas were estimated, including direct dose rates in the area accessible by general public and closest to the HRS facility (see Figure 14.3). For a 250-MeV/u ^{238}U beam at an intensity of 10^7 pps and stopped at S3, the dose rate was found to be 0.1 mrem/h. Lighter beams stopped at S3 produce lower doses. All beams stopped at S1 and S2 loss points produce significantly lower doses.

Dose rates from sky shine are very low; the highest dose rate is 2×10^{-4} mrem/h. Dose rates above the HRS vault roof could be as high as 0.25 mrem/h (for the ^{238}U beam stopped at S1 loss point). Other beams stopped at S1, and all beams stopped at other loss points, produce significantly lower doses.

Radiation levels produced by penetrations in the HRS experimental area shielding walls were also assessed. Radiation levels in the tally location L6, an area above the outer end of the 24" ventilation pipe, were analyzed (see Figure 14.3, "Pipe" in the NE corner). Among several HRS penetrations, this is by far the largest. PHITS Monte-Carlo analysis shows that dose rates at L6 exit are below

the limits. This penetration was also analyzed by using the "labyrinth" method of reference [COS14]. This method is conservative and overestimates radiation levels by ~5 to 30 times compared to the calculations with PHITS. The semi-analytical "labyrinth" method was used on the other vault penetrations; the analysis showed that these penetrations do not affect radiation levels outside of the walls.

14.2.4 Magnet power-supply interlocks

Rare isotope beams are guided from the fragment separator through the HTBL and the Spectrometer Section. A failure or incorrect setting of the magnets in the HTBL and Spectrometer setting could result in beams going in an unintended direction or have uncontrolled properties. To prevent such occurrences, the beam delivery to the HRS will be interlocked if read currents deviate from their set values by more than 1% for dipole magnets and 10% for quadrupole magnets. This interlock will trigger in about ~1 s, which reduces the amount of beam directed in an unintended direction to negligible level.

14.2.5 Summary

A radiation transport analysis was performed to assess the adequacy of the High Rigidity Spectrometer (HRS) experimental area shielding. To encompass the range of possible scenarios, representative beams ^{18}O (light), ^{132}Sn (medium), and ^{238}U (heavy) at 250 MeV/u and 10^7 particles per second (pps) where stopped in beryllium at three beam loss points S1, S2, and S3. Also, to mimic dipole failure scenarios that would result in a beam hitting a concrete wall, three locations, F1, F2, and F3, were identified as source locations. The resulting dose rates in key locations around the facility were scaled to determine the maximum beam intensities (in pps) necessary to meet the maximum dose criterion of 2 mrem/h. For a very large fraction of experiments, the beam intensities will be less than 10^6 pps and these can be performed without addition shielding, as the simulations indicate that the 2 mrem/h criterion is not exceeded for any beams with intensities below 4×10^6 pps. By adding shielding locally near locations where beams are stopped, it will be possible to perform experiments at higher intensities than 10^6 pps. The analysis also showed that penetrations maintain shielding integrity and do not produce significant local dose enhancements. Public exposure due to direct radiation and skyshine are below limits without additional shielding for all beams with intensities of up to 10^7 pps. Note that radiation monitors will be used to continuously monitor these doses. The beam will be stopped in the event that the dose rates exceed 2 mrem/h external to the experimental vault.

14.3 References

[COS14] J.D. Cossairt, Radiation Physics for Personnel and Environmental Protection, Fermilab report TM-1834, Rev 13, March 2014

[GEO18] Dali Georgobiani, HRS Radiation Shielding Analysis, FRIB-T40204-CA-000217, 2018

[GRI18] Peter Grivins, Laboratory Radiation Safety Manual, FRIB-S10300-MA-004597-R001 (Nov. 2018).

[NAS95] NASA Man-Systems Integration Standards, NASA-STD-3000, Volume I, section 3, https://msis.jsc.nasa.gov/sections/section03.htm

[SAT13] T. Sato, K. Niita, N. Matsuda, S. Hashimoto, Y. Iwamoto, S. Noda, T. Ogawa, H. Iwase, H. Nakashima, T. Fukahori, K. Okumura, T. Kai, S. Chiba, T. Furuta and L. Sihver, Particle and Heavy Ion Transport Code System PHITS, Version 2.52, J. Nucl. Sci. Technol. 50:9, 913, 2013

15 EHS&Q assurance

15.1 Introduction

FRIB operates under an established regulatory framework that includes the US Nuclear Regulatory Commission, the State of Michigan, and Michigan State University. The various regulatory agencies establish requirements for HRS design, and operation and provide oversight and inspection of the project's implementation of the requirements. The applicable ESH&Q regulatory requirements can be found in the FRIB Regulatory Requirements document [FRIB-R10103-TD-000014].

The Laboratory has committed to maintaining OHSAS 18001, ISO 14001, ISO 9001, and ISO27001 registered programs. These self-imposed and third-party registered management systems assure that FRIB maintains the current high standards for Occupational Health and Safety, Environmental Management, Quality Management, and Information Security Management required to maintain these certifications.

A risk-based approach is used to determine the need for controls on facilities, systems, or components to protect the public, workers, the environment and the Laboratory's mission. Controls that prevent or mitigate serious events will be formally credited as part of the approved safety envelope.

As used in this document, controls and hazard controls mean those engineered or administrative protective elements that are used to protect against a hazard. Normal process or operational controls are not included in these requirements except to the extent that their use is directly tied to hazard protection.

The concept of credited control is well established in the accelerator safety community. A credited control is defined in DOE Order 420.2C "Safety of Accelerator Facilities" [DOE420], as "controls determined through safety analysis to be essential for safe operation directly related to the protection of personnel or the environment."

FRIB extends the robust principles of credited control management to the management of controls for non-safety hazards of similar risk, such as investment and facility protection. FRIB credited controls consist of credited controls with Environment, Safety and Health (ESH) impact and credited controls without ESH impact. The intent is to manage like risks and hazards in a consistent, rigorous fashion.

The following are guiding principles for hazard controls:

- Controls shall be implemented as interventions that mitigate risk.
- Controls shall be selected using a risk-based approach.
- Controls management shall rely on certain key attributes.

Since the HRS Project is following consensus codes and standards, standard industrial hazards are addressed and the risks minimized by adherence to established policies of Michigan State University applicable to activities of the HRS and by implementing integrated safety management (ISM) practices through its certified ISO and OHSAS programs (ISO 14001, ISO 18001, ISO27001, and OHSAS 18001).

15.2 Hazard analysis and controls

The current FRIB Laboratory Hazard Analysis (HA) [FRIB-T10101-TD-001075] is a comprehensive hazard analysis that covers all aspects of the FRIB project and accelerator facility. The HRS project will be incorporated into this document to assure that hazards have been successfully captured and mitigated.

15.3 Hazard control implementation and management

Controls must be specified using a risk-based approach in which ongoing operations and credible upsets are listed, the probability and consequences are predicted, and a resulting risk is qualified. Controls are used as interventions to mitigate risks. Risks may be personal (for example, injury or illness), environmental (for example, spill, contamination, release to the environment), regulatory (for example, exceedance of a published standard), programmatic (for example, interruption of a user experiment), financial, reputational, or a number of other potential negative consequences.

The FRIB HA examines risks to personnel and the environment and provides a matrix appropriate for the qualification of risks. The selection of engineered and administrative controls depends upon the risk to workers, the public or the environment from the unmitigated hazard (that is, from failure of the controls). Controls must be assigned to reduce risk to a level that is "as low as reasonably practicable" (ALARP). In general, unacceptable risks (for example, high and medium as outlined in the FRIB HA) require the use of credited controls to reduce risks to an acceptable level, while acceptable risks (for example, low and extremely low) use non-credited controls per the ALARP principle.

Categorization of risk (for example, as high, medium, low, or extremely low) is made through a hazard analysis process.

- High risks generally require at a minimum multiple, independent, credited control systems to protect workers or the public from the risk.
- Medium risks should be mitigated using at least one credited (engineered and/or administrative) control system, supplemented by non-credited controls, basic safety management programs and inherent robust design.
- Low risks may be further reduced using a combination of engineered and administrative non-credited controls.
- If the unmitigated risk is extremely low then no additional controls are required, but may be applied as best practice.

15.4 Credited engineered controls

Credited Engineered Controls assure high risk hazards are mitigated. Eight attributes are associated with Credited Engineered Controls (CEC): competence; specificity; monitoring; fail-safe; responsibility; configuration management; initial verification and periodic testing; record keeping. Personnel Protection System (PPS) controls are a special class of Credited Engineered Controls that protect against extreme hazards. A ninth attribute is associated with these controls: independence.

CEC with ES&H impact are selected according to FRIB Requirements for Selecting ESH-Related Credited Controls [FRIB-T10401-AD-000353]. The IEC 61511 (Safety instrumented systems for

the process industry sector) Safety Integrity Level (SIL) process shall be followed for active engineered controls with ESH impact. The operation creating the hazard must stop, or space must be evacuated, when CEC with ESH impact is out of configuration.

15.5 Non-credited controls with ESH impact

Non-credited controls with ESH impact are used to 1) confirm the operability of CECs with ESH impact, also known as "defense in depth", or 2) confirm a specific hazard is mitigated when a regulatory driver with a prescriptive implementation program has been adopted. The "specific hazard" frequently is regarded as a "standard industrial hazard". While still high consequence, the risk is reduced by prescriptive legal requirements (i.e. lockout/tagout in occupational safety acts) and extensive engineering code and practice (i.e. National Electrical and American Society of Mechanical Engineers Codes).

15.6 Selection of credited controls

Once the need for a credited control is determined, a disciplined process has been established to select the set of equipment items (credited engineered controls), and/or administrative items (credited administrative controls) needed to accomplish the required safety function. The selection of credited controls often involves choices between multiple items that could function to control a particular hazard.

FRIB safety related credited controls selection is based on the FRIB Requirements for Selecting Safety Related Credited Controls.

1. When either an active or passive control can be credited to ensure the safety function, the passive control should be selected over the active. This selection is based on the inherently higher reliability of passive devices.

2. If either engineered control(s) or administrative control(s) could perform the needed safety function, the engineered control should be selected over the administrative control. This selection is based on the generally higher reliability of engineered controls versus human actions.

3. When a choice exists between controls that would prevent an event and controls that could mitigate the consequences of the event, the preventive controls should be selected over mitigating controls. This selection is based on the inherent value of preventing accidents as opposed to mitigating their effects.

4. Only those items essential for safe operation directly related to the protection of workers, the public, and the environment should be selected as Credited Controls. The number of Credited Controls should, in general, be minimized and include only a limited subset of the total number of controls employed for overall facility operation. This guidance allows a high degree of operational attention (e.g., monitoring, surveillance, maintenance, control of documentation, etc.) to be devoted to the Credited Controls. To support this selection criterion, Credited Controls that protect against multiple events or receptors are preferred.

5. Where two levels of control are selected, the controls are to be independent such that the failure of one level of control does not cause failure of the other. This criterion ensures that multiple levels of control are not compromised by a single failure.

6. When choosing between a single CEC to address each safety function or a common CEC to address multiple safety functions, the overall risk reduction shall be analyzed and reviewed, taking into consideration common points of failure and configuration management. The default project position is to avoid CECs that fulfill more than one safety function. This guidance prioritizes removing common failure modes.

15.7 Selection of non-credited controls

Non-credited engineered and administrative controls are selected based upon the specific hazards being protected against. Engineered controls are preferred and shall be implemented unless infeasible.

15.8 Management of controls

Credited and non-credited engineered and administrative controls shall be managed per best practice (for example, manufacturer recommendations) and in accordance with this plan and the Functional Safety Program. The technical system owner is responsible for the integrity of hazard controls necessary to safely operate the system. Changes to controls shall follow the Laboratory Configuration Management Plan and Functional Safety Program.

15.9 Management of credited controls

The system owner must ensure that the credited control, whether engineered or administrative, or a combination, is managed to include the following attributes. To accomplish this, a credited control system management plan specifying procedures for fulfilling these elements shall be established by the system owner.

1. **Competence.** Individuals who analyze, specify, design, operate, and maintain credited control systems must be competent in the tasks they perform.
2. **Specificity.** The elements that collectively make up the credited control system must be specified.
3. **Monitoring.** When credited controls provide feedback (for example, alarm status) indicating that the specified protection is being provided, the status of that feedback must be monitored to detect out-of-tolerance conditions and to direct appropriate responses.
4. **Fail-safe.** Credited controls must be configured, when practical, so that in the event of component failure due to internal or external events (including loss of power), the action is to maintain the protective nature of the control. Some credited controls may not be configured to be fail-safe. In these cases there must be sufficient redundancy of protection ("defense in depth") that a single failure will not lead to unacceptable risk.
5. **Responsibility.** Each credited control system must have a specified responsible owner who has the authority and responsibility for assuring that the system is managed per these requirements.
6. **Configuration management.** Before being placed into service, each new credited control system must be reviewed per the FRIB Device Readiness Review (DRR) process. Changes to a credited control system may only be made after a thorough review process to ensure that the level of safety required is maintained by the change. Changes may only be made after approval

by the responsible owner or designee. There may be separate configuration management processes for permanent changes and for temporary changes.

7. **Testing and Verification.** Credited control systems must be initially, and periodically thereafter, tested and verified to be operating properly. Testing intervals are specified in the credited controls system management plan. Procedures for the initial and periodic test and verification procedures must be specified and managed through a formal change control process.

8. **Recordkeeping.** Records of design and approval, as well as procedures for acceptance, testing and verification shall be maintained in a retrievable fashion. The hazard control system owner ensures that these records are maintained.

9. (PPS Only) **Independence.** The functional requirements, configuration, and validation of these controls is approved by the Radiation Safety Officer for radiation safety related PPS controls; and by the Chief Engineer for other PPS controls.

15.10 Compensatory measures

"Compensatory Measures" are temporary actions designed to afford equivalent protection when a CEC has failed or a new requirement arises. Compensatory measures can replace a CEC with an equivalent CEC, or compensatory measures may control a lesser hazard when additional Credited Administrative Controls are put in place to reduce risk. For example, shielding may be reduced when administrative rules are in place to limit beam species to heavy beams as heavy beams. Compensatory Measures need the same approvals as the originally approved CEC.

15.11 Management of non-credited controls

Non-credited controls shall be managed to include the following attributes:

1. **Competence.** Individuals who analyze, specify, design, operate, and maintain non-credited controls must be competent in the tasks they perform.

2. **Configuration management.** Changes to non-credited controls may only be made after assurance that the level of safety required is maintained by the change. Whenever a non-credited control system interacts (for example, signals, dependencies) with a credited control system, or interacts with any system such that the interaction crosses system boundaries or technical system ownership, that interaction must be documented. The documentation must specify the information that each system is receiving from the other, what the expected actions of each system in relation to that information are, and who is responsible for maintaining each side of that interface. The documentation is approved by the owner of the technical system having the hazards being controlled and contains concurring signatures of the hazard control system owners of the systems on all sides of that interface. That interface becomes a configuration controlled element.

3. **Verification.** Non-credited controls must be periodically evaluated to ensure that they continue to be effective. This evaluation may be through inspection, measurement, or other means.

4. **Recordkeeping.** Records of design, approval, acceptance, testing, and verification of non-credited controls must be maintained in a retrievable fashion. Who maintains these records is

generally specified in the institutional program managing the specific hazard for which the non-credited control is used.

15.12 Control identification and maintenance

CECs with ESH impact will be labeled. Workers will be trained to the specific requirements and attributes: competence, configuration management, testing and verification, and record keeping. Functional safety manager will verify color and label scheme for CECs with ESH impact at initial implementation and periodic testing.

Workers will be trained to specific requirements and attributes for Non-credited Controls with ESH impact: competence, configuration management, verification and record keeping.

15.13 Guiding principles of credited engineered controls with ESH Impact

The following summarizes the guiding principles of CECs with ESH Impact:
- CECs with ESH Impact mitigate unacceptable risk by separating humans from hazards
  - Prevent hazard > mitigate hazard > warn of hazard and respond
  - CECs are the first line of defense and must mitigate hazard without relying on non-credited controls
    - Non-credited controls and other layers of protection further mitigate risk per the ALARP principle
  - Work on CECs is considered high impact work and must be planned
  - Operation creating the hazard must stop or the space must be evacuated when the CEC with ESH Impact is out of configuration or in an incorrect state.
    - Restart of operation when CEC is corrected -or- compensatory measures in place
- CEC design must
  - Be based on quantified hazards and risk
  - Be as simple as possible while fully mitigating the hazard
    - Passive CEC > Active CEC
    - Minimize interfaces to other systems
    - Minimize scope and number of CECs
  - Be self-contained; not reliant on other systems or external inputs
  - Minimize the need for humans to assess or react
    - CEC > CAC
    - Human interfaces should be binary states; e.g., Safe (no alarm) or Evacuate (alarm)
    - Human interfaces and desired behavior should be consistent throughout the laboratory when practical
  - Meet the safety function when supporting infrastructure (network, electricity, etc.) fails, and in the event of any single component or function failure; fail-safe
  - Follow best practices:
    - Apply standards (e.g. IEC 61511 / SIL)
    - Follow other national laboratories' practices and guidance

- Use certified and pedigreed components
- CECs must be initially validated and periodically verified
- CECs must be completely and clearly documented throughout their life cycle
  - Hazard and risk assessment
  - Requirements
  - Design documents, calculations, ACLs
  - Safety assurance
  - Reviews
  - Approved configuration(s)
  - Validation and verification results

15.14 Quality assurance

HRS will be designed and built with the assistance of a fully involved Quality Assurance (QA) Program. A Quality Assurance Plan [FRIB-S10300-PL-000148] has been developed and is in use throughout the Laboratory. This plan specifies the program requirements that apply to all Laboratory work through a graded approach to ensure appropriate quality measures are applied in a manner commensurate with the scope.

15.15 References

[DOE420] DOE O 420.2C, Safety of Accelerator Facilities,
https://www.directives.doe.gov/directives-documents/400-series/0420.2-BOrder-c
[FRIB-R10103-TD-000014] FRIB Regulatory Requirements with ESH&Q inputs
[FRIB-S10300-PL-000148] FRIB Laboratory Quality Assurance Plan
[FRIB-T10101-TD-001075] FRIB Hazard Analysis
[FRIB-T10401-AD-000353] FRIB Requirements for Selecting Safety Related Credited Controls